University of Alberta

Modelling studies for Hydrogen Sulfide fuelled SOFCs

by

Dayadeep Monder

A thesis submitted to the Faculty of Graduate Studies and Research in partial fulfillment of the requirements for the degree of **Doctor of Philosophy**.

Department of Chemical and Materials Engineering

Edmonton, Alberta
Fall 2008

I dedicate this dissertation to my grandparents, Niranjan Singh and Ajmer Kaur Sekhon, Didar Singh and Bachan Kaur Monder.

Abstract

Solid oxide fuel cells (SOFCs) are high temperature, ceramic electrolyte fuel cells. Unlike most other fuel cells, which require high purity hydrogen to generate electricity, SOFCs can utilize a variety of fuels, including hydrocarbons. This work presents modelling and experimental work performed on a laboratory scale H_2S-fuelled SOFC equipped with a novel anode that can electro-oxidize H_2S into water vapour and sulphur. Using H_2S, a toxic by-product of the fossil fuel industry, such a fuel cell can potentially generate useful electrical energy while disposing off this toxic pollutant on site.

In this dissertation, I develop a hierarchy of first principles models for H_2S solid oxide fuel cells. The models developed fall into the following four categories: i) detailed models of H_2S electrochemistry; ii) isothermal 1–D and 2–D transport and reaction models of the 'near cell' region that do not take H_2S dissociation into account; iii) chemical thermodynamics models of H_2S dissociation in the fuel channel that also calculate the open circuit voltage (OCV) of the SOFC for the different possible fuels; iv) fully coupled 2-D transport and reaction models for the complete fuel cell assembly that include heat transfer and H_2S dissociation kinetics.

The models in the final category above include all the physics and chemistry in a working H_2S SOFC by including all transport phenomena, thermodynamically consistent kinetics of the chemical/electrochemical reactions, along with the electrical potential distribution in the fuel cell assembly. These multiphysics models are then used to estimate unknown electrochemical parameters, and to understand and explain experimental data from H_2S SOFCs.

Experimental results from H_2S SOFCs exhibit characteristics which are either poorly explained in current literature or not explained at all e.g., an unusual

dependence of cell performance on fuel composition. To support my modelling effort, I and a colleague conducted experiments where the composition and flow rates were varied for both the fuel and oxidant streams to analyze their effect on fuel cell performance. I present these experimental results and demonstrate the importance of thermodynamic and multiphysics modelling in understanding these results.

Acknowledgements

I thank my supervisors Professors K. Nandakumar, Karl Chuang, and Bob Hayes for their guidance during my doctorate program. I want to thank Professor Nandakumar for his extraordinary patience and support, as well as all of his advice and mentoring regarding teaching and scholarship throughout my time as a PhD student. I would also like to thank Prof. Forbes for encouraging me to start the doctorate, and for his support during my time at the University of Alberta.

I thank Profs. Jingli Luo and Karl Chuang for giving me access to the experimental facilities at the Alternative Fuel Cells laboratory, and Dr. Man Liu, Dr. Guo-lin Wei for access to their data. I would also like to acknowledge Vitaly Vorontsov's help in planning and running the experiments used in this work. His experimental work was crucial to my modelling work.

I was lucky to have exceptional colleagues in the Fundamental Modelling of Fuel Cells research group: Ali Abbaspour, Saied Amiri, and Xiaoming Wen. Their questions and encouragement pushed me to learn and to explore further than I would have managed on my own. Along with the above, I benefited immensely from discussions (academic and otherwise) with C. Veeramani, Nemanja Danilovic, Mranal Jain, Srinath Madhavan, Shi Jin, and Monjur Murshed.

I would like to express my gratitude to the community of close friends I gained during my two tenures in Edmonton: Nikhil Rao, Malavika Venkatsubbaiah, Ashish and Reema Malhotra, Rohit and Shaista Patwardhan, Shakir and Arshiya Japanwala, Robin Durnford, Brian Gibson, Debolina Guha Majumdar, Mridula Nath Chakraborty, Anna Yeatman, Andru McCracken, Rashmi Narayan, Shreela Chakrabartty, Brad Bowie, Tram Nguyen, and Gaby Zezulka-Mailloux.

Many thanks to masi (Manjit Pandher) and her boys (Yuri, Karan, Shawn Lovell and Leo) as well as Rachhpal Pandher for their love and support and all the yummy food.

I thank my parents, Mohinder Kaur and Fateh Singh Monder for everything they have given me.

My immeasurable gratitude to Paulomi Chakraborty for her love and unflagging support throughout the journey we have shared thus far, and especially for her patience (and pushing) during the writing of this dissertation.

Table of Contents

List of Tables

List of Figures

List of Symbols

a_k activity of species k

C_t total molar concentration (mole.m^{-3})

c_j integration constant for voltage profile in phase j

C_k molar concentration of k (mole.m^{-3} for gas concentrations, mole.m^{-2} for surface concentrations)

C_p specific heat, mass basis (J.(kg.K)$^{-1}$)

c_p specific heat, mole basis (J.(mole.K)$^{-1}$)

$\tilde{D}_{ij}$ multicomponent composition dependent diffusivity of species i in species j (m^2.s^{-1})

$D_{\mathrm{eff,k}}$ effective diffusivity of component k (m^2.s^{-1})

$D_{\mathrm{K,k}}$ Knudsen diffusivity for k (m^2.s^{-1})

D_{ik} multicomponent Maxwell–Stefan diffusivity of species i in k (m^2.s^{-1})

E Nernst potential (V)

E_oc/OCV open circuit voltage (V)

E^o Nernst potential for unit activities of all participating species (V)

$E^{0'}$ formal potential (V)

F Faraday's constant (96487 C.mole^{-1})

f_k molar flow-rate of species k (moles/s)

G_k	Gibbs free energy of species k (J/mole)
h	heat transfer coefficient for convective heat transfer ($W.(m^2.K)^{-1}$)
H_k	enthalpy of species k (J/mole)
i	cell current density ($A.m^{-2}$)
$i_{j,lim}$	limiting current density for electrode j ($A\ m^{-2}$)
i_j^0	exchange current density for electrode j ($A\ m^{-2}$)
K_{H_2O}	$P_{H_2S,in}(2P - P_{H_2O,in})/P_{H_2O,in}(2P + P_{H_2S,in})$
K_{S_2}	$P_{H_2S,in}(P - P_{S_2,in})/P_{S_2,in}(2P + P_{H_2S,in})$
k_i	kinetic rate constant (units vary)
K_{eq}	equilibrium constant
l_j	length or thickness of j (m)
M	molecular mass (kg/mole)
m_j	integration constant for voltage profile in phase j
P	total pressure (Pa in the transport models, bar in the thermodynamic models)
P_k	partial pressure of k (bar)
q	heat source/sink (Wm^{-3})
$\hat{R}_p$	area specific electrochemical/polarization resistance in an equivalent circuit representation ($\Omega.m^2$)
$\hat{R}_s$	series ohmic area specific resistance in an equivalent circuit representation ($\Omega.m^2$)
R	gas constant ($8.314\ J.mole^{-1}K^{-1}$)
r	distance in radial direction (m)
r_i	reaction rate for reaction i ($moles/(m^2s)$ for surface reactions; $moles/(m^3s)$ for gas phase reactions)

S_k entropy of k (J(mole.K)$^{-1}$)

T temperature (K)

u radial component of mass average velocity (m/s)

$\dot{V}$ temperature corrected volumetric flow rate (m^3/s)

$\tilde{v}$ molar average velocity (m/s)

v axial component of mass average velocity (m/s)

V_{cell} cell voltage (V)

w_k mass fraction of component k

X_{H_2S} conversion of H_2S in the H_2S dissociation reaction

y_k mole fraction of component k

z distance in axial direction (m)

Vectors and Matrices

$\mathbf{I}$ identity matrix

$\mathbf{i}$ current density vector (A.m^{-2})

$\mathbf{j}_i$ diffusive mass flux of component i (kg.m^{-2}s^{-1})

$\mathbf{n}$ normal vector (m)

$\mathbf{N_k}$ the total mass flux of the k^{th} component (kg.m^{-2}s^{-1})

$\mathbf{p}, \mathbf{p}^*$ vectors of parameter values needed to solve the model equations

$\mathbf{t}$ tangent vector (m)

$\mathbf{v}$ mass average velocity vector (m.s^{-1})

Greek letters

$\alpha_{a,k}$ overall anodic charge transfer coefficient for the electrochemical reaction involving k

$\alpha_{c,k}$	overall cathodic charge transfer coefficient for the electrochemical reaction involving k
β	charge transfer coefficient for single electron charge transfer reaction
ϵ_j	porosity of phase j
η	electrochemical activation losses (V)
$\hat{\mu}_k$	chemical potential of k (J/mole)
κ_j	permeability in electrode j (m^2)
λ	thermal conductivity $(W(m.K)^{-1})$
μ	viscosity $(kg(ms)^{-1})$
ϕ_j	electrical potential of phase j
ρ	density $(kg.m^{-3})$
σ_j	electrical conductivity of phase j $(\Omega^{-1}m^{-1})$
τ_j	tortuousity of phase j
θ_k	surface coverage of species k on electrode
ξ_k	stoichiometric coefficient for component k
$\Delta\phi_j^0$	equilibrium potential for electrode j (V)
$\hat{\theta}_k$	surface coverage of species k on electrolyte

Chapter 1

Introduction

1.1 Fuel cells

Fuel cells are energy conversion devices that directly convert the chemical energy of a fuel to electrical energy. In this respect fuel cells are very similar to primary batteries as they work on the same principles of electrochemistry. In both cases the fuel is oxidized at one electrode, called the anode, releasing electrons which travel through the load to the other electrode, the cathode, where they reduce the oxidant. Ions generated at one electrode travel through the electrolyte to the other electrode to complete the circuit. What differentiates fuel cells from batteries is their ability to generate electricity given a continuous supply of fuel and oxidant. Primary batteries have to house the fuel and oxidant in addition to the electrodes and electrolyte and have to be discarded once the reactants run out. While rechargeable or secondary batteries can be recharged, this recharging can be fairly time-consuming and these batteries can only undergo a finite number of charge cycles.

One of the main reasons fuel cell development is getting a lot of attention these days is because fuel cells have very high theoretical efficiencies of energy conversion. The majority of the western world relies heavily on fossil fuel powered thermal plants for electricity generation. Thermal power plants generate heat by burning fuel, and this thermal energy is then converted into mechanical energy, using gas and/or steam turbines, which is finally converted into electrical energy using a generator. This process has an inherently low efficiency due to the multiple energy conversion steps required, and because the conversion of heat to mechanical energy is subject to Carnot cycle efficiency limitations [101]. While mid-sized to

large standalone fuel cell systems can operate at efficiencies of about 50%, some large high temperature fuel cell systems can have an overall efficiency greater than 80% (based on lower heating value) if they include waste heat recovery using gas turbines ([101], [62]). Fuel cell based power plants would therefore use significantly less fuel and thus have lower greenhouse gas emmissions. Extremely low air pollutant (SOx, NOx, CO, etc.) emmissions is another advantage of using fuel cells although it is partly due to the ultra clean fuel required for most fuel cells.

Fuel cells can be designed for power requirements from about a watt to several megawatts. Very few fuel cell systems consist of just one fuel cell. Most individual cells can only supply a few watts at most, depending on the type of cell used. To attain the above scalability, fuel cells are stacked together in series and in parallel. This enormous range in scale means that fuel cells can be used to generate power for anything from a small portable electronic device all the way up to a mid-sized power plant. The technology requirements are of course very different for the above two applications and not all types of fuel cells can be used for all power needs (see table 1.1).

Fuel cells are usually classified based on the electrolyte used in the cells. There are five main types of fuel cells:

1. Polymer electrolyte membrane fuel cells (PEMFCs)
2. Alkaline fuel cells (AFCs)
3. Phosphoric acid fuel cells (PAFCs)
4. Molten carbonate fuel cells (MCFCs)
5. Solid oxide fuel cells (SOFCs)

Although, as stated earlier, all five types of fuel cells work on the same fundamental principles of electrochemistry, the operating conditions, the materials used, possible fuels and oxidants that can be used, and the possible range in power output vary for each type. PEMFCs, AFCs, and PAFCs are also known as low temperature fuel cells and their operating temperatures imply that they can only use either high purity H_2 or methanol as fuel.

These fuel cells are quite readily poisoned by CO (ppm levels for PEMFCs and AFCs). PAFCs operate at relatively higher temperatures around 200°C and can tolerate CO levels of up to 1%. PEMFCs and PAFCs have acidic electrolytes and

need expensive platinum based electrodes. AFCs have a KOH electrolyte, and cheaper nickel based electrodes can be used because the oxygen reduction reaction at the cathode is much easier in an alkaline medium. However, AFCs generally need pure oxygen on the cathode side as the CO_2 in air degrades the alkaline electrolyte.

Direct methanol fuel cells (DMFCs) have also received a lot of attention in the fuel cells research community [139, 39]. As the name implies, DMFCs use methanol as a fuel directly, and are a sub-category of PEMFCs as the electrolyte used is a polymer membrane. Methanol, being a liquid at room temperature, is much easier to handle than H_2 and has a very high volumetric energy density. This makes DMFCs especially attractive as power supplies for small electronic devices such as hand-held personal digital assistants (PDAs) and laptop computers. The main problems with DMFCs are low power density and fuel crossover from the anode to the cathode.

High temperature fuel cells, MCFCs and SOFCs, have many advantages over the other types. The higher operating temperature allows the use of cheaper non-noble metal catalysts on both sides. The anode catalysts for both MCFCs and SOFCs are not poisoned by CO and are actually able to use it as a fuel. The ability to electro-oxidize CO allows the use of reformed hydrocarbons as fuel. Both MCFCs and SOFCs are also able to reform natural gas internally and thus use it directly as fuel. Another advantage high temperature fuel cells have is the possibility of using the exhaust heat in turbines to generate additional electrical power or to use this thermal energy directly for heating applications. It is these cogeneration or hybrid power applications that can increase the overall efficiency of the system up to 80% and higher.

1.1.1 Current status

AFCs and PAFCs are currently the most mature technologies available [23, 57]. AFCs were the first proven fuel cell technology, which led to their use in the Apollo missions by NASA. Current generation AFCs are still being used by NASA for their space shuttle orbiters. The primary reasons they are preferred over the other fuel cell types are simplicity of design, and the excellent kinetics in an alkaline medium, especially on the cathode. This in turn gives AFCs their high electrical efficiencies. AFCs are not suitable for terrestrial applications because they require essentially pure hydrogen as fuel and pure oxygen as oxidant. This however, is not a problem

for space applications where both hydrogen and oxygen are available anyway for spacecraft propulsion. Among the few fuel cell products available in the market are mid to large stationary combined heat and power units using PAFCs [62]. The main disadvantages of PAFCs are the corrosive electrolyte and high cost.

Although MCFCs have attractive features such as the cogeneration of heat and power as well as the ability to use CO and lower hydrocarbons as fuel, research and development appears to be lagging behind that directed toward PEMFCs and SOFCs [57, 118]. The main reasons include materials issues due to the corrosiveness of the electrolyte, the need to recirculate CO_2 from the anode to the cathode, and lower area specific power density compared to other fuel cell types [132].

Most current research in fuel cells is focused on PEMFCs (including direct methanol fuel cells) and SOFCs [20]. Although these technologies are at opposite ends of the fuel cell spectrum, PEMFCs being low temperature units with a proton conducting electrolyte while SOFCs are high temperature fuel cells with oxygen ion conductors as electrolytes, they share the advantage of having solid state electrolytes that are not corrosive.

The key advantages of PEMFCs are that they are capable of very high power densities, and operate at temperatures close enough to ambient to permit quick start-ups and minimize thermal cycling related materials issues. If methanol is used as a fuel, direct methanol PEMFCs (DMFCs) have very high energy densities that gives them an advantage over state of the art batteries [6, 120] although there are significant challenges to be solved before they are widely adopted. Disadvantages of PEM include the high cost of the Pt catalyst and the polymer membrane used, as well as technological problems such as catalyst intolerance to CO, and water management in the membrane electrode assembly (MEA) [32, 33].

Advantages, limitations, and current status of SOFC technology will be discussed in more detail in the next section.

1.2 Solid oxide fuel cells

The solid oxide ion conducting electrolyte that makes the SOFC possible was discovered by Nernst at the end of the 19th century [36]. Nernst was looking for a replacement for carbon filament light bulbs and realized that mixed oxides became ionic conductors at elevated temperatures. His design for the "Nernst glower" became redundant with the introduction of tungsten in light bulb filaments. Al-

though better understanding of why the so-called "Nernst mass", 85% zirconia and 15% yttria, was an ionic conductor had to wait until the 1940s, the first patent on solid electrolyte fuel cells was filed as early as 1905 by Haber. For more early history of SOFCs and their development, I refer the reader to Möbius' account in [36, 35].

A single solid oxide fuel cell consists of a ceramic electrolyte sandwiched between the two electrodes, the anode and the cathode. When these cells are connected together in a stack, another layer called the interconnect is added to provide the electrical connections between the cells. Each of these layers has distinct requirements for reliable SOFC operation. All of them must be able to function at the high temperatures found in SOFCs. The electrodes must be stable in their respective operating atmospheres: the anode in a highly reducing environment and the cathode in a highly oxidizing environment. The electrolyte should not be electronically conducting while the interconnect and the electrodes should be good electronic conductors. The electrolyte and the interconnect need to be stable and retain their electrical conductivities, ionic for the former and electronic for the latter, in both reducing as well as oxidizing environments because they connect to an anode on one side and a cathode on the other. Both the electrolyte and the interconnect also need to be dense enough to prevent any gas crossover, which would result in chemical combustion and thus a lowering of the cell efficiency as well as local hot spots. Any layer in the SOFC should not react with adjoining layers.

By far the most widely used electrolyte for SOFCs is yttria doped zirconia also called yttria stabilized zirconia (YSZ) because the yttria stabilizes the zirconia in its flourite phase. The commonly used composition is 8% molar Y_2O_3 in ZrO_2 which posseses a high ionic conductivity. The comparatively lower conductivity of YSZ means that SOFCs using YSZ as electrolyte, especially those operating at temperatures below 800°C, have to use electrolyte thicknesses below 10 μm. For operating temperatures below about 750°C, electrolytes such as doped ceria and doped lanthanum gallate are preferred because of their substantially higher oxide ion conductivity.

The anode used for most current designs is a Ni-YSZ cermet. Although Ni provides the electronic conductivity as well as the catalytic activity, YSZ is composited with it so that the thermal expansion coefficient matches the electrolyte and to provide an extended reaction zone. The main problems with using Ni as the

anode are its propensity to catalyse coke formation when hydrocarbon fuels are used directly, and structural problems if the anode is exposed to redox cycling. Alternative anodes being researched include Ni-Ceria cermets for the ceria electrolyte based SOFC and Cu-Ceria composites for direct hydrocarbon cells [21, 54, 7].

The oxygen reduction reaction on the cathode is much slower than the oxidation reaction on the anode thus making cathode optimization a critical aspect in SOFCs. For high temperature SOFCs, the cathode most commonly used is a lanthanum strontium manganate (LSM) and YSZ composite. For SOFCs operating at lower temperatures, $(La, Sr)(Co, Fe)O_3$ (LSCF) and doped ceria composites have shown good performance [147, 8].

High temperature SOFCs generally use lanthanum chromite based interconnects and they have been shown to be stable and reliable. However, manufacturing of lanthanum chromite interconnects is difficult and expensive. Recent research has focussed on using metallic interconnects and some ferritic stainless steels have shown good results especially for SOFCs operating at temperatures below about 750°C [9].

Single cells can be classified according to which of the above four layers provides structural support for the cells in a stack or experimental setup. This layer then needs to be stronger and thus thicker than the others. As the electrolyte resistivity is usually quite high, electrolyte supported cells cannot operate at high power, while cathode supported cells result in significant internal losses because of the low diffusivity of oxygen which worsens the already slow oxygen reduction kinetics. If the anode is used as the support layer, the penalty on performance is lower because the diffusivity of hydrogen is high enough and the kinetics of the oxidation reaction are very fast. Therefore, anode supported cells predominate in current SOFC designs. Interconnect supported cells offer the possibility of even better performance and are being used by at least one commercial venture [8, 64].

Another system of classification for SOFCs uses the geometry of the cells. Although designs such as monoliths and segmented cells have been developed for SOFCs [91], current research and development is focussed on tubular and planar fuel cells [72]. Tubular SOFCs attracted a lot of attention initially because they do not need sealing to separate the fuel and the oxidant inside the stack. This is a huge advantage for tubular cells since high temperature sealing is difficult especially when dealing with ceramic materials with high thermal expansion coefficients. Planar SOFCs have to deal with these sealing issues. In spite of this, more recent

research and development has focussed on planar cells [72] because they are capable of much higher power densities (both area based as well as volume based). Recently there has also been a lot of interest in micro-tubular SOFCs [71, 115, 127, 116]. Micro-tubular SOFCs combine the high volumetric power density of planar SOFCs with exceptional resistance to thermal shock due to their low thermal mass. These advantages are important ones for portable applications and applications where a power source must undergo many on-off cycles.

SOFCs afford the most fuel flexibility and offer the highest overall efficiencies of all fuel cell types. Recent research has demonstrated the direct use of hydrocarbons ranging from methane to diesel as fuels for SOFCs [96, 105, 85, 89, 7, 151]. The above advantages as well as the ability to use non-noble metal, and thus much cheaper, electrocatalysts can be attributed to the high temperature operation of SOFCs. The fuel flexibility comes partly from the ability to reform hydrocarbons, either directly on the anode, or indirectly, using the heat produced by the cells. High overall efficiencies are possible because the excess heat produced by the cells/stack is available at high enough temperatures to enable combined heat and power (CHP) units, and/or to drive gas turbines, thus generating more electricity.

The high operating temperature is also responsible for the main problems with SOFCs such as sealing issues, material compatibility issues, and the use of expensive, hard to form, brittle ceramics. These problems can be avoided if the operating temperature can be brought down from 800–1000°C to 500–700°C because at these lower temperatures, sealing is less of a problem, and materials such as ferritic stainless steels can be used as interconnects or cell supports thus keeping costs low and improving the stack's mechanical toughness and durability [20, 21].

The operating temperature is mostly dictated by the electrolyte used because the oxide ion conductors used in SOFCs only attain the required ionic conductivity at elevated temperatures. Thus, recent efforts to lower operating temperature have focused on oxide ion conductors that have high electrical conductivity in the desired 500–700°C region [111, 50, 20] and/or on developing cells with a very thin electrolyte layer (5-30 μm).

Other challenges facing SOFC developers include improving cathode performance, developing better interconnects and interconnect coatings, developing anodes that are resistant to carbon deposition and sulphur poisoning. Another stack level goal for developers is stable long term performance usually defined as maintaining a steady stack voltage while a steady current is drawn. Most of these

issues are related to either materials or to manufacturing process selection and optimization.

For more information about SOFC research and development, the interested reader is referred to the review article by Ormerod [104] and the book edited by Singhal and Kendall [122]. Besides the references listed above, the following review articles are very well written and provide an excellent overview of the state of the art in the field. Atkinson et al.[7] on anodes, Adler [3] on cathode materials and oxygen reduction on these cathodes in particular, Goodenough [50] for a very detailed account of oxide ion conducting electrolytes and Brandon et al.[20], and [57] for general but very good discussions on all materials used in SOFCs.

As seen above, there is a lot of research and development work being performed on SOFCs worldwide, a significant portion of which is focussed on commercialization [17]. There are a whole range of applications that are being developed, from small portable systems delivering tens of watts to megawatt sized hybrid SOFCs and gas turbine plants. Most efforts are however focussed on 1 to 25 kilowatt stationary combined heat and power (CHP) units for residential and commercial use, sub megawatt small hybrid power plants, and 3 to 10 kilowatt auxillary power units (APU) for heavy duty automobiles such as trucks.

1.3 Modelling SOFCs

Before I discuss the modelling of SOFCs, let me describe the various physical and chemical processes in a single solid oxide fuel cell operating on H_2 as fuel. Figure 1.1 shows the different components in a SOFC as well as the movement of the reactants, electrons and ions.

I will discuss anode processes for fuels other than H_2 later. The H_2 molecules are transported through the fuel flow channels and the porous anode to the reaction sites. For most electrode materials these reaction sites are restricted to the so called triple phase boundary (TPB). The TPB is a set of lines in the electrode where the electrode catalyst is in contact with both the gas phase as well as the electrolyte phase[1].

The H_2 molecules then react at these active sites with O^{2-} ions from the electrolyte to give H_2O molecules, and electrons that are taken up by the electrode

[1]To be active for the reaction, the triple phase boundary sites need connections that percolate back to all the three phases

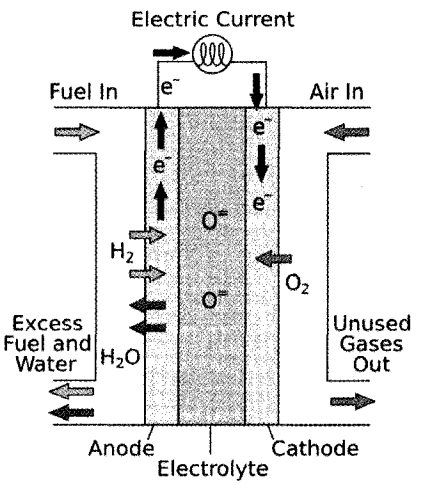

Figure 1.1: Solid oxide fuel cell: a cartoon showing the various components and processes in a SOFC [42]

(1.1). This is known as the fuel oxidation reaction and is one of two electrochemical reactions that must take place in an operating fuel cell. The product H_2O molecules are transported out through the anode and the fuel channels, while the electrons flow through the anode to the external cicuit, and back to the fuel cell at the cathode. This electron flow forms the current produced by the cell.

$$H_2 + O^{2-} \rightarrow H_2O + 2e^- \tag{1.1}$$

$$O_2 + 4e^- \rightarrow 2O^{2-} \tag{1.2}$$

These electrons then combine with O_2 at the cathode TPB through another electrochemical reaction, called the oxygen reduction reaction, to give oxide ions (1.2). The O^{2-} ions in turn travel across the electrolyte to be consumed by the aforementioned fuel oxidation reaction. Thus, the electrical circuit is completed by this ionic transport. Of course, the O_2 molecules have to come through the air channels and the porous cathode to get to the reaction sites.

The above processes can be classified as either transport or electrochemical processes. Reactant delivery and product removal to the fuel cell through the gas channels and electrodes is governed by the principles of fluid mechanics (momentum transfer) and mass transfer. The ionic conduction in the electrolyte and electrodes as well as the electronic conduction in the electrodes is governed by charge conservation and transport principles. In addition to the momentum, mass, and charge transfer processes outlined above, there are several heat transfer processes in the fuel cell. Heat is generated, and in some cases absorbed, by the electrochemical reactions in the electrodes as well as by the ohmic heating due to the flow of current in the cell.

The reactions given by equations (1.1) and (1.2) are only the overall reactions, and each overall reaction proceeds through a complex mechanism with multiple steps. On the cathode side a possible mechanism could start with the oxygen molecules adsorbing on the active sites on the cathode catalyst and dissociating into adsorbed O adatoms. These atoms then accept two electrons each from the cathode, probably in two separate electron transfer steps, before they diffuse along the catalyst surface to combine with oxygen vacancies on the adjoining YSZ surface. These freshly generated oxide ions then travel across the electrolyte layer to participate in the fuel oxidation reaction on the anode.

On the anode side, one of the proposed mechanisms has H_2 molecules adsorbing on active sites on the Ni catalyst and then dissociating into H adatoms. These atoms then diffuse to the three phase boundary before hopping across one by one to an O^{2-} ion on the YSZ surface leaving their electrons in the conducting band of the Ni metal. The water molecules formed on the YSZ surface then desorb, and at the end of the reaction sequence, the Ni sites are available again. The oxide ions on the anode TPB portion of the YSZ are replenished by the ions generated on the cathode and transported through the electrolyte.

All the steps in the reaction mechanisms described above proceed at finite rates that depend on local reactant and product activities as well as, in the case of the electron and ion transfer steps, the local potential difference between the anode and electrolyte phases [102, 98].

All the transport and chemical processes described above can be and have been modelled at many levels or scales and in varying degrees of detail [73]. Next, I briefly discuss why SOFC modelling, or for that matter any fuel cell modelling, is a useful exercise, before looking at how SOFC models are classified.

At a fundamental level, first principles fuel cell models help us understand the basic physical and chemical processes in fuel cells and the interactions between these various processes. From an engineering point of view, mathematical models of fuel cells are design and optimization tools that can help in selecting cell materials, operating conditions, stack design, controller design, among other things. The above capabilities depend on the ability to quickly modify operating conditions or revamp cell design in the model, and examine the effects on cell or stack performance. Thus, models enable simulations or numerical experiments that can dramatically decrease development time for a fuel cell design.

1.3.1 Types of models

As with any fuel cell model, SOFC models can be categorized according to the length scale of interest, and thus can vary from atomistic/molecular level models to complete system level models. Among the many scales in between these lie component layer and cell level models as well as stack level models. Any of these models can also be classified as a time-dependent/dynamic model or a steady-state model.

Here I discuss electrode, cell, and stack level models in terms of their structures and uses. This will be followed by a brief discussion of model inputs, outputs, and parameters. I will close this section with an outline of current activity in SOFC modelling.

The processes modelled in SOFC electrode models typically include: i) flow and mass transfer in the porous media, ii) charge transport in the electron conducting and ion conducting phases, and iii) the chemical and electrochemical reactions. Usually one dimensional models looking at the variation of reaction profiles or current generation through the electrode depth, some of the models built are 2-D or 3-D that take the complex structure of the electrode directly into account [126, 43, 1]. The main use of electrode level models is to study the effects of electrode structure, material composition, particle size, etc. on polarization losses at the electrode. Electrode models can be either steady state or time-dependent. Time-dependent electrode models are used primarily to simulate electrochemical impedance spectra (EIS) experiments [14, 12]. EIS experiments are used to characterize electrode performance, decompose electrode voltage losses, and help in understanding the reaction mechanisms [11, 143].

Models of SOFC cells and stacks model some or all of the transport phenomena

mentioned earlier along with the electrochemistry. These models are used to explore the effects of design parameters and decisions such as materials used, component thicknesses, flow channel design, as well as operating parameters such as flow rates and fuel composition. Stack geometries are fairly complex [72]. Thus, from a design viewpoint, the most useful stack models are three dimensional [56, 80, 148]. However, simplified models that isolate a single cell in the stack or look at a 2-D approximation continue to play a useful role in SOFC development [121].

The output variables of interest in the design and optimization studies mentioned above are cell/stack performance, as measured by the electrical power generated and the efficiency of energy conversion, as well as constraint variables such as maximum temperature, undesirable deposits (e.g., coking), and mechanical stresses caused by the different coefficients of thermal expansion of the components of the cell/stack. The temperature distribution is also of interest because temperature affects the rate of cell/stack degradation through species inter-diffusion between components. Generally, higher temperatures as well as large temperature gradients are undesirable. Thus, although a counter-current flow arrangement of the fuel and air streams might give higher power density for certain operating conditions, a cross-current or co-current flow design might be preferred because a counter-current design leads to higher temperatures and steeper temperature gradients in the stack [112].

As most SOFCs are made primarily from ceramic components, they are highly susceptible to thermal shock. This means that stack start-up as well as operating transients have to be carefully controlled to avoid buildup of catastrophic thermal stresses in the cell/stack components. Time-dependent stack models can guide cell and stack design as well as start-up procedures by predicting temperature and thus stress profiles inside the stack. Although first principles dynamic SOFC cell/stack models are too computationally expensive to be used directly in SOFC system controllers, these models are crucial for designing better controllers for SOFC stacks and systems.

Any model has a set of inputs, a set of model parameters, a set of outputs, as well as a particular structure or functional relationship linking the above. All four entities above are specific to a model and the purpose it is built for. For a cell level SOFC model, inputs would include operating conditions such as the cell voltage along with fuel and air flow rates and pressures, model parameters could include physical dimensions and properties of the cell components, while the

outputs might be the cell temperature and the current or power generated by the cell.

Before any model can be used reliably, it must be validated using experimental data. In many cases, some of the model parameters are uncertain or unknown e.g., chemical reaction rate constants. Sometimes key components of the model e.g., the details of the reaction mechanisms at the electrodes, are uncertain. Since such uncertainties lead to uncertainty in the structure of the model, they are known as structural uncertainties in the modelling literature. In these cases, simulations or numerical experiments using the model can be used, along with carefully chosen experimental data, to estimate uncertain parameters and to test new or revised mechanisms. Thus, model validation and parameter estimation both need experimental data. An example with both usages would be the use of an anode level model along with current-overpotential data from a three electrode setup to estimate anode electrochemical parameters, followed by the use of the estimated anode parameters in a stack model validated by experimental performance data from the stack.

The earliest SOFC model was a single cell level model presented by Debendetti and Vayenas [38]. This model was later extended to model a layer of cells in a cross-flow stack [134]. These models were 2-D in nature and only modelled the average concentrations and temperature in each cell in the stack layer, while ignoring mass transfer and electrochemical kinetics. Since these studies, a large number of models with varying levels of complexity and detail have been built, and reviews can be found in Chapter 11 of the book on SOFCs edited by Singhal and Kendall [73] as well as in [66, 19, 148].

While models for transport phenomena (mass, momentum, heat, and charge) are fairly well established, models for the chemistry and electrochemistry of fuel cells are not as mature. Until recently, there were very few publications that considered fuels more complex than H_2, and most electrochemical models were based on very simple realizations of the Butler-Volmer equation or even on thermodynamically inconsistent versions of it [70]. This paucity of good models of the chemical and electrochemical reactions in fuel cells is primarily due to the complex reaction mechanisms and their specificity to the electrode material used [3]. Thus, the recent appearance of articles that focus on detailed models of fuel reforming chemistry [61, 55] as well as electrochemistry [13, 153] is very encouraging.

A related development in SOFC modelling has been the introduction of de-

tailed time-dependent, fully non-linear electrode and cell level models that allow simulation of EIS studies [143, 12, 152]. Traditionally, linear electrical circuit elements have been used to interpret and explain EIS [11]. The circuit elements obtained after fitting experimental EIS data to a circuit were then assigned to different physical entities such as electrolyte resistance and charge transfer resistances of the electrodes. Instead of the indirect approach above, the new detailed models allow direct simulation and interpretation of the EIS in terms of physically meaningful parameters such as diffusion coefficients, kinetic constants, flow rates, etc.

The length scale in a fuel cell where the fundamental physics and chemistry of fuel reforming and charge transfer reactions as well as ionic transport take place is the atomic or molecular scale. With the advances in computer hardware as well as molecular modelling methods and software, it is now possible to build models at these scales for processes of interest to SOFC researchers. Methods from theoretical chemistry such as density functional theory (DFT), which are based on a quantum mechanical description of the bonds between atoms, have been used to assess the sulphur tolerance [28] and resistance to coking [46, 99] of Ni alloys used as anode materials. Other examples include molecular models of oxide ion vacancy transport in electrolytes [107, 108, 100].

1.4 Hydrogen sulphide and solid oxide fuel cells

Sulphur in natural gas or crude oil has to be removed before the hydrocarbons can be processed efficiently. In most sulphur removal processes, hydrogen sulphide is the by-product which then needs to be disposed of safely because H_2S is highly toxic to most forms of life. As discussed earlier, solid oxide fuel cells offer the greatest fuel flexibility among fuel cells and are capable of running on natural gas and other hydrocarbon fuels. Unfortunately, the hydrogen sulphide (H_2S) present in small quantities (1 - 30 ppm in natural gas, much higher in some diesels[2]) in these fuels is a severe poison for most SOFC anode catalysts, especially Ni. For intermediate temperature SOFCs ($T < 800°C$) with normal Ni based anodes, sulphur concentrations of 0.1 ppm can degrade the cell performance drastically [86]. Therefore, current designs of SOFCs running on hydrocarbons need an on-board desulphurizer, which adds to the complexity of the system.

[2]In terms of sulphur content of the liquid fuel.

There is a lot of ongoing research on development of sulphur tolerant anode materials [49]. Most of the current research seems to suggest that the higher the ionic conductivity of the electrolyte phase in the anode, the higher the sulphur tolerance. Mixed ionic and electronic conducting anodes, especially ceria based anodes, also display high sulphur tolerance [63, 60]. Kurokawa et al.[78] have demonstrated how to increase the sulphur tolerance of a Ni-YSZ anode by infiltrating a nano-layer of ceria particles onto it.

The primary industrial process used to dispose of H_2S is the Claus process [22]. The Claus process converts the gaseous H_2S to sulphur, a solid at ambient temperatures, using a fairly complicated multistage process that has high operating costs. If H_2S can be used as fuel in a fuel cell, it can be disposed off in a much simpler process that generates high quality electrical energy. The earliest studies on the possibility of using H_2S in a fuel cell were conducted by Pujare and coworkers [109, 110]. Since then a number of studies have been published on fuel cells running on H_2S [145, 82, 84, 4, 140, 142, 123, 29, 106]. These studies were experimental ones that evaluated different materials for the anode, anode catalysts, and electrolyte. While some work has been reported on using H_2S in fuel cells with proton conducting electrolytes [142, 123, 29, 106], most studies have used oxide ion conducting electrolytes.

For SOFCs using H_2S directly as fuel, many different anode materials have been investigated including thiospinels [109, 110], Pt [75, 82], various metal sulphides [145, 84, 140], lanthanum strontium vanadate (LSV) [4], Mo doped gadolinium tintanate (GTM) [150], and most recently a mixed ceramic structure with a coating of nano-sized ceria and Ru particles [79]. Although all of these studies present fuel cell performance data in the form of current density and or power density curves, the main goal of these studies was to find materials that lead to stable performance for H_2S fuel cells without degradation over time.

Among the more recent studies, a group at the University of Alberta, Liu et al. (2003) [84] and Wei et al. (2003, 2004) [140, 141] has presented performance data for H_2S fuelled SOFCs using mixed sulphide (and mixed sulphide, metal and electrolyte composite) anodes. This data includes current density curves at different temperatures and fuel and air flow rates. Although some impedance data is given, these data are for complete cells and does not attempt to isolate anode processes from cathode processes. Another recent study from the Georgia Institute of Technology by Aguilar et al. (2004) [4] presents performance data at different

temperatures from a SOFC using an LSV anode. This work also gives performance and impedance data at different fuel compositions to demonstrate the selectivity of the anode to H_2S in preference to H_2. Neither of these studies however, propose a reaction mechanism or give any kinetic parameters.

It is in the presence of such limited data and uncertainties about detailed mechanisms that I attempt to develop a mathematical modelling framework.

There are two possible overall reactions that use H_2S directly in a SOFC:

$$H_2S + \frac{1}{2}O_2 \Leftrightarrow H_2O + \frac{1}{2}S_2 \tag{1.3}$$

$$H_2S + \frac{3}{2}O_2 \Leftrightarrow H_2O + SO_2 \tag{1.4}$$

At the operating temperatures of a SOFC, these reactions are equally favoured thermodynamically and thus produce equilibrium voltages that are very close to each other e.g., 0.782 V for the first and 0.75 V for the second at 800 °C [140]. Besides these reactions, part of the H_2S fed dissociates into H_2 and S_2 and these can then undergo electrochemical oxidation according to (1.5) and (1.6).

$$H_2 + \frac{1}{2}O_2 \Leftrightarrow H_2O \tag{1.5}$$

$$S_2 + 2O_2 \Leftrightarrow 2SO_2 \tag{1.6}$$

It is not yet fully clear which (if any) of these reactions predominates in a SOFC running on H_2S. Some of the above mentioned studies have attempted to figure out which of the above electrochemical reactions predominates on the anode by looking at the open circuit voltage (OCV) [140] and analyzing the anode exhaust gases [145]. However, using the OCV as a guide to decide which reaction dominates is not as trivial as comparing the equilibrium voltage at unit activities. Even the broadly accepted idea that a H_2S SOFC produces more SO_2 in the high current region and more S_2 closer to OCV [4] is based on thermodynamic equilibrium in the gas phase. The extension of the above argument to conclude which electrochemical reaction is predominant on the anode is debatable.

1.5 Scope and plan of dissertation

The primary goal of this work is to build mathematical models for the single H_2S SOFC cell that can then be used to help in further development of H_2S fuelled cells or stacks.

In this work I develop a hierarchy of first principles models for H_2S solid oxide fuel cells. Using these models I describe all the physical and chemical processes in a working fuel cell. Our aim is to gain a better understanding of these processes and the couplings between them. The models are then used to understand and explain experimental data from H_2S SOFCs. Experimental results from H_2S SOFCs exhibit characteristics and trends which are either poorly explained in current literature or not explained at all. One example is an open circuit voltage (OCV) of order 1 for nearly all reported experimental data on H_2S SOFCs. Other examples include the variation of OCV with fuel flow-rate, and an unusual dependence of cell performance on fuel composition.

In Chapter 2, I present and explain model equations for all the transport phenomena in a SOFC assembly. These include gas flow, mass transfer, heat transfer, and charge transport. These model physics and equations are valid for any geometry, and for single cells as well as stacks. However, while describing the boundary conditions, I explain them from a 2-D axi-symmetric perspective for a "button cell" SOFC since all the models developed in this work are for this geometry.

The description of the transport models is followed by a detailed development of electrochemistry with particular attention to hydrogen sulphide in Chapter 3. Understanding electrochemistry is critical if one wants to understand fuel cell operation. I first present some basic electrochemical theory for charge transfer reactions. I then develop and explain a fundamental model for H_2S electrochemistry at the anode. A reaction mechanism is proposed and used to develop the reaction rate and current generation terms for the general case. derive the electrochemical rate equations for a detailed reaction mechanism consisting of multiple elementary chemical and charge transfer steps. Finally, I show how this model can be simplified to a single reaction rate equation using a given set of assumptions.

The fuel side chemistry is not presented until after the Chapter on the experiments conducted because the discussion on fuel dissociation needs to be motivated by the experimental data.

In Chapter 4 I present a range of models created for H_2S SOFC performance

data in Liu, et al. [84]. I use both 1-D and 2-D models to estimate key electrochemical parameters, and then compare the results from the models to demonstrate the importance of correctly modelling the mass transport in the fuel cell. For the given model geometry and flow-rates, mass transport cannot be correctly modelled without including fluid flow. Thus, although a 2-D model is more complex and computationally expensive, it is required to simulate the given data because flow cannot be modelled correctly using a 1-D model.

The experiments that I and a colleague conducted to examine flow-rate and composition effects on H_2S SOFC performance are described in Chapter 5. I present the electrochemical impedance as well as i-V performance data gathered and summarize the trends in the OCV and i-V data. We observed a time-dependence of the i-V curves at all three operation temperatures.

To explain some of the effects seen in the data in Chapter 5, I realized that the thermal dissociation of H_2S in the fuel had to be modelled. In Chapter 6 I present the thermodynamics and kinetics of H_2S dissociation. I then use thermodynamic models to predict fuel cell OCV for fuel mixtures at equilibrium. These models are also used to predict how OCV changes for different anode half cell reactions if the fuel is not at chemical equilibrium.

To run fuel cell simulations that model the H_2S dissociation in the fuel, I had to also model the heat transfer throughout the fuel cell assembly. This is because the H_2S dissociation kinetics is a strong function of temperature and isothermal conditions for the entire cell assembly cannot be assumed. In Chapter 7 I present fully coupled multiphysics models that include H_2S dissociation kinetics. These models are used to simulate the fuel cell experiments described in Chapter 5. I show how most of the trends seen in the experimental data can be explained by these model simulations. I also formulate the mixed OCV[3] problem for a fuel cell and use it to calculate OCV in our model assuming both H_2S and H_2 are electrochemically oxidized. Although the mixed OCV problem has been posed correctly in the literature [70, 53], to the best of our knowledge this is the first demonstrated use in a detailed numerical simulation of a SOFC.

In Chapter 8, I summarize the contributions of this dissertation and make recommendations for future research.

[3]Mixed OCV is the cell voltage at open circuit for a fuel containing more than one chemical species that can be electrochemically oxidized.

Table 1.1: The five different fuel cell types and typical characteristics

	PEMFC	AFC	PAFC	MCFC	SOFC
electrolyte	polymer membrane	KOH	H_3PO_4	Li_2CO_3/ K_2CO_3	YSZ
charge carrier	H^+	OH^-	H^+	CO_3^{2-}	O^{2-}
operating temperature	80°C	60–220°C	200°C	650°C	500–1000°C
anode catalyst	Pt	Pt or Ni	Pt	Ni-Cr	Ni
cathode catalyst	Pt	Pt or Ni	Pt	lithiated NiO-MgO	strontium-doped LaMnO3
fuel compatibility	H_2, CH_3OH	H_2	H_2	H_2, CO, CH_4	H_2, CO, CH_4
power range (W)	1–10^6	10^3–10^5	5×10^4–10^6	10^5–10^8	10^3–10^8
applications	from portable electronics to stationary power plants	space shuttle	stationary power stations	stationary CHP	APUs, stationary CHP

Chapter 2

Transport phenomena in solid oxide fuel cells

All the processes in a working solid oxide fuel cell can be classified either as transport processes such as the flow of gases and charged species, or as chemical/electrochemical processes such as fuel reforming and charge transfer. This Chapter presents the modelling approaches used in this thesis to describe the transport processes.

The particular geometry considered in this thesis is for a "button cell" SOFC (Figure 2.1). The fuel cell itself is a circular yttria stabilized zirconia (YSZ) disk between 200 – 300 μm thick with electrodes on both sides that are from 15 – 100 μm thick. As shown in the top section of Figure 2.1, the fuel delivery to the anode is through a coaxial tube assembly where the inner tube brings the fuel in and the unreacted fuel and products are carried away through the annular space between the inner and outer tubes. The air delivery to the cathode is done in a similar manner on the opposite side of the cell.

By assuming symmetry around the axis, this geometry can be reduced to the 2-D axisymmetric geometry shown in the lower section of Figure 2.1. The simplest model geometry for a button fuel cell considers only the thickness of the fuel cell itself as shown in the bottom section of the figure.

In the next few sections, I present transport models for:

1. flow in the gas channels and electrodes
2. mass transport in the gas channels as well as electrodes
3. heat transfer in the fuel cell assembly

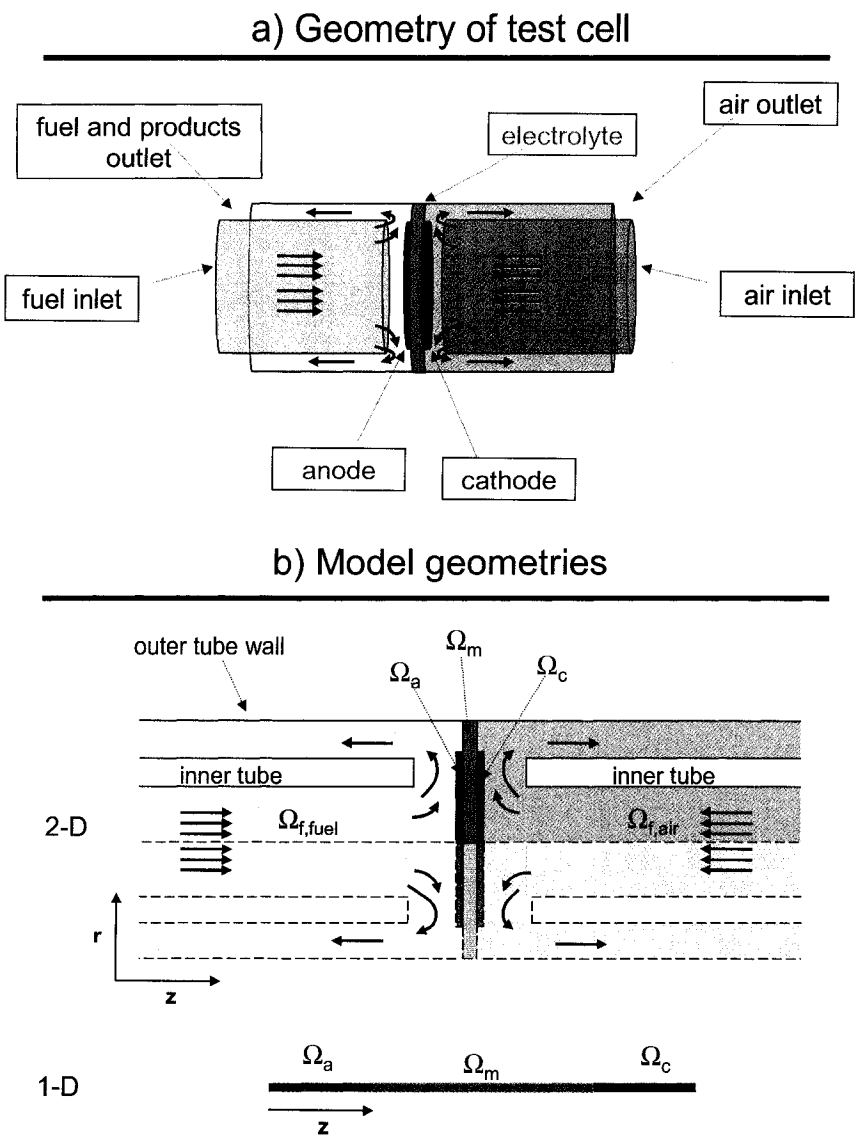

Figure 2.1: a) Schematic of the geometry of a button cell; b) Example model geometries used in this thesis (not to scale)

4. charge transport in the electrolyte and electrodes

All the transport models result in a partial differential equation (PDE) or a system of PDE when describing transport in a general form. This is to be expected because transport processes are spatially distributed. Thus, in the forms given below they can be applied to one, two or three dimensional domains. In addition to the governing PDE, each of these models requires a set of sufficient boundary conditions before it can be solved. I outline the necessary boundary conditions for each model after presenting the PDE. The details of the boundary conditions are presented in Chapters 4 and 7.

2.1 Flow in gas channels and electrodes

Describing the gas flow in the channels and in electrodes is important as it plays an essential role in the transport of reactants to, and the products from the cell.

The weakly-compressible form of the Navier-Stokes equations with variable viscosity is used to model the flow in the channels. This form is chosen over the standard incompressible, constant viscosity form of the Navier-Stokes equations because the temperature and composition gradients in the fuel and air channels lead to density and viscosity variations [77]. The momentum balance equation (2.1) and the continuity equation (2.2) take these viscosity and density variations explicitly into account. Since this work focuses only on steady state solutions for a fuel cell model, the equations given here are the steady state form of the Navier-Stokes equations.

$$\rho\left(\mathbf{v}.\nabla\mathbf{v}\right) = -\nabla P + \nabla.\left[\mu\left(\nabla\mathbf{v} + (\nabla\mathbf{v})^T\right) - \frac{2}{3}\mu(\nabla.\mathbf{v})\mathbf{I}\right] \tag{2.1}$$

$$\nabla.(\rho\mathbf{v}) = 0 \tag{2.2}$$

μ is the viscosity of the fluid, $\mathbf{v}$ is the velocity vector, ρ is the density, P is the pressure, and $\mathbf{I}$ is the identity matrix.

The term on the left of equation (2.1) describes the advection of momentum while the second term on the right is the momentum diffusion or viscous term.

The flow of gases in the electrodes can be described by Darcy's law or the Brinkman equations for flow in porous media. Darcy's law (2.3), a volume averaged

form of the Navier-Stokes equations, describes flow in a porous structure where the transfer of momentum by shear stress is negligible and flow is due to pressure gradients alone. This allows elimination of the velocity components as dependent variables, and solving for the pressure gives the complete solution for the velocity profile. The obtained velocity at a point in the domain is a volume averaged velocity instead of a true velocity inside the pores.

$$\mathbf{v} = -\frac{\kappa}{\mu}\nabla P \tag{2.3}$$

$$\nabla.(\rho\mathbf{v}) = 0 \tag{2.4}$$

κ is the permeability of the porous electrode.

The Brinkman equations can be considered an extension of Darcy's law and allow momentum transport by viscous shear stress (the second term on the right hand side of equation (2.5)). Advection of momentum (the term on the left hand side of equation (2.1)) is negligible and does not need to be included because of the restriction to flow in the porous media. The Brinkman equations retain the velocity components as dependent variables which are solved for along with the pressure. The velocity in the Brinkman equations is also averaged over the pore and solid volume. This allows me to define velocity and pressure continuity boundary conditions at the interface between domains with free flow (gas channels where flow governed by Navier-Stokes equations) and the electrode domains (flow described by Darcy's law or Brinkman equations).

$$\frac{\mu}{\kappa}\mathbf{v} = -\nabla P + \frac{1}{\epsilon}\nabla.\left[\mu\left(\nabla\mathbf{v} + (\nabla\mathbf{v})^T\right) - \frac{2}{3}\mu(\nabla.\mathbf{v})\mathbf{I}\right] \tag{2.5}$$

$$\nabla.(\rho\mathbf{v}) = 0 \tag{2.6}$$

ϵ is the porosity or void fraction of the electrode.

2.1.1 Flow boundary conditions

The following types of boundary conditions are needed for the flow equations:

1. no slip or zero velocity at the boundaries with solid domains such as the inlet and outlet tube walls

2. velocity and pressure continuity at the interface of flow channel and electrode
3. radial symmetry along the central axis of flow in 2-D axi-symmetric models
4. inlet velocity profile at the flow inlet
5. outlet pressure at the flow outlet
6. flow into or out of the electrolyte due to the electrochemical reaction at the electrode-electrolyte interface

2.2 Mass transfer

While the equations above can be used to describe the flow field in the fuel cell, another set of equations is required to calculate the spatial distribution of the individual chemical species in the flow channels and electrodes. The gas phase composition at the reaction sites in the anode and cathode determines both the voltage as well as the current for the cell (see sections 1.3 and 4.6.4). This means that calculating the composition profiles in the fuel cell is of vital importance for a good fuel cell model.

The convection-diffusion equation (2.7) describes the mass transfer of the reactants and products in the flow channels and the electrodes.

$$\nabla . (\mathbf{j}_i + w_i \rho \mathbf{v}) = r_i \tag{2.7}$$

$\mathbf{j}_i$ is the mass flux of i due to composition gradients, ρ is the density of the gas mixture, w_i the mass fraction of the i^{th} component. r_i is the rate of generation of i in the channels or electrodes. Typically, r_i is a chemical reaction rate which is a function of local composition and temperature.

$\mathbf{j}_i$ is called the diffusive flux while $w_i \rho \mathbf{v}$ is the convective flux for component i. $\mathbf{v}$ is the mass average velocity and comes from the solution of the flow equations in section 2.1.

The correct form for the diffusive flux $\mathbf{j}_i$ of i in a multicomponent mixture is given by the Maxwell-Stefan formulation (2.8). Diffusive flux due to thermal gradients is not considered in equation (2.8). Thermal diffusion is important for environments where the thermal gradients are very high e.g., in flames [138]. As

the thermal gradients in our setup are not as severe, contributions to the diffusive flux $\mathbf{j}_i$ from thermal diffusion are ignored in this work.

$$\mathbf{j}_i = -\rho w_i \sum_{j=1}^{n} \tilde{D}_{ij} \left(\nabla y_j + (y_j - w_j) \frac{\nabla P}{P} \right) \tag{2.8}$$

In equation (2.8), n is the total number of species in the mixture, y_j is the mole fraction while w_j is the mass fraction of species j, and $\tilde{D}_{ij}$ is the multicomponent *composition dependent* diffusivity of species i in j.

Mass fractions and mole fractions are related through:

$$w_i = \frac{y_i M_i}{\sum_i y_i M_i} \tag{2.9}$$

$\tilde{D}_{ij}$ are functions of the binary diffusion coefficients D_{ij} and the local composition that require inversion of a $n \times n$ matrix where n is the total number of species.

A simpler formulation for the diffusive flux is the Fick's law form (2.10).

$$\mathbf{j}_i = -\rho \bar{D}_{im} \nabla(w_i) \tag{2.10}$$

$\bar{D}_{im}$ is the mixture averaged diffusion coefficient of component i.

The Fickian expression is an approximation which makes the convection diffusion equations easier to solve. However, using equation (2.10) can lead to mass non-conservation i.e., the resulting mass fractions not adding up to unity.

For more details on the modelling equations for mass transfer please refer to the books by Bird, et al. [16] and Kee, et al. [69].

2.2.1 Mass transfer boundary conditions

The convection diffusion equations for mass transfer in a fuel cell model need the following types of boundary conditions:

1. mass fractions of the chemical species at the fuel and air flow channel inlets

2. flux of species specified by the heterogeneous chemical reaction rate at the inner and outer tube walls[1]

3. mass flux, of the reactants out of, and the products into, the electrodes governed by the local current density at the electrode-electrolyte interface

4. radial symmetry along the axis of the flow channels and the electrodes

2.3 Heat transfer

Another equation is required to describe the temperature profile inside the fuel cell. This is necessary for many reasons. One is that temperature affects the reaction rate of both chemical reactions (such as fuel reforming) as well as the electrochemical reactions that produce current in the cell. Another is that the ionic conductivity of the electrolyte is a strong function of temperature, increasing approximately exponentially with increasing temperature.

The heat equation (2.11) describes the temperature distribution inside a fuel cell assembly.

$$\rho c_P \mathbf{v}.\nabla T = \nabla.(\lambda \nabla T) + q \tag{2.11}$$

c_P is specific heat at constant pressure, T is the temperature, λ is the thermal conductivity, and q is the rate of heat generation.

There are at least four processes in a working fuel cell that cause heating or cooling through the q term:

1. the associated heat of reaction of any chemical reactions in the fuel cell

2. Ohmic heating caused by the flow of current through the fuel cell

3. heating or cooling depending on the entropy change of the electrochemical reactions at the electrodes

4. heating due to the electrochemical or activation voltage losses for a loaded fuel cell

[1]Zero flux for species that do not react on the tube walls (all species in models that do not include chemistry in the gas channels)

2.3.1 Radiation

Solid oxide fuel cells operate at temperatures that are high enough and radiative heat transfer can be important. Thus, radiation heat exchange terms should be included in the boundary conditions. However, if the geometry has a high aspect ratio, i.e., one dimension of the geometry is much longer than the others, radiative heat exchange can be ignored because of negligible shape factors. In this work I do not consider the radiative heat exchange due to participating media i.e., the gases in the fuel cell are assumed to be transparent to radiation and not emit any radiation.

2.3.2 Heat transfer boundary conditions

The heat transfer equation in a fuel cell model needs the following types of boundary conditions:

1. radial symmetry along the axis of the flow channels and the electrodes
2. inlet temperatures for the gas streams
3. radiative heat exchange between boundaries that can "see" each other
4. heat of reaction terms for any surface reactions inside the fuel cell
5. radiation and free convection at uninsulated exterior boundaries
6. specified heat flux or temperature profile for boundaries adjoining a furnace or other heat source

2.4 Charge transport

The performance of a fuel cell is directly described by the voltage of the cell at a particular current. Another equation is required to calculate the voltage and current distribution in the fuel cell electrodes and electrolyte and to describe the electronic and ionic charge transport in those domains.

A general form of ionic charge transport is described by the Nernst-Plank equation which allows for charged species transport by convection and diffusion along with migration due to a potential gradient. For a solid electrolyte, there is no transport by convection and the concentration gradients are generally small enough

to neglect transport by diffusion [101]. Thus, the only transport mechanism to be considered for a charged species in a solid electrolyte is migration which can be described by Ohm's law (2.12). Ohm's law is also adequate to describe electronic charge transport in the electrodes.

$$\nabla.(-\sigma_j \nabla \phi_j) = i^V \tag{2.12}$$

σ_j and ϕ_j are the electrical conductivity and the electrical potential of domain j, and i^V is the volumetric current generation in the domain.

Volumetric current generation is only possible in mixed ionic-electronic or composite electrodes where the electrochemically active region is not restricted to the electrode-electrolyte interface (see section 1.3). In electrodes made of purely electronically conducting material, the current enters (and leaves) the cell through the boundary conditions at the electrode-electrolyte interfaces.

2.4.1 Charge transport boundary conditions

In a fuel cell, the following boundary equations need to be specified for equation (2.12).

1. radial symmetry along the axis of the electrolyte and the electrodes
2. specified terminal potentials, with or without contact resistance, at the anode and cathode current collectors
3. electrical insulation for the appropriate interfaces (e.g., between the electrolyte and outer tube)
4. current density calculated through an electrochemical rate equation for the electrolyte-electrode interface (if the electrochemical reactions are restricted to the above interface)

2.5 Parameters

All the PDE listed above contain physically meaningful parameters which must be available before these equations can be solved. Physical constants e.g., the gas

constant R, and the values assigned to them in the models are summarized in the Nomenclature.

The parameters needed for the flow equations are the density and viscosity for the fuel and air as well as the permeabilities of the electrodes.

At the temperatures and pressures found in an SOFC, gas phase density is given by the ideal gas equation (2.13).

$$\rho = \frac{PM}{RT} \tag{2.13}$$

M is the average molecular mass of fuel or air.

Viscosity for gases at low pressures is usually calculated using equations derived from the kinetic theory of gases. In this work, I use the Chapman-Enskog relation (2.14).

$$\mu = 26.69 \times 10^{-8} \frac{\sqrt{1000\, M_k T}}{\sigma_k^2\, \Omega_k^{2,2}(T^*)} \tag{2.14}$$

σ_k is the collision diameter (in nm) and $\Omega_k^{2,2}(T^*)$ is a collision integral that is a function of reduced temperature. The reader can find more details in standard texts that discuss the properties of gases [113, 69].

The transport properties for a gas mixture are usually calculated using empirical averaging formulae. I calculate the viscosity of a gas mixture through equation (2.15) suggested in [138].

$$\mu_{mix} = \frac{1}{2}\left(\sum_k y_k \mu_k + \frac{1}{\sum_k y_k/\mu_k}\right) \tag{2.15}$$

Experimental values for electrode permeability κ_j were not available and order of magnitude estimates are used based on permeability values calculated for close packings of spheres [114]. I found that the solution was not sensitive to the permeability values used in the model. Permeability values across a range of $10^{-9} - 10^{-14}\mathrm{m}^2/\mathrm{s}$ did not appreciably affect output variables such as the current at a particular cell voltage.

Experimental values for the porosity and tortuosity of the electrodes were not

available and the values assumed are given in chapters 4 and 7.

Binary gas diffusivities are calculated from the Fuller, Schettler and Giddings equation given in [113]. The diffusion coefficient for species i in a mixture with species j is given by equation (2.16).

$$D_{ij} = \frac{10^{-7}T^{1.75}\sqrt{10^3\frac{M_i+M_j}{M_iM_j}}}{P\left[\left(\sum V_i\right)^{\frac{1}{3}} + \left(\sum V_j\right)^{\frac{1}{3}}\right]^2} \tag{2.16}$$

$\sum V_i, \sum V_j$ are diffusion volumes for components i and j and all the other variables have their usual meaning with P in atm.

Knudsen diffusion coefficients in the two electrodes are calculated using equation (2.17).

$$D_{K,k} = \frac{2}{3}r_{pore}\sqrt{\frac{8RT}{\pi M_k}} \tag{2.17}$$

r_{pore} is the average pore radius in the electrode, and M_k is the molecular weight of the species in the electrode.

For the pore sizes in the experimental work modelled in this work, the Knudsen diffusivities are an order of magnitude higher than the bulk gas phase diffusivities. This suggests that Knudsen diffusion does not play a big part in resisting mass transport through the electrodes.

Specific heat at constant pressure for all gas species are calculated using the NASA Glenn Thermodynamic coefficients [88, 24] where c_P for each gas is given by equation (2.18).

$$c_P = R\left(\frac{a_1}{T^2} + \frac{a_2}{T} + a_3 + a_4T + a_5T^2 + a_6T^3 + a_7T^4\right) \tag{2.18}$$

a_i are constants unique to each gas species.

The specific heat of the gas mixture on the fuel or air side is calculated as an

average using equation (2.19).

$$C_{P,mix} = \sum_k \left(\frac{c_{P,k}}{M_k} w_k \right) \tag{2.19}$$

$c_{P,k}$ is the *molar* specific heat, M_k the molecular mass, w_k the mass fraction of component k, and $C_{P,mix}$ is the average specific heat of the gas mixture.

Thermal conductivity for a pure gas is also usually calculated using expressions from the kinetic theory of gases. I use the Stiel and Thodos equation (2.20) given in [113].

$$\lambda_k = \frac{\mu_k}{M_k}(1.15 c_{P,k} + 0.88R) \tag{2.20}$$

I calculate the thermal conductivity of a gas mixture through equation (2.21) given in [113].

$$\lambda_{mix} = \frac{1}{2}\left(\sum_k y_k \lambda_k + \frac{1}{\sum_k y_k/\lambda_k} \right) \tag{2.21}$$

The thermal properties of the solid components in the fuel cell assembly are taken from the literature [90, 95]. The thermal conductivity of the electrodes is calculated by using a volume weighted average as shown in equation 2.22. Admittedly this is a very simple model [40]. For our purposes, this model suffices because the porous domains are very thin in relation to the complete geometry and thus the value for the effective thermal conductivity has a negligible effect on the coupled multiphysics solution.

$$\lambda_{eff} = \epsilon \lambda_{mix} + (1 - \epsilon)\lambda_{solid} \tag{2.22}$$

The electrical conductivities for the electrolyte and electrode materials are also taken from the literature. Electrical conductivity of the anode materials σ_a used has been measured [83] and those values are used in this work. The cathode used in the experiments was Pt, and the value for Pt conductivity at the operating

temperatures is corrected for porosity using relations given in [34]. Values for conductivity of the YSZ electrolyte σ_{m} are obtained using the temperature dependent form given in [5].

2.6 Summary

In this Chapter, I describe the transport phenomena in a SOFC and present the transport models I used in this work. A brief description of each of the transport modes: gas flow, mass transfer, heat transfer, and charge transport, is followed by the governing partial differential equations for the mode and a list of the boundary conditions needed to solve these equations. All the PDE for transport contain certain parameters. I list these parameters and discuss how I obtained the values used in this work.

Chapter 3

Electrochemistry in fuel cells

Charge transfer reactions are critical to the operation of fuel cells as the reaction rates of these processes directly determine the amount of current generated. Electrochemistry is the study of reactions involving charge transfer and gives us the theory to determine the rates of these electrochemical reactions. As outlined in section 1.3, there are two half cell reactions in a fuel cell where charge transfer occurs. In this Chapter, I will present some of the theory behind electrochemical reactions, and use it to develop the reaction rate equations needed for our fuel cell models. For deeper analyses, the reader is referred to the excellent textbooks on electrochemistry by Bockris et al. [18], Schmickler [117], Oldham and Myland [102], and Newman and Thomas-Alyea [98]. For a fuel cell specific introduction to electrochemistry, see the timely book by O'Hayre, et al. [101].

I start by developing the electrochemical reaction rate equation for a general single electron transfer reaction.

3.1 The Butler-Volmer equation

Consider the single electron transfer reaction given by equation (3.1). The forward reaction is a reduction reaction where a species O is reduced to R, and the reverse reaction is thus an oxidation reaction.

$$O + e^- \rightleftarrows R \tag{3.1}$$

The net reaction rate in the forward direction (reduction) is given by equation

(3.2).

$$r = k_f C_O - k_b C_R \tag{3.2}$$

C_O, C_R are local surface molar concentrations, and the kinetic rate constants k_f and k_b are given by equations (3.3) and (3.4).

$$k_f = A_f e^{-\Delta G_c^{\#}/RT} = A_f e^{-(\Delta G_{c,0}^{\#} + \beta FE)/RT} = k_f^o e^{-(\beta FE)/RT} \tag{3.3}$$

$$k_b = A_b e^{-\Delta G_a^{\#}/RT} = A_b e^{-(\Delta G_{a,0}^{\#} - (1-\beta)FE)/RT} = k_b^o e^{((1-\beta)FE)/RT} \tag{3.4}$$

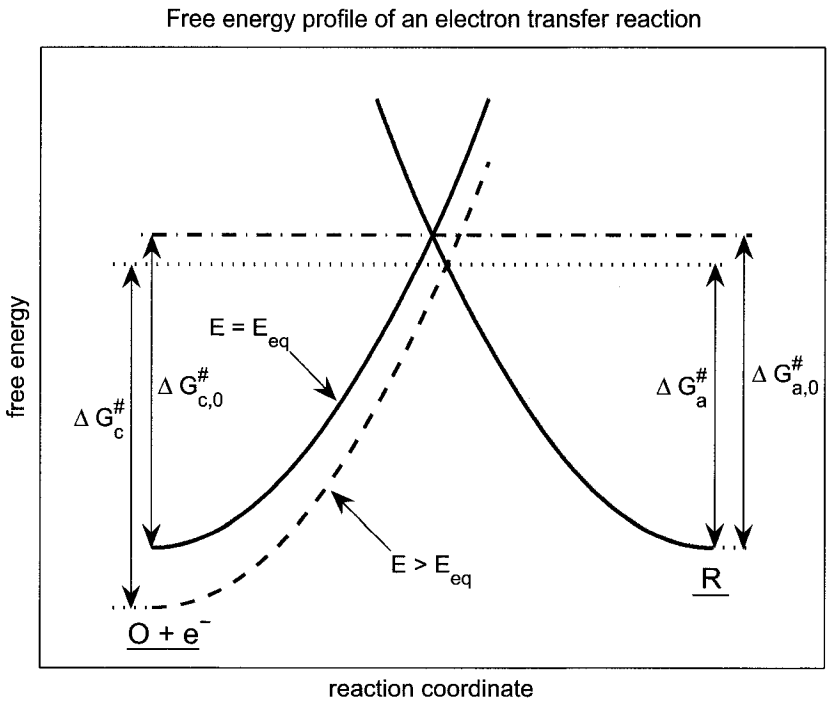

Figure 3.1: Free energy profile for the electron transfer reaction (3.1) going from species O on the right to species R on the right

$\Delta G_c^{\#}$ is the free energy barrier for the reduction reaction, $\Delta G_a^{\#}$ the free energy barrier for the oxidation reaction, F is Faraday's constant, and $E = \phi_{electrode} -$

$\phi_{electrolyte}$ is the electrical potential difference across the electrode-electrolyte interface. k_f° and k_b° are the "purely chemical" rate constants given by equations (3.5) and (3.6). At equilibrium, the height of the energy barriers to the forward and backward reactions are equal $\Delta G_{c,0} = \Delta G_{a,0}$. β can have a value between 0 and 1 (usually assumed to be 0.5) and is called the symmetry or charge transfer coefficient.

$$k_f^\circ = A_f e^{-\Delta G_{c,0}^{\#}/RT} \tag{3.5}$$

$$k_b^\circ = A_b e^{-\Delta G_{a,0}^{\#}/RT} \tag{3.6}$$

Thus, as shown in figure 3.1, for an electrochemical reaction, the height of the forward and backward reaction free energy barriers is a function of the electrical potential of the reaction site E. This in turn makes the net forward reaction rate a function of E.

Having defined the rate equation (3.2), I now consider what happens when reaction (3.1) is at equilibrium. For a mixture of given composition at electrochemical equilibrium, $r = 0$, $C_R = C_{R,in}, C_O = C_{O,in}$, and $E = E_{in}$. Thus, E_{in} is the equilibrium electrode potential for the inlet composition. Substituting the above into equation 3.2 leads to:

$$k_f^\circ e^{-(\beta F E_{in})/RT} C_{O,in} = k_b^\circ e^{((1-\beta)F E_{in})/RT} C_{R,in} \tag{3.7}$$

$$e^{fE_{in}} = \frac{k_f^\circ C_{O,in}}{k_b^\circ C_{R,in}} \tag{3.8}$$

$$E_{in} = \frac{1}{f} \ln \frac{k_f^\circ C_{O,in}}{k_b^\circ C_{R,in}} \tag{3.9}$$

$f = F/RT$ in equation (3.9)

If both the reactants and products are at unit activity, $E = E^\circ, r = 0$ and $C_R = 1, C_O = 1$. Equation 3.2 with the above conditions gives:

$$k_f^o e^{-(\beta F E^o)/RT} = k_b^o e^{((1-\beta)FE^o)/RT} \tag{3.10}$$

$$e^{fE^o} = \frac{k_f^o}{k_b^o} \tag{3.11}$$

$$E^o = \frac{1}{f} \ln \frac{k_f^o}{k_b^o} \tag{3.12}$$

By substituting equation (3.12) into equation (3.9),

$$E_{in} = \frac{1}{f} \left[\ln \frac{k_f^o}{k_b^o} + \ln \frac{C_{O,in}}{C_{R,in}} \right] \tag{3.13}$$

$$E_{in} = E^o + \frac{1}{f} \ln \frac{C_{O,in}}{C_{R,in}} \tag{3.14}$$

$$E_{in} = E^o + \frac{RT}{F} \ln \frac{C_{O,in}}{C_{R,in}} \tag{3.15}$$

Equation (3.15) is the famous Nernst equation written for reaction (3.1). E^o is the standard unit activity electrode potential for reaction (3.1), and is given by equation (3.16).

$$E^o = \frac{-\Delta G^o}{F} \tag{3.16}$$

ΔG^o is the standard free energy change of reaction (3.1).

In electrochemistry, how far a reaction is from equilibrium is usually defined by the overpotential $\eta_{in} = E - E_{in}$.

Writing equation (3.2) in terms of the overpotential η_{in} and using equation (3.9):

$$r = k_f^{\circ} C_O e^{-\beta f \eta_{in} - \beta \ln (k_f^{\circ} C_{O,in} / k_b^{\circ} C_{R,in})} - k_b^{\circ} C_R e^{(1-\beta) f \eta_{in} + (1-\beta) \ln (k_f^{\circ} C_{O,in} / k_b^{\circ} C_{R,in})} \tag{3.17}$$

$$r = k_f^{\circ} C_O \left(\frac{k_f^{\circ} C_{O,in}}{k_b^{\circ} C_{R,in}} \right)^{-\beta} e^{-\beta f \eta_{in}} - k_b^{\circ} C_R \left(\frac{k_f^{\circ} C_{O,in}}{k_b^{\circ} C_{R,in}} \right)^{1-\beta} e^{(1-\beta) f \eta_{in}} \tag{3.18}$$

$$r = \left(k_f^{\circ} C_{O,in}\right)^{1-\beta} \left(k_b^{\circ} C_{R,in}\right)^{\beta} \frac{C_O}{C_{O,in}} e^{-\beta f \eta_{in}} - \left(k_f^{\circ} C_{O,in}\right)^{1-\beta} \left(k_b^{\circ} C_{R,in}\right)^{\beta} \frac{C_R}{C_{R,in}} e^{(1-\beta) f \eta_{in}} \tag{3.19}$$

$$r = \left(k_f^{\circ} C_{O,in}\right)^{1-\beta} \left(k_b^{\circ} C_{R,in}\right)^{\beta} \left(\frac{C_O}{C_{O,in}} e^{-\beta f \eta_{in}} - \frac{C_R}{C_{R,in}} e^{(1-\beta) f \eta_{in}} \right) \tag{3.20}$$

From the stoichiometry of reaction (3.1), the current produced would be given by equation (3.21).

$$i = Fr \tag{3.21}$$

$$i = i_{in}^{\circ} \left(\frac{C_O}{C_{O,in}} e^{-\beta f \eta_{in}} - \frac{C_R}{C_{R,in}} e^{(1-\beta) f \eta_{in}} \right) \tag{3.22}$$

$$i_{in}^{\circ} = F \left(k_f^{\circ} C_{O,in}\right)^{1-\beta} \left(k_b^{\circ} C_{R,in}\right)^{\beta} \tag{3.23}$$

Faraday's constant F, the charge on 1 mole of electrons, converts the reaction rate to a current. The kinetic parameter i_{in}° is called the exchange current density.

One can also write equation 3.2 in terms of an alternative overpotential $\eta_{\circ} = E - E^{\circ}$ and then use equation 3.12 to get equation (3.29).

$$r = k_f^{\circ} C_O e^{-\beta f \eta_{\circ} - \beta \ln (k_f^{\circ} / k_b^{\circ})} - k_b^{\circ} C_R e^{(1-\beta) f \eta_{\circ} + (1-\beta) \ln (k_f^{\circ} / k_b^{\circ})} \tag{3.24}$$

$$r = k_f^{\circ} C_O \left(\frac{k_f^{\circ}}{k_b^{\circ}} \right)^{-\beta} e^{-\beta f \eta_{\circ}} - k_b^{\circ} C_R \left(\frac{k_f^{\circ}}{k_b^{\circ}} \right)^{1-\beta} e^{(1-\beta) f \eta_{\circ}} \tag{3.25}$$

$$r = \left(k_f^{\circ}\right)^{1-\beta} \left(k_b^{\circ}\right)^{\beta} C_O e^{-\beta f \eta_{\circ}} - \left(k_f^{\circ}\right)^{1-\beta} \left(k_b^{\circ}\right)^{\beta} C_R e^{(1-\beta) f \eta_{\circ}} \tag{3.26}$$

$$r = \left(k_f^{\circ}\right)^{1-\beta} \left(k_b^{\circ}\right)^{\beta} \left(C_O e^{-\beta f \eta_{\circ}} - C_R e^{(1-\beta) f \eta_{\circ}} \right) \tag{3.27}$$

From stoichiometry again:

$$i = Fr \tag{3.28}$$

$$i = i^{\circ}\left(C_O e^{-\beta f \eta_{\circ}} - C_R e^{(1-\beta) f \eta_{\circ}}\right) \tag{3.29}$$

$$i^{\circ} = F\left(k_f^{\circ}\right)^{1-\beta}\left(k_b^{\circ}\right)^{\beta} \tag{3.30}$$

If I define equilibrium in terms of local surface concentrations, I get equation (3.31).

$$i = i_s^{\circ}\left(e^{-\beta f \eta_s} - e^{(1-\beta) f \eta_s}\right) \tag{3.31}$$

where

$$i_s^{\circ} = F\left(k_f^{\circ} C_O\right)^{1-\beta}\left(k_b^{\circ} C_R\right)^{\beta} \tag{3.32}$$

$$\eta_s = E - E_s \tag{3.33}$$

$$E_s = \frac{1}{f} \ln \frac{k_f^{\circ} C_O}{k_b^{\circ} C_R} \tag{3.34}$$

All three forms of the net electrochemical reaction rate or current, equations (3.22), (3.29), (3.31) are equivalent forms of what is called the Butler-Volmer equation.

In most cases r, i, i° are defined as rates per unit apparent electrode area which gives i and i° the units of current per unit area (A/m^2).

For a reaction such as (3.35), the rate equation needs to be modified to account for the n electrons transfered.

$$O' + ne^{-} \rightleftarrows R' \tag{3.35}$$

If the above reaction takes place in a single step, similar analysis to the above leads to equation (3.36) for the net reduction current.

$$i = i^{\circ}\left(C_O e^{-n\beta f \eta_{\circ}} - C_R e^{n(1-\beta) f \eta_{\circ}}\right) \tag{3.36}$$

Frequently, a more general form equation (3.37) is used. For (3.37) to be

thermodynamically consistent[1], $\alpha_a + \alpha_c$ must be a multiple of n, the number of electrons transferred in the overall reaction (3.35). Writing equation (3.37) in the form of (3.22) leads to equation (3.38).

$$i = i^{o}\left(C_O e^{-\alpha_c f \eta_o} - C_R e^{\alpha_a f \eta_o}\right) \tag{3.37}$$

$$i = i^{o}_{in}\left(\frac{C_O}{C_{O,in}} e^{-\alpha_c f \eta_{in}} - \frac{C_R}{C_{R,in}} e^{\alpha_a f \eta_{in}}\right) \tag{3.38}$$

3.2 Rate equations for fuel cell electrode reactions

The overall half-cell reactions on a fuel cell electrode all involve the transfer of multiple electrons. For the case of the H_2S SOFC with H_2O and S_2 as products, the two half-cell reactions are given below where (3.39) is the anode half reaction and (3.40) is the cathode half reaction for the H_2 SOFC.

$$H_2S + O^{2-} \rightleftarrows H_2O + \frac{1}{2}S_2 + 2e^- \tag{3.39}$$

$$\frac{1}{2}O_2 + 2e^- \rightleftarrows O^{2-} \tag{3.40}$$

If I assume that the reactions above occur in a single step (as written), the electrochemical rate equations for them, using equation (3.37), would be given by equations (3.41), and (3.42).

$$i_a = i^{o}_{a}\left(C_{H_2S} e^{\alpha_{a,H_2S} f \eta_a} - C_{H_2O}\sqrt{C_{S_2}}\, e^{(2-\alpha_{a,H_2S}) f \eta_a}\right) \tag{3.41}$$

$$i_c = i^{o}_{c}\left(\sqrt{C_{O_2}}\, e^{-\alpha_{c,O_2} f \eta_c} - e^{(2-\alpha_{c,O_2}) f \eta_c}\right) \tag{3.42}$$

i_j are the anodic and cathodic current densities, while i^o_j and $\alpha_{j,k}$ are the exchange current densities and charge transfer coefficients respectively. The subscript a denotes the anode while c denotes the cathode.

[1]To be thermodynamically consistent, the rate equation must reduce to the equilibrium relationship when the net reaction rate goes to zero. The reader is referred to the discussion at the end of section 3.2

The above equations can also be written in the form given by equation (3.38), giving equations (3.43), and (3.44) below.

$$i_a = i^{\circ}_{a,in}\left(\frac{C_{\mathrm{H_2S}}}{C_{\mathrm{H_2S,in}}}e^{\alpha_{a,\mathrm{H_2S}}f\eta_{a,in}} - \frac{C_{\mathrm{H_2O}}\sqrt{C_{\mathrm{S_2}}}}{C_{\mathrm{H_2O,in}}\sqrt{C_{\mathrm{S_2,in}}}}e^{(2-\alpha_{a,\mathrm{H_2S}})f\eta_{a,in}}\right) \tag{3.43}$$

$$i_c = i^{\circ}_{c,in}\left(\sqrt{\frac{C_{O_2}}{C_{O_2,in}}}e^{-\alpha_{c,\mathrm{O_2}}f\eta_{c,in}} - e^{(2-\alpha_{c,\mathrm{O_2}})f\eta_{c,in}}\right) \tag{3.44}$$

The assumption that either of these half-cell reactions occurs in a single step is however theoretically suspect for two reasons. A reaction with multiple electrons transfered together is unlikely [117, 102]. Secondly, complex heterogeneous reactions involving three different phases, like the two above, usually occur in multiple "elementary" steps.

Next I will develop one such reaction mechanism for the H_2S oxidation half reaction (3.39) and present the corresponding rate equations.

3.2.1 A H_2S electro-oxidation mechanism

A general heterogeneous chemical reaction consists of several elementary reactions such as adsorption of reactants, reactions on the surface between adsorbed species, and desorption of products. Although the electrode materials for the experiments discussed in this work are transition metal sulphides, in general the electrode material can be any electronic conductor. For a SOFC, the electrolyte is an oxide by definition and in this work, the electrolyte was yttria stabilized zirconia or YSZ.

In this reaction mechanism I assume there are active sites on the anode, designated (a), as well as the electrolyte (e). All the oxygen species remain on the electrolyte (e) sites, and only protons can be transferred across from the (a) sites to the (e) sites. The fuel H_2S can only adsorb onto free sites on the anode. Another assumption for this mechanism is that all the species in the reactions below are local to the active three phase boundary (tpb) on the anode side. Surface diffusion from either surface toward the tpb is not considered.

$$H_2S + V_a \rightleftarrows H_2S.V_a \tag{3.45}$$

$$H_2S.V_a + V_a \rightleftarrows SH.V_a + H.V_a \tag{3.46}$$

$$SH.V_a + V_a \rightleftarrows S.V_a + H.V_a \tag{3.47}$$

$$O_O^x + V_e \rightleftarrows O^{2-}.V_e + V_O^{\cdot\cdot} \tag{3.48}$$

$$H.V_a + O^{2-}.V_e \rightleftarrows OH^-.V_e + V_a + e^- \tag{3.49}$$

$$OH^-.V_e + H.V_a \rightleftarrows H_2O.V_e + V_a + e^- \tag{3.50}$$

$$H_2O.V_e \rightleftarrows H_2O + V_e \tag{3.51}$$

$$2S.V_a \rightleftarrows S_2 + 2V_a \tag{3.52}$$

V_e is a surface site on the electrolyte, V_a is a surface site on the anode, O_O^x is an O in the electrolyte bulk, and $V_O^{\cdot\cdot}$ is an oxygen vacancy in the electrolyte bulk.

There are four surface species on the anode ($H_2S.V_a$, $HS.V_a$, $S.V_a$, $H.V_a$) and three on the electrolyte ($H_2O.V_e$, $OH^-.V_e$, $O^{2-}.V_e$), not counting the vacant sites on each phase.

Briefly, the reaction sequence is:

1. A molecule of H_2S adsorbs onto a vacant anode surface site.
2. Adsorbed H_2S dissociates to give SH and H species on the anode surface.
3. The SH dissociates further into an S and H.
4. On the electrolyte side, an oxygen from the bulk moves to a surface vacancy, leaving a bulk vacancy behind.
5. The first of the adsorbed hydrogen atoms jumps across to a surface oxygen on the electrolyte, leaving its electron and an anode site on the anode. The surface oxygen becomes a surface hydroxl having acquired the proton.
6. The second adsorbed hydrogen atom jumps across to the surface hydroxl on the electrolyte, leaving its electron and an anode site on the anode. The surface hydroxl thus becomes a surface water molecule.
7. The water molecule on the electrolyte surface desorbs leaving an oxygen vacancy behind.

8. Two surface S atoms on the anode combine and desorb leaving two vacant anode sites behind.

The net rates of reaction for each of the steps above are given by mass action kinetics (3.53)...(3.60).

$$r_1 = k_1 P_{\mathrm{H_2S}} \theta_a - k_{-1} \theta_{\mathrm{H_2S}} \tag{3.53}$$

$$r_2 = k_2 \theta_{\mathrm{H_2S}} \theta_a - k_{-2} \theta_{\mathrm{SH}} \theta_{\mathrm{H}} \tag{3.54}$$

$$r_3 = k_3 \theta_{\mathrm{SH}} \theta_a - k_{-3} \theta_{\mathrm{S}} \theta_{\mathrm{H}} \tag{3.55}$$

$$r_4 = k_4 \hat{\theta}_e - k_{-4} \hat{\theta}_O \tag{3.56}$$

$$r_5 = k_5 \theta_{\mathrm{H}} \hat{\theta}_O e^{(1-\beta_5) f E_a} - k_{-5} \hat{\theta}_{OH} \theta_a e^{-\beta_5 f E_a} \tag{3.57}$$

$$r_6 = k_6 \hat{\theta}_{OH} \theta_{\mathrm{H}} e^{(1-\beta_6) f E_a} - k_{-6} \hat{\theta}_{\mathrm{H_2O}} \theta_a e^{-\beta_6 f E_a} \tag{3.58}$$

$$r_7 = k_7 \hat{\theta}_{\mathrm{H_2O}} - k_{-7} P_{\mathrm{H_2O}} \hat{\theta}_e \tag{3.59}$$

$$r_8 = k_8 \theta_{\mathrm{S}}^2 - k_{-8} P_{\mathrm{S_2}} \theta_a^2 \tag{3.60}$$

P_k is the partial pressure of gas species k, θ_m is the surface coverage of species m on the anode, E_a is the anode electrical potential, $\hat{\theta}_n$ is the surface coverage of species m on the electrolyte, and k_i, k_{-i} are the temperature dependent forward and backward rate constants for reaction i in the list (3.45)...(3.52). The units for the reaction rates r_i are mole/($\mathrm{m_{tpb}}$.s) where $\mathrm{m_{tpb}}$ is the length of the active triple phase boundary (tpb) in the anode in metres. Reactions 5 and 6 will generally have different charge transfer coefficients β_i.

The surface coverage θ_m is defined as the ratio of the number of sites occupied by species m to the total number of sites available on the anode surface. $\hat{\theta}_n$ is defined similarly for the electrolyte surface.

The species balance equations for this reaction mechanism are obtained by (3.61) and (3.62).

$$C_{a,\,total} \frac{d\theta_m}{dt} = \sum_i \xi_{m,i} r_i \tag{3.61}$$

$$C_{e,\,total} \frac{d\hat{\theta}_n}{dt} = \sum_i \xi_{m,i} r_i \tag{3.62}$$

$C_{a,\,total}$ and $C_{e,\,total}$ are the total molar surface concentration of active sites on

the anode and the electrolyte, and $\xi_{m,i}$ is the stoichiometric coefficient of species m in reaction i. Assuming only the tpb is active, the units of these quantities would be moles of active sites/m tpb.

For example, equation (3.61) written for θ_{SH} would be:

$$C_{a,\,total}\frac{d\theta_{\mathrm{SH}}}{dt} = (r_2 - r_1) \tag{3.63}$$

Doing the site balance for the surface coverages gives:

$$\theta_a + \theta_{\mathrm{S}} + \theta_{\mathrm{H}} + \theta_{\mathrm{SH}} + \theta_{\mathrm{H_2S}} = 1 \tag{3.64}$$

$$\hat{\theta}_e + \hat{\theta}_O + \hat{\theta}_{OH} + \hat{\theta}_{\mathrm{H_2O}} = 1 \tag{3.65}$$

These summation equations are needed to close the system of equations given by (3.61) and (3.62). Since the rate equations involving charge transfer contain the electrode potential E_a as a variable, another equation is needed to account for the time variation of E_a. This charge balance equation is given by (3.66) for the mechanism here.

$$C_{dl}\frac{dE_a}{dt} = i_a - F(r_5 + r_6) \tag{3.66}$$

C_{dl} is the double layer capacitance (per unit tpb length) of the anode.

This makes eight ordinary differential equations (4 for the anode species, 3 for the electrolyte species, 1 for the anode potential), and two algebraic equations, that need to be solved together for a full transient solution.

If all the kinetic constants are available or can be estimated, then I can integrate the surface species rate equations given by (3.61) and (3.62) along the tpb, the active region in the anode. For the steady state solution, one can set the time derivatives in the equations above to zero. This would result in a system of ten algebraic equations. These systems of equations (time-dependent or steady state) need to be coupled to the gas phase mass transfer equations presented in section 2.2 to obtain local partial pressures P_k. These equations also need to be coupled to the charge transport equations discussed in section 2.4 to obtain the local electrical potential E_a.

If the kinetic constants required above are unavailable or if one do not want to

solve the coupled equations above, one can make certain assumptions to make the above problem computationally tractable.

Rate equations assuming a rate determining step

One of the simplifications possible is when one reaction in the mechanism is much slower than the rest. The rate of the overall reaction is then determined by the rate of this rate determining step (RDS). As the other reactions in the mechanism can proceed at much faster rates, they can be assumed to be in quasi-equilibrium. With these assumptions, the overall rate equation can be derived for a particular rate determining step. I present the resulting overall rate equations for two different rate determining steps below. The analysis and detailed derivations are given in appendix A.

If (3.54) (dissociation of H_2S) is rate controlling, the current density is given by:

$$i_{a,2} = i^{o}_{a,2}\left(P_{H_2S} - P_{H_2O}\sqrt{P_{S_2}}e^{-2f\eta_a}\right) \tag{3.67}$$

$$i^{o}_{a,2} = \frac{2FK'_1}{\left(1 + K'_2\sqrt{P_{S_2}} + K'_3\sqrt{P_{H_2O}}e^{-f\eta_a} + K'_4\sqrt{P_{H_2O}P_{S_2}}e^{-f\eta_a} + K'_5P_{H_2S}\right)^2} \tag{3.68}$$

$\eta_a = E_a - E^{o}_{a}$ and K'_l are various combinations of the rate constants k_i, k_{-i}.

If (3.58) (second proton transfer) is rate controlling, the current density is given by:

$$i_{a,6} = i^{o}_{a,6}\left(\frac{P^2_{H_2S}}{P_{H_2O}P_{S_2}}e^{(4-\beta_6)f\eta_a} - P_{H_2O}e^{-\beta_6 f\eta_a}\right)$$

$$i^{o}_{a,6} = \frac{2FK'''_1}{\left(1 + K'''_2\sqrt{P_{S_2}} + K'''_3P_{H_2S} + K'''_4\frac{P_{H_2S}}{\sqrt{P_{H_2O}}}e^{f\eta_a} + K'''_5\frac{P_{H_2S}}{\sqrt{P_{H_2O}P_{S_2}}}e^{f\eta_a}\right)} \times \frac{1}{\left(1 + K'''_6 + K'''_7P_{H_2O} + K'''_8\frac{P_{H_2S}}{\sqrt{P_{H_2O}P_{S_2}}}e^{2f\eta_a}\right)} \tag{3.69}$$

As seen in equations (3.67) and (3.69), the overall rate equation is of the form (3.70), and the terms in the denominator are dependent on the electrical potential

of the electrode.

$$i_a = i_a^{\circ}\left(\frac{P_{H_2S}^{x_{an}}}{P_{H_2O}^{y_{an}}P_{S_2}^{z_{an}}}e^{\alpha_{an}f\eta_a} - \frac{P_{H_2O}^{y_{ca}}P_{S_2}^{z_{ca}}}{P_{H_2S}^{x_{ca}}}e^{-\alpha_{ca}f\eta_a}\right) \tag{3.70}$$

$$\alpha_{an} + \alpha_{ca} = 2\gamma = 2(x_{an} + x_{ca}) = 2(y_{an} + y_{ca}) = 4(z_{an} + z_{ca}) \tag{3.71}$$

γ is either 1 or 2, and the number 2 multiplying γ is the number of electrons transfered for the overall anode reaction. The subscript a denotes the anodic term while c denotes the cathodic term.

The reaction orders for the three reactants and products in equation (3.70) are such that all such overall rate equations are thermodynamically consistent. I demonstrate this below by confirming that setting $i_a = 0$ in equation (3.70) leads to the Nernst equation for the anode equilibrium potential (3.76).

$$\frac{P_{H_2S}^{x_{an}}}{P_{H_2O}^{y_{an}}P_{S_2}^{z_{an}}}e^{\alpha_{an}f(E_{eq}-E^{\circ})} = \frac{P_{H_2O}^{y_{ca}}P_{S_2}^{z_{ca}}}{P_{H_2S}^{x_{ca}}}e^{-\alpha_{ca}f(E_{eq}-E^{\circ})} \tag{3.72}$$

$$e^{(\alpha_{an}+\alpha_{ca})f(E_{eq}-E^{\circ})} = \frac{P_{H_2O}^{y_{an}+y_{ca}}P_{S_2}^{z_{an}+z_{ca}}}{P_{H_2S}^{x_{an}+x_{ca}}} \tag{3.73}$$

$$e^{2\gamma f(E_{eq}-E^{\circ})} = \frac{P_{H_2O}^{\gamma}P_{S_2}^{\gamma/2}}{P_{H_2S}^{\gamma}} \tag{3.74}$$

$$2\gamma\frac{F}{RT}(E_{eq} - E^{\circ}) = \gamma\ln\frac{P_{H_2O}P_{S_2}^{0.5}}{P_{H_2S}} \tag{3.75}$$

$$E_{eq} = E^{\circ} + \frac{RT}{2F}\ln\frac{P_{H_2O}P_{S_2}^{0.5}}{P_{H_2S}} \tag{3.76}$$

3.3 Parameters

The parameters needed to calculate the electrochemical reaction rate depend on the model used for the electrochemistry. A detailed reaction model with multiple elementary steps requires all the kinetic constants for the elementary steps k_i, k_{-i} along with the charge transfer coefficients β_i for the charge transfer steps. A model developed using the rate determining step assumption also requires several kinetic parameters (e.g., K_i in equation (3.69)) and at least one charge transfer coefficient. A simpler model equation such as (3.41) has only two parameters i° and β (or α_a).

Determining the parameters required for any of these models needs reliable

experimental data such as electrode polarization data using a 3-electrode setup and carefully designed fuel composition. These can then be used to determine the correct reaction orders and charge transfer coefficients for the given electrode. I present some experimental data in Chapter 5 where the fuel composition was varied to examine the effect on full fuel cell performance. However, since the setup did not allow an extra reference electrode, I could not isolate the anode's performance. In Chapters 4 and 7 I demonstrate the use of parameter estimation for obtaining kinetic parameters in equations similar to equations (3.41) and (3.42).

3.4 Discussion

The mechanism presented in section 3.2.1 is one of many that can be proposed for the electrochemical oxidation of H_2S. The only reliable method to arrive at the correct or at least a better mechanism is to validate the model against carefully controlled experiments. In the absence of electrode polarization data for different gas compositions, it is impossible to confirm any mechanism or rate equation. For the case of hydrogen sulphide, the situation is further complicated by the dissociation of H_2S into H_2 and S_2. Thus, there is more than one component in the fuel that can be electro-oxidized at the anode. I will examine this problem in some detail in Chapters 6 and 7.

In Chapter 4, I will use the electrochemical rate equations given in equations (3.43) and (3.44) while in Chapter 7 I use the forms given by equations (3.41) and (3.42). These simpler rate equations are used since they have the least number of parameters (only i_j^o if I make the common assumption of $\beta_j = 0.5$), and there is no anode side half cell data for the electrode materials used to validate the more involved models of the type in section 3.2.1 above.

Chapter 4

Models for published data

In this Chapter[1], I will present models for the fuel cell investigated by Liu et al. [84]. The fuel cell is in the shape of a circular disc held between the air outlet tube on one side and the fuel outlet tube on the other. On both sides, inflow occurs through the inner tube and the outflow through the annulus between the inner and outer tubes. Both the air and fuel sides are at atmospheric pressure. This geometry is very common and is also known as a "button cell". The data sets that are used in this work to validate the models are from a sample cell that used Co-Mo-S mixed with Ag as anode, and Pt as cathode. The electrolyte was 8 mole % YSZ. The cell assembly and the gas feeds and outlets are held in a temperature controlled furnace.

I present four different models of increasing complexity and examine their fit to experimental data given in [84]. Of these, the first two are one-dimensional models that solve for the electrochemistry as well as electrical potential and mass transfer in the electrodes. I start with the simplest model possible that explicitly calculates the output voltage of the cell given the current being drawn from it. This model is derived using a one dimensional analysis along the axis of the cell and calculates the three voltage loss terms: the electrical resistance losses, the mass transfer losses, and the electrochemical activation losses separately by ignoring the coupling between the mass transfer and electrochemistry. The second model is a refined version of the first where the mass transfer losses and the electrochemical activation losses are coupled and cannot be calculated explicitly. For this model, the performance of the cell is calculated by solving a set of coupled non-linear algebraic equations. The third and fourth models are two dimensional axi-symmetric

[1]Versions of this Chapter are published as [93] and [94]

models where the flow, mass transfer, voltage fields, and electrochemical reaction are all modelled. The fourth model is identical to the third, except the diffusive mass transfer is modelled using the multi-component Maxwell-Stefan formulation instead of Fick's law. The resulting coupled partial differential equations are solved using finite element methods (FEM).

As seen in Chapters 2 and 3, in order to solve these models, various parameters such as diffusion coefficients, viscosities, electrical conductivities of the electrodes and electrolyte, and electrochemical reaction rate parameters need to be defined. While many of these parameters are known or can be estimated, some, such as exchange current densities for the electrochemical reactions in the electrodes are not known with any certainty. There are no data on electrochemical kinetic parameters for H_2S anodes in literature. While there is some kinetic data for O_2 reduction on Pt cathodes, there is little agreement in the SOFC research community on the reaction mechanisms [3]. Since there is no reliable data for the electrochemical kinetic parameters, I use non-linear least squares estimation in this work to estimate the kinetic parameters in all four models.

I start by describing the model geometries and discussing the assumptions I use. The computational modelling tools used to frame and solve these models are described next. The governing equations for transport phenomena and electrochemistry have already been introduced in Chapters 2 and 3. However, for completeness, I next list all the model equations and boundary conditions here and discuss the model parameters. I then introduce the mathematical formulation used for estimating the unknown parameters. The results of the parameter estimation are presented next, and I examine these estimates and the quality of the fit of the models to the experimental data to draw conclusions on the fidelity and usefulness of the models.

4.1 Model geometry

The 1-D and 2-D model geometries are given in Figure 4.1. In developing the 2-D models, the cylindrical geometry of the experimental cell and the symmetry around the central axis is used to reduce the modelling domain to a 2-D axi-symmetric domain as shown in the top section of Figure 4.1. The subdomains in this reduced domain are (going left to right): (i) the fuel flow channel, $\Omega_{f,fuel}$ (ii) the anode, Ω_a (iii) the electrolyte, Ω_m (iv) the cathode, Ω_c and (v) the air flow channel, $\Omega_{f,air}$.

Although the tubes carrying the reactants and products in the fuel cell assembly were 40 cm long, I only model the 5 cm adjacent to the fuel cell. This is done to reduce the size of the computational domains. The 1-D model geometry, given in the bottom section of Figure 4.1 does not consider the flow channels as the inherently 2-D flow field cannot be modelled correctly in a 1-D model.

In the 2-D models, the current collectors are located at the vertical interface between the flow and electrode subdomains on both sides. In the 1-D model, the anode current collector is the left-most point of the domain while the cathode current collector is the right-most point in the domain.

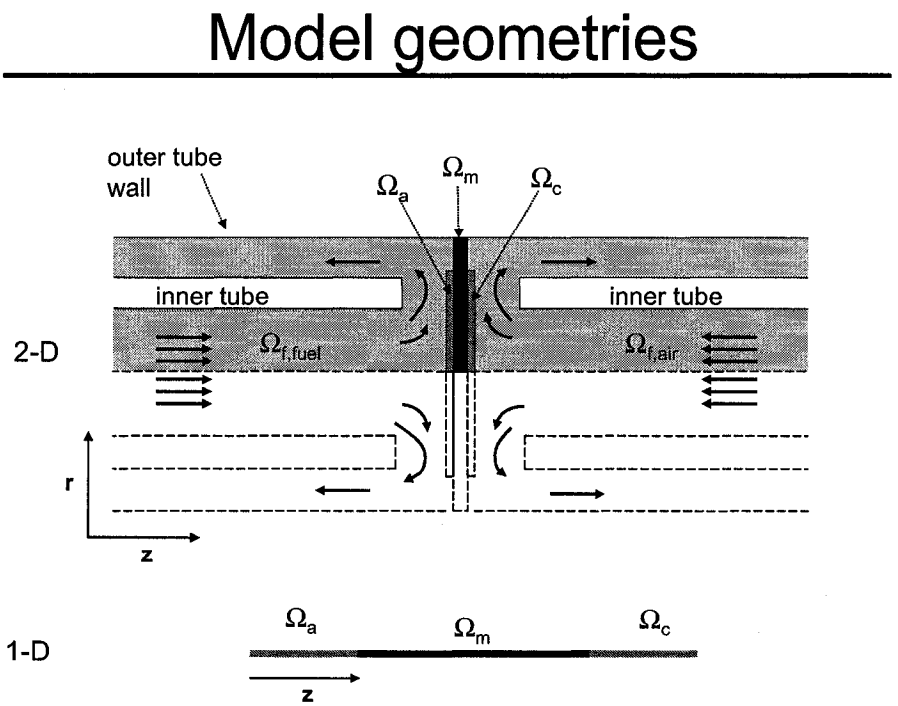

Figure 4.1: 1-D and 2-D model geometries (not to scale)

4.2 Model assumptions

Although the overall oxidation reaction for H_2S oxidation to S_2 (4.1) has been presented in earlier Chapters, it is reproduced here for easier reference.

$$H_2S + \frac{1}{2}O_2 \Leftrightarrow H_2O + \frac{1}{2}S_2 \tag{4.1}$$

The main assumptions used in the models presented are:

1. all models presented in this Chapter are isothermal
2. the only electrochemical reaction modelled on the anode is the oxidation of H_2S to H_2O and S_2 (reaction 4.13) even though there are probably other reactions occuring simultaneously
3. the open circuit voltage is taken as the zero current voltage in the data set being modelled
4. in the 1-D models, the absolute pressure is assumed constant in the electrodes

I explain these assumptions in more detail in relevant subsections.

The assumption that all models are isothermal is justified in the current study for the following reasons:

- The experimental cell modelled is in a temperature controlled electric furnace.
- The current density drawn from the cell is relatively small, which means the heat generation is also small.
- Although the fuel and air streams are not preheated before they are fed to the SOFC, the flow-rates are quite small (25 ml/min) and allow the gases to come up to cell temperature by the time they get to the actual cell. The above was verified by modelling only the fluid flow and heat transfer using an extended 2-D geometry similar to that described in Chapter 7.

4.2.1 Open circuit voltage

In most fuel cell models, the open circuit voltage (OCV) or the equilibrium voltage across a fuel cell is calculated using the Nernst equation [102]. In all the models discussed in this Chapter however, the open circuit voltage, E_{oc} is taken from experimental data instead of being calculated using the Nernst equation. This is done primarily because the Nernst equation contains the compositions of the products (H_2O and S_2 for reaction 4.1) as well as the reactants. These were not measured during the experiments [84] that are modelled here. Although I assume inlet concentrations for (H_2O and S_2 for reaction 4.1) in the models later in this Chapter, the Nernst potentials predicted are not consistent with the measured OCV values.

Also, the open circuit voltage in a H_2S SOFC is possibly a mixed voltage from the different possible reactions at the anode [145, 4, 140]. Modelling a mixed voltage requires that the kinetics of each possible electrochemical reaction be considered. This in turn requires additional kinetic parameter values for each reaction, and as discussed earlier, these are unavailable for the anode used in the experiments. This is also the reason why reaction 4.1 is the only electrochemical reaction modelled here. In Chapter 7, I model the OCV using Nernst equation and also revisit the problem of calculating a mixed open circuit voltage.

4.3 Modelling tools

The one-dimensional models are solved using MATLAB [129] while COMSOL Multiphysics [31] is used to solve the two-dimensional models. MATLAB is a general purpose computational software platform and language. COMSOL Multiphysics is a finite element method based modelling package for the simulation of any physical process that can be described using ordinary or partial differential equations. It has an easy to use graphic user interface that handles all modelling steps from geometry generation and meshing, to defining the differential equations and boundary conditions, to solving and post-processing the results. COMSOL Multiphysics has a MATLAB interface that allows easy transfer of data from one to the other. It is this interface that allows the use of optimization routines available in MATLAB for the parameter estimation described later.

4.4 Decoupled 1-D explicit model

In developing this model I followed a similar approach to that detailed in Kim et al. [74] and Chan et al. [25]. A one-dimensional analysis was done along the thickness of the cell (Figure 4.1) to obtain a model equation (4.2) that relates the voltage of the working cell, V_{cell} to the current density, i drawn from the cell.

$$V_{\text{cell}} = E_{\text{oc}} - i\hat{R}_{\Omega} - \eta_{\text{act-anode}} - \eta_{\text{act-cathode}} - \eta_{\text{conc-anode}} - \eta_{\text{conc-cathode}} \quad (4.2)$$

$\hat{R}_{\Omega}$ is the total ohmic resistance (cell area specific) of the cell, η_{act} are the activation voltage losses at the anode and cathode, and η_{conc} are the concentration (mass transfer) voltage losses. The activation and concentration (mass transfer) voltage losses in the model are given in the equations (4.3 ... 4.7) below.

$$\hat{R}_{\Omega} = \left.\frac{l}{\sigma}\right|_{\text{YSZ}} + \left.\frac{l}{\sigma}\right|_{\text{anode}} + \left.\frac{l}{\sigma}\right|_{\text{cathode}} + \hat{R}_{\text{contact}} \quad (4.3)$$

$$\eta_{\text{act-anode}} = \frac{2RT}{n_e F} \sinh^{-1}\left(\frac{i}{2i_{\text{a}}^{\text{o}}}\right) \quad (4.4)$$

$$\eta_{\text{act-cathode}} = \frac{2RT}{n_e F} \sinh^{-1}\left(\frac{i}{2i_{\text{c}}^{\text{o}}}\right) \quad (4.5)$$

$$\eta_{\text{conc-anode}} = -\frac{RT}{2F} \ln\left(\frac{1 - i/i_{\text{a, lim}}}{(1 + K_{\text{H}_2\text{O}}\, i/i_{\text{a, lim}})\sqrt{1 + K_{\text{S}_2}\, i/i_{\text{a, lim}}}}\right) \quad (4.6)$$

$$\eta_{\text{conc-cathode}} = -\frac{RT}{4F} \ln\left(1 - \frac{i}{i_{\text{c, lim}}}\right) \quad (4.7)$$

$$i_{\text{a, lim}} = \frac{P_{\text{H}_2\text{S,in}}}{(2 + P_{\text{H}_2\text{S,in}}/P)} \frac{4FD_{\text{H}_2\text{S, eff}}}{RTl_{\text{a}}} \quad (4.8)$$

$$i_{\text{c, lim}} = \frac{P_{\text{O}_2\text{,in}}}{(1 - P_{\text{O}_2\text{,in}}/P)} \frac{4FD_{\text{O}_2\text{, eff}}}{RTl_{\text{c}}} \quad (4.9)$$

l is the length and σ the electrical conductivity of the electrode or electrolyte. n_e is the number of electrons transferred in the electrode reaction, and P is the total or absolute pressure. For both the 1-D models, I assume that P is constant at 1.013×10^5 Pa in both electrodes. The ohmic resistance, given by equation (4.3), includes the area specific resistance of the zirconia electrolyte, the electrodes and the contact resistance. Any current lead wire or inter-phase resistance is bundled into $\hat{R}_{\text{contact}}$. The activation losses assume a Butler-Volmer [102] kinetic expression

where the charge transfer coefficients are 0.5, and i_a^o, i_c^o are the exchange current densities. K_{H_2O} in equation (4.6) is a function of initial partial pressures of H_2O and H_2S, while K_{S_2} is a function of initial partial pressures of S_2 and H_2S. The concentration voltage loss terms have the limiting current densities $i_{a,\,lim}$ and $i_{c,\,lim}$ as parameters, which in turn are functions of, among other things, the effective diffusivities of the reactants, $D_{k,\,eff}$. Effective diffusivity is a function of the bulk diffusivity D_k, Knudsen diffusivity $D_{K,k}$, and the ratio of porosity to tortuousity ϵ/τ.

$$D_{k,\text{eff}} = \frac{\epsilon/\tau}{\left({D_k}^{-1} + {D_{K,k}}^{-1}\right)} \tag{4.10}$$

The solutions to the mass transfer equations for the reactants and products are used to obtain the above terms for the concentration losses. The form of the mass transfer equations, and thus the solutions are identical to those for the 1-D coupled model discussed in the next section. These solutions or concentration profiles (4.23 ... 4.25) however, need to be linearized to get the explicit form for the concentration losses. Of course, the 1-D explicit model does not consider the coupling between the activation and concentration losses because the form of the Butler–Volmer equation used (4.4, 4.5) does not contain any concentration terms, while the 1-D implicit model does so through the concentration terms in the electrochemical rate equations (4.19, 4.20).

4.5 Coupled 1-D implicit model

The governing ordinary differential equations (ODEs) used in the 1-D implicit model are presented in this section. A 1-D model for this geometry cannot consider flow and mass transfer in the channels. Thus, the model equations only need to describe the mass transfer in the electrodes and the voltage distribution in the anode, cathode, and electrolyte. The model domain is a line that extends from the current collector on the anode to the current collector on the cathode along the axis of the cell and includes the electrodes and the electrolyte (see bottom of Figure 4.1).

4.5.1 Governing equations: mass transfer and voltage

Mass transfer

The reactants, oxygen on the cathode side and hydrogen sulphide on the anode side, are transported from the flow channels to their respective electrode-electrolyte interfaces where the reaction occurs. Similarly, the products on the anode side are transported from the anode-electrolyte interface into the fuel flow channel. This mass transfer of the reactants and products is modelled using the convection-diffusion equation, where diffusion is modelled using Fick's law:

$$\frac{d}{dz}\{-D_{k,\text{eff}}\frac{dC_k}{dz} + \tilde{v}C_k\} = 0 \tag{4.11}$$

$$\tilde{v} = -\frac{i}{FC_\text{t}}\sum_k \frac{\xi_k}{n_k} \tag{4.12}$$

C_k is the molar concentration of the k^{th} component, C_t the total molar concentration, ξ_k is the stoichiometric coefficient and n_k the number of electrons transferred per molecule of component k in the electrode electrochemical reaction, and $\tilde{v}$ is the mole average velocity of the gas. $k = \{H_2S, H_2O, S_2\}$ in the anode and $\{O_2\}$ in the cathode. As no carrier gas is used on the anode side in the experiments, I can model transport of H_2S and H_2O on the anode side and obtain the concentration of S_2 at any point by using the identity: $C_{S_2} = C_\text{t} - C_{H_2S} - C_{H_2O}$. I obtain equation (4.12) for $\tilde{v}$ by considering the overall molar flux towards or away from the reaction interface and assuming that the total pressure, and thus the total molar concentration remains constant in the electrodes.

Potential distribution

The fuel reacts on the anode-electrolyte interface and releases electrons. These electrons travel through the anode to the outer circuit and come around through the cathode to the cathode-electrolyte interface where they are consumed in the reaction with oxygen. To complete the circuit, the oxide ions produced at the cathode-electrolyte interface travel across the electrolyte to the anode-electrolyte interface.

$$H_2S + O^{2-} \Leftrightarrow H_2O + \frac{1}{2}S_2 + 2e^- \tag{4.13}$$

$$O_2 + 4e^- \Leftrightarrow 2O^{2-} \tag{4.14}$$

The voltage and current distribution in the electrodes and the electrolyte due to this electronic and ionic transport is modelled using Ohm's law:

$$\frac{d}{dz}\left(-\sigma_j \frac{d\phi_j}{dz}\right) = 0 \tag{4.15}$$

σ_j is the electrical conductivity and ϕ_j is the electrical potential of the j^{th} sub-domain (anode, electrolyte, or cathode).

4.5.2 Boundary conditions

To get the concentration and voltage profiles, the following boundary conditions need to be solved:

- Concentrations of O_2 in air, and H_2S, H_2O in fuel given at the inlets

$$\begin{aligned} C_{H_2S}|_{\partial\Omega_{\text{fuel,inlet}}} &= C_{H_2S,\text{in}} \\ C_{H_2O}|_{\partial\Omega_{\text{fuel,inlet}}} &= C_{H_2O,\text{in}} \\ C_{O_2}|_{\partial\Omega_{\text{air,inlet}}} &= C_{O_2,\text{in}} \end{aligned} \tag{4.16}$$

- Molar flux, of the reactants into, and the products out of, the electrolyte governed by the local current density at the electrode-electrolyte interface

$$\begin{aligned} \left(-D_{H_2S,\text{eff}}\frac{dC_{H_2S}}{dz} - \frac{i_{\text{anode}}C_{H_2S}}{4FC_t}\right)\Bigg|_{\partial\Omega_{\text{anode,electrolyte}}} &= \frac{i_{\text{anode}}}{2F} \\ \left(-D_{H_2O,\text{eff}}\frac{dC_{H_2O}}{dz} - \frac{i_{\text{anode}}C_{H_2S}}{4FC_t}\right)\Bigg|_{\partial\Omega_{\text{anode,electrolyte}}} &= -\frac{i_{\text{anode}}}{2F} \\ \left(-D_{O_2,\text{eff}}\frac{dC_{O_2}}{dz} - \frac{i_{\text{cathode}}C_{O_2}}{4FC_t}\right)\Bigg|_{\partial\Omega_{\text{cathode,electrolyte}}} &= -\frac{i_{\text{cathode}}}{4F} \end{aligned} \tag{4.17}$$

- The voltage at the anode and cathode current collectors is specified

$$\begin{aligned} -\sigma_{\mathrm{a}} \frac{d\phi_{\mathrm{a}}}{dz}\bigg|_{\partial\Omega_{\mathrm{anode,collector}}} &= (\phi_{\mathrm{a}} - 0)\left[\frac{\sigma}{l}\right]_{\mathrm{contact}} \\ -\sigma_{\mathrm{c}} \frac{d\phi_{\mathrm{c}}}{dz}\bigg|_{\partial\Omega_{\mathrm{cathode,collector}}} &= (\phi_{\mathrm{c}} - V_{\mathrm{cell}})\left[\frac{\sigma}{l}\right]_{\mathrm{contact}} \end{aligned} \tag{4.18}$$

  $[\sigma/l]_{\mathrm{contact}}$ is the reciprocal of the area specific contact and lead resistance for each electrode.

- Current density at the electrode-electrolyte interfaces is given by the electrochemical reaction rate, which is dependent on the local concentrations of the active species and the local voltage difference between the electrode and the electrolyte [102]

$$\begin{aligned} -\sigma_{\mathrm{a}} \frac{d\phi_{\mathrm{a}}}{dz}\bigg|_{\partial\Omega_{\mathrm{anode,electrolyte}}} = i^{\mathrm{o}}_{\mathrm{a,in}} \Bigg\{ & \frac{C_{\mathrm{H_2S}}}{C_{\mathrm{H_2S,in}}} \exp\left(\frac{2(1-\beta)\eta_{\mathrm{a}}F}{RT}\right) \\ & - \frac{C_{\mathrm{H_2O}}}{C_{\mathrm{H_2O,in}}} \sqrt{\frac{C_{\mathrm{S_2}}}{C_{\mathrm{S_2,in}}}} \exp\left(\frac{-2\beta\eta_{\mathrm{a}}F}{RT}\right) \Bigg\} \end{aligned} \tag{4.19}$$

$$\begin{aligned} -\sigma_{\mathrm{c}} \frac{d\phi_{\mathrm{c}}}{dz}\bigg|_{\partial\Omega_{\mathrm{cathode,electrolyte}}} = i^{\mathrm{o}}_{\mathrm{c,in}} \Bigg\{ & \sqrt{\frac{C_{\mathrm{O_2}}}{C_{\mathrm{O_2,in}}}} \exp\left(\frac{-2\beta\eta_{\mathrm{c}}F}{RT}\right) \\ & - \exp\left(\frac{2(1-\beta)\eta_{\mathrm{c}}F}{RT}\right) \Bigg\} \end{aligned} \tag{4.20}$$

$$\begin{aligned} -\sigma_{\mathrm{a}} \frac{d\phi_{\mathrm{a}}}{dz}\bigg|_{\partial\Omega_{\mathrm{anode,electrolyte}}} &= -\sigma_{\mathrm{m}} \frac{d\phi_{\mathrm{m}}}{dz}\bigg|_{\partial\Omega_{\mathrm{anode,electrolyte}}} \\ -\sigma_{\mathrm{c}} \frac{d\phi_{\mathrm{c}}}{dz}\bigg|_{\partial\Omega_{\mathrm{cathode,electrolyte}}} &= -\sigma_{\mathrm{m}} \frac{d\phi_{\mathrm{m}}}{dz}\bigg|_{\partial\Omega_{\mathrm{cathode,electrolyte}}} \end{aligned} \tag{4.21}$$

$$\eta_{\mathrm{a}} = \phi_{\mathrm{anode}} - \phi_{\mathrm{electrolyte}} - E_{\mathrm{a,\,in}}$$
$$\eta_{\mathrm{c}} = \phi_{\mathrm{cathode}} - \phi_{\mathrm{electrolyte}} - E_{\mathrm{c,\,in}} \tag{4.22}$$

$i_{\mathrm{a}}^{\mathrm{o}}$ and $i_{\mathrm{c}}^{\mathrm{o}}$ are the exchange current densities of the anode and cathode, β is the charge transfer coefficient, $C_{k,in}$ are the inlet component concentrations and $E_{\mathrm{a,\,in}}$ and $E_{\mathrm{c,\,in}}$ are the anode and cathode equilibrium potentials.

The boundary conditions (4.19, 4.20) are the electrochemical rate equations first introduced in Chapter 3. The equations used in both the 1-D implicit model as well as the 2-D models in this Chapter is (3.41) written in the form of (3.22). While a chemical rate equation depends on local species concentrations, an electrochemical rate equation depends on local species concentrations as well as the local potential difference between the electrode and electrolyte phases.

Solution of the mass transfer ODEs and boundary conditions gives the component partial densities and electric potentials as functions of current density and distance from the anode current collector along the cell axis:

$$C_{\mathrm{H_2S}} = -2C_{\mathrm{t}} + (2C_{\mathrm{t}} + C_{\mathrm{H_2S,in}}) \exp\left(-\frac{iz}{4C_{\mathrm{t}}FD_{\mathrm{H_2S,eff}}}\right) \tag{4.23}$$

$$C_{\mathrm{H_2O}} = 2C_{\mathrm{t}} + (-2C_{\mathrm{t}} + C_{\mathrm{H_2O,in}}) \exp\left(-\frac{iz}{4C_{\mathrm{t}}FD_{\mathrm{H_2O,eff}}}\right) \tag{4.24}$$

$$C_{\mathrm{O_2}} = C_{\mathrm{t}} + (-C_{\mathrm{t}} + C_{\mathrm{O_2,in}}) \exp\left(-\frac{i[z - (l_{\mathrm{a}} + l_{\mathrm{m}} + l_{\mathrm{c}})]}{4C_{\mathrm{t}}FD_{\mathrm{O_2,eff}}}\right) \tag{4.25}$$

$$\phi_j = m_j z + c_j \tag{4.26}$$

m_j and c_j are integration constants for the voltage profile equation for the j^{th} sub-domain (anode, electrolyte, or cathode).

Although I obtain the concentration profiles above, they are functions of the current density which in turn is a function of the concentrations at the inter phase boundaries. The electric potential boundary conditions ((4.18) .. (4.22)) provide a set of coupled non-linear algebraic equations that cannot be solved analytically. In this work, these six equations in six unknowns (m_j and c_j), are solved numerically using MATLAB [129].

4.6 2-D models

The first 2-D model solves the i) weakly-compressible Navier-Stokes equations and Darcy's law for velocity and pressure in the flow channels and electrodes respectively, ii) convection-diffusion mass transfer equations for partial densities of H_2S, H_2O, S_2 on the fuel side and O_2 on the air side and, iii) Laplace equation (Ohm's law) for the voltage/current distribution in the electrodes and electrolyte.

The second 2-D model uses the Maxwell-Stefan equations (instead of Fick's law) to model the multicomponent mass transfer in the fuel cell.

4.6.1 Flow in gas channels

The fluid flow in the fuel and air channels is important as it describes the transport of reactants to and the products from the cell. I use the weakly compressible form of the Navier Stokes equations (4.27) as discussed in Chapter 2 to model flow in the gas channels.

$$\begin{aligned} &-\nabla.\left[\mu\left(\nabla\mathbf{v}+(\nabla\mathbf{v})^T\right)-\frac{2}{3}\mu(\nabla.\mathbf{v})\mathbf{I}\right]+\rho\left(\mathbf{v}.\nabla\mathbf{v}\right)+\nabla P=0 \\ &\nabla.(\rho\mathbf{v})=0 \end{aligned} \tag{4.27}$$

μ is the viscosity of the fluid, $\mathbf{v}$ is the velocity vector, ρ is the density, P is the pressure, and $\mathbf{I}$ is the identity matrix.

Boundary Conditions (channel flow)

- zero velocity (no-slip) at the walls

$$\mathbf{v}=0|_{\partial\Omega_{\text{walls}}} \tag{4.28}$$

- velocity continuous across the channel-electrode interfaces

$$\mathbf{v}^{\text{flow channels}}=\mathbf{v}^{\text{electrodes}}|_{\partial\Omega_{\text{flow channels}-\text{electrodes}}} \tag{4.29}$$

- fully developed laminar flow at the fuel and air inlets for given volumetric

flow-rates:

$$u = 0, \quad v = \frac{2\dot{V}}{\pi r_{inner}^2}\left[1 - \left(\frac{r}{r_{inner}}\right)^2\right] \tag{4.30}$$

u and v are the r and z components of the velocity vector, $\dot{V}$ is the temperature corrected volumetric flow-rate, and r_{inner} is the inner radius for the inlet tube.

- pressure specified and flow normal to the boundary at the outlets of the flow channels.

$$P = 0, \quad \mathbf{t}.\mathbf{v} = 0 \tag{4.31}$$

$\mathbf{t}$ is the tangent vector to the boundary.

- Radial symmetry along the axis of the flow channels

$$\left.\frac{\partial v}{\partial r}\right|_{r=0} = 0, \quad u|_{r=0} = 0 \tag{4.32}$$

4.6.2 Flow in electrodes

The flow in the porous electrodes is modelled using Darcy's law:

$$\begin{aligned} \mathbf{v} &= -\frac{\kappa}{\mu}\nabla P \\ \nabla.(\rho\mathbf{v}) &= 0 \end{aligned} \tag{4.33}$$

κ is the permeability of the porous electrode.

Boundary Conditions (electrode flow)

- pressure at each electrode-flow channel interface is equal to the pressure in the flow channel at that interface

$$P_{\text{anode}}|_{\partial\Omega_{\text{anode,fuel channel}}} = P_{\text{fuel channel}}|_{\partial\Omega_{\text{anode,fuel channel}}} \tag{4.34}$$

$$P_{\text{cathode}}|_{\partial\Omega_{\text{cathode,air channel}}} = P_{\text{air channel}}|_{\partial\Omega_{\text{cathode,air channel}}} \tag{4.35}$$

- flow into the electrodes at the electrode-electrolyte interface is the net difference in the amount of the products being formed and the reactants being consumed at that interface

$$-\mathbf{n}.\mathbf{v}|_{\partial\Omega_{\text{electrode,electrolyte}}} = \frac{1}{\rho}\left(\frac{i_{\text{electrode}}}{F}\sum_k \frac{\xi_k M_k}{n_k} + \sum_k \mathbf{n}.\mathbf{j}_k\right) \tag{4.36}$$

  $\mathbf{n}$ is the normal vector, $i_{\text{electrode}}$ is the current density, M_k the molar weight, and $\mathbf{j}_k$ is the diffusive flux of the k^{th} component.

- Radial symmetry along the axis of the cell

$$\left.\frac{\partial P}{\partial r}\right|_{r=0} = 0 \tag{4.37}$$

4.6.3 Mass transfer

The two mass transfer models used for the 2-D fuel cell models in this work were also described in Chapter 2. The convection-diffusion equation (4.38) is used in both models to describe the mass transfer of the reactants and products in the flow channels and the electrodes.

$$\nabla.\mathbf{j}_i + \rho\mathbf{v}.\nabla w_i = 0 \tag{4.38}$$

The diffusive flux is given by Fick's law (4.39) in the first 2-D model, and by the Maxwell–Stefan diffusive flux (4.40) in the second [16].

$$\mathbf{j}_i = -\rho\bar{D}_i\nabla(w_i) \tag{4.39}$$

$\mathbf{j}_i$ is the diffusive flux of i, ρ is the density of the gas mixture, w_i the mass fraction of the i^{th} component. $\bar{D}_i$ is the diffusivity of component i: bulk diffusivity

in the flow channels, effective diffusivity in the electrodes. Mass fractions are used instead of mole fractions or molar concentrations in the Fick diffusive flux term because the mass transfer is coupled to the fluid flow equations where the fluid velocity **v** is a mass average quantity.

$$\mathbf{j}_i = -\rho w_i \sum_{j=1}^{n} \tilde{D}_{ij} \left(\nabla y_j + (y_j - w_j) \frac{\nabla P}{P} \right) \tag{4.40}$$

In equation (4.40), n is the total number of species in the mixture, y_j is the mole fraction of species j, and $\tilde{D}_{ij}$ is the multicomponent composition dependent diffusivity of species i in j, which is given by:

$$\frac{y_i y_k}{D_{ik}} = -w_i w_k \frac{\sum_{j \neq i} (\mathrm{adj} B_i)_{jk}}{\sum_{j \neq i} \tilde{D}_{ij} (\mathrm{adj} B_i)_{jk}} \tag{4.41}$$
$$(B_i)_{kj} = D_{kj} - D_{ij}, i \neq j$$

D_{ik} are multicomponent Maxwell–Stefan diffusivities that for low density gas mixtures can be approximated by composition independent binary diffusivities, and can be estimated using the Fuller, Schettler and Giddings equation. The values used in this work are given in section 4.7.

Mass fractions and mole fractions are related through:

$$w_j = \frac{y_j M_j}{\sum_j y_j M_j} \tag{4.42}$$

For Fick's law, effective diffusivity in the electrodes is defined in equation (4.10), but for Maxwell-Stefan mass transfer, equation (4.43) is used.

$$D_{ik,\mathrm{eff}} = \frac{\epsilon}{\tau} D_{ik} \tag{4.43}$$

As discussed earlier, no carrier gas is used on the anode side in the experiments. Thus, I can model transport of H_2S and H_2O on the anode side and obtain the mass fraction of S_2 at any point by using the identity: $w_{S_2} = 1 - w_{H_2S} - w_{H_2O}$.

Boundary Conditions (Convection-diffusion equation)

- mass fraction of O_2 in air, and H_2S, S_2, H_2O in fuel given at the flow channel inlets

$$\begin{aligned} w_{H_2S}|_{\partial\Omega_{\text{fuel,inlet}}} &= w_{H_2S,\text{in}} \\ w_{H_2O}|_{\partial\Omega_{\text{fuel,inlet}}} &= w_{H_2O,\text{in}} \\ w_{O_2}|_{\partial\Omega_{\text{air,inlet}}} &= w_{O_2,\text{in}} \end{aligned} \tag{4.44}$$

- zero flux at the inner and outer tube walls

$$\begin{aligned} \mathbf{n}.\mathbf{N}_k|_{\partial\Omega_{\text{walls}}} &= 0 \\ \mathbf{N}_k &= \mathbf{j}_k + \rho w_k \mathbf{v} \end{aligned} \tag{4.45}$$

  $\mathbf{N}_k$ is the total mass flux of the k^{th} component.

- mass flux, of the reactants out of, and the products into, the electrodes governed by the local current density at the electrode-electrolyte interface

$$\begin{aligned} -\mathbf{n}.\mathbf{N}_{H_2S}|_{\partial\Omega_{\text{anode,electrolyte}}} &= -\frac{M_{H_2S} i_{\text{anode}}}{2F} \\ -\mathbf{n}.\mathbf{N}_{H_2O}|_{\partial\Omega_{\text{anode,electrolyte}}} &= \frac{M_{H_2O} i_{\text{anode}}}{2F} \\ -\mathbf{n}.\mathbf{N}_{O_2}|_{\partial\Omega_{\text{cathode,electrolyte}}} &= -\frac{M_{O_2} i_{\text{cathode}}}{4F} \end{aligned} \tag{4.46}$$

- radial symmetry along the axis of the flow channels and the electrodes

$$\left.\frac{\partial w_k}{\partial r}\right|_{r=0} = 0 \tag{4.47}$$

4.6.4 Voltage and current distribution

The voltage and current distribution in the electrodes and the electrolyte due to this electronic and ionic transport is modelled using the vector form of Ohm's law:

$$\begin{aligned}
\nabla.(-\sigma_{\mathrm{m}}\nabla\phi_{\mathrm{m}}) &= 0 \\
\nabla.(-\sigma_{\mathrm{a}}\nabla\phi_{\mathrm{a}}) &= 0 \\
\nabla.(-\sigma_{\mathrm{c}}\nabla\phi_{\mathrm{c}}) &= 0
\end{aligned} \tag{4.48}$$

σ_{m}, σ_{a}, σ_{c} are electrical conductivities of the electrolyte, anode and cathode, and ϕ_{m}, ϕ_{a}, ϕ_{c} are electrical potentials of the electrolyte, anode, and cathode.

Boundary Conditions (Ohm's law)

- the voltage at the anode and cathode current collectors is specified

$$\begin{aligned}
\mathbf{n}.\mathbf{i}_{\mathrm{anode}}|_{\partial\Omega_{\mathrm{anode,collector}}} &= (\phi_{\mathrm{a}} - 0)\left[\frac{\sigma}{l}\right]_{\mathrm{contact}} \\
\mathbf{n}.\mathbf{i}_{\mathrm{cathode}}|_{\partial\Omega_{\mathrm{cathode,collector}}} &= (\phi_{\mathrm{c}} - V_{\mathrm{cell}})\left[\frac{\sigma}{l}\right]_{\mathrm{contact}} \\
\mathbf{i}_j &= -\sigma_j\nabla\phi_j
\end{aligned} \tag{4.49}$$

  $\mathbf{i}$ is the current density vector, $[\sigma/l]_{\mathrm{contact}}$ is the area specific contact and lead conductance.

- electrical insulation at the outer tube walls

$$\begin{aligned}
\mathbf{n}.\mathbf{i}_{\mathrm{anode}}|_{\partial\Omega_{\mathrm{walls}}} &= 0 \\
\mathbf{n}.\mathbf{i}_{\mathrm{cathode}}|_{\partial\Omega_{\mathrm{walls}}} &= 0 \\
\mathbf{n}.\mathbf{i}_{\mathrm{electrolyte}}|_{\partial\Omega_{\mathrm{walls}}} &= 0
\end{aligned} \tag{4.50}$$

- current density at the electrode-electrolyte interfaces is given by the electrochemical reaction rate

$$-\mathbf{n}.\mathbf{i}_{\text{anode}}|_{\partial\Omega_{\text{anode,electrolyte}}} = i_{\text{a}}^{\text{o}}\left\{\frac{y_{\text{H}_2\text{S}}}{y_{\text{H}_2\text{S,in}}}\exp\left(\frac{2(1-\beta)\eta_{\text{a}}F}{RT}\right)\right.$$
$$\left.-\frac{y_{\text{H}_2\text{O}}}{y_{\text{H}_2\text{O,in}}}\sqrt{\frac{y_{\text{S}_2}}{y_{\text{S}_2\text{,in}}}}\exp\left(\frac{-2\beta\eta_{\text{a}}F}{RT}\right)\right\} \quad (4.51)$$

$$-\mathbf{n}.\mathbf{i}_{\text{cathode}}|_{\partial\Omega_{\text{cathode,electrolyte}}} = i_{\text{c}}^{\text{o}}\left\{\sqrt{\frac{y_{\text{O}_2}}{y_{\text{O}_2\text{,in}}}}\exp\left(\frac{-2\beta\eta_{\text{c}}F}{RT}\right)\right.$$
$$\left.-\exp\left(\frac{2(1-\beta)\eta_{\text{c}}F}{RT}\right)\right\} \quad (4.52)$$

$$\eta_{\text{a}} = \phi_{\text{anode}} - \phi_{\text{electrolyte}} - E_{\text{a, in}}$$
$$\eta_{\text{c}} = \phi_{\text{cathode}} - \phi_{\text{electrolyte}} - E_{\text{c, in}} \quad (4.53)$$

y_k are the mole fractions at the boundary, $y_{k,in}$ are the inlet mole fractions.

- radial symmetry along the axis of the electrodes and the electrolyte

$$\left.\frac{\partial\phi_j}{\partial r}\right|_{r=0} = 0 \quad (4.54)$$

4.6.5 2-D Meshing

The mesh generated for the 2-D models above had 3853 triangular elements, which translates to 30229 degrees of freedom. I used the non-linear parametric solver (with the UMFPACK direct solver for the linear subsystem) in COMSOL Multiphysics to solve the model at equally spaced voltage intervals from near OCV to 0 V. Grid independence of the results was insured by comparing the model output for the current density at 0 V and 850°C, against a mesh 4 times denser. The relative error in the calculated current denstiy was of the order of 10^{-6} between the mesh used in this work (with 3853 elements) and the test mesh with 15412 elements.

4.7 Parameters used in the models

Table 4.1: Temperature independent parameters in the models

Parameter	units	value
P	Pa	1.013×10^5
$\dot{V}_{\text{fuel}}$	ml/min	25
$\dot{V}_{\text{air}}$	ml/min	25
$y_{H_2S,in}$	–	0.985
$y_{H_2O,in}$	–	0.01
$y_{O_2,in}$	–	0.21
ϵ	–	0.4
τ	–	4
$r_{\text{pore,av}}$	m	2×10^{-6}
l_{a}	m	10^{-4}
l_{c}	m	10^{-4}
l_{m}	m	2×10^{-4}
κ_{a}	m^2	10^{-14}
κ_{c}	m^2	10^{-14}

There are a number of parameters in the models presented above and these parameters need to be estimated before the models can be solved. Physical constants, such as the gas constant R, and the values assigned to them in the models are summarized in the Nomenclature. Transport parameters needed include diffusivities, viscosities, and electrical conductivities, while the electrochemical parameters needed are equilibrium electrode potential, exchange current density and the charge transfer coefficient for each electrode.

Binary diffusion coefficients D_{ij} are estimated using the Fuller, Schettler and Giddings relation given in Reid et al., 1987 [113]. Knudsen diffusion coefficients $D_{\text{K},k}$ are calculated assuming smooth round pores. Viscosity of the gases on both sides of the fuel cell $\mu_{\text{air}}, \mu_{\text{fuel}}$ is estimated using Brokaw's method also outlined in [113]. The density of the gases are calculated using the ideal gas law and the mass fractions of the components. Experimental values for electrode permeability κ were not available and order of magnitude estimates are used based on permeability values calculated for close packings of spheres [114].

Electrical conductivity of the anode materials σ_{a} used was measured by Liu, 2004 [83] and those values are used here. The cathode used in the experiments was Pt, and the values for both electrode conductivities at the operating temperatures

Table 4.2: Temperature dependent parameter values used

Parameter	units	750°C	800°C	850°C
D_{H_2S,H_2O}	m^2/s	1.89×10^{-4}	2.05×10^{-4}	2.23×10^{-4}
D_{H_2S,S_2}	m^2/s	9.12×10^{-5}	9.91×10^{-5}	1.07×10^{-4}
D_{H_2O,S_2}	m^2/s	1.42×10^{-4}	1.54×10^{-4}	1.67×10^{-4}
D_{O_2,N_2}	m^2/s	1.8×10^{-4}	1.96×10^{-4}	2.12×10^{-4}
D_{K,H_2S}	m^2/s	1.06×10^{-3}	1.09×10^{-3}	1.12×10^{-3}
D_{K,H_2O}	m^2/s	1.46×10^{-3}	1.50×10^{-3}	1.53×10^{-3}
D_{K,S_2}	m^2/s	7.76×10^{-4}	7.94×10^{-4}	8.13×10^{-4}
D_{K,O_2}	m^2/s	1.1×10^{-3}	1.12×10^{-3}	1.15×10^{-3}
μ_{air}	$kg.(m.s)^{-1}$	3.71×10^{-5}	3.82×10^{-5}	3.93×10^{-5}
μ_{fuel}	$kg.(m.s)^{-1}$	3.7×10^{-5}	3.85×10^{-5}	4.01×10^{-5}
$\Delta\phi_c^0$	V	0.886	0.880	0.872
σ_a	$(\Omega.m)^{-1}$	13.1	9.88	5.26
σ_c	$(\Omega.m)^{-1}$	1.11×10^6	1.06×10^6	1.02×10^6
σ_m	$(\Omega.m)^{-1}$	1.49	2.39	3.66
$[\sigma/l]_{contact}$	$\Omega^{-1}m^{-2}$	7670	7000	7730

are corrected for porosity using equation (4.55) given in [34]. Values for conductivity of the YSZ electrolyte σ_a are obtained using the temperature dependent form given in [5].

$$\sigma_{\text{electrode, eff}} = \epsilon\sigma_{\text{electrode}} \tag{4.55}$$

The equilibrium potential of the cathode $\Delta\phi_c^0$ is set to the value of the open circuit potential at each operating temperature while the equilibrium potential of the anode ϕ_a^0 is set to zero. The open circuit potential at each operating temperature is taken from the experimental $i-V$ data sets. The charge transfer symmetry coefficients β in the electrochemical rate equations (4.19, 4.20, 4.51, 4.52) are assigned the defualt value of 0.5 [102]. As experimental values for exchange current densities are not available, I estimate them using the models and experimental $i-V$ data. The estimation procedure is explained in the next section.

The overall wire lead and contact resistance is calculated by comparing the cell's $i-V$ curve to the IR compensated $i-V$ curve at the different operating temperatures. The overall cell area specific resistance is given by equation (4.56), where V_{IR} is the IR compensated cell voltage and V is the actual cell voltage when

a current density of i is drawn from the cell. Four such values taken at different points of the $i-V$ curve are averaged and the known resistances of the different cell layers are subtracted from the overall resistance to obtain the overall wire lead and contact resistance for the cell (4.58). This overall resistance is then divided into equal halves in the models and placed at the current collectors for each electrode.

$$\hat{R}_\Omega = \frac{V_{\mathrm{IR}} - V}{i} \tag{4.56}$$

$$\left[\frac{l}{\sigma}\right]_{\mathrm{contact,t}} = \hat{R}_\Omega - \left[\frac{l}{\sigma}\right]_{\mathrm{YSZ}} - \left[\frac{l}{\sigma}\right]_{\mathrm{anode}} - \left[\frac{l}{\sigma}\right]_{\mathrm{cathode}} \tag{4.57}$$

$$\left[\frac{l}{\sigma}\right]_{\mathrm{contact}} = \frac{1}{2}\left[\frac{l}{\sigma}\right]_{\mathrm{contact,t}} \tag{4.58}$$

The numerical values of all the parameters used are given in tables 4.1 and 4.2.

4.8 Estimation of uncertain parameters

As discussed earlier, the electrochemical parameters on the anode side are completely unknown whereas those on the cathode side are uncertain. In this work I estimate exchange current densities i_{a}° and i_{c}° using non-linear least squares [131]. This method minimizes the sum of the squares of the difference between experimental data points and the model output by varying the parameters to be estimated.

The data is filtered before being sent to the estimation algorithm. This filtering includes:

1. The Robust Lowess smoothing method provided in MATLAB's Curve Fitting Toolbox was used to smooth the $i - V$ data. [130].

2. Repeating data points and data values against the trend are removed.

3. Current density values are interpolated for an equally spaced vector of voltage values to get a $i-V$ matrix of a manageable size. For all four models used in this study, the V vector was defined by 16 equally spaced points that went from 99% of the open circuit potential of the cell to 0 V.

The parameter estimation routine takes this matrix of $i - V$ data at each temperature and uses the models to iterate to i_0 values that fit the given data

best. The 1-D explicit model calculates the cell voltage as a function of specified average current density while the 1-D implicit and the 2-D models calculate current density for a specified cell operating voltage. Thus, the parameter estimation needs to be set up differently depending on the model being fitted.

4.8.1 Mathematical formulation for 1-D explicit model

$$\min_{\mathbf{x}} \sum_{k=1}^{n} \{V_{\mathrm{m}}(i_k, T) - V_{k,T}\}^2$$

subject to:

$$V_{\mathrm{m}} = f\,(i, T, \mathbf{x}, \mathbf{p})$$
$$\mathbf{x}_l \leq \mathbf{x} \leq \mathbf{x}_u$$

$V_{\mathrm{m}}(i_k, T)$ is the output cell voltage given by the model for the current density i_k while $V_{k,T}$ is the experimentally observed cell voltage at current density i_k and operation temperature T. The vector $\mathbf{x}$ contains the unknown parameters (i°_{a}, i°_{c} in this case), and $\mathbf{x}_l, \mathbf{x}_u$ are the lower and upper bounds for these parameters. The vector $\mathbf{p}$ represents the known parameters (e.g., σ_j, $D_{j,\mathrm{eff}}$) needed to solve the model for V_{m}, and n is the number of data points. The function $f()$ represents the 1-D explicit fuel cell model.

4.8.2 Mathematical formulation for 1-D implicit and 2-D models

$$\min_{\mathbf{x}} \sum_{k=1}^{n} \{i_{\mathrm{m}}(V_k, T) - i_{k,T}\}^2$$

subject to:

$$i_{\mathrm{m}} = \mathbf{g}\,(V, T, \mathbf{x}, \mathbf{p}^*)$$
$$\mathbf{x}_l \leq \mathbf{x} \leq \mathbf{x}_u$$

$i_m(V_k, T)$ is the output cell current density given by the model for a cell voltage of V_k and $i_{k,T}$ is the experimentally observed current density for the same cell voltage of V_k. The vector $\mathbf{p}^*$, again represents the known parameters needed to solve the model for i_m. The function $\mathbf{g}()$ represents the fuel cell model.

4.8.3 Computational resources used

I ran all parameter estimation routines using the function *lsqnonlin* in the MATLAB Optimization Toolbox [131]. The 1-D explicit model's parameter estimation took $\approx$ 1 second on a 3 GHz Intel Pentium computer. The 1-D implicit model's parameter estimation took $\approx$ 5 minutes while parameter estimation for the 2-D models took from 5–14 hours per data set. As seen in the section on modelling, the 1-D explicit model calculates the output $V_m(i)$ as an explicit function of i, while the 1-D implicit model needs to solve a system of 6 coupled non-linear algebraic equations to calculate $i_m(V)$. For the 2-D models presented here, COMSOL Multiphysics solves for $\sim 30,000$ degrees of freedom to calculate the current drawn by the cell at a given cell voltage.

4.9 Results and discussion

The results of the parameter estimation for all four models are summarized in Table 4.3. The last column on the right hand side gives the scaled fit for all the models at the three temperatures. These numbers are obtained by scaling the normalized fit with the maximum value in the data being fitted: $\frac{\sqrt{\sum (V_m - V_k)^2/n}}{\max(V_k)}$ for the 1-D explicit model and $\frac{\sqrt{\sum (i_m - i_k)^2/n}}{\max(i_k)}$ for the other two models.

There are several trends that can be discerned from this data. The first one is that i_a^o and i_c^o increase with increasing temperature for all the models. This trend is expected for catalyzed electrochemical reactions.

Model fit to data improves with increasing temperature for all the models. The models fit the data at 850°C better than at 800°C and 750°C (see figures 4.2, 4.3, 4.4). A simplistic explanation for this trend is that the performance curves become less non-linear and thus easier to fit, with increasing temperature. However, the models do allow a non-linear $i - V$ response through the electrochemical rate equations (4.51 and 4.52). I believe this mismatch, more severe at lower temperatures due to the lower i_j^o, is partly due to the anomalous OCV values. The measured

Table 4.3: Parameter estimation results

Model used	T (°C)	i_a^o (A/m^2)	i_c^o (A/m^2)	Scaled fit –
1-D explicit	750	70.0	70.0	2.85×10^{-2}
	800	180.7	180.6	1.50×10^{-2}
	850	344.9	344.9	3.98×10^{-3}
1-D implicit	750	60.1	62.3	4.14×10^{-2}
	800	157.5	163.3	2.15×10^{-2}
	850	300.0	309.1	9.32×10^{-3}
2-D Fickian mass transfer	750	55.0	73.3	4.14×10^{-2}
	800	181.7	187.2	2.51×10^{-2}
	850	571.1	356.3	1.59×10^{-2}
2-D Maxwell–Stefan	750	54.1	74.5	4.13×10^{-2}
	800	163.9	199.3	2.50×10^{-2}
	850	565.8	362.9	1.60×10^{-2}

OCV values for this data set are significantly lower than values normally seen for SOFCs running on dry H_2S (> 1V). This points to a possible voltage/current leak [101].

Another reason can be the symmetric charge transfer coefficients (1 for both exponential terms with $\beta = 0.5$) used in the electrochemical rate equations (4.19, 4.20, 4.51, 4.52). These values are obtained by assuming a reaction mechanism with a rate controlling two electron transfer step. Ongoing research in our group is focussing on deriving better electrochemical rate equations.

According to the scaled fit values in Table 4.3 the 1-D explicit model seems to give a better fit to the data at all three temperatures. It does seem counter-intuitive that a model that I know to be too simple to explain all that is happening in the fuel cell gives a better fit to the experimental data. However, visual examination of the model fit for the different models to the experimental $i - V$ data does not show any significant difference between the fit for the 1-D *vs* 2-D models, and as I note later, the 1-D models cannot correctly calculate the coupled activation and concentration losses, especially at the low flow-rates used here.

All models give values for i_a^o and i_c^o that give a fair Arrhenius temperature dependence. The Arrhenius plot for the i_a^o and i_c^o given by the 2-D model using Maxwell–Stefan mass transfer is shown in Figure 4.5. This plot gives the i^o *vs.* 1/T

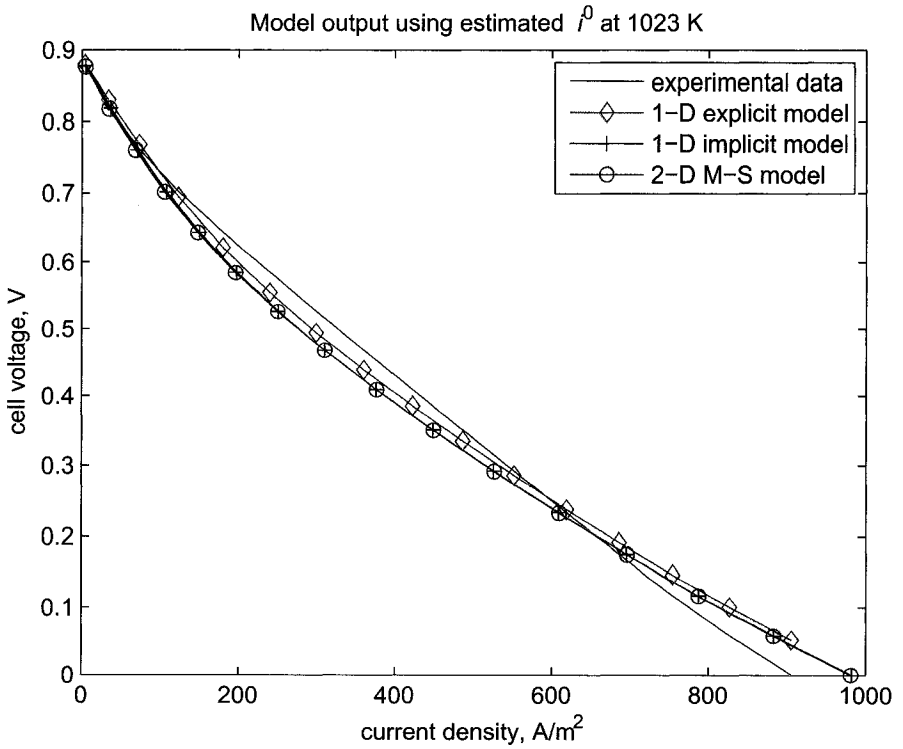

Figure 4.2: Model output using optimized i° at 750°C

curves obtained with pre-exponentials and activation energies calculated using the optimal i_a° and i_c°. The plot also shows the actual optimal values for the exchange current densities used to calculate the least squares fitted values for A_j and E_j in equations (4.59). These pre-exponential factors and activation energies are given in Table 4.4.

$$\begin{aligned} i_a^{\circ} &= A_a e^{-E_a/(RT)} \\ i_c^{\circ} &= A_c e^{-E_c/(RT)} \end{aligned} \tag{4.59}$$

4.9.1 The 1-D models

The main difference between the 1-D explicit and the 1-D implicit models is that in the explicit model the reaction rate is independent of the local species concen-

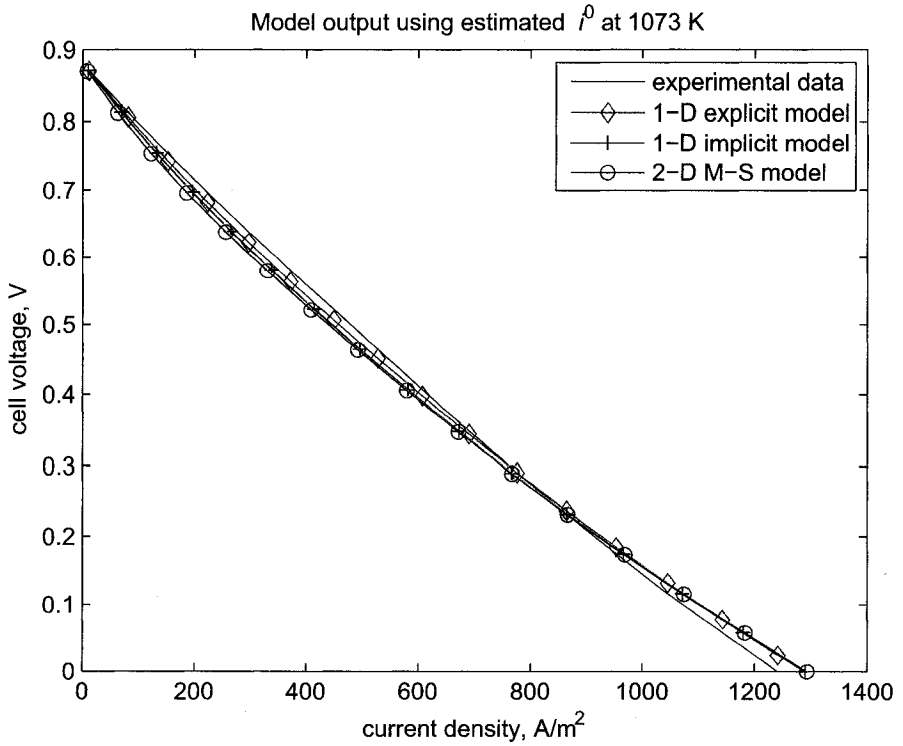

Figure 4.3: Model output using optimized i^o at 800°C

Table 4.4: Arrhenius parameters estimated for i^o in 2-D Maxwell–Stefan model

	A (A/m^2)	E (KJ/mole)
i_a^o	1.41×10^{13}	224
i_c^o	4.35×10^9	152

trations (equations 4.4 and 4.5) whereas the reaction rate in the implicit model depends on the local concentrations at the reaction surface (equations 4.19 and 4.20). In the implicit model the reaction rate is thus coupled to the mass transfer whereas the activation and concentration losses are decoupled and separable in the explicit model. The above difference between the two models however gives no clear indication as to how it would affect i^o estimates.

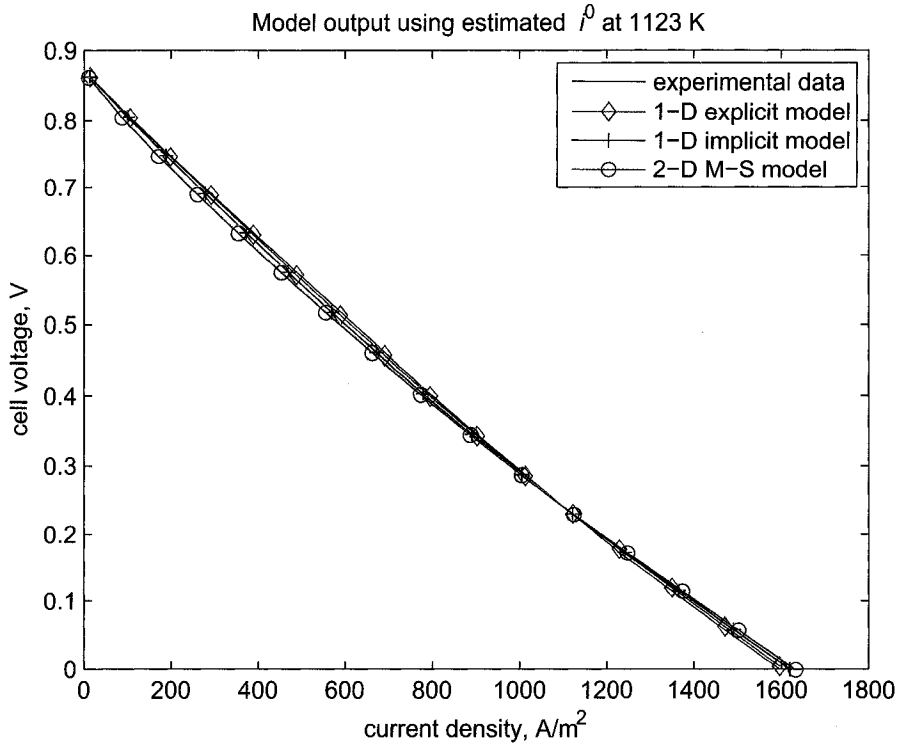

Figure 4.4: Model output using i^o at 850°C

4.9.2 1-D implicit model *vs* 2-D Fick model

For all the three data sets or temperatures, the i^o values in the 1-D implicit model are lower than those in the 2-D model using Fick mass transfer. This difference can be explained by the difference in species concentrations at the interface between the electrodes and the electrolyte in the two models. The 2-D model accounts for flow and mass transfer in the gas channels and is thus able to include the mass transfer resistance in the flow domain. The 1-D implicit model cannot account for the inherently two-dimensional flow field in a button cell and cannot account for mass transfer in the channels correctly. Therefore the parameter estimation for the 1-D implicit model ends up assigning a higher activation resistance (lower i^o). A plot of the mass fraction profile of O_2 along the axis of the cell is given in Figure 4.6. This supports the above discussion by illustrating the difference between the 1-D and 2-D models in predicting concentrations at the cathode-electrolyte boundary (surface where the cathode reaction occurs).

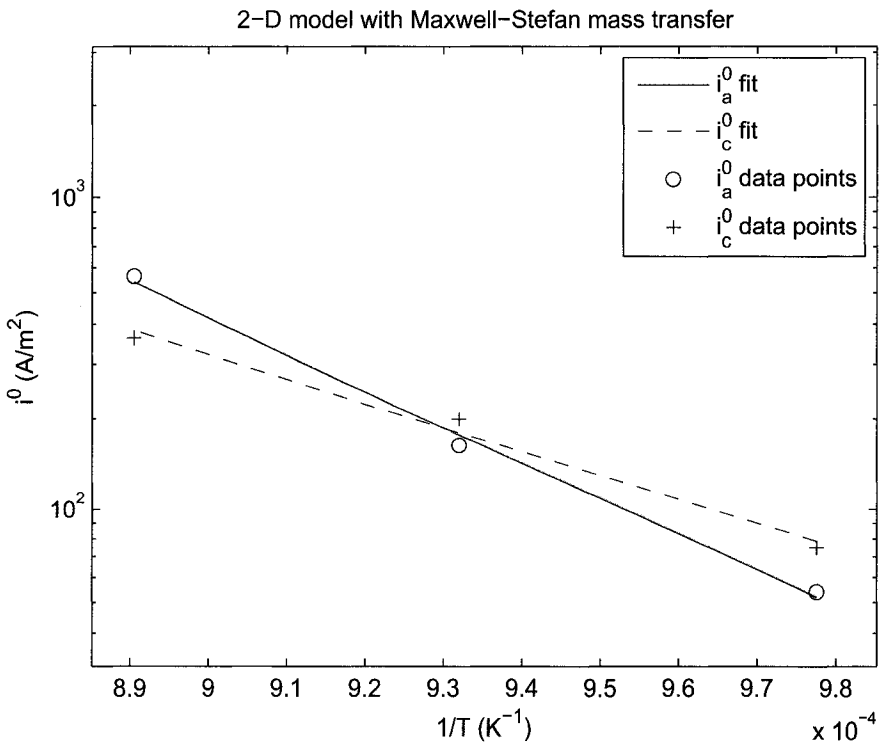

Figure 4.5: Arrhenius plot for i° from 2-D M–S model

The above discussion also implies that if sufficiently high flow-rates are used, the 1-D implicit model will approximate the 2-D model better. This is verified in Figure 4.7 where two $i - V$ curves generated using the 2-D Maxwell–Stefan model are compared to the experimental data at 850°C. The two curves given have the same values for i_a° and i_c°: the parameter estimates for the 1-D implicit model. The flow-rates of the gas streams however, are 25 ml/min for one curve and 250 ml/min for the other. As clearly seen in Figure 4.7, the model output for the higher flow-rate is able to approximate the experimental data quite well even though the kinetic parameters used are obtained from the 1-D model. This is because the higher flow-rate dramatically decreases the mass transfer resistance in the gas channels.

The radial variation of species concentrations is insignificant as seen in Figure 4.8. The rise in w_{O_2} from the left to the right of Figure 4.8 is due to diffusion into the electrode from the edge at the right.

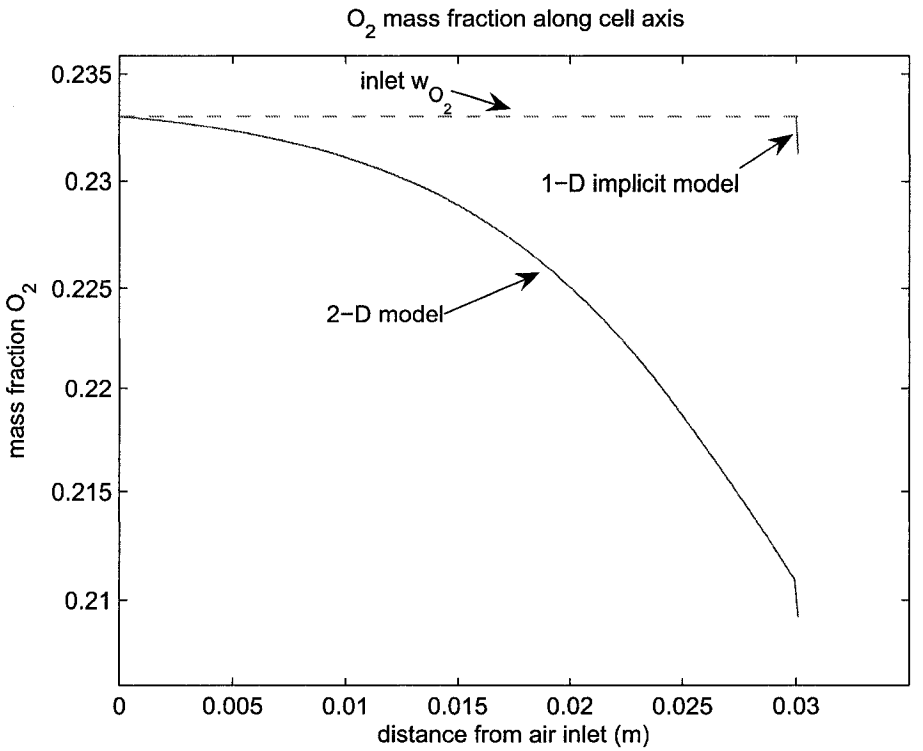

Figure 4.6: O_2 mass fraction profiles along axis for the 1-D implicit and 2-D models at 850°C

4.9.3 The 2-D models

The 2-D models used differ only in how they compute the mass transfer of the different species. The Maxwell–Stefan mass transfer formulation is superior to the Fick mass transfer form because it correctly accounts for the variation in the diffusivites of the different components with composition [128].

Taking the 2-D model with Maxwell–Stefan mass transfer to be the most faithful model, I now discuss the profiles of the different voltage losses in the SOFC. Figure 4.9 gives the cell voltage as well as various voltage losses (commonly called overpotentials) as a function of cell current density according to the second 2-D model at 850°C.

The plot clearly shows that the highest voltage loss is due to the contact/current lead resistances which account for 2.68 Ω or 80% of the total ohmic resistance of 3.33 Ω at 850°C. The anodic and cathodic activation losses, respectively are next

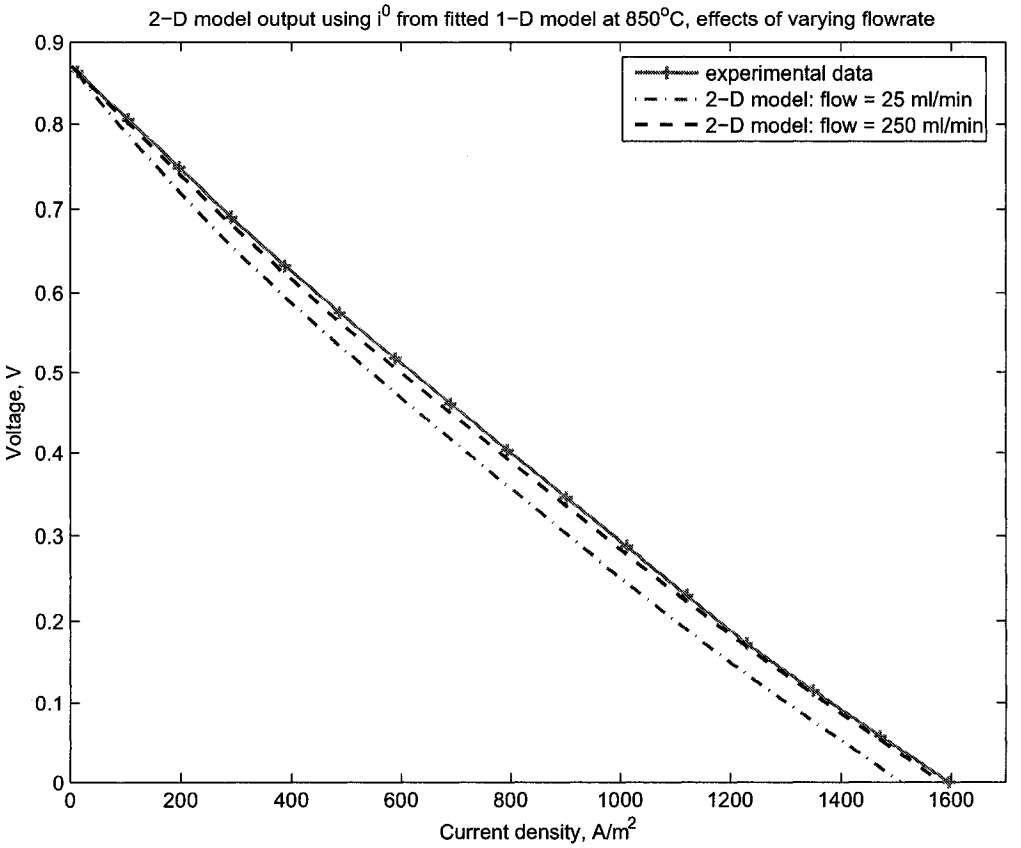

Figure 4.7: 2-D model output using i^o from 1-D model at 850°C at different flow rates

highest, followed by the ohmic loss in the electrolyte. The ohmic loss in the anode is roughly 14 times smaller than the ohmic loss in the electrolyte, while that in the cathode is another 4 orders of magnitude smaller than in the anode. The relative magnitudes of the different ohmic losses can also be readily calculated from the resistivity values and the breadths of the different phases (tables 4.1, 4.2).

Figure 4.10 gives the mass fractions of the reactants near the electrode – electrolyte assembly in the modelled SOFC at an operating voltage of 0 Volt (short-circuited cell drawing maximum current). The vertical boundary on the left is the axis of symmetry of the cell, the gap in the middle is the electrolyte, and the top half is the fuel side while the bottom half the air side. The mass fraction of H_2S on the fuel side and the mass fraction of O_2 on the air side is shown using

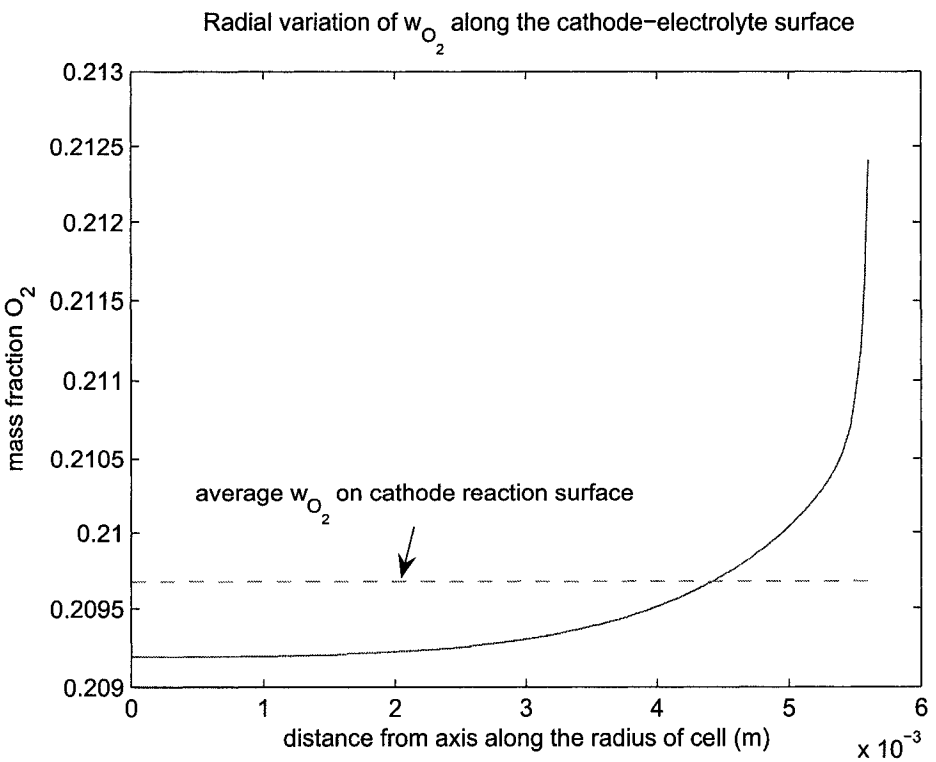

Figure 4.8: O_2 mass fraction radial profile in the 2-D Maxwell-Stefan model at 850°C

a colour scale given on the right hand side of the figure. It is readily apparent that even at maximum current, the cell operating conditions are well away from the reactant starved regime where what are normally termed concentration losses become dominant. The stream-lines for the flow in the channels and the electrodes are also plotted in Figure 4.10 and shows the flow turning around after hitting the electrodes. The streamlines enter the electrolyte at the cathode and appear at the anode electrolyte boundary to show how the oxygen is transported across the cell from the cathode through the electrolyte to the anode, where it comes out as H_2O.

4.10 Summary

I present four models of increasing complexity and compare their ability to simulate cell performance data for a button cell SOFC fuelled by H_2S. As the electrochem-

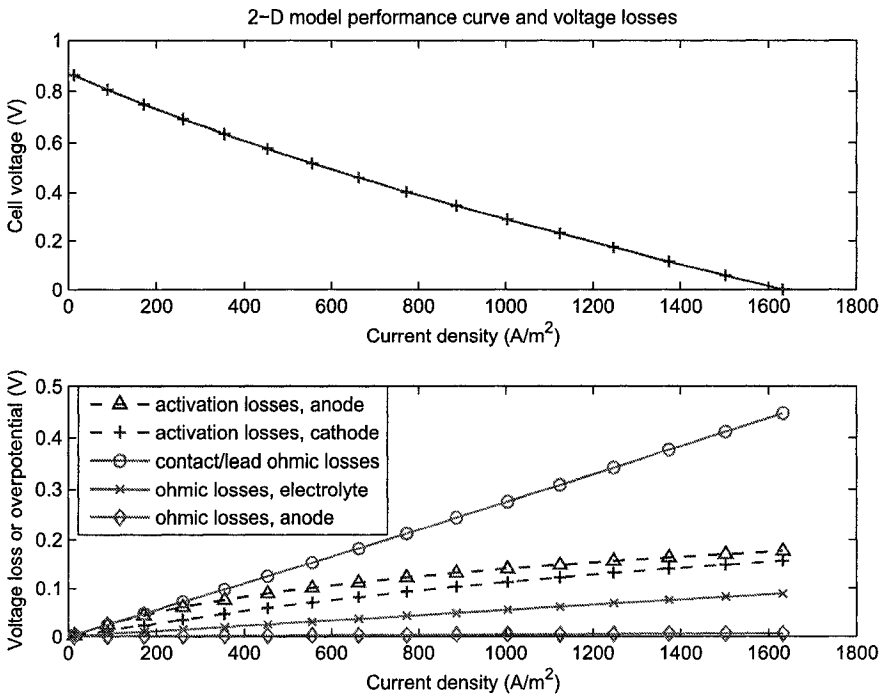

Figure 4.9: Voltage loss profiles in the 2-D Maxwell-Stefan model at 850°C

ical parameters for the reactions at both electrodes are unknown, I use non-linear least squares to estimate them for all four models. Examination of these parameter estimates, and the fit between the model output and experimental data used, allows me to identify expected patterns in the parameters and compare the four models and their ability to simulate SOFC operation. I suggest the 2-D model with Maxwell–Stefan mass transfer be used in further modelling studies because it is the one that accounts for the mass transfer resistance and thus the activation resistance accurately, and is the most comprehensive of the four models presented here.

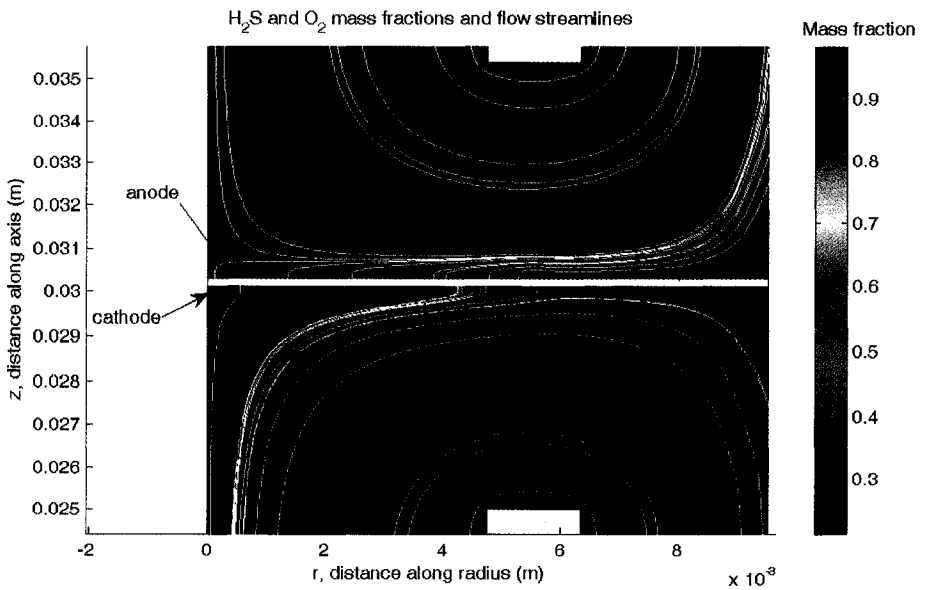

Figure 4.10: Mass fraction profiles of the reactants and flow streamlines in the 2-D Maxwell-Stefan model at 0 V, 850°C

Chapter 5

Experiments performed to investigate flow-rate and composition effects

In the previous Chapter, I discussed experimental data on H_2S SOFCs available in the literature. Many questions about the performance characterization of SOFCs running on H_2S cannot be answered using the data available. For example, the open circuit voltage for a H_2S SOFC is undefined if the water vapour and sulphur vapour content is unknown. While the sulphur vapour content can be calculated by modelling H_2S dissociation in the fuel delivery channel (see the next two Chapters), unless the fuel is humidified, its water vapour content is unknown. An examination of the research literature on H_2S SOFCs reveals that none of the studies defines the actual Nernst potential for their operating conditions. In fact, the reason they have to resort to comparing the equilibrium potential at unit activities for all reactants and products is that the concentrations of the products for the anode reactions they consider are unknown.

Similarly, unless the fuel composition is varied systematically, one can only speculate as to which of the components in the fuel is electrochemically oxidized in a H_2S SOFC. Also, although Wei et al [140] discuss the dependence of H_2S SOFC performance on flowrate, their analysis of the flowrate dependence of open circuit potential is flawed[1]. As I shall show later in Chapter 7, the flow-rate dependence of the OCV also gives us clues as to whether H_2S is directly oxidized or not.

In this Chapter, I describe the experiments we performed to try and shed light

[1]They equate H_2S partial pressure with flowrate.

on some of the issues mentioned above. Specifically, we wanted to analyze the composition and flowrate (especially of the fuel) dependence of a H_2S fuelled SOFC. The experiments were performed by Vitaly Vorontsov and the author at the Alternative Fuel Cell Laboratory housed at the National Institute of Nanotechnology. Vitaly is a PhD student in Chemical and Materials Engineering at the University of Alberta under Dr. Jing-li Luo and Dr. Karl T. Chuang.

5.1 Description of the experimental setup

The experiments were performed using a button cell setup inside a temperature controlled electric furnace. The fuel cells were electrolyte supported with a 0.3 mm thick, 1 inch (2.54 cm) diameter, electrolyte disc made of 8 mole % yttria stabilized zirconia purchased from Intertec Southwest. The anode material used was a molybdenum vanadiam sulphide MoV_2S_4 developed in the above mentioned laboratory. This mixed transition metal sulphide was prepared using a solid state reaction techniques detailed in [135]. This anode material was screen printed onto the electrolyte and dried under an IR lamp. Subsequently, the anode and electrolyte were heated in N_2 for two hours at 1050°C. After cooling the disc, the cathode (Pt) was painted onto the other side using Pt ink (Heraeus).

The fuel cell was held in the middle of an assembly of two pairs of coaxial alumina tubes. In this assembly, the inner tubes carry the reactants toward the cell from both ends. The unreacted reactants and products are carried away through the annular space between the inner and outer tubes. The outer tubes in the assembly was sealed against the electrolyte disc using a ceramic sealant (Aremco 503). The inner tubes had a ceramic spacer at the end facing the cell, and the spacer pushed the current collector against the electrode on each end. This was done to get a good contact between the current collector and electrode. The spacer also allows easier alignment of the alumina tubes that carry the gas streams.

The current collector on the fuel or anode side was a 0.5 mm gold mesh spot welded to gold wire which carried the current outside the assembly. A Pt mesh (also 0.5 mm) served as current collector for the cathode side and was attached to a Pt wire which carried the current.

The cathode side gas inlet of the assembly was attached to a mass flow controller which metered the flow of the oxidant (air or pure O_2). The anode side gas inlet of the assembly was joined to two lines, one of which came directly from the fuel

side mass flow controllers, while the other came through a small water bubbler at room temperature. This allowed us to switch between dry and humidified fuel as anode side inlet gas using a 3-way valve.

Three flow controllers were used to meter the flow-rates of H_2S, N_2, and H_2 gases on the fuel side. The exits of these flow controllers entered a single line which was then split through the 3-way valve described above. The fuel side composition and flow-rate were controlled by adjusting the flow-rates of H_2S, N_2, and H_2 gases. All three controllers on the fuel side were Brooks 5850S digital mass flow controllers which we calibrated using N_2 before running the fuel cell experiments.

The tube furnace was a Thermolyne F79300 with a 12" or 30 cm heated section with a single thermocouple in the centre for temperature control. The furnace specifications state the middle 3" (7.6 cm) section is within 0.6°C while the middle 6" (15.2 cm) section is within 3°C. The furnace thermocouple was calibrated using an external K type thermocouple before starting the fuel cell experiments. At the temperatures used in the experiments, the offset in the furnace thermocouple was of the order of 10°C and we applied the appropriate corrections during the fuel cell experiments.

The electrical measurements were carried out using the Solartron 1287 electrochemical interface. A Solartron 1255B frequency response analyzer was used to do the electrochemical impedance spectroscopy (EIS) measurements.

For all measurements, the anode was the working electrode and the cathode was the counter electrode. The setup as used did not allow for separate reference electrodes and the anode was designated as the reference electrode for the EIS measurements. Two wires from the electrochemical interface connected to each of the two current leads coming out of the fuel cell setup. One wire on each side carried the current while the other monitored (or controlled) the voltage.

5.2 Experimental procedure

The wires and current collectors were placed in the two tube assemblies which were then put together and placed on supports aligned with the split tube furnace. The fuel cell disc was then attached carefully to the two outer tubes in the assemblies using a ceramic sealant. Before sealing the cell, we ensured the current collectors were in contact with the electrodes. After sealing the cell in the assembly, the fuel side tubing was tested for leaks. The furnace was closed and the assembly

was heated up according to the vendor specified temperature program to cure the sealing. Dry air was flowed through the cathode side and dry N_2 through the anode side while the sealant was being cured.

After the assembly had gone through the sealant curing temperature program, the assembly was heated up to 750°C at 2°C/min for the first set of experiments. The anode side flow was switched to dry H_2S when the temperature reached 600°C.

We performed a series of EIS and $i-V$ measurements at 750°C while varying the composition and flow-rate of the fuel. While the flow-rate on the cathode side was kept at 100 ml/min, the cathode side gas was switched between air and O_2. All flow-rates reported here are flow-rates at standard conditions of 1 atmosphere and 20°C.

After completing the measurements at 750°C, the temperature was ramped to 800°C and then to 850°C at 2°C/min. At both temperatures, a series of EIS and $i-V$ measurements were taken at each particular set of flow and composition conditions. At 800°C, the anode and cathode side flows were maintained at 100 ml/min and the cathode side gas was O_2. At 850°C, both composition and total flow-rate were varied on the anode side. On the cathode side, the flow was switched from air and O_2 after three measurements for different anode flows. All measurements except for one, which was at a cathode flow-rate of 50 ml/min O_2, were done at a cathode flow of 100 ml/min O_2.

5.3 The electrochemical measurements

The impedance spectra at each set of conditions was analyzed using ZView while CorrView was used to visualize the $i-V$ data. The EIS measurements were done in the $10^5 - 0.1$ Hz frequency range using a 10 or 20 mV sinusoidal voltage excitation at open circuit conditions. The potentiodynamic measurements for fuel cell $i-V$ performance were performed at a scan rate of 5 mV/s. The EIS and $i-V$ data was acquired using ZPlot and CorrWare. All of these software packages are distributed by Scribner Associates Inc.

ZView allows the user to fit an equivalent circuit to the EIS data. The equivalent circuits elements used for SOFCs normally include [11, 10]:

1. a series resistance (R_s) to account for the electrolyte, electrode and wire resistances

2. an inductor (L) for the inductance of the wires and the measuring setup

3. a number of constant phase elements (CPE_i) in parallel with resistors (R_i) for modelling the electrochemical resistances of the electrodes

Separating the contribution of individual electrode processes is non-trivial [92] and was not attempted. The EIS curves were fitted primarily to extract the overall ohmic resistance, as well as estimates for the total polarization resistance at open circuit conditions.

The EIS data was fitted to the simple equivalent circuits shown in figure 5.1 using ZView. The inductor is included to account for the cumulative inductive effects of the circuit (e.g., the current leads). Each parallel combination of a CPE with a resistor models a depressed semicircle arc in the impedance spectra. The EIS data at 750°C and 800°C showed just two depressed semicircles. Thus, the equivalent circuit used for fitting the data at these temperatures has an inductor, a series resistance, and two constant phase elements in parallel with resistors. As the data at 850°C showed an additional low frequency arc, the equivalent circuit has an inductor, a series resistance, and three constant phase elements in parallel with resistors. The impedance of each of the above elements is given in table 5.1.

Table 5.1: Equivalent circuit elements

Type	Symbol	Impedance
Series resistance	R_s	R_s
Inductor	L	$i\omega L$
Polarization resistance	R_j	R_j
Constant phase	CPE_i	$1/\left((i\omega)^n T\right)$

The units of R_s, R_j are Ω, the inductance L is in Henry, the angular frequency ω is in radians/second, the pseudo-capacitance T is in Farad, and the exponent n is dimensionless.

In theory, the separated electrode polarization resistances at open circuit can be used to calculate the electrode kinetic parameters. I did not attempt this because, 1) separating the electrode resistances is not easy, 2) even the active anode electrochemical reaction is not known with any certainty for this type of fuel cell. Of the many fitted parameters obtained from the EIS data, I will use only the value of R_s (actually $\hat{R}_s$, the area specific series resistance) in the discussion in the rest of the Chapter.

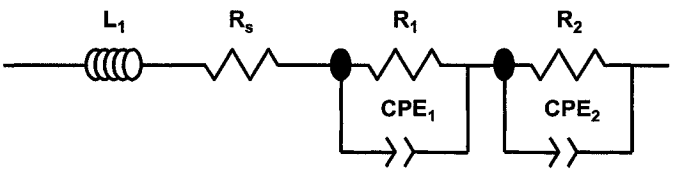

a) Equivalent circuit used for EIS data at 750°C and 800°C

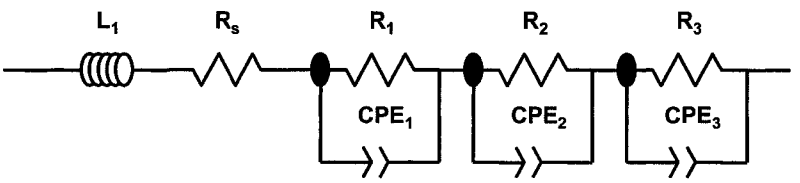

b) Equivalent circuit used for EIS data at 850°C

Figure 5.1: Equivalent circuits used for fitting the electrochemical impedance spectra

5.4 The experimental runs

Three runs of the experiment were attempted with distinct cells of the type described above. The first run was the most successful and we obtained a comprehensive set of data on the flow and composition dependence of both OCV and the $i - V$ performance of the cell. The second run failed as the fuel cell sample fractured while the fuel cell assembly was being heated up to operation temperature. The third run was only partially successful. The cell OCV was steady when we started the experiments after bringing the assembly up to 750°C. However, both the impedance and $i - V$ data showed anomalous behaviour with very high polarization resistance in the impedance spectra and a hump in the $i - V$ curve (see figure 5.2). The $i - V$ curves obtained were similar in shape to the $i - V$ data presented in [140].

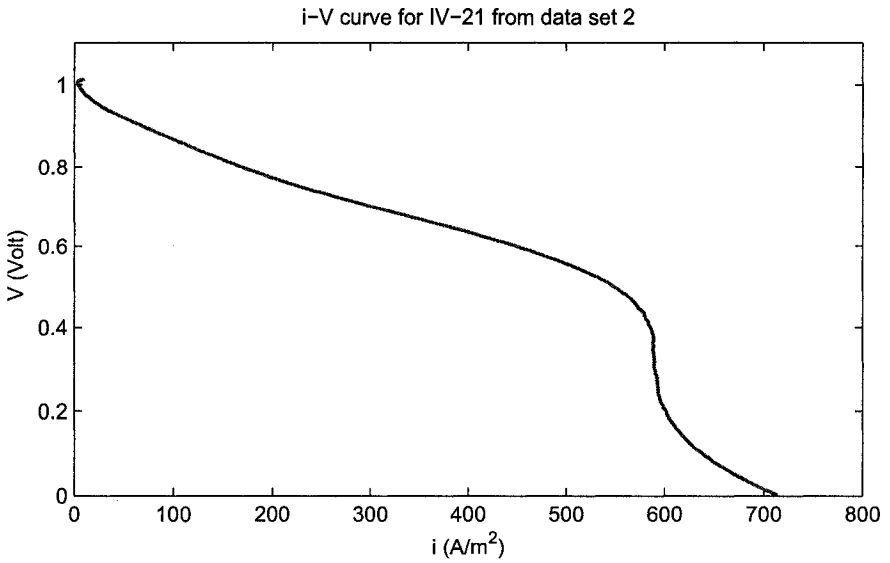

Figure 5.2: A sample $i - V$ curve from data set 2

All the data from the first run (sample 1) will be referred to as data set one, and the data from the third run will be called data set two.

In the rest of the Chapter, I will describe 1) the flow-rate and composition dependence of the open circuit potential data from data set one and two, and 2) the flow-rate, composition and time dependence of the $i - V$ curves from the first run (data set one).

5.5 The data on composition and flow-rate effects

In the following discussion of gas composition and flow-rate effects on cell performance, the behaviour described is isolated by ensuring that the operating conditions besides the variable of interest in the data sets being compared, are held constant. Thus, when the effects of gas composition on the anode side are described, the total flow-rate on both sides as well as the inlet composition on the cathode does not change for the data compared.

5.5.1 OCV

The open circuit voltage for any electrochemical cell is the voltage across the cell when there is no current flowing through the cell. Cell voltage is defined as the potential of the cathode with respect to the potential of the anode.

Cathode side inlet gas composition effects

In both data sets, switching from air to O_2 or vice-versa [2] resulted in a change in OCV very close to that predicted theoretically by the Nernst equation (table 5.2). The Nernst equation for the cathode is given by equation (5.2).

$$E_{cathode} = E^{o}_{O_2} + \frac{RT}{4F} \ln a_{O_2} \tag{5.1}$$

$$E_{cathode} = E^{o}_{O_2} + \frac{RT}{4F} \ln y_{O_2} \frac{P}{P^o} \tag{5.2}$$

P is the total pressure and P^o is the reference pressure (1 bar).
The difference in OCV $E_{O_2} - E_{air}$ is thus given by equation (5.3).

$$\begin{aligned} E_{O_2} &= E^{o}_{O_2} + \frac{RT}{4F} \ln 1 \frac{P}{P^o} \\ E_{air} &= E^{o}_{O_2} + \frac{RT}{4F} \ln 0.21 \frac{P}{P^o} \\ E_{O_2} - E_{air} &= \frac{RT}{4F} \ln \frac{1}{0.21} \end{aligned} \tag{5.3}$$

[2] While keeping the flow-rate and composition on the anode side the same. 100 ml/min humidified H_2S in all three cases.

Table 5.2: Cathode side gas composition effect on OCV

T	data set	EIS #s	observed $E_{O_2} - E_{air}$	theoretical $E_{O_2} - E_{air}$
750°C	1	11,12	34 mV	34 mV
750°C	2	12,15	34 mV	34 mV
800°C	1	2,15	36 mV	36 mV
850°C	1	7,9	37 mV	38 mV

Anode side inlet gas composition effects

At all three temperatures and for both data sets, the following trends can be seen.

1. In fuel mixtures containing only H_2S and N_2, the greater the H_2S content (volume or mole fraction), the higher the OCV (figure 5.3).

2. In fuel mixtures containing H_2S, N_2, and H_2, the greater the H_2 content, the higher the OCV. This is illustrated in figures 5.4, and 5.5. For the data shown, the H_2S mole fraction was held constant and the H_2 mole fraction was varied.

Effect of cathode side gas (oxidant) flow-rate

During the first run, cathode side gas flow-rate was not changed, except for once during the tests at 850°C which lead to a 1 mV change in OCV. In the second run, the cathode side gas flow-rate was varied from 20 to 200 ml/min and had no effect on cell OCV.

Effect of fuel flow-rate

As the inlet fuel flow-rate on the anode side was increased, the OCV of the cells tested increased. This behaviour was consistent at the three operation temperatures and in both data sets (figure 5.6).

5.5.2 $i - V$ curves

The dependence of cell voltage on the current being drawn defines the performance of a fuel cell under specific operating conditions such as operating temperature, inlet gas compositions and flow-rates. As current scales linearly with active cell

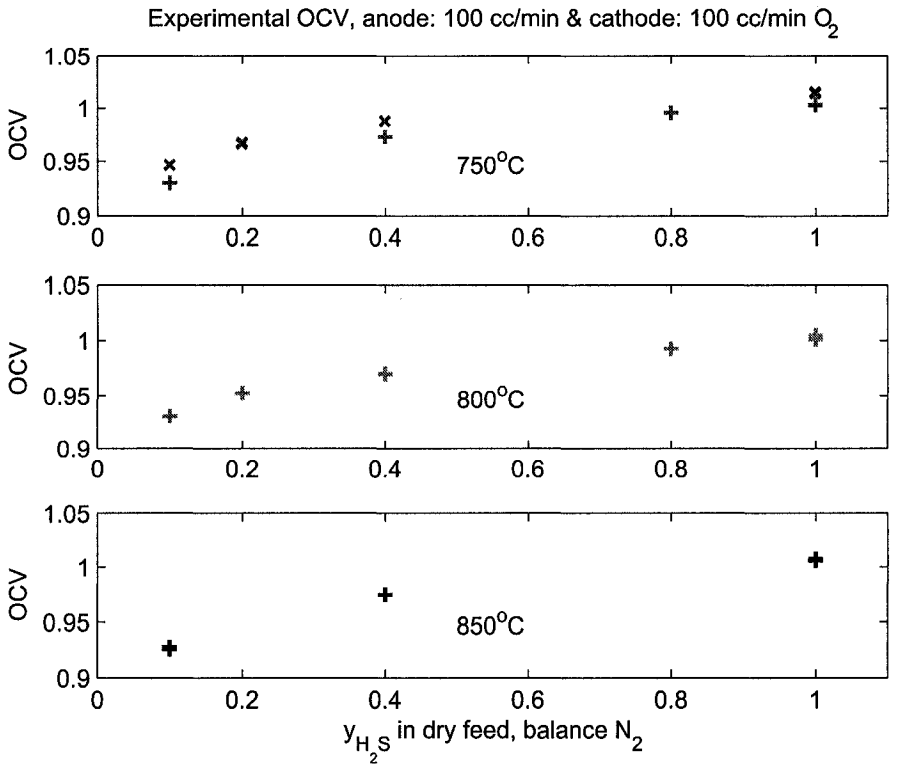

Figure 5.3: OCV as a function of H_2S content (no H_2 in fuel); $+ \rightarrow$ experimental data set 1, $\times \rightarrow$ experimental data set 2

area, the current density (current generated per unit active area of the cell) is the variable normally used in a fuel cell performance curve.

The maximum current density, denoted as i_{0V} that can be drawn is a useful metric when discussing $i - V$ curves. The maximum current is when the cell voltage is 0 Volt i.e, the cell is short circuited. Other useful metrics that will be used in this Chapter are the polarization resistance at 1/3, 2/3, times the maximum current density as well as at the maximum current density ($\hat{R}_p(0.33i_{0V})$, $\hat{R}_p(0.67i_{0V})$, $\hat{R}_p(i_{0V})$). The polarization resistance at a particular current is defined in equation (5.6).

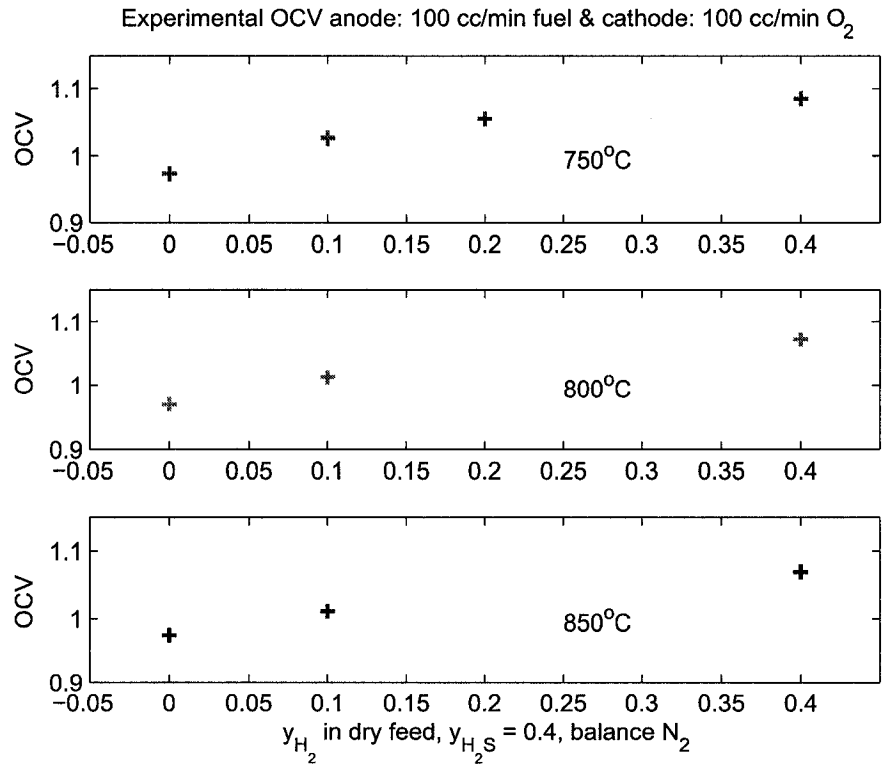

Figure 5.4: OCV as a function of H_2 content for data set 1, y_{H_2S} fixed at 0.4

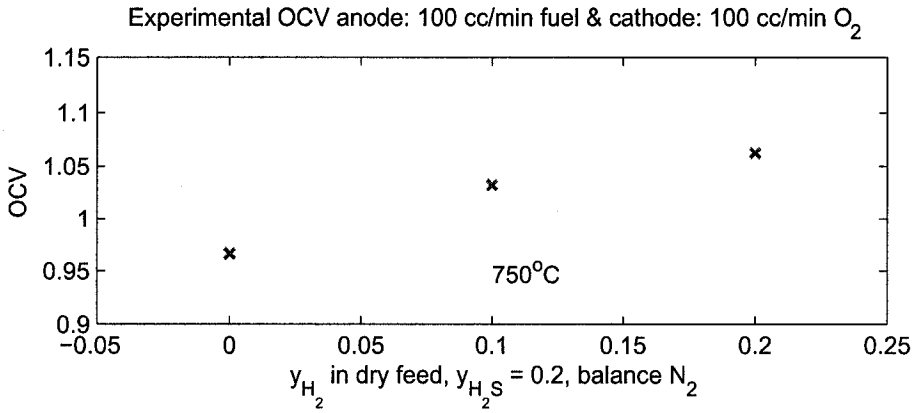

Figure 5.5: OCV as a function of H_2 content for data set 2, y_{H_2S} fixed at 0.2

$$V(i) = E - i\left[\hat{R}_s + \hat{R}_p(i)\right] \tag{5.4}$$

$$\frac{dV(i)}{di} = -\hat{R}_p(i) - \hat{R}_s \tag{5.5}$$

$$\hat{R}_p(i) = -\frac{dV(i)}{di} - \hat{R}_s \tag{5.6}$$

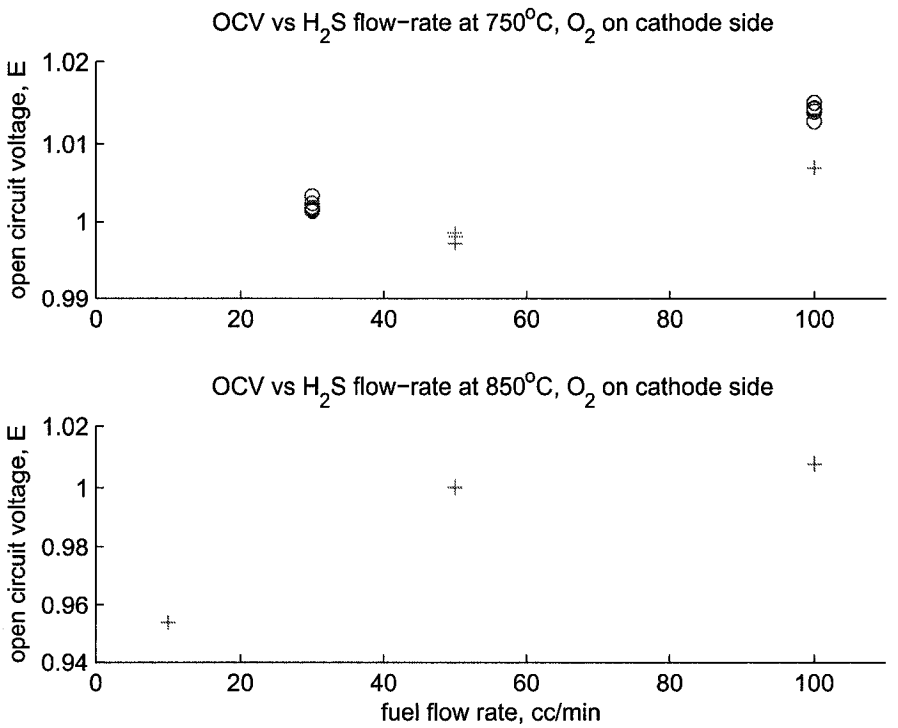

Figure 5.6: OCV as a function of fuel flow-rate (O → data set 2)

The $\hat{R}_s$ value was taken from the corresponding fitted impedance spectrum, and the slope of the $i - V$ curve was calculated from a fitted smooth spline approximation of the $i - V$ data. As mentioned earlier, only the data obtained from the first run will be discussed here.

Effect of cathode side composition, air vs O_2

As shown in figure 5.7, switching from air to O_2 on the cathode side lead to a substantial increase in performance at both 750 and 850°C. An $i - V$ curve with air on the cathode was not measured at 800°C.

Effect of anode side composition

In the following discussion, the inlet fuel composition will denoted as [flow of dry H_2S – flow of dry N_2 – flow of dry H_2]. Thus, I will refer to a measurement with

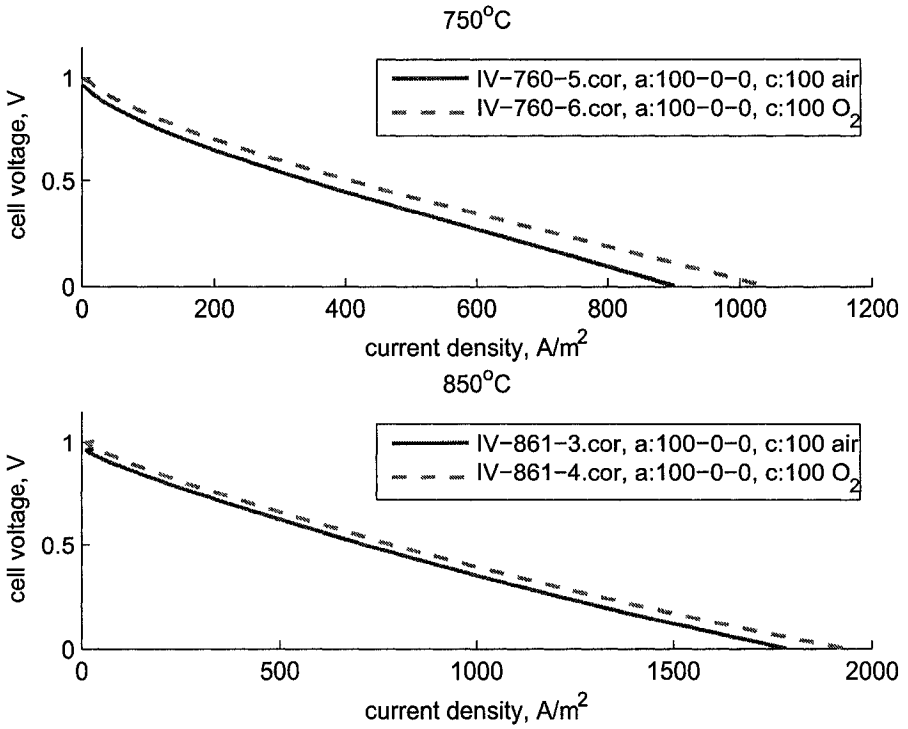

Figure 5.7: Effect of switching from air to O_2

40% H_2S, 50% N_2, and 10% H_2 at dry flow-rate of 100 ml/min as [40–50–10]. All references to mole fractions will be on a dry basis and for a total flow of 100 ml/min unless otherwise noted. Most of the data is for fuel humidified at 22°C and any measurement with dry fuel will be flagged explicitly.

Fuel mixtures of H_2S and N_2 The data discussed here is presented in table 5.3.

At 750°C, $\hat{R}_p(i_{0V})$ decreased and i_{0V} increased, as y_{H_2S} was decreased from 100% to 80% to 40%. This however, could be a result of the cell performance improving with time. The time dependence of the cell performance or cell "activation" behaviour is discussed at the end of this section.

At 800°C, $\hat{R}_p$ was indifferent to a reduction in y_{H_2S} from 100% to 80% and 40%. In tests performed the next day however, $\hat{R}_p$ increased as y_{H_2S} was reduced from 100% to 10%. When y_{H_2S} was then increased to 20%, $\hat{R}_p$ decreased. The

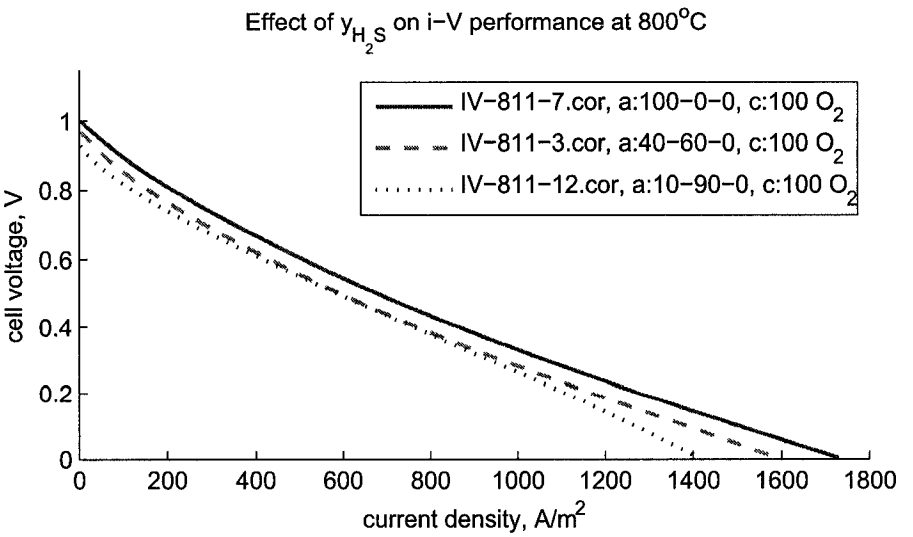

Figure 5.8: Effect of H_2S mole fraction on $i - V$ performance

relative indifference to decreasing y_{H_2S} on the first day could again be because of cell "activation".

At 850°C, $\hat{R}_p(i_{0V})$ increased when y_{H_2S} was reduced from 100% to 40% and then further to 10%. However, the $\hat{R}_p$ traces were quite noisy for some measurements at 850°C. Examining the $i - V$ curves directly, the performace for $y_{H_2S} = 40\%$ is comparable or even better than than for pure H_2S.

We missed a measurement at 750°C for 10% H_2S in N_2. However, at both 800 and 850°C, the $i - V$ curve measured for 10% H_2S - 90% N_2 has a convex downwards shape near the maximum current. This shape usually suggests mass transfer limitations which become dominant at higher current density [101].

Fuel mixtures of H_2S, N_2 and H_2 The data discussed here is presented in table 5.4.

At all three operation temperatures, the ohmic resistance ($\hat{R}_s$) increased when H_2 was added to the fuel gas. As the mole fraction of H_2 was increased, $\hat{R}_s$ increased further. This effect was reversible i.e., when the H_2 was removed from the fuel inlet stream, $\hat{R}_s$ returned to the value for H_2 free fuel.

At 750°C, $\hat{R}_p(i_{0V})$ decreased when the fuel mixture was changed from [40–60–0] to [40–50–10] or when 10% H_2 was introduced into a 40% H_2S fuel gas. $\hat{R}_p(i_{0V})$ did not change substantially when the fuel composition was changed from [40–50–10]

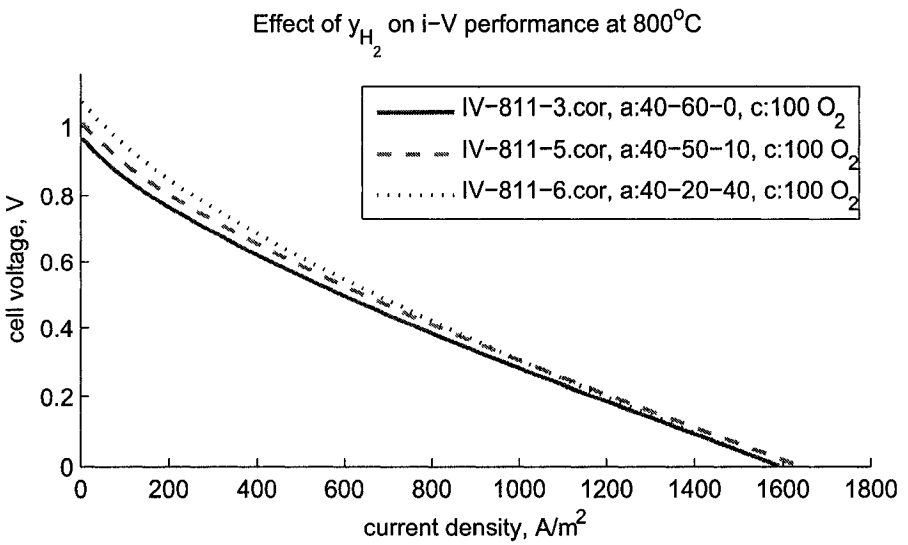

Figure 5.9: Effect of adding H_2 to fuel: 1

to [40–40–20] and then to [40–20–40].

At 800°C, $\hat{R}_p(i_{0V})$ did not change much when the fuel composition was changed from [40–60–0] to [40–50–10] and then to [40–20–40]. Also at 800°C, $\hat{R}_p(i_{0V})$ was reduced significantly when the 20% H_2 was added to a 20% H_2S (in N_2) fuel gas.

At 850°C, $\hat{R}_p(i_{0V})$ decreased when the fuel composition was changed from [40–60–0] to [40–50–10]. However, $\hat{R}_p(i_{0V})$ increased when the H_2 content of the fuel was then changed from [40–50–10] to [40–20–40].

Changing fuel composition from [20–80–0] to [20–60–20] at 800°C, and from [10–90–0] to [10–80–10] at 850°C, lowered $\hat{R}_p(i_{0V})$. This change in $\hat{R}_p(i_{0V})$ is a result of the added H_2 eliminating the convex downwards shape for low H_2S mole fraction in the fuel, as seen in figure 5.10. The contact of the current collector and the anode might have shifted around this time. This is suggested by the increase in $\hat{R}_s$ from 3.6 $\Omega.cm^2$ to 4.1 $\Omega.cm^2$ between two EIS measurements at [10–90–0] at 850°C. This change in $\hat{R}_s$ was reversed after the fuel composition was changed to [100–0–0].

We measured $i - V$ curves with and without fuel humidification at 800°C to examine the effect of water vapour content on the performance of the cell. As seen in figure 5.11, although the OCV is higher for dry fuel, the maximum current obtained is very close to that for the humidified fuel. Except for the initial low

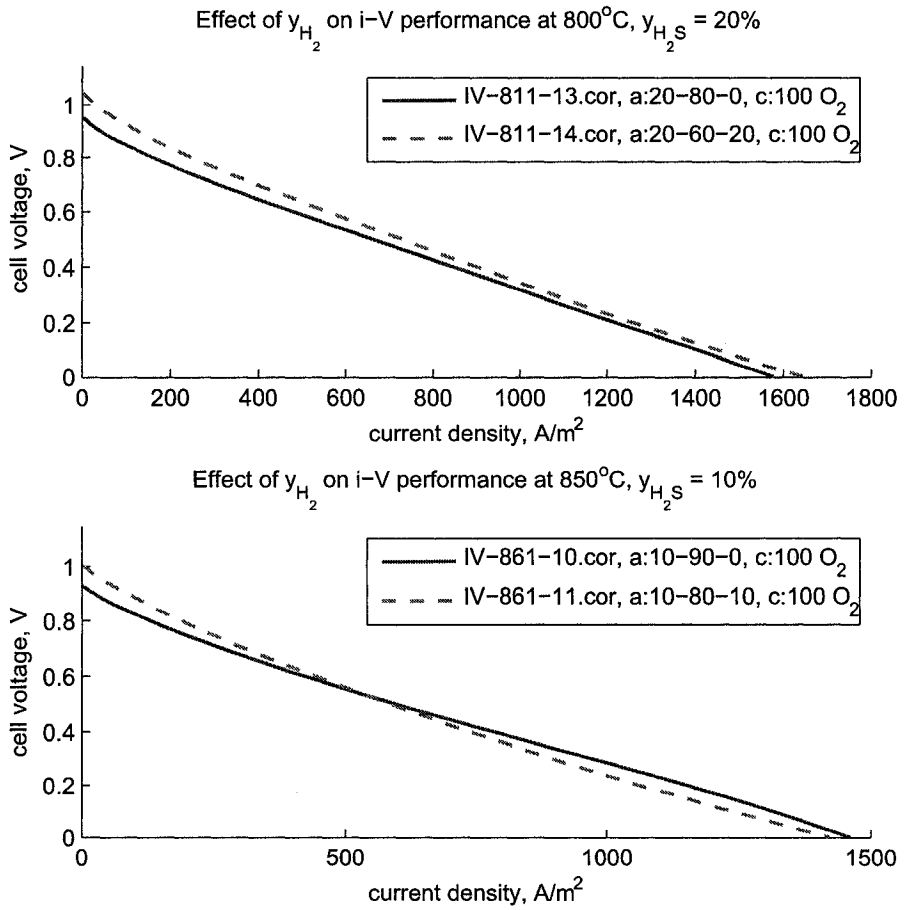

Figure 5.10: Effect of adding H_2 to dilute H_2S

current section, the performance for dry as well as humidified fuel is similar.

Effect of cathode side gas flow-rate

Because we were primarily interested in the anode, the cathode side flow-rate was only varied once. Decreasing the flow-rate from 100 ml/min to 50 ml/min lead to a significant drop in cell performance as seen in figure 5.12 ($\hat{R}_p(i_{0V})$ increased from 0.4 to 0.5 $\Omega.cm^2$). However, as this measurement was taken towards the end of the experiments at 850°C, the decreased performance could be due to the cell deactivation described at the end of this section.

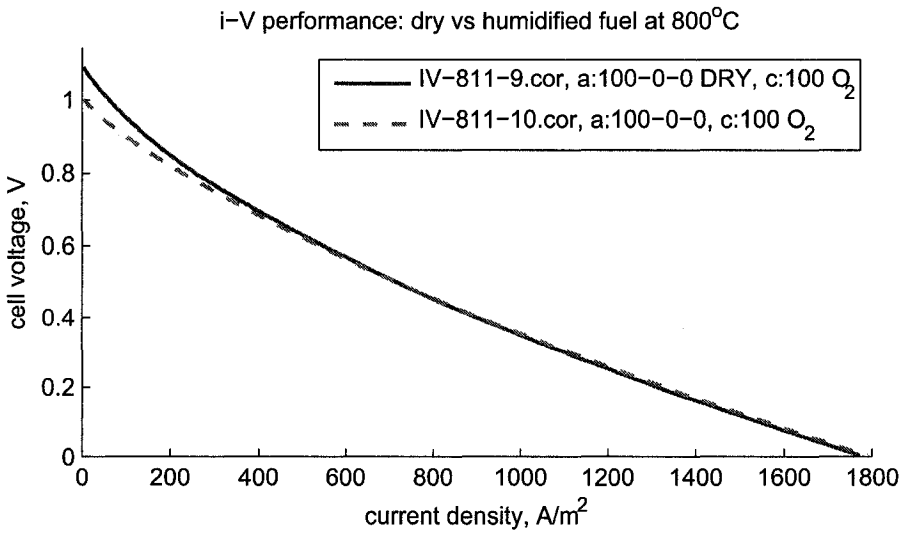

Figure 5.11: Effect of fuel humidification on cell performance

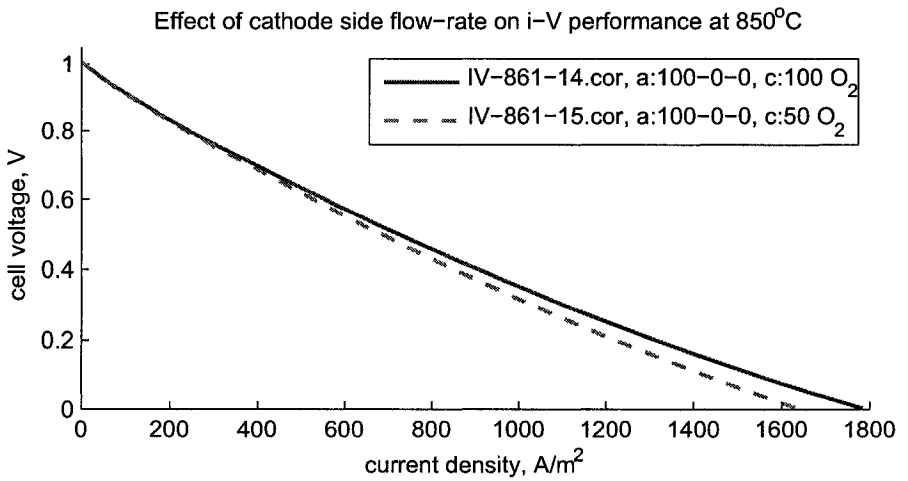

Figure 5.12: Effect of cathode side gas (O_2) flow-rate on cell performance

Effect of anode side flow-rate

At 750°C, increasing the fuel flow-rate from 50 ml/min to 100 ml/min resulted in a marginal increase in performance.

Fuel flow-rate was not varied at 800°C.

The $\hat{R}_p$ traces were quite noisy for some measurements at 850°C and should

not be used to compare $\hat{R}_p(i_{0V})$ values for the two flow-rates. For comparing these measurements, I will use i_{0V} values. At 850°C, increasing the fuel flow-rate from 10 ml/min to 50 ml/min resulted in very little change in i_{0V} although OCV increased by almost 50 mV. Further increasing the flow-rate to 100 ml/min lead to a decrease in i_{0V}. Changing the fuel flow-rate later from 100 ml/min to 50 ml/min lead to a slight increase in i_{0V}.

Activation and deactivation of the cell with time

At 750°C, the cell performance improved over time as seen by comparing IV-6, IV-11, and IV-15 (table 5.5). All measurements are for humidified H_2S at 100 ml/min on the anode side and 100 ml/min O_2 on the cathode side. The Time column in table 5.5 is the time elapsed from the very first measurement using humidified fuel at 750°C.

At 800°C, the $i-V$ performance improves initially and then stays more or less the same. This can be seen by comparing IV-1 with IV-7, IV-8, IV-10 and IV-11 (table 5.5).

At 850°C, the $i-V$ performance decreases throughout. The deactivation seems fairly slow at first, compare IV-4, 5, and 6. However, when comparing the above three measurements with IV-12, IV-14, and IV-16, the deactivation is readily apparent (table 5.5).

5.6 Discussion of the data

In this section I discuss the trends seen in the data presented in the previous section.

The open circuit voltage of the cell increased as inlet y_{H_2S} was increased in a mixture of H_2S and N_2. OCV also increased as inlet y_{H_2} was increased in a mixture where the inlet y_{H_2S} was held constant. The fuel flow-rate affects OCV as well. The higher the flow-rate, the higher the OCV. Oxidant flow-rate has no effect while y_{O_2} effects OCV in accordance with the Nernst equation.

Decreasing y_{H_2S} does not affect $i-V$ performance unless $y_{H_2S} < 0.4$. The performance worsens noticeably as y_{H_2S} is decreased from 40% to 20%, and then to 10%.

Adding H_2 to the fuel inlet stream lead to an increase in the ohmic resistance of the cell. One explanation for this curious effect could be a phase transformation in

the anode leading to an increased interfacial resistance between the anode and the electrolyte. The polarization resistance does not change much with the addition of H_2 to the fuel, which suggests that this anode material is not active to H_2 electro-oxidation. On the other hand, adding H_2 to fuel with low y_{H_2S} dramatically improved $i-V$ performance in the high current region (figure 5.10). This effect will be analyzed in more detail in Chapter 7 where I present multiphysics simulations of $i - V$ performance for different fuel compositions.

Fuel cell flow rate did not affect $i - V$ performance. As the oxidant flow was only changed once, and the $i - V$ measurement was performed at the end of the experimental run, no conclusions could be drawn on how flow-rate of oxidant effects $i - V$ performance.

5.7 Summary

In this Chapter, I described the experiments we conducted to systematically examine composition and flow-rate effects on H_2S SOFC performance. The data obtained was then analyzed to isolate trends that might help answer questions such as the nature of the electrochemical reactions on the anode. Critical examination of the data confirms some of the trends reported in the literature. I use the data summarized in this Chapter to help build and validate fuel cell models in Chapters 6 and 7. Models using chemical thermodynamics are used to model and explain the composition and flow-rate effects on OCV in Chapter 6. In Chapter 7, I extend the multiphysics models presented in Chapter 4 to include H_2S dissociation kinetics. This allows me to explain the OCV data, as well as the main trends in the $i - V$ performance data presented in the current Chapter.

Table 5.3: Dependence of cell performance on y_{H_2S}

$[H_2S - N_2 - H_2]$ (ml/min)	Time (hh:mm)	T (°C)	IV (#)	OCV (Volt)	i_{0V} (A/m^2)	$R_p(0.33i_{0V})$ (Ω)	$R_p(0.67i_{0V})$ (Ω)	$R_p(i_{0V})$ (Ω)
[100–0–0]	1:38	750	6	1.003	1037	5.2	3.7	3.6
[80–20–0]	2:12		7	0.996	1068	4.8	3.4	3.3
[40–60–0]	3:52		10	0.973	1117	4.2	2.9	2.8
[100–0–0]	7:24	800	1	1.001	1612	2.9	1.5	1.0
[80–20–0]	8:12		2	0.993	1568	2.9	1.6	1.0
[40–60–0]	8:49		3	0.970	1591	2.7	1.3	1.4
[100–0–0]	24:24		11	1.005	1768	2.2	1.3	0.8
[10–90–0]	24:47		12	0.931	1413	2.3	2.1	3.3
[20–80–0]	25:46		13	0.952	1579	2.1	2.0	2.2
[100–0–0]	30:38	850	6	1.007	1906	2.1	1.1	0.4
[40–60–0]	31:08		7	0.975	1889	1.5	0.8	0.8
[10–90–0]	32:41		10	0.927	1462	2.2	1.7	3.6

Table 5.4: Dependence of cell performance on y_{H_2}

$[H_2S - N_2 - H_2]$ (ml/min)	Time (hh:mm)	T (°C)	IV (#)	OCV (Volt)	i_{0V} (A/m^2)	$R_p(0.33i_{0V})$ (Ω)	$R_p(0.67i_{0V})$ (Ω)	$R_p(i_{0V})$ (Ω)	R_s (Ω)
[40–60–0]	3:52	750	10	0.973	1117	4.2	2.9	2.8	4.0
[40–50–10]	5:05		12	1.026	1156	4.4	2.8	2.5	4.2
[40–40–20]	5:25		13	1.055	1155	4.5	2.8	2.6	4.3
[40–20–40]	6:02		14	1.085	1147	4.8	3.1	2.6	4.4
[40–60–0]	8:49	800	3	0.970	1591	2.7	1.3	1.4	3.5
[40–50–10]	9:31		5	1.012	1639	2.7	1.4	0.9	3.6
[40–20–40]	9:52		6	1.072	1589	3.1	1.6	1.0	3.8
[20–80–0]	25:46		13	0.952	1579	2.1	2.0	2.2	3.5
[20–60–20]	26:14		14	1.047	1644	2.2	1.7	1.3	3.8
[40–60–0]	31:08	850	7	0.975	1889	1.5	0.8	0.8	3.4
[40–50–10]	31:40		8	1.011	1846	2.2	1.1	0.4	3.5
[40–20–40]	32:03		9	1.069	1680	2.8	1.7	0.8	3.8
[10–90–0]	32:41		10	0.927	1462	2.2	1.7	3.6	3.6
[10–80–10]	33:05		11	1.004	1420	2.6	1.6	1.0	4.4*

Table 5.5: Time dependence of cell performance during the first experiment. Anode side: 100 ml/min H_2S; Cathode side: 100 ml/min of O_2

Time (hh:mm)	T (°C)	IV (#)	OCV (Volt)	i_{0V} (A/m^2)	$R_p(0.33i_{0V})$ (Ω)	$R_p(0.67i_{0V})$ (Ω)	$R_p(i_{0V})$ (Ω)
1:38		6	1.003	1037	5.2	3.7	3.6
4:33	750	11	1.003	1151	4.4	3.1	2.8
6:25		15	1.004	1197	4.1	2.8	2.6
7:24		1	1.001	1612	2.9	1.5	1.0
10:10	800	7	1.001	1730	2.5	1.3	0.8
21:50		8	1.005	1749	2.5	1.4	1.0
23:38		10	1.005	1789	2.4	1.4	0.8
24:24		11	1.005	1768	2.2	1.3	0.8
29:56		4	1.006	1925	2.1	0.9	0.3
30:15	850	5	1.007	1915	2.1	1.4	0.1
30:38		6	1.007	1906	2.1	1.1	0.4
33:33		12	1.007	1816	2.4	1.2	0.4
34:16		14	1.007	1783	2.4	1.3	0.4
47:52		16	1.008	1316	4.0	2.4	2.1

Chapter 6

H_2S dissociation and its effect on cell open circuit voltage

At temperatures above 700°C, hydrogen sulphide starts to dissociate into hydrogen and gaseous sulphur [149]. In this Chapter, I discuss the effect of H_2S dissociation on the open circuit voltage of a H_2S fuelled SOFC. In section 6.1, I examine the thermodynamics of H_2S dissociation to see how the equilibrium degree of dissociation varies with inlet composition and reaction temperature.

The open circuit voltage of a H_2S fuelled SOFC can be defined for different oxidation reactions on the anode. As seen in section 1.4, one possible reaction is the direct oxidation of H_2S to give H_2O and S_2, while another is the oxidation of H_2 to H_2O. Although the Nernst potential is identical for all possible electrochemical reactions when the fuel is at chemical equilibrium, this is not the case if the fuel is not at equilibrium. In section 6.2, I define and calculate the Nernst potential for some of the possible oxidation reactions in order to examine the effect of H_2S dissociation on these Nernst potentials.

For the fuel gas to come to equilibrium at a particular temperature, it must have a sufficient residence time at that temperature. As described in the previous Chapter (section 5.6), the experimental setup does not guarantee this. To calculate the actual extent of H_2S dissociation and the resulting fuel composition at the anode, I need to solve the coupled transport and reaction problem in the fuel delivery channel. To solve the coupled problem above, I need a kinetic model for H_2S dissociation. In section 6.3, I examine the literature for kinetic models of H_2S dissociation.

6.1 Chemical thermodynamics of H_2S dissociation

The equilibrium composition of a reacting mixture at specified temperature and pressure is the composition where the Gibbs free energy of the mixture (G) is minimized [124]. This can be formulated as:

$$\mathbf{min}_{\ n_j}\ G = \sum_{j}^{N_{species}} \hat{\mu}_j n_j \tag{6.1}$$

$$s.t.$$

$$\sum_{j}^{N_{species}} b_{ij} n_j = \sum_{j}^{N_{species}} b_{ij} n_j^{\circ}$$

$\hat{\mu}_j$ is the chemical potential and n_j the number of moles of species j in the mixture, while n_j° is the initial number of moles, and b_{ij} is the number of atoms of element i in a molecule of species j.

The above constrained minimization problem is equivalent to the following unconstrained minimization of the Lagrangian of the system.

$$\mathbf{min}_{\ n_j,\lambda_i}\ L = \sum_{j}^{N_{species}} \hat{\mu}_j n_j + \sum_{i}^{N_{elements}} \lambda_i \left(\sum_{j}^{N_{species}} b_{ij} n_j - \sum_{j}^{N_{species}} b_{ij} n_j^{\circ} \right) \tag{6.2}$$

λ_i are the Lagrange multipliers for the equality constraints [48].

The solution to the unconstrained problem (6.2) is given by driving the derivatives of L to zero i.e., solving the $N_{species} + N_{elements}$ equations given by (6.3) and (6.4).

$$\frac{\partial L}{\partial n_j} = \hat{\mu}_j + \sum_{i}^{N_{elements}} \lambda_i b_{ij} = 0 \tag{6.3}$$

$$\frac{\partial L}{\partial \lambda_i} = \sum_{j}^{N_{species}} b_{ij} n_j - \sum_{j}^{N_{species}} b_{ij} n_j^{\circ} = 0 \tag{6.4}$$

For an ideal gas mixture, the chemical potential of a species is given by (6.5).

$$\hat{\mu}_j = G_j^o + RT \ln a_j = G_j^o + RT \ln \left(\frac{P}{P^o} \frac{n_j}{n} \right) = G_j^o + RT \ln (\frac{P y_j}{P^o}) \tag{6.5}$$

G_j^o is the Gibbs free energy of j at the specified temperature and 1 bar pressure, a_j is the activity of j, $n = \sum_j n_j$ the total number of moles, P is the total pressure while P^o is the reference pressure (1 bar), and y_j is the mole fraction of j.

6.1.1 Solving for chemical equilibrium

As shown above, solving for the equilibrium composition of a reacting mixture requires the minimization of Gibbs free energy while constraining the elemental composition of the reaction mixture to that of the initial mixture. To solve equations (6.3) and (6.4), I need G_j^o as functions of temperature. In this Chapter, I used the thermodynamic property functions given in the NASA thermodynamic database [88] to calculate $G_j^o(T)$. The Gibbs free energy minimization was done using Cantera [52] from within the MATLAB environment. Cantera is an open source multipurpose software package for solving chemically reacting flow problems. Cantera uses thermodynamic property functions with fewer parameters from an older form of the NASA thermodynamic database [87].

6.1.2 Chemical species considered in Gibbs free energy minimization

While formulating the above equilibrium problem the user has to specify which chemical species are allowed in the reaction mixture. In my analysis, I included the following molecules and radicals: $H_2S, H_2, H_2O, S_2, S_8, N_2, S, SH, SN, SO, SO_2, SO_3, S_2O, H_2O_2, NH, NH_2, NH_3, NH_2OH, NO, NO_2, NO_3, N_2H_2, N_2H_4, N_2O, N_2O_3, N_2O_4, N_2O_5, N_3, N_3H, O, OH, O_2, O_3, H$. My results showed trace amounts for several of these species, and I will only consider the following species in the discussion: $H_2S, H_2, H_2O, S_2, N_2, SH, SO_2, O_2$.

6.1.3 Summary of equilibrium results

Since I am primarily interested in what happens to the H_2S in the fuel, I define the extent of reaction X_{H_2S} in (6.6) and use it to track the degree of dissociation.

X_{H_2S} is a measure of how much of the H_2S in the inlet fuel is converted into the products.

$$X_{H_2S} = \frac{n_{H_2S,reacted}}{n_{H_2S,in}} \tag{6.6}$$

The model described above returns the equilibrium composition in mole fractions at the temperature and pressure specified. To calculate X_{H_2S}, I use equation (6.7) which is obtained from a mole balance of the S in the outlet stream.

$$X_{H_2S} = \frac{n_{H_2S,reacted}}{n_{H_2S,in}} = \frac{\sum_{j \neq H_2S}^{N_{species}} b_{Sj} n_j}{\sum_{j}^{N_{species}} b_{Sj} n_j} = \frac{\sum_{j \neq H_2S}^{N_{species}} b_{Sj} y_j}{\sum_{j}^{N_{species}} b_{Sj} y_j} \tag{6.7}$$

I ran the above chemical equilibrium models varying the inlet composition, and the temperature to examine the effects of these variables on the equilibrium composition. The range of inlet fuel composition and the temperature conditions used for these calculations were the same as those used in the fuel cell experiments that we conducted (Chapter 5). All calculations are for a total pressure of 1 atmosphere.

Table 6.1: Equilibrium conversion of H_2S and equilibrium composition at 750–850°C

	750°C	800°C	850°C
X_{H_2S}	5.5%	7.6%	10.1%
y_{H_2S}	0.896	0.868	0.835
y_{H_2}	5.21×10^{-2}	7.09×10^{-2}	9.33×10^{-2}
y_{H_2O}	2.53×10^{-2}	2.51×10^{-2}	2.48×10^{-2}
y_{S_2}	2.61×10^{-2}	3.54×10^{-2}	4.66×10^{-2}
y_{SH}	3.70×10^{-5}	7.56×10^{-5}	1.44×10^{-4}
y_{SO_2}	4.94×10^{-7}	6.37×10^{-7}	8.11×10^{-7}
y_{O_2}	6.88×10^{-21}	5.53×10^{-20}	3.73×10^{-19}

The first results are for humidified H_2S (97.4% H_2S, 2.6% H_2O) brought to chemical equilibrium at 750°C, 800°C, and 850°C. The equilibrium conversion and the mole fractions of some of the key components in the equilibrated fuel are presented in table 6.1. One can clearly see that the equilibrium extent of reaction,

$X_{H_2S,equil}$ increases with increasing temperature. Also, S_2 is the dominant form of sulphur for the fraction of H_2S that reacts.

The results in table 6.1 were obtained using Cantera through MATLAB. I also used a program (CEA) available directly from the NASA Glenn Research Center website [24] to calculate equilibrium compositions for the same inlet fuel mixtures and obtained different but similar results (the same first two significant digits). CEA uses the new thermodynamic property functions [88] which are considered more accurate than the ones used by Cantera. Except for where Cantera was used to get equilibrium compositions, I used the newer functions to calculate all thermodynamic quantities (e.g., E^o, c_p, ΔH, ΔS) in this thesis through custom written MATLAB functions.

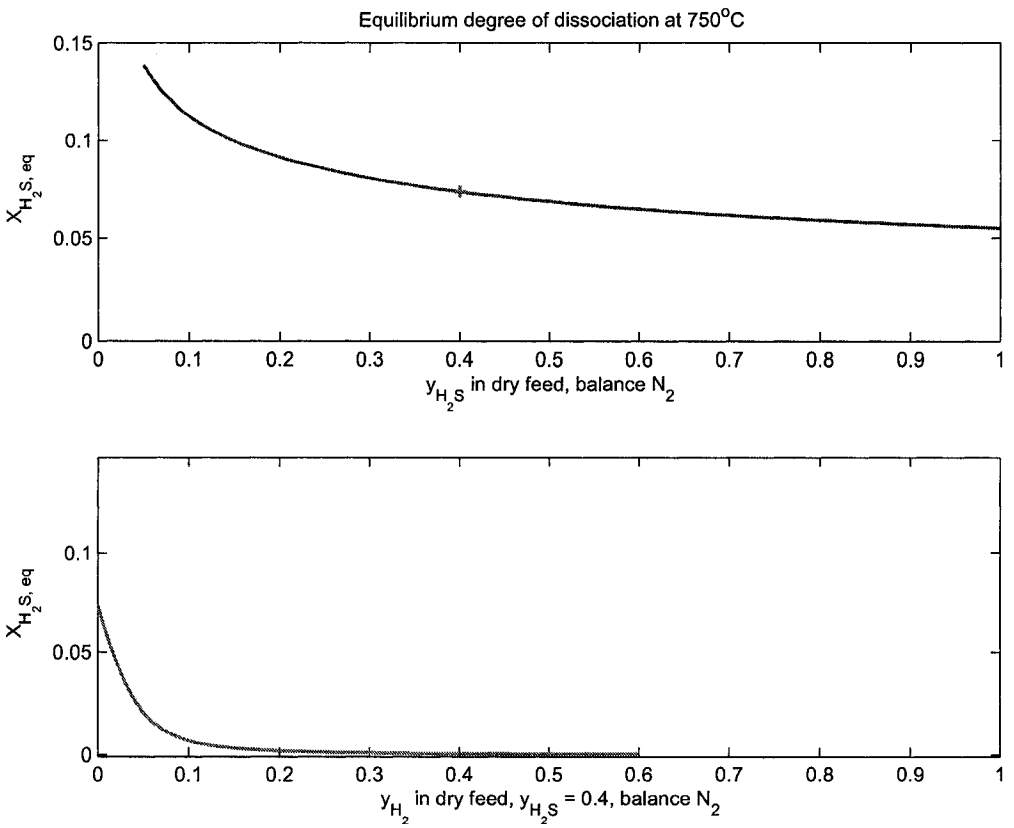

Figure 6.1: Equilibrium conversion of H_2S in a fuel mixture at 750°C as a function of inlet composition

Figure 6.1 shows $X_{H_2S,equil}$ at 750°C as function of inlet composition. In a

mixture of humidified H_2S and N_2, $X_{H_2S,equil}$ increases as the inlet H_2S content is decreased or the inert (N_2) content is increased. $X_{H_2S,equil}$ decreases very quickly as the inlet H_2 content is increased in an mixture with fixed H_2S content ($y_{H_2S} = 0.4$).

To summarize, the following trends can be seen clearly from the equilibrium models:

1. $X_{H_2S,equil}$ increases with increasing temperature.

2. $X_{H_2S,equil}$ increases with increasing dilution of the inlet H_2S.

3. $X_{H_2S,equil}$ decreases as more H_2 is added to the inlet mixture.

All three trends can be explained by the Le Chatelier principle. The primary overall reaction in a humidified mixture of H_2S, H_2, and N_2 is the dissociation of H_2S into H_2 and S_2 (reaction (6.15)), which is endothermic thus explaining the first trend. Adding a product in the inlet suppresses the forward reaction, which explains the third trend. The second trend is somewhat tricker, but can be explained as the effect of decreasing the partial pressures of the reacting components for a system where decreasing pressure will drive the forward reaction.

6.2 Nernst potentials for the possible electrochemical reactions on anode

Having calculated the chemical equilibrium compositions for a given inlet fuel mixture, I can now check how the electrochemical equilibrium or Nernst potentials are affected.

For each component in the fuel that can be oxidized, I can write down the Nernst equation to describe the equilibrium potential for the electrochemical oxidation of that component. As seen above, in the H_2S SOFC, the fuel gas at the anode contains finite quantities of at least three possible fuels: H_2S, H_2, and S_2. The overall reactions and the Nernst potentials for these three fuels are given below.

$$H_2S + \frac{1}{2}O_2 \Leftrightarrow H_2O + \frac{1}{2}S_2 \tag{6.8}$$

$$H_2 + \frac{1}{2}O_2 \Leftrightarrow H_2O \tag{6.9}$$

$$S_2 + 2O_2 \Leftrightarrow 2\,SO_2 \tag{6.10}$$

$$E_{H_2S \rightarrow S_2} = E^{\circ}_{H_2S} + \frac{RT}{2F} \ln \left\{ \frac{P_{H_2S}\sqrt{P_{O_2}}}{P_{H_2O}\sqrt{P_{S_2}}} \right\} \tag{6.11}$$

$$E_{H_2} = E^{\circ}_{H_2} + \frac{RT}{2F} \ln \left\{ \frac{P_{H_2}\sqrt{P^{o}}}{P_{H_2O}\sqrt{P_{O_2}}} \right\} \tag{6.12}$$

$$E_{S_2} = E^{\circ}_{S_2} + \frac{RT}{8F} \ln \left\{ \frac{P_{S_2}P^2_{O_2}}{P^2_{SO_2}P^{o}} \right\} \tag{6.13}$$

In table 6.2, I list the unit activity equilibrium potential E° and calculated Nernst voltages for the three reactions (6.11)...(6.13) at 750°C for three different inlet fuel compositions with air on the cathode side. Also listed is the oxygen Nernst potential calculated according to equation (6.14).

$$E_{O_2} = \frac{RT}{4F} \ln \left\{ \frac{P_{O_2,\,\text{cathode}}}{P_{O_2,\,\text{anode}}} \right\} \tag{6.14}$$

Thus, although the unit activity equilibrium potentials E° are very different for the different fuel oxidation reactions, the Nernst potentials for all components of a fuel at chemical equilibrium are identical to four significant digits[1]. In fact, I show in appendix B that the Nernst potential for any component in a mixture *at chemical equilibrium* is the same.

[1]Here again, I used both Cantera as well CEA to calculate the equilibrium compositions. The Nernst potentials given in table 6.2 were calculated using the equilibrium compositions from CEA. The values calculated using Cantera were identical to two significant digits.

Table 6.2: Nernst potentials for fuel brought to equilibrium at 750°C

Fuel	E^o	$E_{[100-0-0]}$	$E_{[10-90-0]}$	$E_{[40-20-40]}$
H_2	0.977	0.988	0.918	1.076
H_2S	0.782	0.988	0.918	1.076
S_2	0.734	0.988	0.918	1.076
O_2	–	0.988	0.918	1.076

6.2.1 Comparing experimental OCV data with Nernst potentials for fuel at equilibrium

In figures 6.2 and 6.3, I compare the experimental OCV data as a function inlet fuel composition with the Nernst potential given by the thermodynamic model. The equilibrium Nernst potential matches the experimental data very well, with a small offset, as I vary the H_2S or H_2 content. However, if I assume that the fuel is at equilibrium when it reaches the anode even at a fuel flow-rate of 100 ml/min, then I cannot explain the decrease in OCV with decreasing fuel flow-rate seen in the experiments.

6.2.2 Nernst potentials for a fuel not at equilibrium

I showed that for a fuel at chemical equilibrium it does not matter which reaction is used to calculate the Nernst potential, which is the same as the OCV. What if the fuel is not at equilibrium? To answer this question, one has to simplify the problem. As seen above, chemical thermodynamics predicts that the products from the dissociation of H_2S molecules can include species such as H_2, S, S_2, S_8, SH, etc. However, as S_2 is the primary stable product containing S at the fuel cell operation temperature, I can consider only the overall dissociation reaction given by (6.15). Also, I will restrict my attention to the Nernst potentials for the H_2S and H_2 oxidation reactions.

$$H_2S \Leftrightarrow H_2 + \frac{1}{2}S_2 \tag{6.15}$$

To calculate the Nernst potentials for the H_2S and H_2 oxidation reactions, I need the gas phase compositions for H_2S, H_2, H_2O, and S_2. The reaction mixture compositions for calculating the Nernst potentials in figure 6.4 were obtained using

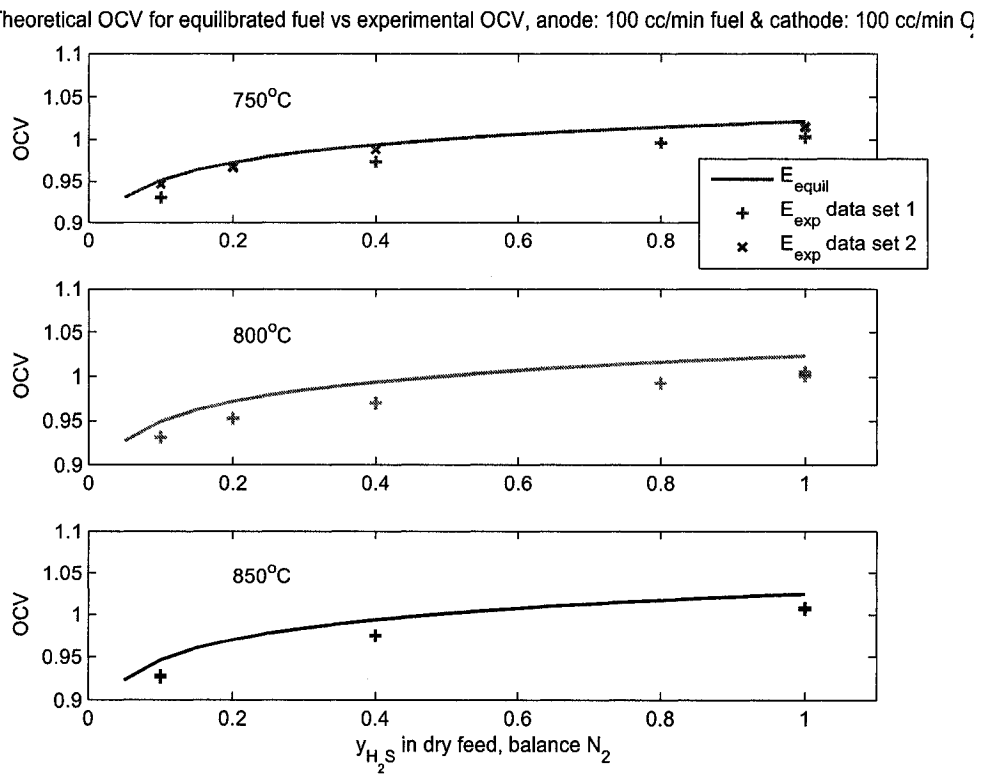

Figure 6.2: Nernst potential for fuel at chemical equilibrium as a function of inlet H_2S mole fraction

equations (6.16)...(6.22) below. In these equations, X_{H_2S} was varied from the inlet composition (97.4% H_2S, 2.6% H_2O) to the equilibrium composition to get E_{H_2S} and E_{H_2} as functions of X_{H_2S}.

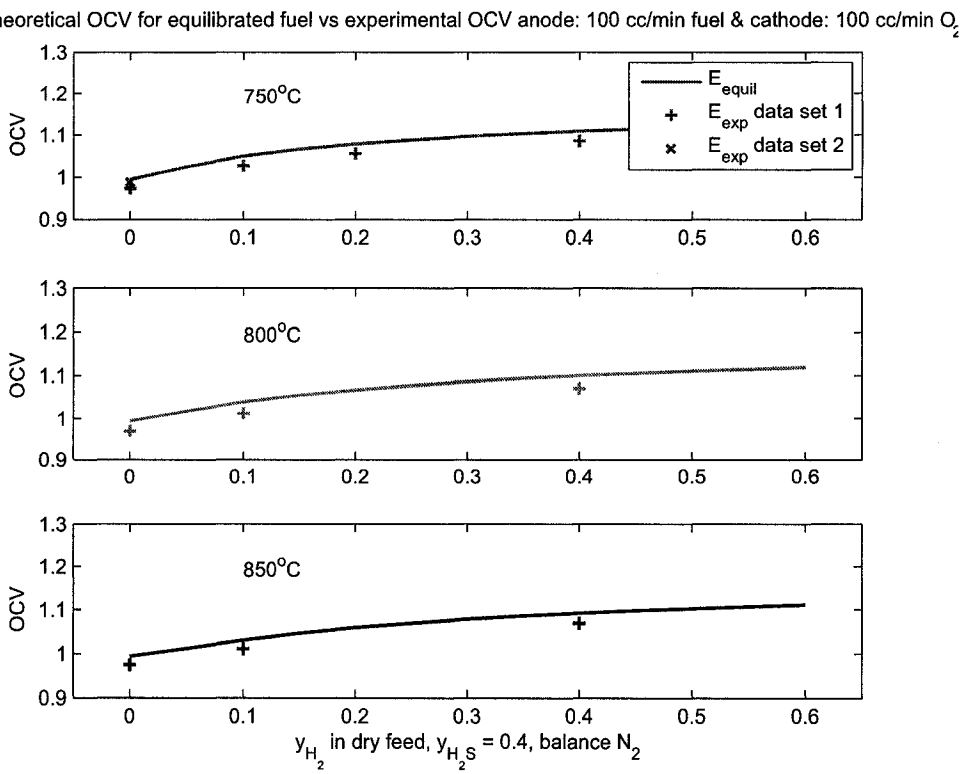

Figure 6.3: Nernst potential for fuel at chemical equilibrium as a function of inlet H_2S mole fraction

$$f_{H_2S} = f_{H_2S,\,in}(1 - X_{H_2S}) \tag{6.16}$$

$$f_{H_2} = f_{H_2,\,in} + f_{H_2S,\,in}(X_{H_2S}) \tag{6.17}$$

$$f_{S_2} = f_{H_2S,\,in}\left(\frac{X_{H_2S}}{2}\right) \tag{6.18}$$

$$f_{H_2O} = f_{H_2O,\,in} \tag{6.19}$$

$$f_{N_2} = f_{N_2,\,in} \tag{6.20}$$

$$f_{total} = f_{H_2S,\,in}\left(1 + \frac{X_{H_2S}}{2}\right) + f_{H_2O,\,in} + f_{N_2,\,in} \tag{6.21}$$

$$y_k = \frac{f_k}{f_{total}} \tag{6.22}$$

f_k is the volumetric or molar flow-rate of component k.

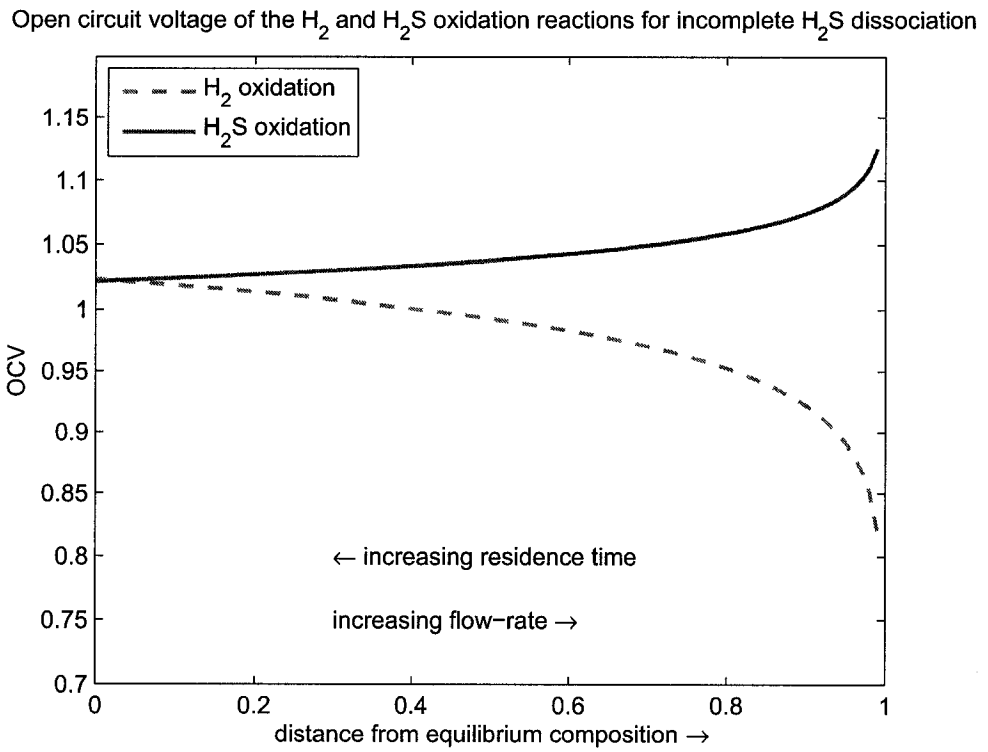

Figure 6.4: E_{H_2S} and E_{H_2} in a fuel mixture at 750°C as a function of the approach to equilibrium composition

Figure 6.4 shows how the Nernst potentials for the H_2S and H_2 oxidation reactions converge as the reaction mixture composition goes from the inlet composition to the equilibrium composition. If the mixture is not at equilibrium, the Nernst potentials for H_2S, E_{H_2S} is higher than the equilibrium value while the Nernst potential for H_2, E_{H_2} is lower than the equilibrium value. This clearly shows that if the dissociation reaction is not at equilibrium, the OCV for a fuel cell anode active to H_2S oxidation would be higher than that for an anode active only to H_2 oxidation.

As discussed in Chapter 5, the open circuit voltage was a function of the fuel flow-rate. The higher the flow-rate, the higher the measured OCV. To explain this flow-rate dependence qualitatively, I use arguments from chemical reaction engineering [44]. In reaction engineering terms, for a flow reactor, the higher the reactant gas flow-rate, the lower the residence time of the reactants. The lower the

residence time, the lower the conversion of reactants to products. If the primary electrochemical reaction on the anode was H_2 oxidation, increasing the flow-rate, thus decreasing the extent of reaction, would result in a decrease in OCV. On the other hand, if the primary electrochemical reaction on the anode was H_2S oxidation, increasing the flow-rate, thus decreasing the extent of reaction, would result in an increase in OCV. Thus, from this discussion, an increase in OCV with increasing flow-rate points to preferential H_2S oxidation at the anode.

To do a quantitative analysis, I need to model the kinetics of H_2S dissociation in the fuel inlet line as the fuel heats up in the assembly. I will model the kinetics of the above reaction and simulate the effect of flow-rate on fuel cell OCV directly in Chapter 7.

In this work, I do not model the heterogeneous dissociation reaction on the anode electrocatalyst for the following reasons:

1. There are no studies where the above reaction has been studied using the catalyst used for the experiments described in Chapter 5.

2. The total amount of reaction on the anode is not expected to be high because of its relatively small volume compared to the fuel channel.

To estimate how much of the reaction occurs on the anode *vs* inside the fuel channel, one can use the catalytic H_2S dissociation kinetics/rate equations for catalysts such as MoS_2 and then incorporate those within the multiphysics model described in the next chapter. I did not attempt the above exercise in this work.

In the next section, I briefly present the gas phase H_2S dissociation kinetic models I use in those fuel cell simulations.

6.3 Kinetics of H_2S dissociation

The H_2S dissociation reaction (6.15) has been studied extensively in the research literature because of academic and industrial interest in two different processes: 1) the Claus process and 2) H_2 production. The Claus process is a well established industrial process for the conversion of H_2S into solid sulphur and H_2S dissociation is one of the reactions in the Claus process [68, 15]. H_2S dissociation to produce H_2 is an attractive proposition because H_2 is a highly valuable chemical and fuel [149, 58, 2].

Zaman and Chakma [149] give a very good review of the different processes such as thermal catalytic and non-catalytic methods, photochemical methods, electrochemical methods, etc. that have been investigated to dissociate H_2S.

In this work, H_2S dissociation occurs in the fuel inlet tube. As the fuel is brought up to temperature, the H_2S can dissociate both in the gas phase, as well as on the surface of the alumina inlet tube. There has been some debate in the literature on whether alumina is active for the H_2S dissociation reaction [67, 58]. The anode is probably active for H_2S dissociation as well.

There are several kinetic models available in the literature for reaction (6.15) in the gas phase. These models range from a single overall rate equation [67, 41, 103, 2, 68, 59] to a reaction mechanism with rate equations for each elementary step [144, 119, 15]. Among the models in the former category, some models either do not consider the backward reaction in (6.15) (H_2S formation from H_2 and S_2), or the models are not thermodynamically consistent.

For the rate equation to consider both the forward and backward rates, it is written in the form of (6.23).

$$r_{overall} = r_f - r_b \tag{6.23}$$

$$r_f = k_f C_{H_2S}^{x_f} C_{H_2}^{y_f} C_{S_2}^{z_f} \tag{6.24}$$

$$r_b = k_b C_{H_2S}^{x_b} C_{H_2}^{y_b} C_{S_2}^{z_b} \tag{6.25}$$

The exponents x, y, z are reaction orders for the three reacting gas species.

For a H_2S dissociation model to be thermodynamically consistent, the ratio of the forward reaction rate constant to the backward reaction rate constant should equal the equilibrium constant for the reaction. The equilibrium constant for H_2S dissociation (6.15) is given by (6.26).

$$K_{eq} = \frac{a_{H_2}\sqrt{a_{S_2}}}{a_{H_2S}} \tag{6.26}$$

$$K_{C,eq} = \frac{C_{H_2}\sqrt{C_{S_2}}}{C_{H_2S}} = K_{eq}\sqrt{C^o} \tag{6.27}$$

$$K_{P,eq} = \frac{P_{H_2}\sqrt{P_{S_2}}}{P_{H_2S}} = K_{eq}\sqrt{P^o} \tag{6.28}$$

P^o and C^o are reference concentration and pressure respectively.

Thus for the thermodynamic consistency of the overall rate equation (6.23), at equilibrium or when $r_f = r_b$, (6.23)..(6.25) along with (6.27) give us the following rules (6.30)..(6.32). The same rules apply if the rate equation uses partial pressures instead of molar concentrations.

$$K_{C,eq} = \frac{k_f}{k_b} = C_{H_2S}^{x_b - x_f} C_{H_2}^{y_b - y_f} C_{S_2}^{z_b - z_f} = \frac{C_{H_2}\sqrt{C_{S_2}}}{C_{H_2S}} \tag{6.29}$$

$$x_b - x_f = -1 \tag{6.30}$$

$$y_b - y_f = 1 \tag{6.31}$$

$$z_b - z_f = 0.5 \tag{6.32}$$

Three different kinetic models for H_2S dissociation are presented below. All of these models give overall rate equations that are thermodynamically consistent according to the above criteria.

Hawboldt et al. [59] developed their rate equation (6.33) using data from a quartz-coiled reactor housed in a high-temperature furnace and operated at $T = 850 - 1150°C$ and atmospheric pressure. They include a S_2 partial pressure term in the forward rate to account for reaction auto-acceleration effects.

$$r_{gas} = k_f \left(P_{H_2S}\sqrt{P_{S_2}} - \frac{P_{H_2}P_{S_2}}{K_{P,eq}} \right) \tag{6.33}$$

$$k_f = A_f e^{\frac{-E_f}{RT}} \tag{6.34}$$

$$A_f = 5260 \frac{\text{mol}}{\text{cm}^3\,\text{s}\,\text{atm}^{1.5}} = 5.16 \times 10^9 \frac{\text{mol}}{\text{m}^3\,\text{s}\,\text{bar}^{1.5}} \tag{6.35}$$

$$E_f = 45.0 \frac{\text{kcal}}{\text{mol}} = 188 \frac{\text{kJ}}{\text{mol}} \tag{6.36}$$

Harvey et al. [58] developed their rate equations (6.37) and (6.41) using data from a tubular alumina reactor housed in a high-temperature furnace and operated at $T = 1077 - 1327°C$ and $P = 0.15 - 0.3$ bar. They found that H_2S conversion depended on the available surface area of alumina in the reactor and proposed that alumina is active to the dissociation reaction.

$$r_{gas} = k_f \left(C_{H_2S} - \frac{C_{H_2}\sqrt{C_{S_2}}}{K_{C,eq}} \right) \tag{6.37}$$

$$k_f = A_f e^{-E_f/RT} \tag{6.38}$$

$$A_f = 1.3 \times 10^{11}\ \mathrm{s}^{-1} \tag{6.39}$$

$$E_f = 286\ \frac{\mathrm{kJ}}{\mathrm{mol}} \tag{6.40}$$

$$r_{surface} = k_{f,s}\frac{S}{V}\left(C_{H_2S}^{0.1} - \left[\frac{C_{H_2}\sqrt{C_{S_2}}}{K_{C,eq}} \right]^{0.1} \right) \tag{6.41}$$

$$k_{f,s} = A_{f,s} e^{-E_{f,s}/RT} \tag{6.42}$$

$$A_{f,s} = 1.3 \times 10^6\ \frac{\mathrm{m}}{\mathrm{s}} \left(\frac{\mathrm{mol}}{\mathrm{m}^3} \right)^{0.9} \tag{6.43}$$

$$E_{f,s} = 194\ \frac{\mathrm{kJ}}{\mathrm{mol}} \tag{6.44}$$

S/V is the surface to volume ratio of the reactor.

Kaloidas and Papayannakos [67] also developed their model equation 6.45 using data from an alumina tubular reactor. The operating temperatures they investigated were in the range $T = 600 - 860°C$ and for total pressures in the range $P = 1.3 - 3.0$ bar. These operating conditions are closest to the conditions in the fuel inlet tube in our experiments.

$$r_{gas} = k_f \left(P_{H_2S}\sqrt{P_{S_2}} - \frac{P_{H_2}P_{S_2}}{K_{P,eq}} \right) \tag{6.45}$$

$$k_f = A_f e^{\frac{-E_f}{RT}} \tag{6.46}$$

$$A_f = 784\ \frac{\mathrm{mol}}{\mathrm{cm}^3\,\mathrm{s\,atm}} = 7.74 \times 10^8 \frac{\mathrm{mol}}{\mathrm{m}^3\,\mathrm{s\,bar}} \tag{6.47}$$

$$E_f = 46.8\ \frac{\mathrm{kcal}}{\mathrm{mol}} = 196 \frac{\mathrm{kJ}}{\mathrm{mol}} \tag{6.48}$$

6.4 Summary

As H_2S dissociates at the operation temperatures seen in our experiments, I need to account for this dissociation reaction in the fuel cell models. In this Chapter I examined the thermodynamics and kinetics of H_2S dissociation. I developed thermodynamic models that calculate the equilibrium composition of a fuel mixture as a function of inlet fuel composition and operation temperature. I then used the output from these models to calculate the Nernst potentials for the possible electrochemical oxidation reactions. I also modelled how these Nernst potentials change is the fuel mixture is not at chemical equilibrium. To correctly model the dissociation in fuel mixtures not at equilibrium, I need to consider the reaction kinetics for H_2S dissociation. While I do not develop the kinetic models needed for the above reaction here, I present some appropriate models available in the research literature on H_2S dissociation and discuss their usefulness for my purposes. In the next Chapter, I build complete multiphysics models that include H_2S dissociation kinetics to examine the effect of this reaction on the performance of H_2S fuelled SOFCs.

Chapter 7

SOFC models including H_2S dissociation

In this Chapter, I present models for the fuel cell setup used in the experiments described in Chapter 5. Although I have already presented a range of H_2S SOFC models in Chapter 4, those models are not capable of modelling the experiments we performed. To model the flow-rate and composition effects on fuel cell performance observed in our experiments correctly, I need models that can predict the open circuit voltage and the electrochemical performance of the cell. To calculate these, I need local concentrations of the electrochemically active species at the anode and the cathode. Although the inlet oxidant composition can be used as the composition at the cathode, the H_2S in the fuel dissociates in the fuel inlet channel, which means the fuel composition at the anode is not the same as the inlet fuel composition even at open circuit conditions. To calculate the fuel composition at the anode, I need to model the reactions in the fuel channel correctly. As the dissociation reaction is a strong function of temperature, I need the temperature profile in the fuel channel to calculate the extent of reaction in the fuel. This link between the fuel chemistry and the temperature distribution is a two way link as the H_2S dissociation reaction is endothermic. Thus, the local temperature in the fuel channel is dependent on the local rate of reaction, and the local rate of reaction is dependent on the local temperature. To assess the degree of coupling between the thermal model and the dissociation reaction chemistry as well as to answer questions such as whether the flow-rate affects cell temperature directly by cooling the cell, I need to extend the fuel cell models presented in Chapter 4 by including the following capabilities in my models.

1. Modelling the heat transfer and thus the temperature profile in the fuel cell assembly.

2. Modelling the H_2S dissociation reaction in the fuel cell assembly to calculate the fuel composition at the anode.

3. Predicting the open circuit voltage of the cell as well as the electrochemical reaction rates using the local gas phase compositions at the anode and cathode.

7.1 Geometry

The model geometry is a 2-D axi-symmetric geometry similar to the geometry used in Chapter 4. The two main differences from the earlier geometry are the length of the geometry and the inclusion of ceramic spacers between the inner/inlet tubes and the current collectors.

The fuel cell assembly consists of the following components, all of which are considered in the model geometry:

- The alumina tubes that carry the fuel and air/O_2 to the cell, and the product and unreacted gases away from the cell. The tubes on both sides are 40 cm long each of which 25 cm are inside the furnace.

- The machined ceramic spacers that fit over the inlet tubes and are used to push the current collectors against the electrodes. These spacers also help align the inlet tubes with the outer tubes.

- The current collectors on both sides. The current collectors in the experiments were made of Au or Pt mesh. In my models, I assume that they offer no resistance to flow and thus do not model them explicitly.

- The fuel cell consisting of the anode, electrolyte and cathode. As the thickness of the Pt cathode was much lower than that of the anode and electrolyte layers ($\sim 10 - 20\mu$m vs 100 μm and 300 μm), I model the cathode as a 1-D boundary.

The aspect ratio (length/breadth) of the model geometry used is 63. Thus, It is difficult to show the entire geometry. Figure 7.1 gives a view of the middle

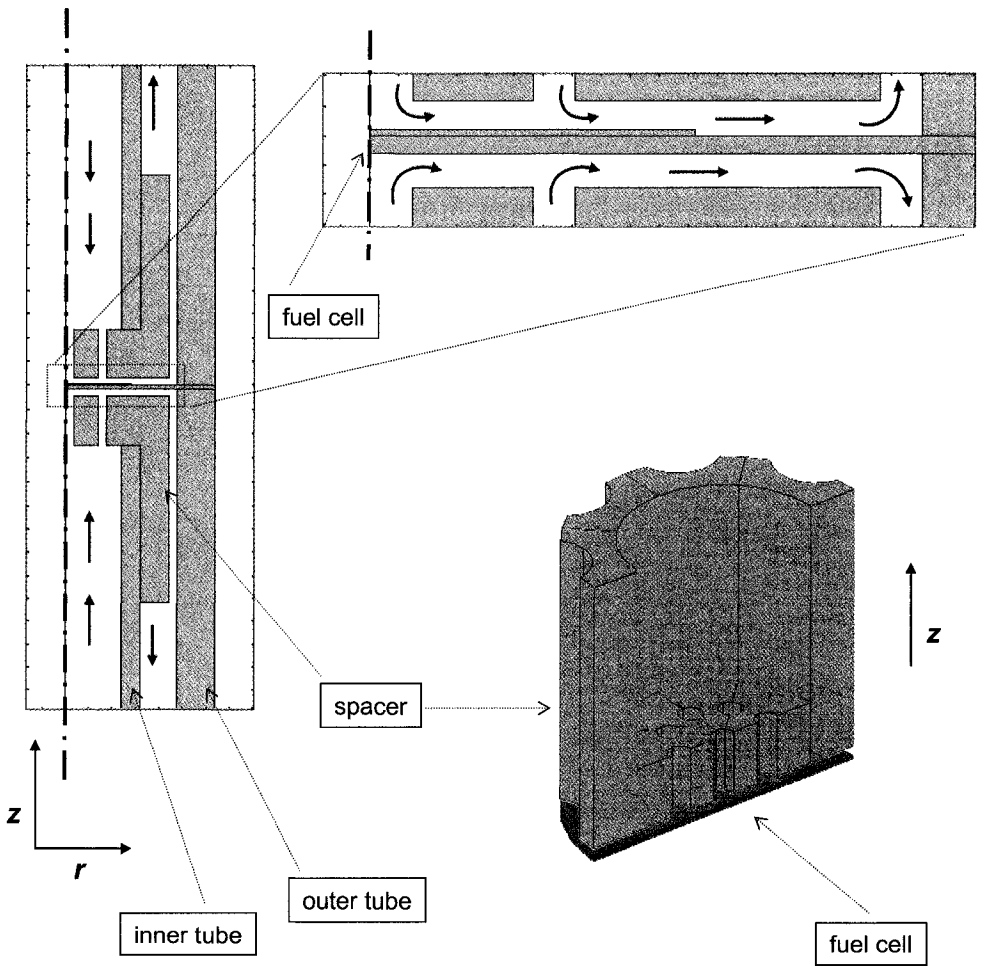

Figure 7.1: 2-D axi-symmetric model geometry and 3-D cut-away of a spacer

of the geometry as well as a close-up of the fuel cell showing the flow in the gas channels. The axis of symmetry is marked using a black dash-dot line for the two views. The section above the cell is the fuel section while the section below is the air/O_2 section.

A 3-D cut-away of the spacers used is also shown in figure 7.1. I calculated the cross-section area available for flow in the spacer and used that to develop the approximated 2-D spacer geometry.

7.2 2-D model

The 2-D model I present here is an extension of the models in Chapter 4. In addition to solving for flow, mass transfer, and charge transport, the models in this Chapter also take heat transfer, H_2S dissociation in the fuel into account, as well as multiple electrochemical reactions at the anode. Thus, the governing equations solved in these models include the i) weakly-compressible Navier-Stokes equations and Brinkman equation for velocity and pressure in the flow channels and electrodes respectively, ii) Maxwell-Stefan convection-diffusion mass transfer equations for partial densities of H_2S, H_2O, S_2 on the fuel side and O_2 on the air side, iii) the general heat transfer equation for temperature in the entire fuel cell assembly and, iv) Laplace equation (Ohm's law) for the voltage/current distribution in the electrodes and electrolyte.

Although I have listed the governing PDEs in Chapters 2 and 4, as the boundary conditions used here are different, I present PDEs again here along with the boundary conditions used.

7.2.1 Flow in gas channels and electrodes

The governing equations for flow in the gas channels:

$$\begin{aligned} &-\nabla.\left[\mu\left(\nabla\mathbf{v}+(\nabla\mathbf{v})^T\right)-\frac{2}{3}\mu(\nabla.\mathbf{v})\mathbf{I}\right]+\rho\left(\mathbf{v}.\nabla\mathbf{v}\right)+\nabla p=0 \\ &\nabla.(\rho\mathbf{v})=0 \end{aligned} \tag{7.1}$$

The Brinkman equation is used for flow in the anode as it allows for easier implementation of the boundary conditions at the anode's interface with the fuel

channel.

$$\frac{\mu}{\kappa}\mathbf{v} = -\nabla p + \frac{1}{\epsilon}\nabla.\left[\mu\left(\nabla\mathbf{v} + (\nabla\mathbf{v})^T\right) - \frac{2}{3}\mu(\nabla.\mathbf{v})\mathbf{I}\right]$$
$$\nabla.(\rho\mathbf{v}) = 0 \tag{7.2}$$

Boundary Conditions (channel and electrode flow)

- zero velocity (no-slip) at the walls

$$\mathbf{v} = 0|_{\partial\Omega_{\text{walls}}} \tag{7.3}$$

- fully developed laminar flow at the fuel and air inlets for the given volumetric flow-rates:

$$u = 0, \;\; v = \frac{2\dot{V}}{\pi r_{inner}^2}\left[1 - \left(\frac{r}{r_{inner}}\right)^2\right] \tag{7.4}$$

- pressure specified and flow normal to the boundary at the outlets of the flow channels.

$$p = 0, \;\; \mathbf{t}.\mathbf{v} = 0 \tag{7.5}$$

- Radial symmetry along the axis of the flow channels

$$\left.\frac{\partial v}{\partial r}\right|_{r=0} = 0, \quad u|_{r=0} = 0 \tag{7.6}$$

- velocity continuous across the channel-anode interfaces

$$\mathbf{v}^{\text{flow channels}} = \mathbf{v}^{\text{electrodes}}|_{\partial\Omega_{\text{flow channels}-\text{electrodes}}} \tag{7.7}$$

- flow into the anode at the anode-electrolyte interface is given by the electrochemical reaction(s) at that interface

The general equation for flow into a fuel cell electrode is given by (7.8) below.

$$-\mathbf{n}.\mathbf{v}|_{\partial\Omega_{\text{electrode,electrolyte}}} = \frac{1}{\rho}\left(\frac{1}{F}\sum_j\left\{i_j\left(\sum_k \frac{\xi_{k,j}M_{k,j}}{n_{k,j}}\right)\right\} + \sum_k \mathbf{n}.\mathbf{j}_k\right) \quad (7.8)$$

Equation (7.8) written for an anode that electro-oxidizes both H_2S and H_2 gives (7.9).

$$\mathbf{n}.\mathbf{v}|_{\partial\Omega_{\text{anode}}} = \frac{1}{\rho}\left(\frac{i_{H_2S}(2M_{H_2S} - 2M_{H_2O} - M_{S_2})}{4F} + \frac{i_{H_2}(M_{H_2} - M_{H_2O})}{2F} - \mathbf{n}.\mathbf{j}_{H_2S} - \mathbf{n}.\mathbf{j}_{H_2O} - \mathbf{n}.\mathbf{j}_{H_2} - \mathbf{n}.\mathbf{j}_{S_2} - \mathbf{n}.\mathbf{j}_{N_2}\right) \quad (7.9)$$

- flow into the electrolyte at the cathode-electrolyte interface is given by the oxygen being consumed at that interface

  Equation (7.10) is (7.8) written for the cathode.

$$\mathbf{n}.\mathbf{v}|_{\partial\Omega_{\text{cathode}}} = \frac{1}{\rho}\left(\frac{i_{\text{cathode}}M_{O_2}}{4F} - \mathbf{n}.\mathbf{j}_{O_2} - \mathbf{n}.\mathbf{j}_{N_2}\right) \quad (7.10)$$

  The cathode is modelled as an interface because it is much thinner than the electrolyte.

7.2.2 Mass transfer

The convection-diffusion equation (7.11) is used to describe the mass transfer of the reactants and products in the flow channels and the electrodes.

$$\nabla.\mathbf{j}_k + \rho\mathbf{v}.\nabla w_k = r_k \quad (7.11)$$

Since I am modelling H_2S dissociation in the fuel, r_k is non-zero for $i = H_2S, H_2, S_2$ and the source terms for these components are related by (7.12) where

r_{H_2} is given by one of the rate equations for r_{gas} in section 6.3

$$r_{H_2S} = -r_{H_2} = -2r_{S_2} \tag{7.12}$$

The diffusion term is given by the Maxwell-Stefan equation (7.13), which has already been described in section 4.6.3.

$$\mathbf{j}_k = -\rho w_k \sum_{j=1}^{n} \tilde{D}_{kj} \left(\nabla y_j + (y_j - w_j) \frac{\nabla p}{p} \right) \tag{7.13}$$

Boundary Conditions (Convection-diffusion equation)

- mass fraction of O_2 in air, and H_2S, S_2, H_2O in fuel given at the flow channel inlets

$$\begin{aligned} w_{H_2S}|_{\partial\Omega_{\text{fuel,inlet}}} &= w_{H_2S,\text{in}} \\ w_{H_2O}|_{\partial\Omega_{\text{fuel,inlet}}} &= w_{H_2O,\text{in}} \\ w_{O_2}|_{\partial\Omega_{\text{air,inlet}}} &= w_{O_2,\text{in}} \end{aligned} \tag{7.14}$$

- flux at the inner and outer tube walls

$$\mathbf{n}.\mathbf{N}_k|_{\partial\Omega_{\text{walls}}} = M_k \, r_{k,\,surface} \tag{7.15}$$

$$\mathbf{N}_k = \mathbf{j}_k + \rho w_k \mathbf{v} \tag{7.16}$$

$\mathbf{N}_k$ is the total mass flux of the k^{th} component and $r_{k,\,surface}$ is the rate of generation of k on the surface if the surface catalyzes a reaction involving k. In this work, the only case where I consider a surface reaction is when using (6.41) for H_2S dissociation on the fuel tube surface.

- mass flux, of the reactants out of, and the products into, the electrodes governed by the local current density at the electrode-electrolyte interface

$$
\begin{aligned}
-\mathbf{n}.\mathbf{N}_{H_2S}|_{\partial\Omega_{anode,electrolyte}} &= -\frac{M_{H_2S} i_{H_2S}}{2F} \\
-\mathbf{n}.\mathbf{N}_{H_2O}|_{\partial\Omega_{anode,electrolyte}} &= \frac{M_{H_2O}(i_{H_2S} + i_{H_2})}{2F} \\
-\mathbf{n}.\mathbf{N}_{H_2}|_{\partial\Omega_{anode,electrolyte}} &= -\frac{M_{H_2} i_{H_2}}{2F} \\
-\mathbf{n}.\mathbf{N}_{S_2}|_{\partial\Omega_{anode,electrolyte}} &= \frac{M_{S_2} i_{H_2S}}{2F} \\
-\mathbf{n}.\mathbf{N}_{O_2}|_{\partial\Omega_{cathode,electrolyte}} &= -\frac{M_{O_2} i_{cathode}}{4F}
\end{aligned} \tag{7.17}
$$

- radial symmetry along the axis of the flow channels and the electrodes

$$
\left.\frac{\partial w_k}{\partial r}\right|_{r=0} = 0 \tag{7.18}
$$

7.2.3 Charge transport

As described in section 4.6.4, the voltage and current distribution in the anode and the electrolyte due to this electronic and ionic transport is modelled using the vector form of Ohm's law (7.19). I model the cathode only as an interface, and thus do not need a separate equation for it.

$$
\begin{aligned}
\nabla.(-\sigma_m \nabla\phi_m) &= 0 \\
\nabla.(-\sigma_a \nabla\phi_a) &= 0
\end{aligned} \tag{7.19}
$$

Boundary Conditions (Ohm's law)

- the voltage at the anode current collector is specified

$$
\begin{aligned}
\mathbf{n}.\mathbf{i}_{anode}|_{\partial\Omega_{anode,collector}} &= (\phi_a + V_{cell}) \left[\frac{\sigma}{l}\right]_{contact} \\
\mathbf{i}_{anode} &= -\sigma_a \nabla\phi_a
\end{aligned} \tag{7.20}
$$

$\mathbf{i}$ is the current density vector, $[\sigma/l]_{contact}$ is the area specific contact and lead

conductance.

- electrical insulation at the insulated boundaries

$$\mathbf{n}.\mathbf{i}_{\text{electrolyte}}|_{\partial\Omega_{\text{insulated}}} = 0 \tag{7.21}$$

- current density at the electrode-electrolyte interfaces is given by the electrochemical reaction rate

$$-\mathbf{n}.\mathbf{i}_{\text{anode}}|_{\partial\Omega_{\text{anode,electrolyte}}} = i_{H_2S} + i_{H_2} \tag{7.22}$$

$$i_{H_2S} = i^{o}_{a,\,H_2S}\left\{P_{H_2S}\exp\left(\frac{\alpha_{a,\,H_2S}\,\eta_{H_2S}\,F}{RT}\right) - P_{H_2O}\sqrt{P_{S_2}}\exp\left(\frac{-(2-\alpha_{a,\,H_2S})\eta_{H_2S}\,F}{RT}\right)\right\} \tag{7.23}$$

$$i_{H_2} = i^{o}_{a,\,H_2}\left\{P_{H_2}\exp\left(\frac{\alpha_{a,\,H_2}\,\eta_{H_2}\,F}{RT}\right) - P_{H_2O}\exp\left(\frac{-(2-\alpha_{a,\,H_2})\eta_{H_2}\,F}{RT}\right)\right\} \tag{7.24}$$

$$-\mathbf{n}.\mathbf{i}_{\text{cathode}}|_{\partial\Omega_{\text{cathode,electrolyte}}} = i^{o}_{c}\left\{\sqrt{P_{O_2}}\exp\left(\frac{-\alpha_{c,O_2}\,\eta_c F}{RT}\right) - \exp\left(\frac{(2-\alpha_{c,O_2})\eta_c F}{RT}\right)\right\} \tag{7.25}$$

$$\begin{aligned}
\eta_{H_2S} &= \phi_a - \phi_{electrolyte} - E^o_{H_2S} \\
\eta_{H_2} &= \phi_a - \phi_{electrolyte} - E^o_{H_2} \\
\eta_c &= \phi_c - \phi_{electrolyte} - E^o_{O_2} \\
\phi_c &= 0
\end{aligned} \tag{7.26}$$

Equation (7.22) allows for oxidation of both H_2S and H_2. P_k are the partial pressures (in bar) at the boundary, $\alpha_{a,k}$ are the anodic charge transfer coefficients on the anode, and α_{c,O_2} is the cathodic charge transfer coefficient on the cathode.

In all models discussed in this Chapter, $E^o_{O_2} = 0$ and $E^o_{H_2}, E^o_{H_2S}$ are calculated from the free energy of the overall H_2 and H_2S oxidation reactions respectively (equations 7.27 and 7.28).

$$E^o_{H_2} = \frac{\Delta G_{H_2+O_2/2\rightarrow H_2O}}{2F} \tag{7.27}$$

$$E^o_{H_2S} = \frac{\Delta G_{H_2S+O_2/2\rightarrow H_2O+S_2/2}}{2F} \tag{7.28}$$

In the models in Chapter 4, the cathode terminal potential gave the cell voltage and the anode terminal potential was set to zero. In the models in this Chapter, the potential at the anode is negative while the potential at the cathode is kept at zero. This makes it easier to calculate the equilibrium potentials for the different fuel species (H_2S and H_2). The voltage of the fuel cell is given by the negative of the anode potential at the anode current collector or terminal (7.29).

$$V_{cell} = -\phi_a|_{a,cc} \tag{7.29}$$

- radial symmetry along the axis of the cell assembly

$$\left.\frac{\partial \phi_j}{\partial r}\right|_{r=0} = 0 \tag{7.30}$$

7.2.4 Heat transfer

The temperature distribution in the fuel cell assembly is modelled by equation (7.31) first presented in section 2.3.

$$\rho C_p \mathbf{v}.\nabla T = \nabla.(\lambda \nabla T) + q \tag{7.31}$$

C_p is specific heat at constant pressure, T is the temperature, λ is the thermal conductivity, and q is the rate of heat generation. While equation (7.31) is valid for all subdomains within the fuel cell assembly, the parameters ρ, c_p, λ, and the source term q are different for each subdomain.

The different heat source/sink terms q are:

1. the heat of reaction of the H_2S dissociation (and re-association) reaction on the fuel side

$$q_{fuel} = r_{\mathrm{H_2S}} \Delta H_{\mathrm{H_2S\ dissociation}} \tag{7.32}$$

   The dissociation of H_2S is endothermic and thus results in cooling in the fuel inlet where the forward reaction occurs. $\Delta H_{\mathrm{H_2S\ dissociation}}$ is a function of temperature and is calculated using the thermodynamic functions described in section 6.1.

2. Ohmic heating caused by the flow of current through the fuel cell

$$q_{\mathrm{vol,\,anode},\,\Omega} = \sigma_{\mathrm{a}} \left|\nabla \phi_a\right|^2 \tag{7.33}$$

$$q_{\mathrm{vol,\,electrolyte},\,\Omega} = \sigma_{\mathrm{m}} \left|\nabla \phi_m\right|^2 \tag{7.34}$$

$q_{\text{vol, anode, }\Omega}$ and $q_{\text{vol, electrolyte, }\Omega}$ are volumetric heat sources in the anode and electrolyte.

3. heating or cooling depending on the entropy change of the electrochemical reactions at the electrodes

$$q_{\text{anode, }\Delta S} = -T\left(\Delta S_{H_2}\frac{i_{H_2}}{2F} + \Delta S_{H_2S}\frac{i_{H_2S}}{2F}\right) \tag{7.35}$$

$$q_{\text{cathode, }\Delta S} = -T\Delta S_{\text{cathode}}\frac{i_{H_2S} + i_{H_2}}{2F} \tag{7.36}$$

As $q_{j,\,\Delta S}$ are the heat sources/sinks due to the entropy change of the electrochemical reactions, they are located at the electrode-electrolyte interfaces.

ΔS_{H_2} and ΔS_{H_2S} are the entropy changes for the H_2 (7.37) and H_2S (7.38) oxidation reactions, and $\Delta S_{\text{cathode}}$ is the entropy change for the oxygen reduction reaction (7.39).

$$\Delta S_{H_2} = S^{\circ}_{H_2O} - S^{\circ}_{H_2} + R\ln\left(\frac{P_{H_2}}{P_{H_2O}}\right) \tag{7.37}$$

$$\Delta S_{H_2S} = S^{\circ}_{H_2O} + \frac{1}{2}S^{\circ}_{S_2} - S^{\circ}_{H_2S} + R\ln\left(\frac{P_{H_2S}}{P_{H_2O}\sqrt{P_{S_2}}}\right) \tag{7.38}$$

$$\Delta S_{\text{cathode}} = -\frac{1}{2}S^{\circ}_{O_2} + \frac{R}{2}\ln P_{O_2} \tag{7.39}$$

S°_k in the entropy of k at the local temperature and is calculated using the thermodynamic functions described in section 6.1. The total thermal energy released/absorbed calculated using the above equations (and given by summing the appropriate $q_{j,\,\Delta S}$) is expected to be accurate. However, as the entropies of the charged species are not included in the above equations, the distribution of the heating/cooling at the two electrodes might be incorrect.

4. heating due to the electrochemical or activation voltage losses for a loaded fuel cell

When a fuel cell generates current, the voltage across the cell drops from the thermodynamic Nernst potential. The portion of this potential drop that is due to the electrochemical reaction, discussed in some detail in section

3.1, is called the activation overpotential. This reduction in the electrode potential also leads to heating at the electrode-electrolyte interfaces. These heat source terms are given by equations (7.40) and (7.41) while the local activation overpotentials are given by equations (7.42 ... 7.44).

$$q_{\text{anode, act}} = |\, i_{H_2S}\, \eta_{H_2S,\,s}| + |\, i_{H_2}\, \eta_{H_2,\,s}| \tag{7.40}$$

$$q_{\text{cathode, act}} = |\, i_{\text{cathode}}\, \eta_{c,\,s}| \tag{7.41}$$

$$\eta_{H_2S,\,s} = \phi_a - \phi_{\text{electrolyte}} - E^{\circ}_{H_2S} - \frac{RT}{2F} \ln\left(\frac{P_{H_2O}\sqrt{P_{S_2}}}{P_{H_2S}}\right) \tag{7.42}$$

$$\eta_{H_2,\,s} = \phi_a - \phi_{\text{electrolyte}} - E^{\circ}_{H_2} - \frac{RT}{2F} \ln\left(\frac{P_{H_2O}}{P_{H_2}}\right) \tag{7.43}$$

$$\eta_{c,\,s} = \phi_c - \phi_{\text{electrolyte}} - E^{\circ}_{O_2} - \frac{RT}{4F} \ln P_{O_2} \tag{7.44}$$

Boundary conditions (Heat transfer)

- radial symmetry along the axis of the cell assembly

$$\left.\frac{\partial T}{\partial r}\right|_{r=0} = 0 \tag{7.45}$$

- specified inlet temperature of fuel and air/O_2 gas streams

$$\begin{aligned} T|_{\partial\Omega_{\text{fuel, inlet}}} &= T_{\text{fuel, in}} \\ T|_{\partial\Omega_{\text{air, inlet}}} &= T_{\text{air, in}} \end{aligned} \tag{7.46}$$

- temperature profile along furnace

  The furnace specifications are used to calculate the temperature profile on the outside surface of the fuel cell assembly. The point conditions used are:

- T at the center of the assembly (the location of the fuel cell) is equal to the operating temperature.
- T 1.5 inch (3.81 cm) on either side of the center is 0.6°C lower than the operating temperature.
- T 3 inches (7.62 cm) on either side of the center is 3°C lower than the operating temperature.
- T at the edge of the furnace is 100°C lower than the operating temperature.

These T point values are connected using a cubic spline to generate a smooth profile T_{wall}.

$$T|_{\partial\Omega_{\text{furnace, wall}}} = T_{\text{wall}} \tag{7.47}$$

- convective flux only at outlets

$$\begin{aligned} \mathbf{n}.(-\lambda\nabla T)|_{\text{fuel, out}} &= 0 \\ \mathbf{n}.(-\lambda\nabla T)|_{\text{air, out}} &= 0 \end{aligned} \tag{7.48}$$

- free convection and radiation along external boundary of outer tubes

$$\mathbf{n}.(-\lambda\nabla T)|_{\text{outer}} = h(T - T_{\text{ambient}}) + \epsilon_{rad}\sigma_{rad}\left(T^4 - T^4_{\text{ambient}}\right) \tag{7.49}$$

h is the convective heat transfer coefficient, T_{ambient} is the temperature of the ambient around the fuel cell assembly, ϵ_{rad} is the emissivity of the external surface, and σ_{rad} is the Stefan-Boltzmann constant for radiation. The radiation terms assume that all surfaces are gray bodies with a wavelength independent emissivity that is equal to the surface's absorptivity.

- radiation heat exchange between internal surfaces

The net energy flux leaving an internal surface q_{rad} due to radiation heat exchange with its surroundings is given by (7.50).

$$q_{rad} = J_{rad} - G_{rad} = \epsilon_{rad}\left(\sigma_{rad}T^4 - G_{rad}\right) \tag{7.50}$$

$$G_{rad} = G_{rad,m} + F_{\text{ambient}}\sigma_{rad}T^4_{\text{ambient}} \tag{7.51}$$

J_{rad} is the radiosity for the surface or the radiation leaving the surface due to the surface temperature, while G_{rad} is the total radiation incident on the surface. The first term in (7.51), $G_{rad,m}$ is the mutual radiation arriving from the surrounding surfaces, and the second term is the radiation arriving at the surface from the ambient. F_{ambient} is the view factor of the ambient from the surface, and T_{ambient} is the temperature of the ambient. $G_{rad,m}$ and F_{ambient} are complex surface integrals determined by the geometry, and in the case of $G_{rad,m}$, the temperatures of the surrounding surfaces.

7.3 Parameters

There are a number of parameters in the models presented above and values for these parameters need to be assigned or calculated before the models can be solved. Physical constants, such as the gas constant R, and the values assigned to them in the models are summarized in the Nomenclature. Model parameters that are independent of temperature are listed in table 7.1.

Table 7.1: Temperature independent physical parameters in the models

Parameter	units	value
porosity	–	0.4
τ	–	4
$r_{\text{pore,av}}$	m	2×10^{-6}
l_{a}	m	10^{-4}
l_{m}	m	3×10^{-4}
κ_{a}	m^2	10^{-14}
ρ_{YSZ}	kg.m^{-3}	5600
$\rho_{Al_2O_3}$	kg.m^{-3}	3900

As mentioned in the relevant subsections, all gas phase thermodynamic properties are calculated as functions of temperature using the NASA Glenn thermodynamic database [88]. This covers parameters such as molar specific heat, reaction

enthalpies, entropies, and free energies. Standard electrode reaction potentials are calculated from the free energy change of the overall reaction as outlined in 7.2.3.

Transport parameters needed include fuel and air density, viscosities, diffusivities, thermal and electrical conductivities. All gas phase transport properties are calculated using the methods outlined in section 2.5.

Thermal conductivity (in $W(m.K)^{-1}$) and specific heat of the tubes ($J(kg.K)^{-1}$) in the fuel cell assembly are taken from [95] and are given in equations (7.52) and (7.53) as function of temperature ($T_{\circ C}$ in °C).

$$\lambda_{Al_2O_3} = 5.85 + 15360\frac{\exp(-0.002\ T_{\circ C})}{516 + T_{\circ C}} \tag{7.52}$$

$$C_{P,\,Al_2O_3} = 1117 + 0.14\ T_{\circ C} - 411\exp(-0.006\ T_{\circ C}) \tag{7.53}$$

Thermal conductivity and specific heat of the YSZ electrolyte are taken from [90] and are listed in table 7.2. The densities of the alumina tubes and the electrolyte are given in table 7.1.

The emissivity of the alumina tubes is given by (7.54) taken from [51].

$$\epsilon_{Al_2O_3} = \begin{cases} 0.78 - 3.4545 \times 10^{-4}(T - 400) & 400\,K \leq T \leq 1500\,K \\ 0.78 & T < 400\,K \end{cases} \tag{7.54}$$

The heat transfer coefficient for natural convection from the sections of the outer tubes that lie outside the furnace is given by (7.56). The correlation (7.55) is for natural convection from horizontal tubes and is taken from [65].

$$Nu = 0.36 + \frac{0.518\,Ra^{1/4}}{\left(1 + (0.559/Pr)^{9/16}\right)^{4/9}} \tag{7.55}$$

$$h = \frac{Nu\,\lambda}{D} \tag{7.56}$$

$$Pr = \frac{C_P \mu}{\lambda} \tag{7.57}$$

$$Ra = \frac{g(T - T_\infty)D^3\rho^2 C_P}{\lambda\,\mu\,T_\infty} \tag{7.58}$$

Nu is the Nusselt number, Pr is the Prandtl number, and Ra is the Rayleigh

number.

The physical properties of air required to calculate the dimensionless numbers are evaluated at the local temperature and $T_\infty = 295$ K is the ambient temperature. C_P is the specific heat at constant pressure on a mass basis.

Electrical conductivity of the anode material σ_a used is unavailable and I assume the same values as used for the anode in Chapter 4. These values, given in table 7.2 for the anode conductivity at the operating temperatures are corrected for porosity using equation (4.55) given in [34]. The electrical conductivity of the electrolyte YSZ is calculated using (7.59) given in [5].

$$\sigma_{YSZ} = \frac{100}{0.03685 + 0.002838 \exp(10300/T)} \tag{7.59}$$

The overall wire lead and contact resistance is calculated by subtracting the anode and electrolyte resistance from the $\hat{R}_s$ values obtained from fitting the EIS spectra at each different operating condition (see section 5.3). The overall cell area specific resistance is given by equation (7.60). The overall wire lead and contact resistance for the cell given by (7.61) is placed at the current collector for the anode. The values calculated for humidified H_2S at the three operating temperatures are given in table 7.2.

$$\hat{R}_s = \left[\frac{l}{\sigma}\right]_{YSZ} + \left[\frac{l}{\sigma}\right]_{anode} + \left[\frac{l}{\sigma}\right]_{contact} \tag{7.60}$$

$$\left[\frac{l}{\sigma}\right]_{contact} = \hat{R}_s - \left[\frac{l}{\sigma}\right]_{YSZ} - \left[\frac{l}{\sigma}\right]_{anode} \tag{7.61}$$

Table 7.2: Temperature dependent parameter values used

Parameter	units	750°C	800°C	850°C
λ_{YSZ}	$W(m.K)^{-1}$	1.75	1.63	1.5
$C_{P,YSZ}$	$J(kg.K)^{-1}$	650	650	650
σ_a	$(\Omega.m)^{-1}$	13.1	9.88	5.26
σ_m	$(\Omega.m)^{-1}$	1.49	2.39	3.66
$[\sigma/l]_{contact}$	$\Omega^{-1}.m^{-2}$	5220	4670	4180

The electrochemical kinetic parameters needed are exchange current density

and the charge transfer coefficient for each electrode reaction. The charge transfer symmetry coefficients α_j in the electrochemical rate equations (7.23), (7.24), and (7.25) are assigned the default symmetric value of $2 \times \beta = 1$. As experimental values for exchange current densities are not available, I estimate them using the models and experimental $i - V$ data. The estimation procedure and results are given in section 7.7.

7.4 Computational details

All model simulations in this Chapter were performed using COMSOL Multiphysics 3.4. The mesh used for the 2-D models consisted of over 37,000 triangular elements. This translates to more than 350,000 degrees of freedom (dof) for each simulation. The exact number of dof depended on whether or not I include radiative heat exchange between internal surfaces. All the 2-D models required ≥ 2 GB of RAM to solve. The 1-D models used in the section on parameter estimation were also run using COMSOL and the degrees of freedom for those models were ~ 100.

The 2-D models without internal radiation took between three to five minutes to solve for one set of parameter values. This translated to between one and two hours to solve for a full $i-V$ curve. The models that included internal radiation took 2–3 times as long. The 2-D simulations were done using the COMSOL client/server tools where the COMSOL server ran on multiprocessor computers with ≥ 5 GB of RAM. Some of the simulations were performed using two or four processors. Using more than one processor helped cut down the computational time, although the scale-up was not linear.

7.5 Choosing a kinetic model for H_2S dissociation

The model developed in section 7.2 allows me to include H_2S dissociation in the fuel. However, before I can use this model I need to decide on a kinetic model for the H_2S dissociation/synthesis reaction in the fuel channel. In figure 7.2, I plot the Nernst voltages for the H_2 and H_2S oxidation reactions obtained using the three different kinetic models as a function of fuel flow-rate.

The model by Harvey et al. [58] predicts that the fuel mixture is close to equilibrium even at 750°C. As a result the flow-rate has little effect on the Nernst

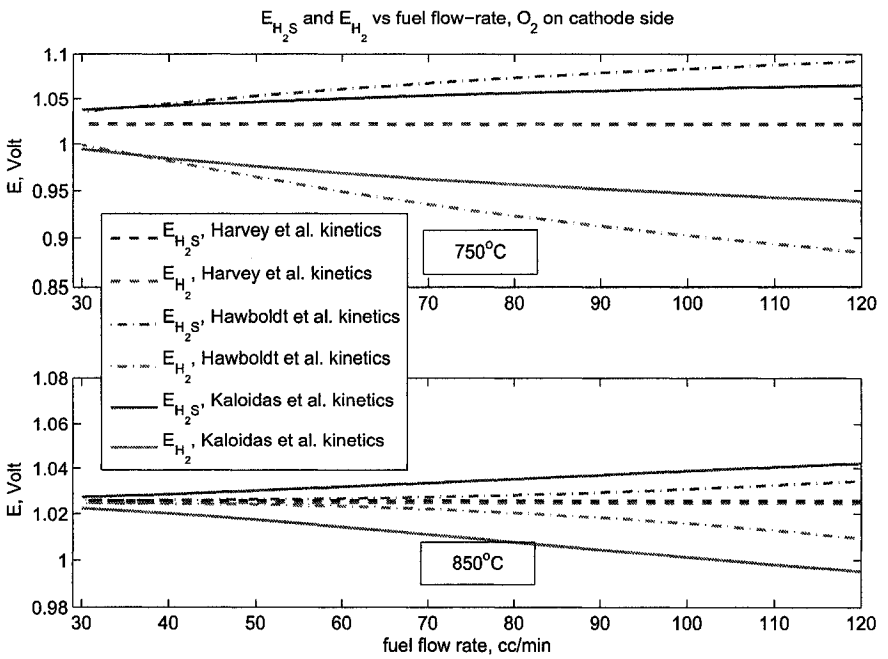

Figure 7.2: Predicted E_{H_2S} and E_{H_2} using different H_2S dissociation models

potentials which both approach the equilibrium value. Both the Hawboldt model [59] and the Kaloidas model [67] show a flow-rate dependence for the Nernst potentials. This indicates that the Harvey kinetics are much "faster" than the other two models. I will use the model by Kaloidas, et al. [67] in the rest of this Chapter. The reasons why I chose their model over the Hawboldt model are listed below, and all of them point to the experimental operating conditions given in Kaloidas, et al. [67] being closer to ours.

1. The Kaloidas model was generated using data that spans the temperature range I am interested in. The temperature range for the Kaloidas data was 600–860°C range while that for the data used by Hawboldt et al. [59] was 850–1150°C and the range for the data used by Harvey et al. [58] was 1077–1327°C.

2. Kaloidas, et al. [67] fit their kinetic model using a non-isothermal model taking the temperature profile along the reactor into account, whereas Hawboldt, et al. [59] used an isothermal model.

3. Kaloidas, et al. [67] used an alumina tubular reactor, while Hawboldt, et al. used a coiled quartz reactor.

4. Kaloidas, et al. ran their experiments using undiluted H_2S (99.6%), while Hawboldt, et al. used dilute H_2S (0.5–2.5%). All of our experiments were at concentrations higher than the ones used by Hawboldt, et al.

7.6 Simulations for single fuel OCV

In this section I take up the discussion from section 6.2.2, where I speculated on how the operating conditions affect open circuit voltage when the fuel is not at chemical equilibrium.

The results in this section were generated by calculating the average of the Nernst potentials E_{H_2S} and E_{H_2} (defined by equations 6.11 and 6.12) over the anode-electrolyte interface for the inlet compositions and operation temperatures specified. The electrochemical kinetic constants $i^{\circ}_{a,\,H_2S}$, $i^{\circ}_{a,\,H_2}$ and i°_{c} are all set to zero to freeze all the electrochemical reactions.

7.6.1 Effect of fuel flow-rate on OCV

Figure 7.3 compares the model predictions for the Nernst voltages E_{H_2S}, E_{H_2} as a function of flow-rate against the experimental data first presented in Chapter 5. The trend in the experimental data sets of increasing OCV with increase in flow-rate is captured very well by the model results for E_{H_2S}. As expected from the discussion in section 6.2.2, E_{H_2} decreases with increasing flow-rate. If the fuel were at equilibrium, the flow-rate would have no effect on OCV and E_{H_2S} and E_{H_2} would be equal (section 6.2).

The open circuit voltages for the same fuel compositions were higher by 12 to 17 millivolts in data set 2 (compared to data set 1). A possible reason for the OCV difference between data sets, and the offset between the experimental data and the model predictions for E_{H_2S} could be a small air leak either in the fuel inlet line or in the cell sealing.

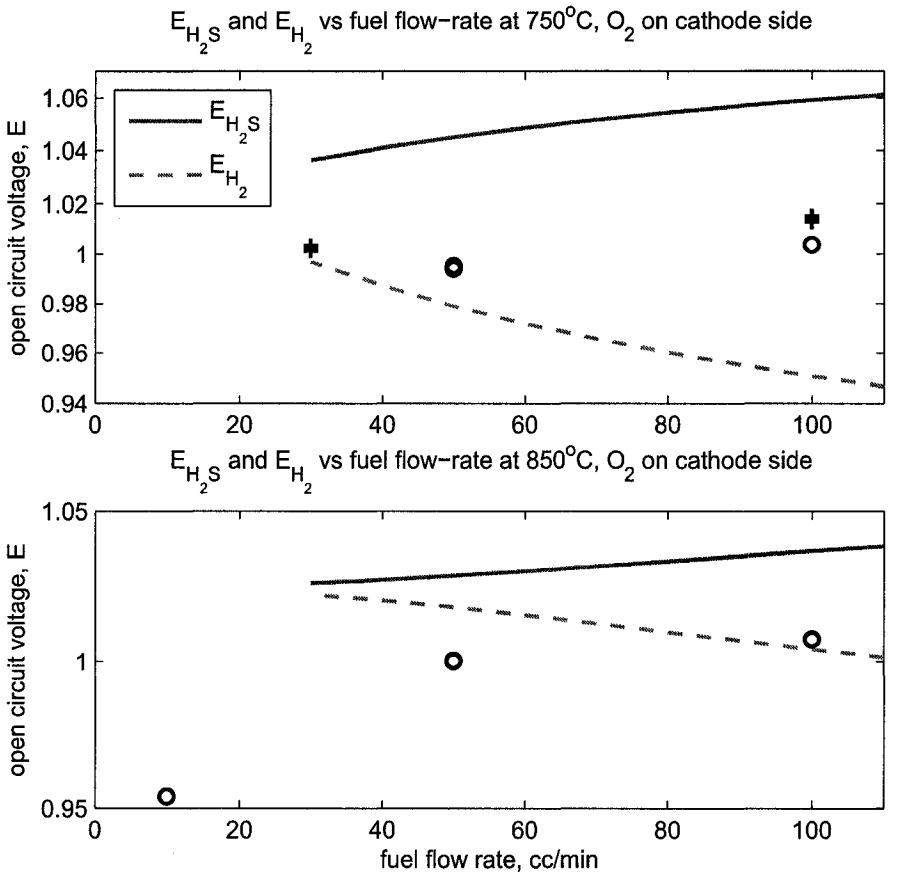

Figure 7.3: Predicted E_{H_2S} and E_{H_2}, and experimental OCV values as a function of fuel flow-rate; O $\rightarrow$ experimental data set 1, + $\rightarrow$ experimental data set 2

7.6.2 Effect of $y_{H_2S,\,in}$ on OCV

For both the experimental data as well as the simulations discussed here, the total fuel flow-rate (dry basis) was held at 100 ml/min.

Figure 7.4 compares the model predictions for the Nernst voltages E_{H_2S}, E_{H_2} as a function of inlet H_2S mole fraction in a mixture of H_2S and N_2 against experimental data. The trend of decreasing OCV with decreasing $y_{H_2S,\,in}$ is matched by both E_{H_2S} and E_{H_2}. However, the offset between E_{H_2} and the experimental data is different at each temperature. Also, the E_{H_2} values lie below the experimental values, and the open circuit voltage for a cell can never be lower than the theoretical Nernst potential. The offset between E_{H_2S} and the experimental data is much more consistent between operation at the three temperatures with E_{H_2S} greater

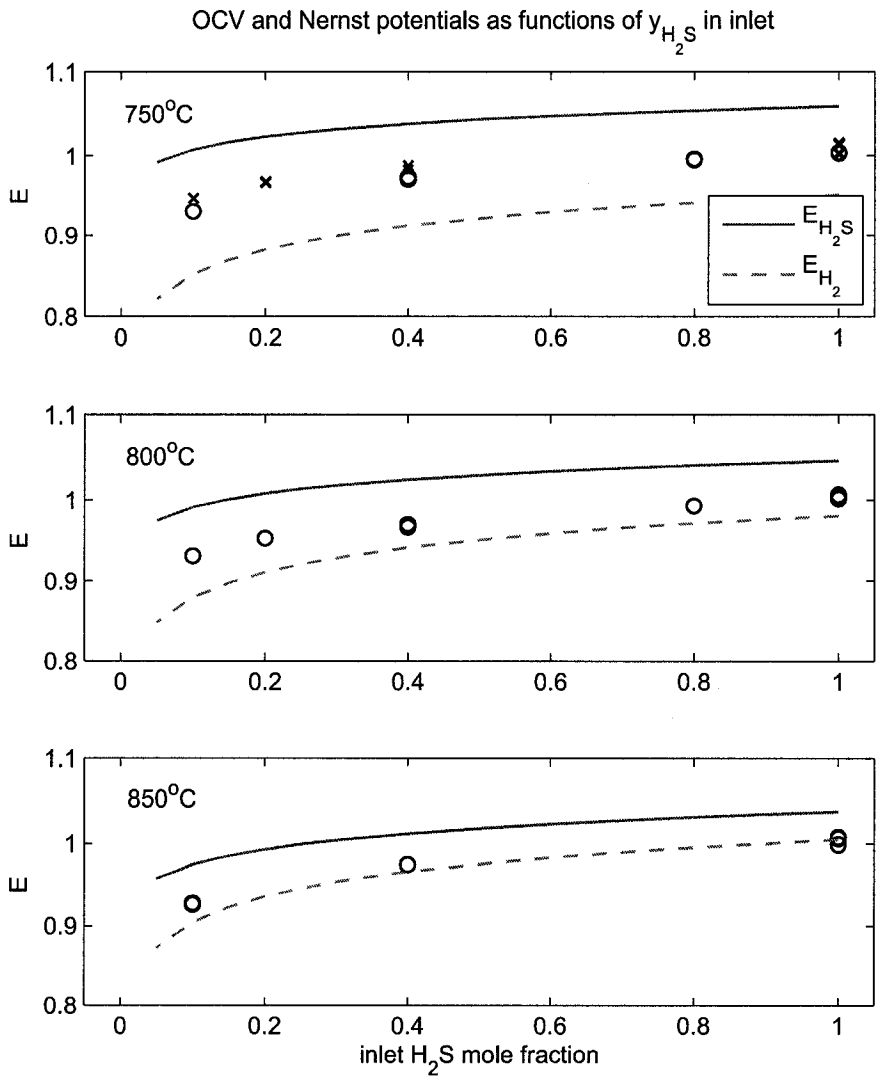

Figure 7.4: Predicted E_{H_2S} and E_{H_2}, and experimental OCV values as a function of inlet fuel y_{H_2S}; O → experimental data set 1, × → experimental data set 2

than the measured OCV values by 55–75 mV at 750°C, by 45–60 mV at 750°C, and by 30–50 mV at 850°C.

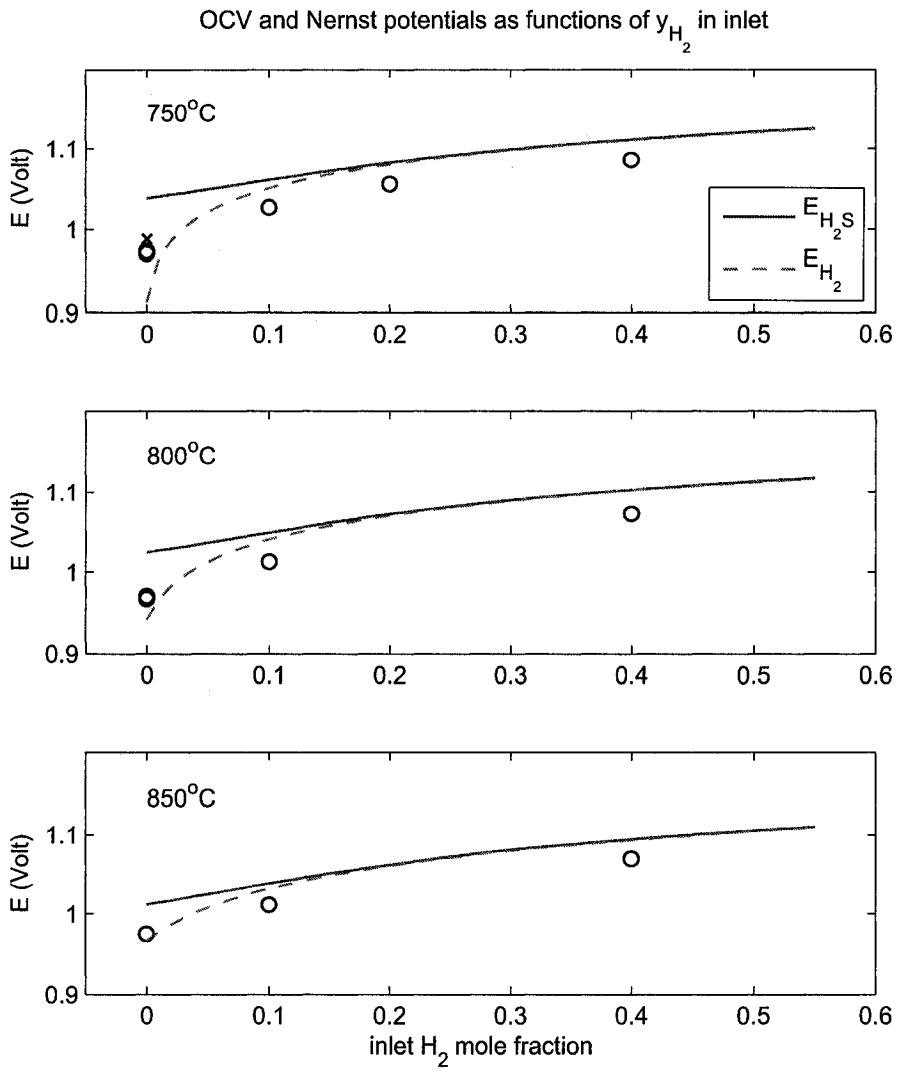

Figure 7.5: Predicted E_{H_2S} and E_{H_2}, and experimental OCV values as a function of $y_{H_2,\text{in}}$, $y_{H_2S,\text{in}} = 0.4$; O $\rightarrow$ experimental data set 1, $\times \rightarrow$ experimental data set 2

7.6.3 Effect of $y_{H_2,\text{in}}$ on OCV

For both the experimental data as well as the simulations discussed here, the total fuel flow-rate (dry basis) was held at 100 ml/min. The dry H_2S flow-rate was held constant at 40 ml/min ($y_{H_2S,\text{in}} = 0.4$).

In figure 7.5, I compare the model predictions for E_{H_2S}, E_{H_2} as a function of inlet H_2 mole fraction in a mixture of H_2S, H_2 and N_2 against experimental data. Again, the trend in the experimental data of increasing OCV with increase in $y_{H_2,\,in}$ is followed by both E_{H_2S} and E_{H_2}.

The E_{H_2S} and E_{H_2} values are very close to each other for $y_{H_2,\,in} > 0.15$. This is to be expected, because as H_2 content in the fuel is increased, the equilibrium dissociation of H_2S goes down drastically (see figure 6.1 and the discussion in 6.1.3). The lower the equilibrium extent of reaction, the quicker the approach to equilibrium. Thus, the reaction is no longer kinetically controlled as it is close to equilibrium, as seen here for $y_{H_2,\,in} > 0.15$.

For $y_{H_2,\,in} < 0.15$ in figure 7.5, E_{H_2} drops sharply, an effect not seen in the experimental data. Again, the offset between E_{H_2S} and the experimental data is more consistent at all three temperatures.

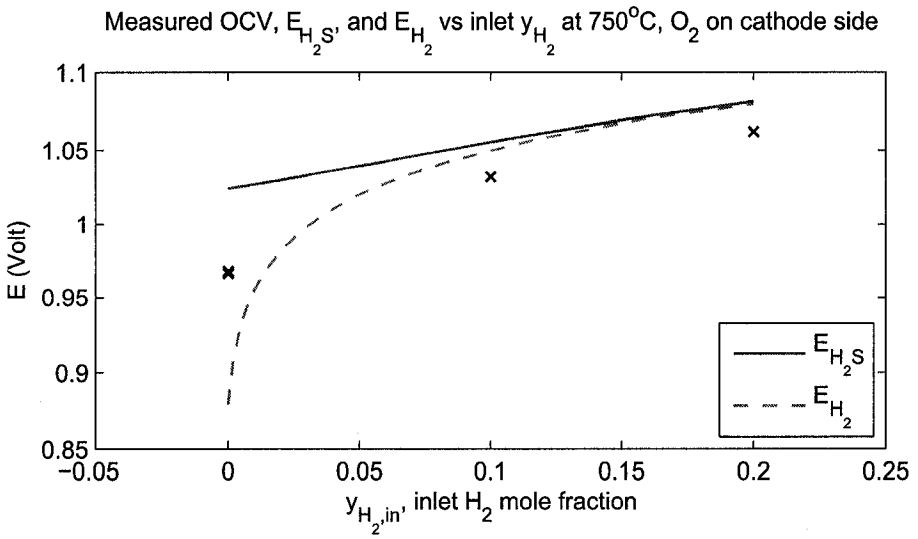

Figure 7.6: Predicted E_{H_2S} and E_{H_2}, and experimental OCV values (data set 1) as a function of $y_{H_2,\,in}$, $y_{H_2S,\,in} = 0.2$

Figure 7.6 compares the model predictions for E_{H_2S}, E_{H_2} as a function of inlet H_2 mole fraction in a mixture where $y_{H_2S,\,in} = 0.2$ against experimental values from data set 2. The discussion above for simulations and experimental values with $y_{H_2S,\,in} = 0.4$ is also valid for the data in this figure, and E_{H_2S} captures the trend in the experimental data much better than E_{H_2}.

From the analysis in section 6.2.2 and the discussion above, it seems more likely that electro-oxidation of H_2S is the primary reaction on the anode.

7.7 i^o estimation from $i - V$ curves

Thus far in this Chapter, I have discussed model results where the electrochemical reactions are assumed to be in equilibrium. To model the $i-V$ performance curves for a fuel cell I need electrochemical kinetic parameters. In this section, I present some results for parameter estimation of the above kinetic parameters. I then discuss the validity of these parameters by comparing the parameters estimated from $i - V$ curves for a range of operating conditions.

I estimated the electrochemical kinetic parameters using a very similar procedure to that in Chapter 4. The model used for the estimation described below is a 1-D model that solves only the mass transfer and charge transport equations in the fuel cell electrodes and electrolyte. The inlet mass fractions for this 1-D model are obtained by averaging the mass fractions at the electrode–fuel channel interface from a solution of the full 2-D axi-symmetric model described in section 7.2. The 1-D model is used to reduce computation time for the parameter estimation. This simplification is justified when the fuel and air flow-rates are high enough (the reader is referred to the discussion in section 4.9.2). The fuel and oxygen flow-rate is high (100 standard ml/min) in the $i-V$ data sets for which I run the parameter estimation. At this flow-rate, the resistance to mass transfer in the fuel channel is low enough that by using the local concentrations of the fuel components from the 2-D model solution at open circuit, I can solve for the $i - V$ curve using the 1-D model. Later in this section, I will validate this assumption by comparing the solutions for the two models using identical parameters.

The data pre-treatment before it is sent to the estimation algorithm is as follows.

1. The $i-V$ data is filtered first to remove any obvious artifacts. For the $i-V$ curves dicussed in Chapter 5, the only feature removed was a kink or hook near the OCV. A close-up of the OCV region for one of the $i - V$ curves is shown in figure 7.7.

2. Current density values are interpolated for an equally spaced vector of voltage values to get a $i - V$ matrix of a manageable size. For the models used to estimate parameters, the i vector was defined by either 6 or 18 equally spaced points that spanned the entire range for each particular $i - V$ curve.

The formulation of the parameter estimation problem is given below (7.62).

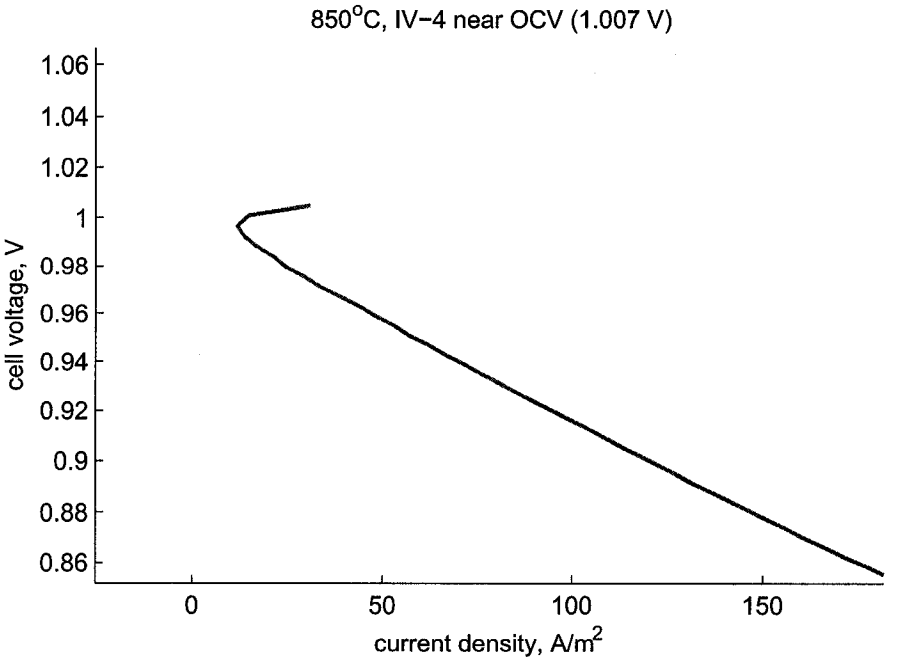

Figure 7.7: Near OCV region with the kink artifact for iV-4 at 850°C

$$\min_{\mathbf{x}} \sum_{k=1}^{n} \{i_{\mathrm{m}}(V_k, T) - i_{k,T}\}^2 \tag{7.62}$$

subject to:

$$i_{\mathrm{m}} = \mathbf{g}\left(V, T, \mathbf{x}, \mathbf{p}^*\right) \tag{7.63}$$

$$\mathbf{x}_l \leq \mathbf{x} \leq \mathbf{x}_u \tag{7.64}$$

$i_{\mathrm{m}}(V_k, T)$ is the output cell current density given by the model for a cell voltage of V_k at temperature T, $i_{k,T}$ is the experimentally observed current density for the same cell voltage of V_k, and n is the number of equally spaced points along the $i-V$ curve. The vector $\mathbf{x}$ is the vector of unknown electrochemical kinetic constants estimated by the minimization, and $\mathbf{x}_l, \mathbf{x}_u$ are the lower and upper bounds for these parameters. The vector $\mathbf{p}^*$ represents the known parameters needed to solve the model for i_{m}. The function $\mathbf{g}()$ represents the fuel cell model.

To assess the quality of the fit between the experimental data and simulated

data using the output parameter estimates, I use the scalar defined in equation (7.65). The lower the value for 'Scaled fit', the closer the match between the model simulations and the experimental data.

$$\text{Scaled fit} = \frac{\sqrt{\sum (i_m - i_k)^2 / n}}{\max(i_k)} \tag{7.65}$$

As seen in figures 7.4 and 7.5, there is an offset between the measured OCV values and the simulated Nernst potentials E_{H_2S}, E_{H_2}. Within the parameter estimation, I shift the entire experimental $i-V$ curve vertically so that the shifted experimental OCV coincides with the simulated OCV. This correction is only applied when the OCV from the simulation is higher than the experimental OCV, and is done to remove the offset in OCV tentatively attributed to a small air leak on the fuel side[1].

7.7.1 Parameter estimation results

I ran the parameter estimation for three different parameter combinations:

1. $i^o_{H_2S}$ and $i^o_{O_2}$ i.e., only H_2S is oxidized on the anode.
2. $i^o_{H_2}$ and $i^o_{O_2}$ i.e., only H_2 is oxidized on the anode.
3. $i^o_{H_2S}$, $i^o_{H_2}$, and $i^o_{O_2}$ i.e., both H_2S and H_2 are oxidized on the anode.

Case 1: $i^o_{H_2S}$ and $i^o_{O_2}$

I start by discussing the parameter estimates for case 1. The $i^o_{H_2S}$, $i^o_{O_2}$ values estimated from data where the fuel flows were $[100-0-0]$ (humidified H_2S) are given in table 7.3 for all three operation temperatures. This table shows how the estimated parameters change with time as well as how they change with increasing temperature. The scaled fit values are significantly worse at 750°C than at the other temperatures. At $T = 750$°C, both $i^o_{H_2S}$ and $i^o_{O_2}$ increase with time to reflect the activation behaviour discussed in section 5.5.2. The deactivation of the cell at 850°C is reflected in a noticeable reduction in $i^o_{O_2}$, while $i^o_{H_2S}$ is largely unaffected.

[1] See section 7.6.1

Table 7.3: Time dependence of cell performance reflected in estimated $i^{\circ}_{H_2S}$ and $i^{\circ}_{O_2}$

Time (hh:mm)	T (°C)	IV (#)	$i^{\circ}_{H_2S}$ (A/m^2)	$i^{\circ}_{O_2}$ (A/m^2)	Scaled fit –
1:38		6	1.13×10^3	4.93×10^1	3.47×10^{-2}
4:33	750	11	1.45×10^3	6.37×10^1	2.30×10^{-2}
6:25		15	1.62×10^3	7.17×10^1	1.80×10^{-2}
7:24		1	1.30×10^3	3.38×10^2	2.66×10^{-3}
10:10	800	7	1.20×10^3	6.68×10^2	4.30×10^{-3}
21:50		8	1.14×10^3	6.00×10^2	2.78×10^{-3}
23:38		10	1.33×10^3	6.72×10^2	3.02×10^{-3}
24:24		11	1.31×10^3	6.33×10^2	2.92×10^{-3}
29:56		4	1.42×10^3	1.40×10^3	6.83×10^{-3}
30:15	850	5	1.43×10^3	1.30×10^3	6.68×10^{-3}
30:38		6	1.41×10^3	1.22×10^3	6.67×10^{-3}
33:33		12	1.32×10^3	1.06×10^3	7.80×10^{-3}
34:16		14	1.32×10^3	8.80×10^2	7.35×10^{-3}
47:52		16	1.87×10^3	1.19×10^2	1.15×10^{-2}

The $i^{\circ}_{H_2S}$ and $i^{\circ}_{O_2}$ values estimated using data with inlet fuel composition other than $[100 - 0 - 0]$ are quite different. The parameter estimates for varying H_2S content in a mixture of H_2S and N_2 are given in table 7.4 while those for varying H_2 content in a mixture of H_2S, H_2, and N_2 are given in table 7.5.

In table 7.4, at all three temperatures, both the $i^{\circ}_{H_2S}$ and the $i^{\circ}_{O_2}$ estimates increase as the H_2S content in the fuel is decreased. For instance, at 750°C $i^{\circ}_{H_2S}$ goes from 1128 A/m^2 to 2928 A/m^2 as the fuel flow-rates change from $[100-0-0]$ to $[40-60-0]$. Although this increase is partly due to the cell activation behaviour, by comparing estimates for IV-10 and IV-11, one can see that the value for $i^{\circ}_{H_2S}$ drops to 1447 from 2928 A/m^2 as the inlet fuel flows are changed back to $[100-0-0]$ from $[40 - 60 - 0]$.

The $i^{\circ}_{H_2S}$ estimates at all three temperatures increase as the H_2 content in the fuel is increased. As shown in table 7.5, $i^{\circ}_{H_2S}$ increases further from 2928 A/m^2 to 4388 A/m^2 as H_2 is added to change the fuel flow-rates from $[40 - 60 - 0]$ to $[40 - 20 - 40]$. The $i^{\circ}_{O_2}$ estimates are not affected as dramatically at 750°C, but neither are they completely independent of changes in inlet y_{H_2}. At 800 and 850°C however, $i^{\circ}_{O_2}$ decrease dramatically with increasing H_2 in the fuel.

Parameter estimates for y_{H_2S} content lower than 40% differ considerably from

Table 7.4: Dependence of cell performance on y_{H_2S} reflected in estimated $i^o_{H_2S}$ and $i^o_{O_2}$

$[H_2S - N_2 - H_2]$ (ml/min)	Time (hh:mm)	T (°C)	IV (#)	$i^o_{H_2S}$ (A/m^2)	$i^o_{O_2}$ (A/m^2)	Scaled fit –
$[100 - 0 - 0]$	1:38		6	1.13×10^3	4.93×10^1	3.47×10^{-2}
$[80 - 20 - 0]$	2:12	750	7	1.44×10^3	5.40×10^1	2.92×10^{-2}
$[40 - 60 - 0]$	3:52		10	2.93×10^3	6.84×10^1	1.77×10^{-2}
$[100 - 0 - 0]$	4:33		11	1.45×10^3	6.37×10^1	2.30×10^{-2}
$[100 - 0 - 0]$	7:24		1	1.30×10^3	3.38×10^2	2.66×10^{-3}
$[80 - 20 - 0]$	8:12	800	2	1.16×10^3	3.79×10^2	2.17×10^{-3}
$[40 - 60 - 0]$	8:49		3	2.18×10^3	5.46×10^2	1.66×10^{-3}
$[100 - 0 - 0]$	10:10		7	1.20×10^3	6.68×10^2	4.30×10^{-3}
$[100 - 0 - 0]$	24:24		11	1.31×10^3	6.33×10^2	2.92×10^{-3}
$[10 - 90 - 0]$	24:47		12	1.61×10^4	1.86×10^2	2.57×10^{-2}
$[20 - 80 - 0]$	25:46		13	8.38×10^3	3.33×10^2	1.54×10^{-2}
$[100 - 0 - 0]$	30:38		6	1.41×10^3	1.22×10^3	6.67×10^{-3}
$[40 - 60 - 0]$	31:08	850	7	2.15×10^3	1.13×10^5	3.13×10^{-3}
$[10 - 90 - 0]$	32:41		10	1.34×10^4	3.01×10^2	2.08×10^{-2}
$[100 - 0 - 0]$	33:33		12	1.32×10^3	1.06×10^3	7.80×10^{-3}

i^o estimates for higher y_{H_2S}. The scaled fit values for these estimates are also worse than for other sets at the same temperature. The estimated parameter scaled fit improves with the addition of H_2 to the fuel mixture.

Case 2: $i^o_{H_2}$ and $i^o_{O_2}$

As in case 1, $i^o_{H_2}$ and $i^o_{O_2}$ values reflect the cell activation (at 750°C) and deactivation (at 850°C) behaviour[2]. The estimated $i^o_{H_2}$ values increase from 4168 A/m^2 to 9765 A/m^2, while the $i^o_{O_2}$ values increase from 67 A/m^2 to 99 A/m^2, as the inlet fuel flows change from $[100 - 0 - 0]$ to $[40 - 60 - 0]$. This increase in $i^o_{H_2}$ and $i^o_{O_2}$ is similar to that seen for $i^o_{H_2S}$ and $i^o_{O_2}$ in case 1.

Unlike case 1 where $i^o_{H_2S}$ increased further with the addition of H_2, $i^o_{H_2}$ at 750°C in case 2 decreased from 9765 A/m^2 to 499 A/m^2 when the fuel is changed from $[40-60-0]$ to $[40-20-40]$. Again, $i^o_{O_2}$ are also affected, showing a decrease from 99 A/m^2 to 51 A/m^2. The trends for both $i^o_{H_2}$ and $i^o_{O_2}$ are similar at the other two temperatures.

[2]Tables of the parameter estimates for case 2 are in appendix C

Table 7.5: Dependence of cell performance on y_{H_2} reflected in estimated $i^{\circ}_{H_2S}$ and $i^{\circ}_{O_2}$

$[H_2S - N_2 - H_2]$ (ml/min)	Time (hh:mm)	T (°C)	IV (#)	$i^{\circ}_{H_2S}$ (A/m^2)	$i^{\circ}_{O_2}$ (A/m^2)	Scaled fit –
[40 – 60 – 0]	3:52		10	2.93×10^3	6.84×10^1	1.77×10^{-2}
[40 – 50 – 10]	5:05	750	12	3.34×10^3	6.44×10^1	1.81×10^{-2}
[40 – 40 – 20]	5:25		13	3.78×10^3	6.28×10^1	2.07×10^{-2}
[40 – 20 – 40]	6:02		14	4.39×10^3	6.24×10^1	2.30×10^{-2}
[100 – 0 – 0]	6:25		15	1.62×10^3	7.17×10^1	1.80×10^{-2}
[40 – 60 – 0]	8:49		3	2.18×10^3	5.46×10^2	1.66×10^{-3}
[40 – 50 – 10]	9:31	800	5	2.68×10^3	5.17×10^2	3.09×10^{-3}
[40 – 20 – 40]	9:52		6	6.05×10^3	2.32×10^2	1.31×10^{-3}
[100 – 0 – 0]	10:10		7	1.20×10^3	6.68×10^2	4.30×10^{-3}
[20 – 80 – 0]	25:46		13	8.38×10^3	3.33×10^2	1.54×10^{-2}
[20 – 60 – 20]	26:14		14	9.60×10^3	4.19×10^2	6.08×10^{-3}
[40 – 60 – 0]	31:08		7	2.15×10^3	1.13×10^5	3.13×10^{-3}
[40 – 50 – 10]	31:40	850	8	2.40×10^3	1.82×10^3	6.09×10^{-3}
[40 – 20 – 40]	32:03		9	4.94×10^3	3.47×10^2	3.11×10^{-3}
[10 – 90 – 0]	32:41		10	1.34×10^4	3.01×10^2	2.08×10^{-2}
[10 – 80 – 10]	33:05		11	9.41×10^3	7.54×10^2	2.37×10^{-3}
[100 – 0 – 0]	33:33		12	1.32×10^3	1.06×10^3	7.80×10^{-3}

Case 3: $i^{\circ}_{H_2S}$, $i^{\circ}_{H_2}$, and $i^{\circ}_{O_2}$

In case 3 I estimate both $i^{\circ}_{H_2S}$ and $i^{\circ}_{H_2}$, thus allowing the model to consider the electro-oxidation of both H_2S and H_2[3].

As in cases 1 and 2, the activation of the cell at 750°C is seen in an increase in all parameter estimates with time, and the deactivation at 850°C is apparent in the decrease seen in $i^{\circ}_{O_2}$.

Table C.4 shows how some of the parameter estimates are identical to those for case 1 or case 2. There are also many instances where the values of scaled fit are almost identical between several distinct sets of parameters. I give some examples in table 7.6. On closer examination, one can see that the $i^{\circ}_{O_2}$ values are very close to each other in these sets of estimates, while the $i^{\circ}_{H_2S}$ and $i^{\circ}_{H_2}$ values vary over a wide range, one increasing in value if the other decreases. This means that for all the composition effects examined below, finding trends for the $i^{\circ}_{H_2S}$ and

[3]Tables of the parameter estimates for case 3 are in appendix C

Table 7.6: Sets of estimated $i^o_{H_2S}$, $i^o_{H_2}$, and $i^o_{O_2}$ that fit the $i - V$ data equally well

T (°C)	IV (#)	$i^o_{H_2S}$ (A/m^2)	$i^o_{H_2}$ (A/m^2)	$i^o_{O_2}$ (A/m^2)	Scaled fit –
750	15	6.96×10^2	1.89×10^3	6.82×10^1	1.812×10^{-2}
		1.62×10^3	0	7.17×10^1	1.823×10^{-2}
800	11	8.80×10^2	7.20×10^2	6.33×10^2	2.914×10^{-3}
		7.16×10^2	1.02×10^3	6.35×10^2	2.917×10^{-3}
		1.24×10^3	1.04×10^2	6.33×10^2	2.920×10^{-3}
850	6	8.36×10^2	8.91×10^2	1.21×10^3	6.660×10^{-3}
		8.88×10^2	8.08×10^2	1.21×10^3	6.660×10^{-3}
		5.98×10^2	1.27×10^3	1.21×10^3	6.662×10^{-3}
		1.41×10^3	0	1.22×10^3	6.668×10^{-3}

$i^o_{H_2}$ estimates is not possible.

The $i^o_{O_2}$ estimates at all three temperatures increase as the H_2S content in the fuel is decreased (table C.3).

The $i^o_{O_2}$ estimates at all three temperatures decrease as the H_2 content in the fuel is increased (table C.4).

Summary of the i^o estimation results

I ran all parameter estimation routines using the function *lsqnonlin* in the MATLAB Optimization Toolbox [131]. The parameter estimation using 6 points along the $i - V$ curve for cases 1 and 2 took between 10 minutes to a few hours for each $i - V$ curve on a computer cluster[4] with AMD Opteron 2 GHz processors. Parameter estimation for case 3 took approximately three times longer.

I summarize the i^o estimation results here to assess the usefulness of the parameter estimates. For all three cases, the cell activation and deactivation seen in the $i - V$ data, and first discussed in Chapter 5 is reflected in the parameter estimates. Although the trends in the estimates have already been described, I discuss the composition dependence of the estimates below, and attempt to describe the temperature dependence of the i^o estimates using an Arrhenius analysis.

For all three cases considered, changes in fuel and oxidant (not shown) composition lead to changes in both the anodic and cathodic exchange current densities. This indicates that the electrochemical rate equations I use are not completely

[4]All parameter estimation runs were single processor processes.

Table 7.7: Arrhenius parameters estimated for i^o using case 1 estimates

	A (A/m^2)	E $(KJ/mole)$
$i^o_{H_2S}$	323	-13.2
$i^o_{O_2}$	2.07×10^{16}	285

correct. I know that the electrochemical rate equations are simplified overall representations of complex multi-step processes at the electrodes (e.g., the mechanism outlined in section 3.2.1). Thus, it is not surprising that an investigation of fuel composition effects leads to the conclusion that the rate equations used here are inadequate. One possibility is that the reaction orders or the charge transfer coefficients in the electrochemical kinetic equations are incorrect, and that by fitting these one can get more consistent results for the other kinetic parameters. However, that would lead to too many fitting parameters, which is undesirable. In my analysis, using three parameters resulted in sets of very different estimates that fit the data equally well. For instance, table 7.6 shows that for case 3, several parameter sets fit the $i - V$ data equally well.

For the Arrhenius analysis, I chose the case 1 parameter estimates for $i - V$ curves 750–15, 800–10, and 850–4 (given in table 7.3). These $i - V$ curves showed the highest performance at the three operating temperatures. The $i^o_{H_2S}$ estimates for all three temperatures stay within 20% of the value at 750°C, and the values at 800 and 850°C are actually lower than the value at 750°C giving a negative Arrhenius activation energy (table 7.7). On the other hand, estimates for $i^o_{O_2}$ increase dramatically with increase in temperature. The $i^o_{O_2}$ value at 800°C is over nine times the value at 750°C, while the $i^o_{O_2}$ value at 850°C is just over twice as large as the value at 800°C. The Arrhenius plot for the above data is given in figure 7.8. This plot gives the i^o *vs.* 1/T curves obtained with pre-exponentials and activation energies calculated using the optimal $i^o_{H_2S}$ and $i^o_{O_2}$. The plot also shows the actual optimal values for the exchange current densities used to calculate the least squares fitted values for the pre-exponential factors and activation energies, which are given in table 7.7.

I could have chosen other parameter sets from case 2 or case 3 to get similar estimates for the activation energies of the i^o. Although it is tempting to conclude that the anode-side electrochemical kinetics are temperature independent while the cathode kinetics are not, the sensitivity of the estimates to inlet compositions

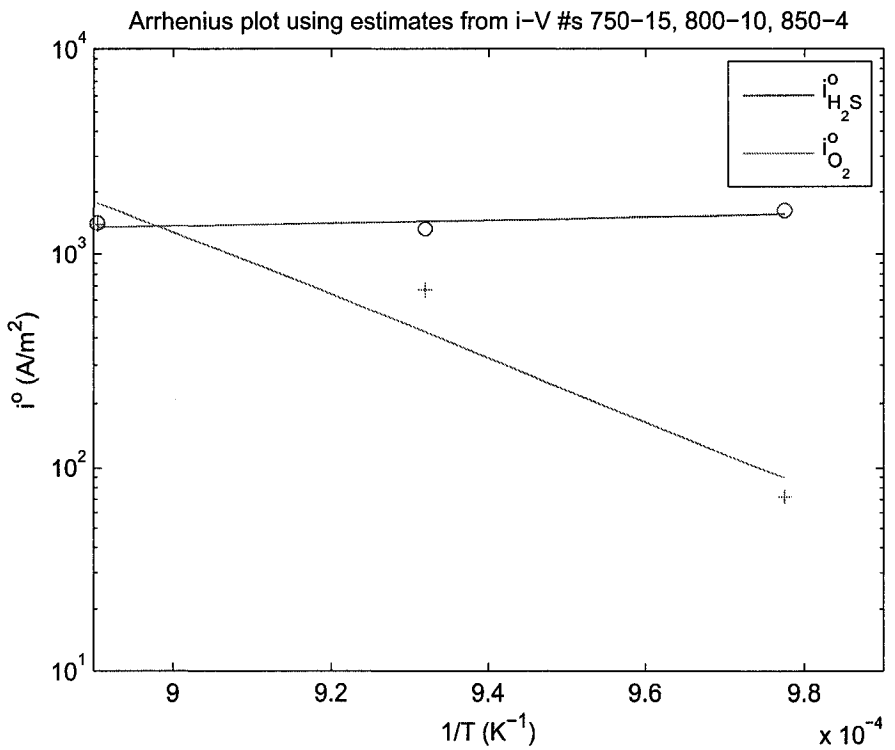

Figure 7.8: Arrhenius plot for $i^{\circ}_{H_2S}$ and $i^{\circ}_{O_2}$ from case 2 estimates

indicates that the electrochemical rate equations do not model the kinetics adequately. Thus, it would be imprudent to use the parameter estimates for the electrochemical rate constants to make any conclusions. In other words, I feel that this analysis of the $i - V$ curves cannot be used to point to whether H_2S or H_2 or both are utilized as fuel.

However, the estimates for the exchange current densities obtained here can be used to complete the model definition, and thus use it for some limited validation against experimental data, as well as for parametric studies. In the next section I look at how the model predictions compare against the experimental data.

7.8 Case studies: model predictions and capabilities

In this section I present some case studies to compare model predictions against experimental data from Chapter 5, and to illustrate the capabilities of the models developed. All simulations in this section are done at $T = 850°C$. I use the first and the last set of i^o values estimated for IV–850–6 from table 7.6. This allows me to compare the effect of allowing electro-oxidation of both H_2 and H_2S (case 3 in the parameter estimation study, previous section) *vs* only allowing the electro-oxidation of H_2S (case 1 in the previous section). The title (or text within the plot) for all the plots in this section lists the i^o parameters used.

7.8.1 1-D and 2-D model output vs experimental data

Figure 7.9 compares experimental $i-V$ data IV–850–6 against 1–D and 2–D model output using estimated i^o values. The 1–D and 2–D models give nearly identical output thus validating the use of the 1–D model for the parameter estimation. One can clearly see that the model OCV values are higher than the experimental OCV. This OCV offset is greater for case 1 than for case 3 because the OCV for case 3 is a mixed OCV.

7.8.2 Cathode side gas composition, air vs O_2

Figure 7.10 and table 7.8 compare experimental $i-V$ data and 2–D model predictions using air as oxidant against those using O_2 as oxidant. The model predictions show a similar change in the $i-V$ curve and the OCV as the experimental data (IV–850–3 and IV–850–4).

Table 7.8: Using air vs O_2: model predictions vs experimental data

	Air on cathode		O_2 on cathode	
	OCV (V)	i_{0V} (A/m^2)	OCV (V)	i_{0V} (A/m^2)
Experimental	0.970	1785	1.007	1925
2-D model, H_2S	1.001	1808	1.039	1958
2-D model, H_2S & H_2	0.986	1770	1.024	1918

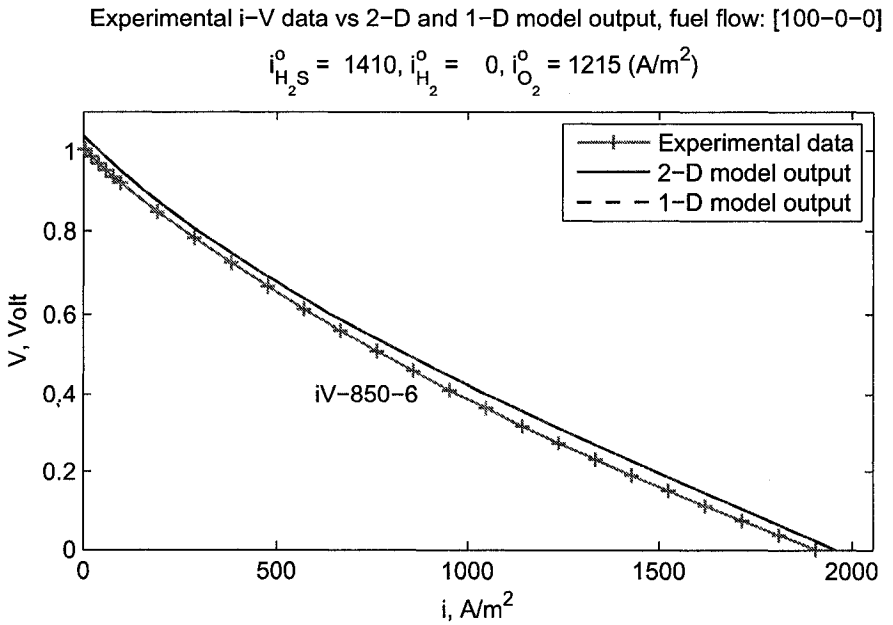

(a) Case 1

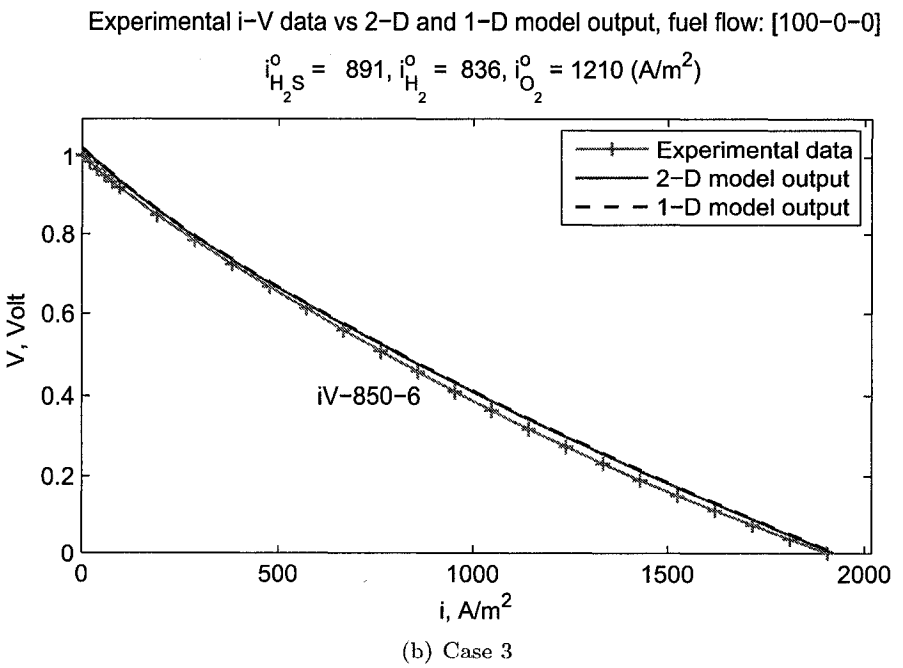

(b) Case 3

Figure 7.9: Experimental $i - V$ data and model output

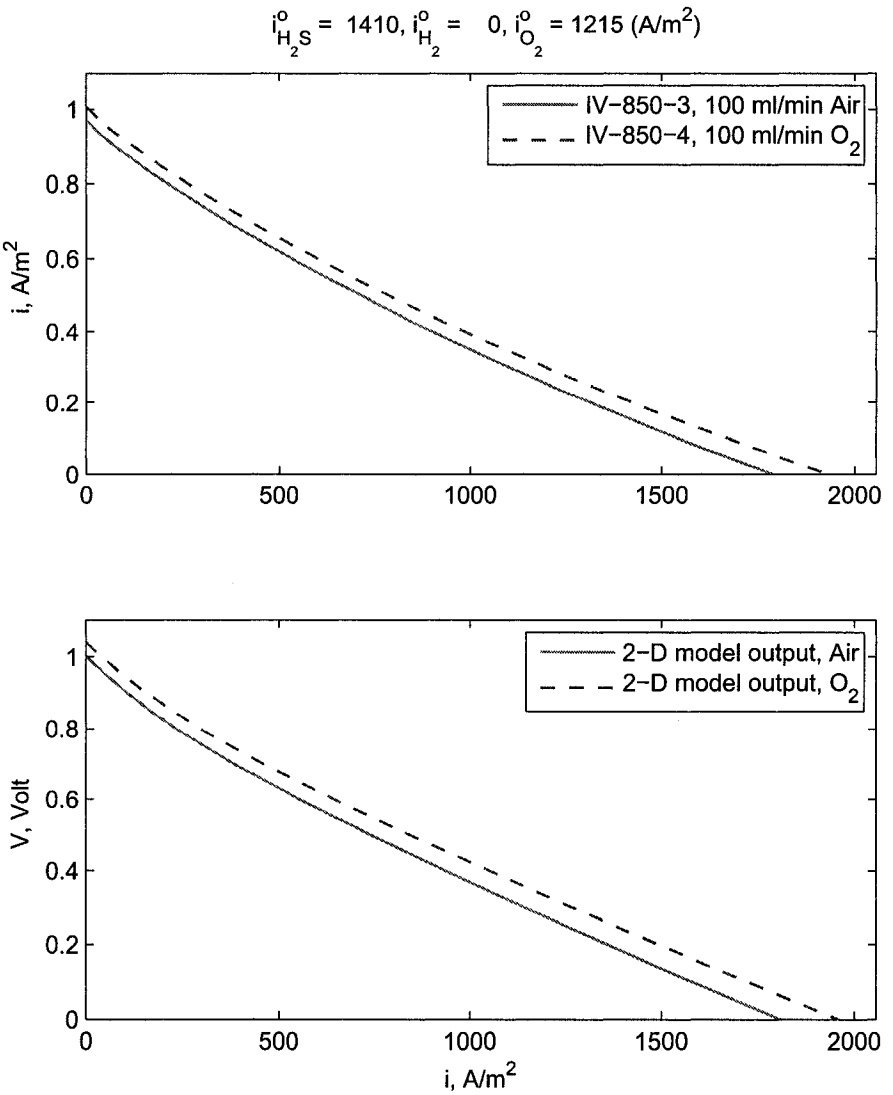

Figure 7.10: Experimental $i - V$ data and 2–D model output; air vs O_2

7.8.3 Fuel flow-rate

Figure 7.11 and table 7.9 compare experimental $i - V$ data and 2–D model predictions for fuel flow-rates of 50 ml/min and 100 ml/min. The model predicts that the $i - V$ curve does not change by much with this change in flow. It is difficult to make any distinction between the model output for the two different fuel flows by visual examination of the model output. From the data in table 7.9, some differ-

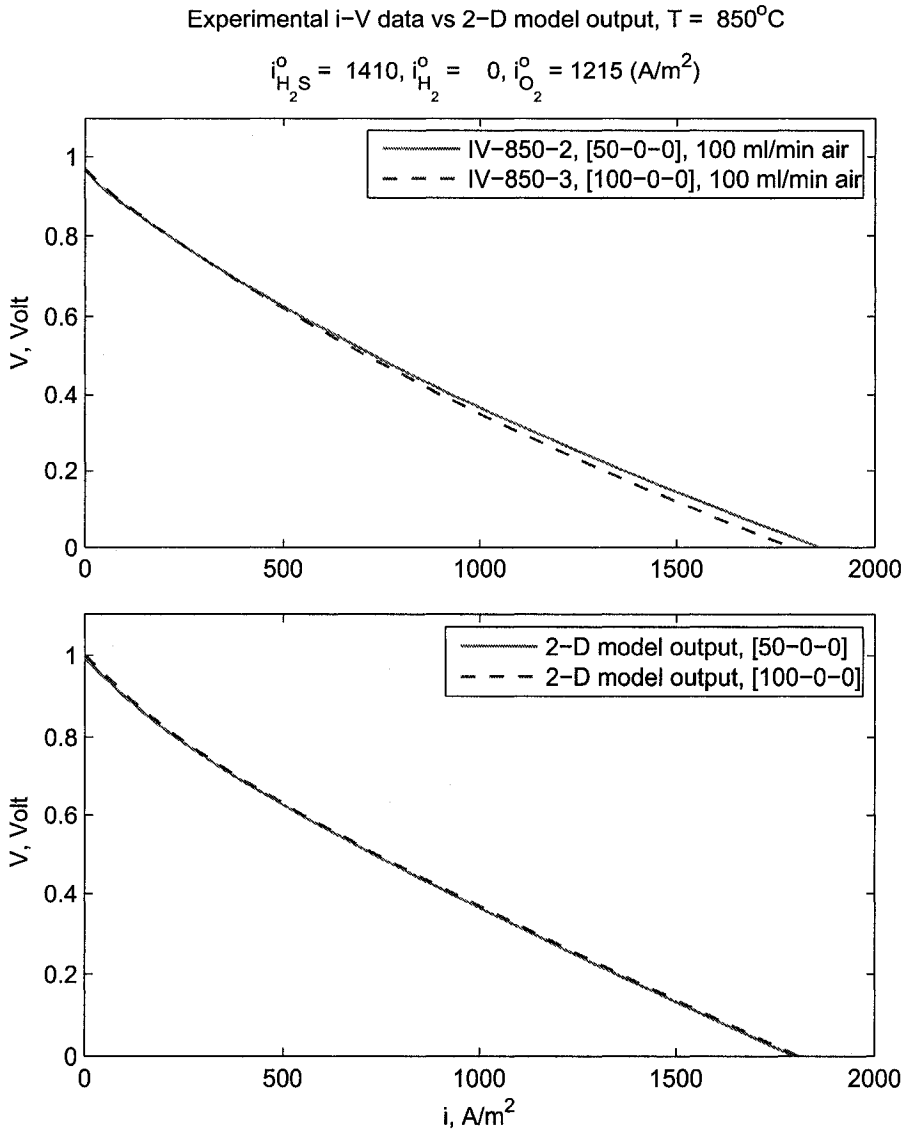

Figure 7.11: Experimental $i - V$ data and 2–D model output; fuel flow-rate

ences become apparent. The model that considers oxidation of both H_2 and H_2S predicts a slight drop in both OCV and maximum current. The model considering only the oxidation of H_2S predicts an increase in both OCV and maximum current. The experimental data shows a small increase in OCV and a significant decrease in i_{0V}[5].

[5]See section 5.5.2 for a discussion on cell activation and deactivation

Table 7.9: Effect of fuel flow-rate: model predictions vs experimental data

	$[50-0-0]$		$[100-0-0]$	
	OCV (V)	i_{0V} (A/m^2)	OCV (V)	i_{0V} (A/m^2)
Experimental	0.963	1856	0.970	1785
2-D model, H_2S	0.992	1796	1.001	1808
2-D model, H_2S & H_2	0.987	1782	0.986	1770

7.8.4 Fuel composition

H_2S in N_2

Figure 7.12 illustrates the effect of lowering y_{H_2S} in the fuel. Both the model (used for this figure) that considers the oxidation of H_2S alone, as well as the model that considers the oxidation of H_2S and H_2 show similar fit to the experimental data. Both models also give very similar output for the fuel compositions shown in figure 7.12. One noteworthy difference is somewhat lower OCV for the model that considers oxidation of H_2S and H_2. This is expected from the previous discussion on mixed OCV.

The model does not fit the experimental data for a fuel flow of $[10-90-0]$ (10 ml/min H_2S, 90 ml/min N_2) well. This is expected because, as seen in the previous section, the i^o estimates for this fuel flow are very different from those for a fuel flow of $[100-0-0]$.

The experimental data for a fuel flow of $[10-90-0]$ (IV-850-10) shows a drop-off in current in the high current region to indicate a mass transfer limit. According to the 2–D model, the $i-V$ curve for a highly dilute fuel $[1-99-0]$ (1% H_2S in N_2, total flow 100 ml/min), does not show significant mass transfer limitations. This could mean either a much lower porosity than used for the model, or a different flow pattern near the cell. The later is possible since there was a small gap between the inlet fuel tube and the spacer in the experimental set-up (see figure 7.1). This gap can allow the short-cutting of the fuel flow from the inlet tube to the outlet tube before the fuel gets to the anode.

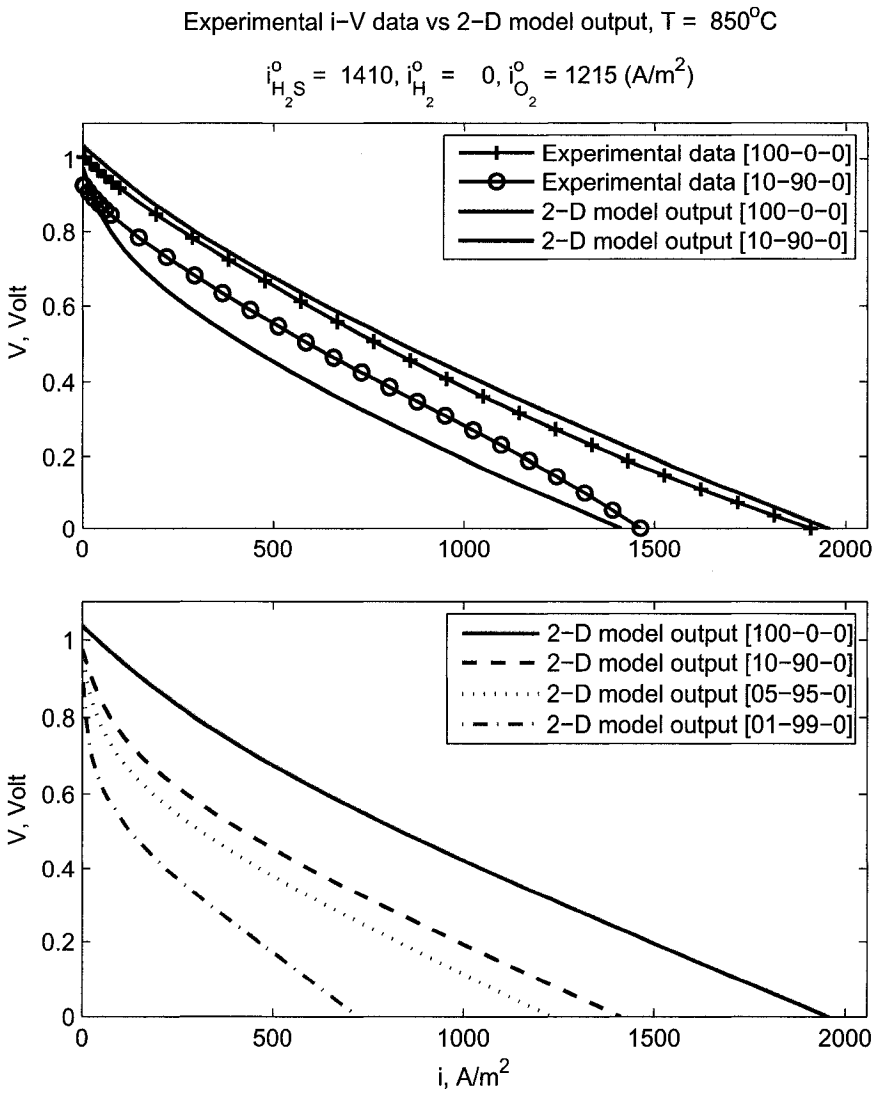

Figure 7.12: Experimental $i - V$ data and 2–D model output; inlet y_{H_2S} in fuel

Effect of adding H_2

Figures 7.13 and 7.14 illustrate the effect of adding H_2 to the fuel. For all simulations, the increase in ohmic resistance seen in the impedance spectra for fuel with added H_2 is explicitly taken into account. This is what leads to a lower maximum current for the fuel with H_2 (seen in figure 7.13) compared to the output for fuel without H_2. In figure 7.14 however, since both H_2 and H_2S are electro-oxidized,

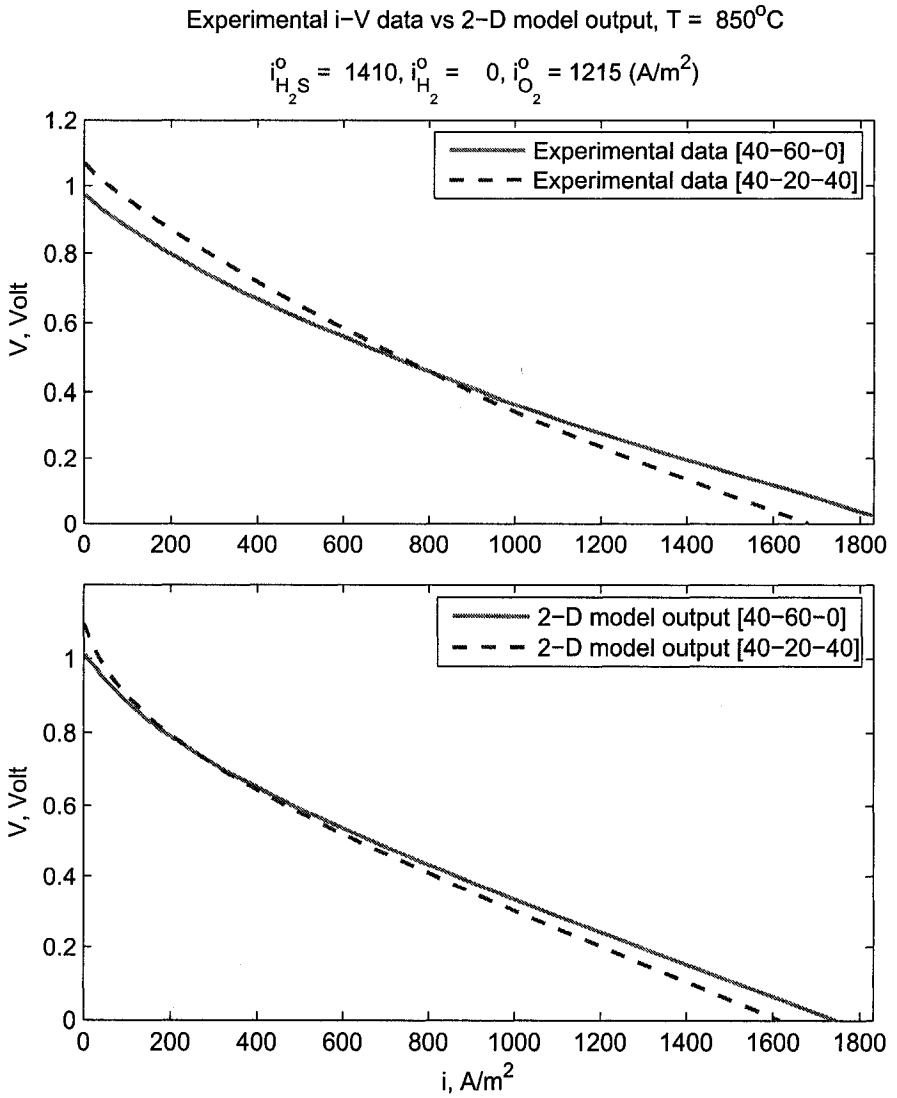

Figure 7.13: Experimental $i - V$ data and 2–D model output; inlet y_{H_2} in fuel; only H_2S oxidized

the increased ohmic resistance has little effect and the performance for fuel with H_2 is significantly higher than for fuel without H_2.

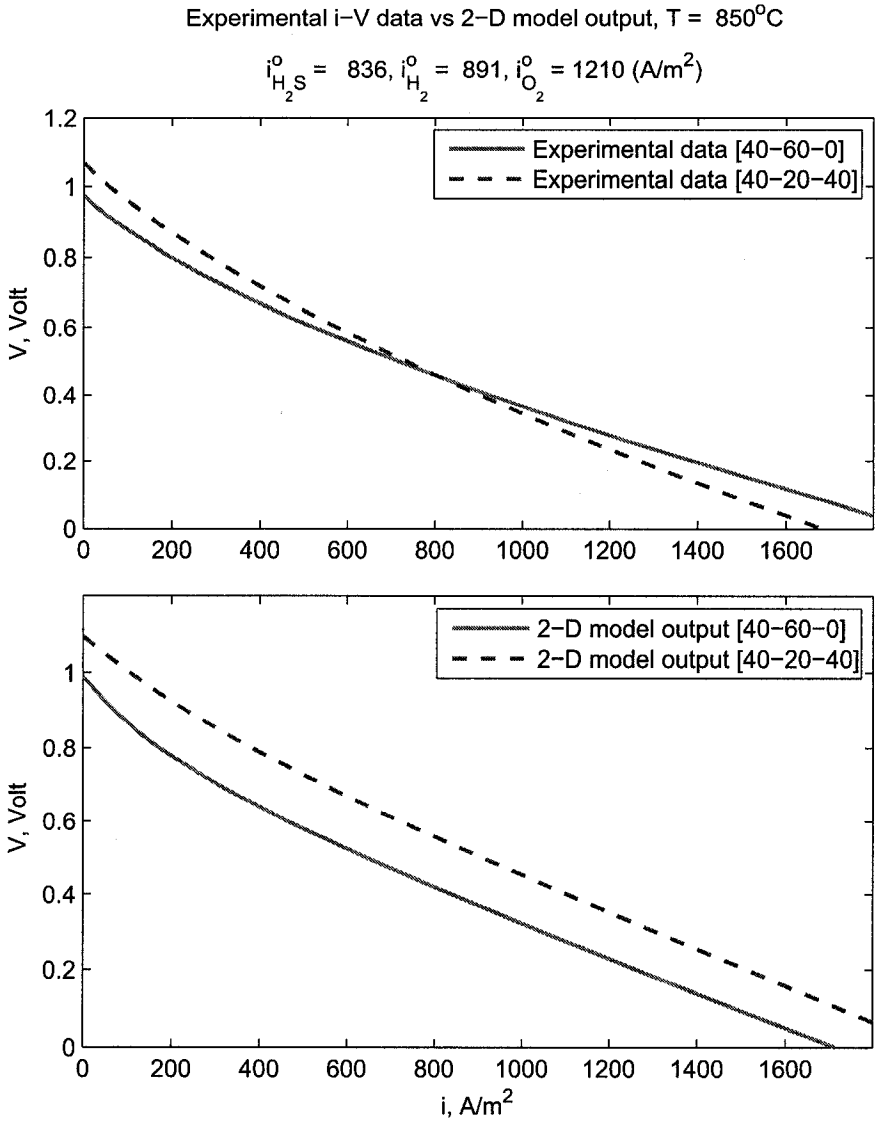

Figure 7.14: Experimental $i - V$ data and 2–D model output; inlet y_{H_2} in fuel; both H_2S and H_2 oxidized

7.8.5 Radiation between internal surfaces

Figure 7.15 gives the temperature, y_{H_2S}, and y_{H_2} profiles along the fuel channel axis from the fuel inlet to the anode. The solid lines are obtained using the model that includes radiative heat exchange between internal surfaces while the dashed lines are from the model that does not include internal radiation. The upper plot shows

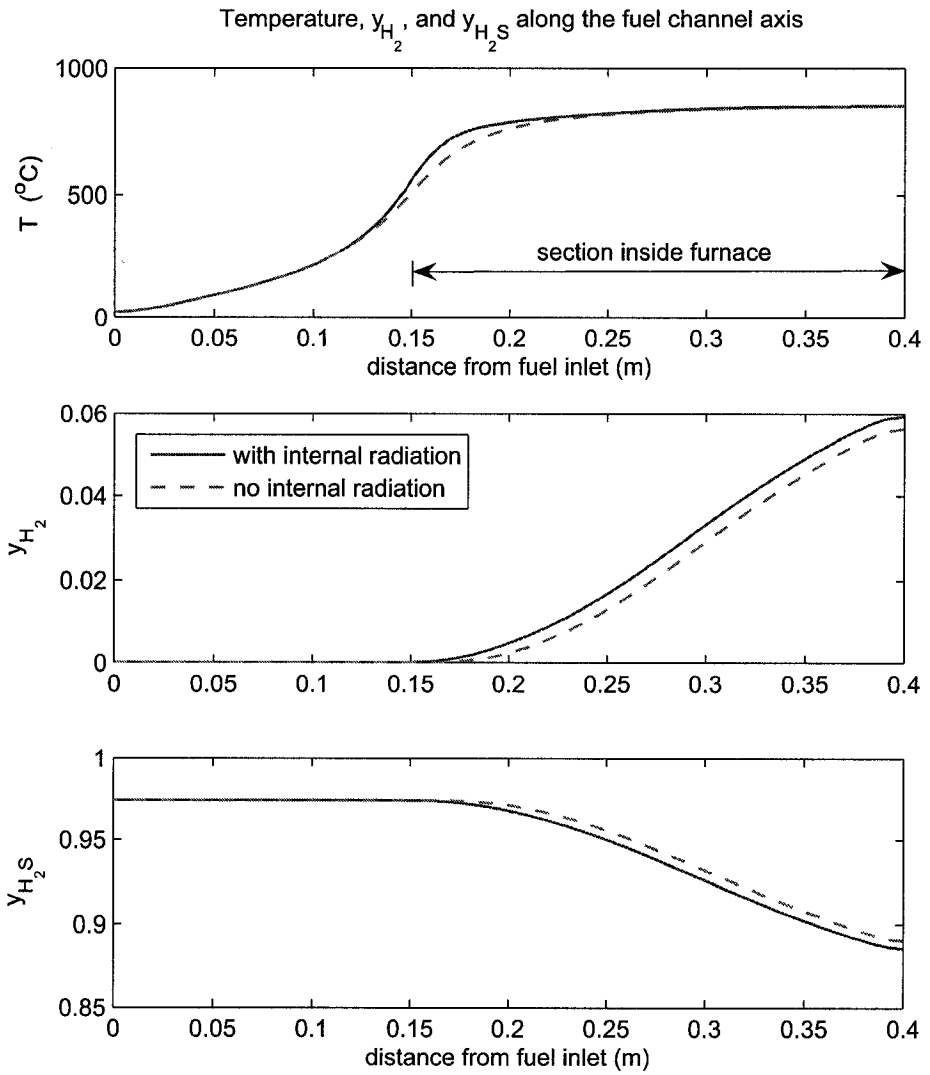

Figure 7.15: Effect of including radiation between internal surfaces

how the fuel heats up earlier in the channel for the model considering internal radiation. Thus, the dissociation of the H_2S starts earlier. This can be confirmed by examining the other two plots which show a higher y_{H_2} and a lower y_{H_2S} for this model. As the dissociation starts earlier, the extent of dissociation of the H_2S in the fuel is higher for the model considering internal radiation. The difference in fuel composition seen in the middle and lower plot leads to a slightly lower

E_{H_2S} (higher E_{H_2}) for this model, as seen in table 7.10. Another consequence of including internal radiation is a lower cell temperature.

The simulations of $i - V$ curves give slightly different results depending on whether or not internal radiation is included in the model due to the above noted differences in local anode temperature and fuel composition. These differences are however fairly small, as seen in table 7.10 which lists the maximum current values obtained from simulations using case 1 i^o estimates.

The plots in figure 7.15 as well as the temperatures and Nernst potentials in table 7.10 are for open circuit conditions.

Table 7.10: Effect of including internal radiation

	T (°C)	E_{H_2S} (V)	E_{H_2} (V)	i_{0V} (A/m^2)
with internal radiation	848.6	1.037	1.004	1957
no internal radiation	849.3	1.039	1.001	1958

7.8.6 Cell heating/cooling

All results in this section were generated using the 2–D model including radiation between internal surfaces. The fuel flows were $100 - 0 - 0$, while the cathode side flow was 100 ml/min O_2.

Figure 7.16 shows the variation in cell temperature with increasing fuel flow-rate. The cell temperature decreases with increasing fuel flow, but the change in temperature for an increase in flow from 50 ml/min to 100 ml/min is only 0.15°C (for the model that includes internal surface radiative heat exchange, 0.3°C for the model that does not include internal radiation). Thus, one of the conjectures to explain a flow-rate dependence of OCV: that the cell is cooled by increasing the fuel flow-rate, is unfounded as varying the fuel flow-rate in the 50–100 ml/min range is not expected to cool the cell.

Figure 7.17 shows the variation in temperature along the axis of the cell assembly, going away from the cell toward the gas inlets. The temperature on the fuel side is lower by about 2.5°C than the temperature in the air/O_2 channel (measured 2 cm from the cell in both cases). This is the cooling effect from the H_2S dissociation reaction.

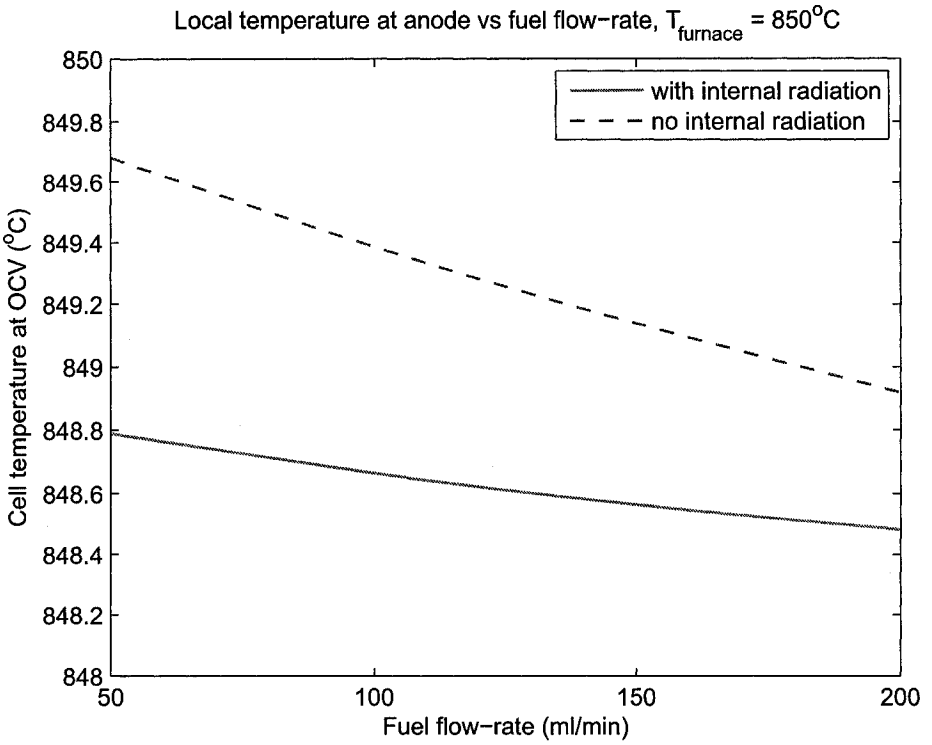

Figure 7.16: 2–D model prediction of cell temperature vs fuel flow-rate

Figure 7.18 shows how the temperature of the active area of the cell changes as one draws more current from it. The upper plot gives the average temperature along the two electrodes while the lower plot shows how the temperature distribution changes along the anode. The cathode temperature was slightly higher at all currents. The temperature gradient across the thickness of the cell increased with increasing current, but was less than 0.5°C for the highest current.

Figures 7.19 and figure 7.20 show the variation in magnitude of the heat source and sink terms as the cell current increases. As seen in the middle plot in figure 7.20, the entropic term on the anode side is negative. This translates to the cooling of the anode seen above in the small temperature gradient between the electrodes. The overall contribution of the entropic terms is also a net cooling as seen in figure 7.19. As discussed in section 7.2.4, although the sum of the anode and cathode entropic terms is expected to be correct, the distribution of the entropic heating/cooling between the electrodes may not be correct.

As the current increases, the activation and ohmic heating terms soon over-

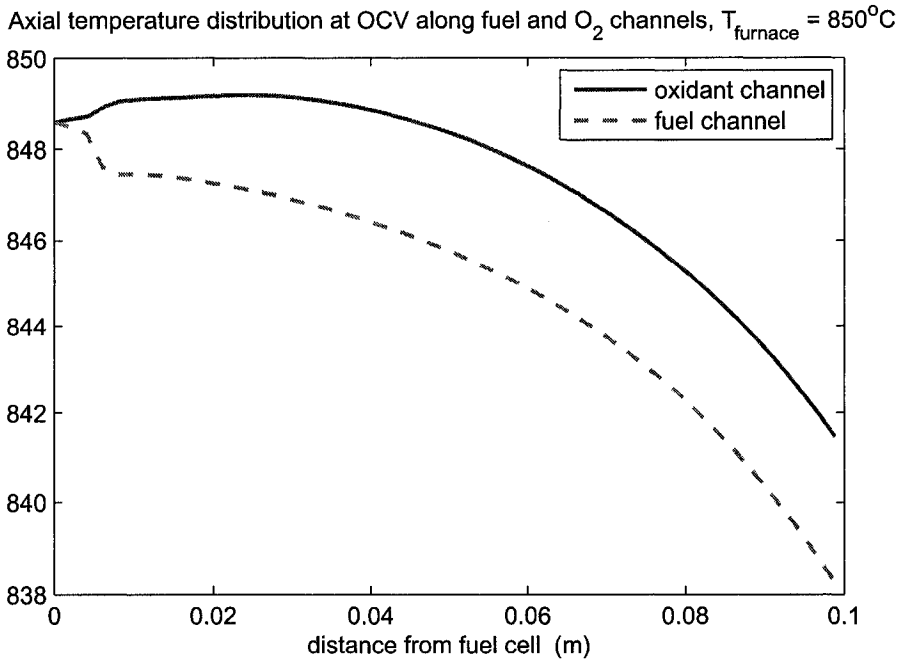

Figure 7.17: 2–D model prediction of axial temperature distribution along the fuel and oxidant channels

power the cooling due to the total entropic term and the cell starts to heat up.

7.8.7 Voltage losses

Figure 7.21 shows how the various voltage losses change as increasing current is drawn from the cell. The highest ohmic voltage loss is due to the current lead resistances which account for 1.5 Ω or 44% of the total ohmic resistance of 3.4 Ω at 850°C. The contact resistance is the next highest ohmic loss term and is of a similar magnitude to the electrolyte resistance at this temperature. The anode resistance is roughly one fourth the electrolyte resistance. Among the activation losses, the anode activation losses are roughly four times greater than the cathode activation losses. The profiles in figure 7.21 are for O_2 on the cathode side. For air on the cathode side, the only change is in the cathode activation losses which increase by $\sim 40\%$.

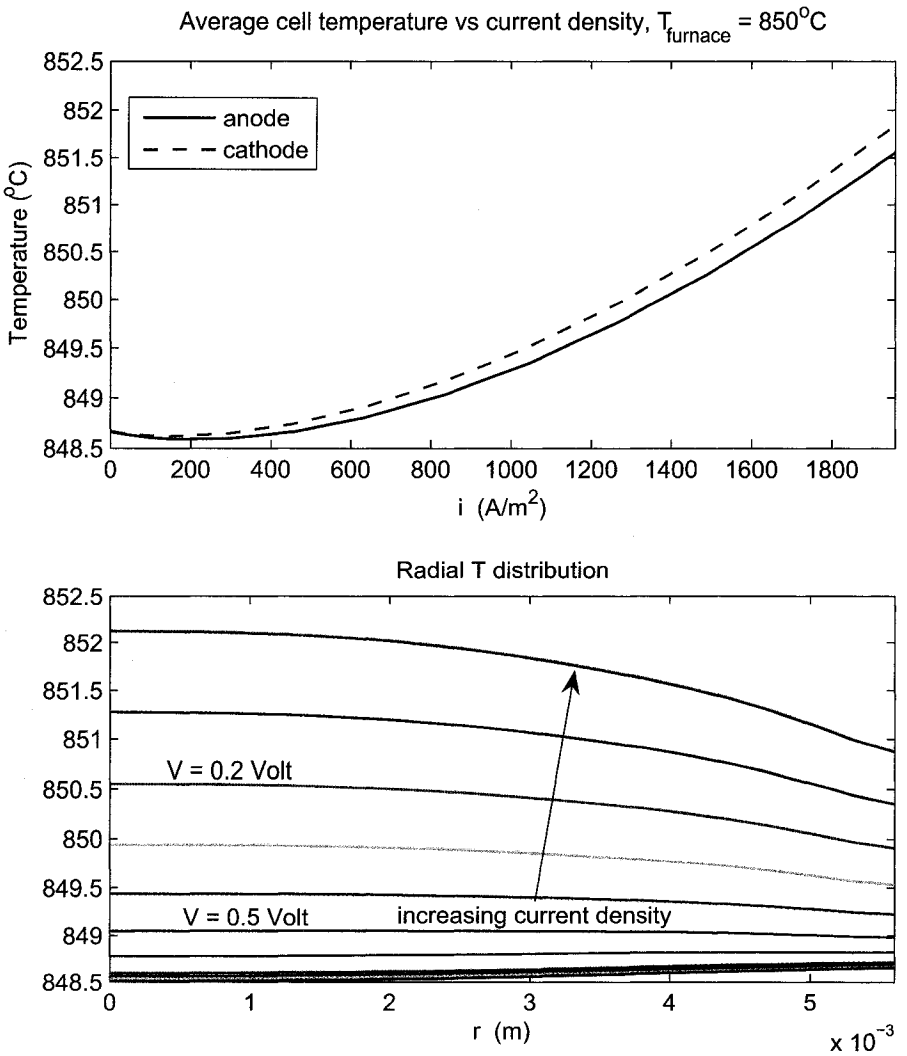

Figure 7.18: 2–D model prediction of the cell temperature vs current

7.8.8 Mixed open circuit voltage (OCV)

I use the case 3 i^o values estimated for IV–850–6 to simulate a mixed open circuit potential for an anode that can oxidize more than one component in a fuel mixture. The upper plot in figure 7.22 shows the total current density vs cell voltage curve as well as the individual current density curves due to H_2S and H_2 oxidation. The lower plot is a close-up of the low current region of the $i - V$ curves and illustrates

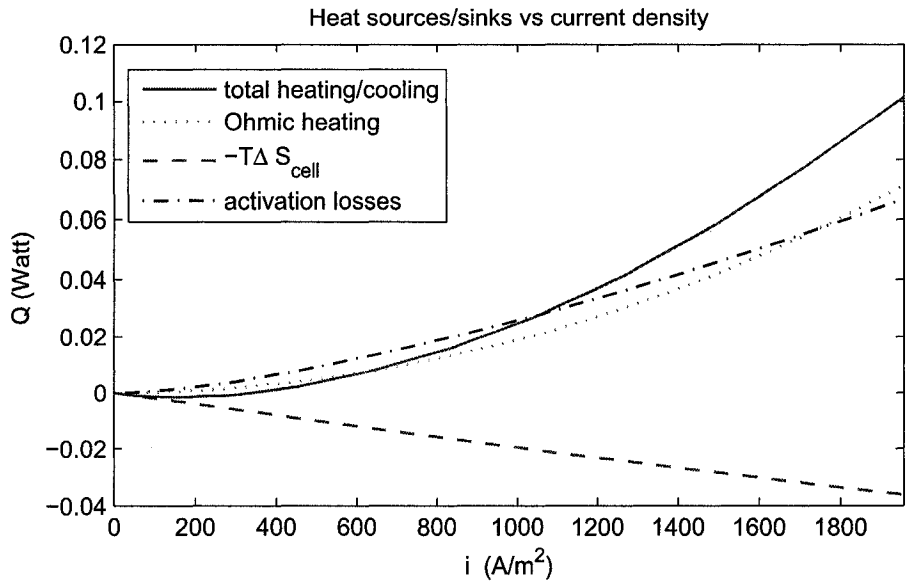

Figure 7.19: 2–D model prediction of cell heating/cooling: total ohmic, entropic, and activation

how the OCV for a mixed fuel is the cell voltage where the sum of the currents due to the different fuels is zero. As expected, the mixed OCV lies between the Nernst potentials for H_2S and H_2 oxidation. However, the Nernst potentials for the two fuels are different from the cell voltages where the corresponding fuel currents go to zero. This interesting behaviour is a consequence of the two reactions at the anode occurring simultaneously and thus being subject to one anode potential.

7.9 Summary

In this Chapter I presented comprehensive multiphysics models for a H_2S SOFC that take all the important transport phenomena, fuel chemistry, as well as electrochemistry at both electrodes into account. The fuel chemistry model used as well as the electrochemistry models developed are thermodynamically consistent, which allows me to predict cell OCV correctly. The complete models allowed me to simulate the experiments summarized in Chapter 5.

The first set of simulations compare the predicted open circuit voltage for the H_2S and H_2 electro-oxidation reactions on the anode as functions of composition and flow-rate. By comparing these model predictions against the experimental

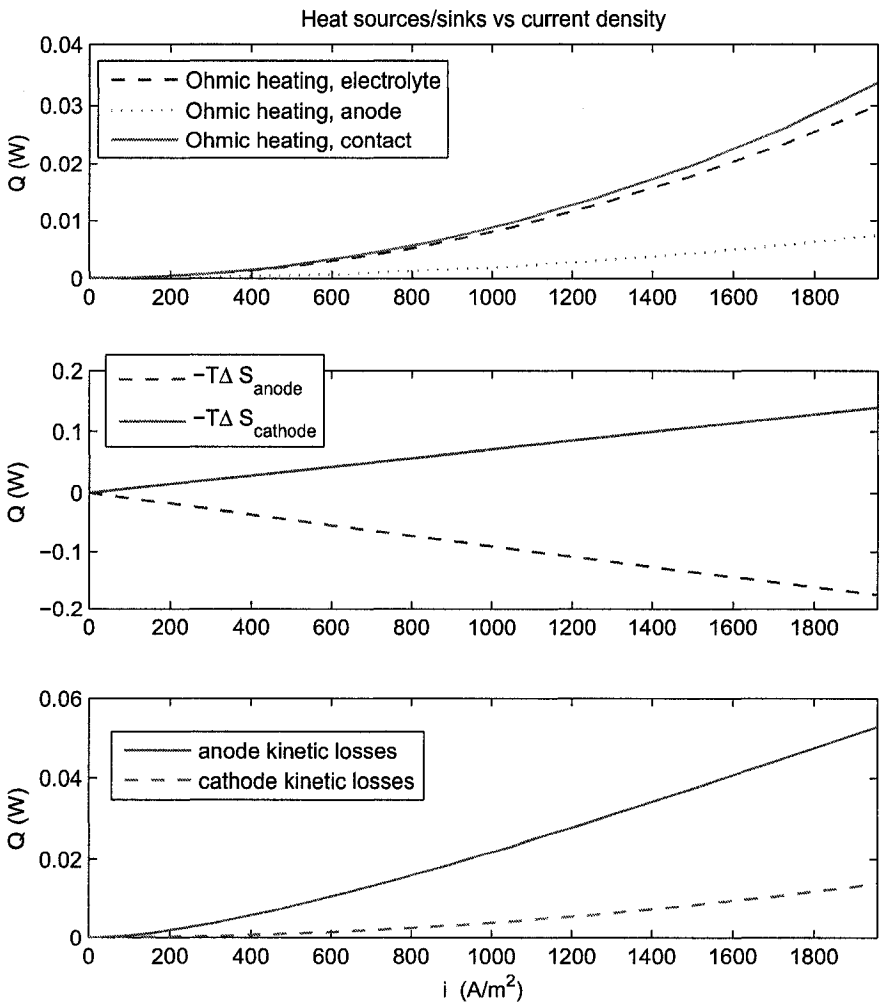

Figure 7.20: 2–D model prediction of cell heating/cooling: individual ohmic, entropic, and activation contributions

data presented in Chapter 5, I suggest that H_2S, not H_2, is the primary electrochemically active species in the fuel.

As the electrochemical kinetic parameters are unknown, I estimated them from experimental data using non-linear least squares. This was only partly successful as seen in section 7.7.1. However, these parameter estimates allowed me to completely define the models, and thus use them to predict cell performance for various parametric studies.

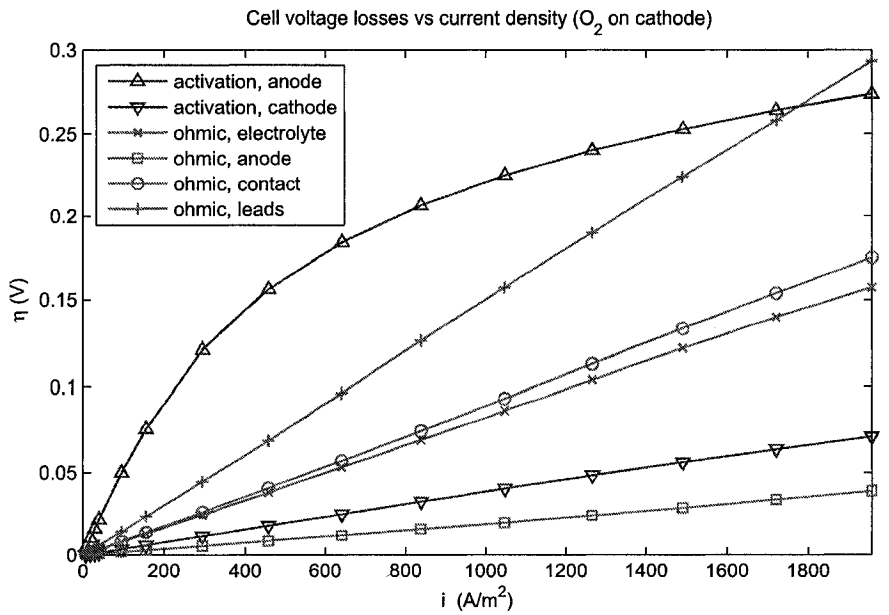

Figure 7.21: 2–D model prediction of cell voltage losses: individual ohmic and activation contributions

I used the model simulations to predict cell performance or $i - V$ curves. This allows me to compare how the model outputs change with changing test conditions for different models. Which component in the fuel is electro-oxidized at the anode is one of the big unanswered questions for H_2S fueled fuel cells. The models developed here allow me to consider simultaneous H_2S and H_2 oxidation and predict the combined/mixed fuel OCV and $i - V$ curves along with detailed modelling of the contribution to the overall performance by each component. The model formulation and development is general and can be used to simulate the performance of any multi-fuel fuel cell. This ability allows me to predict changes in performance that depend on which fuel components are electrochemically active.

I examined the model outputs for variations in temperature, fuel composition and flow-rate, as well as oxidant composition, and compared the model predictions for single and dual fuel models with experimental data. Finally, I demonstrated some of the capabilities of the model and the amount of detail that can be obtained from these models.

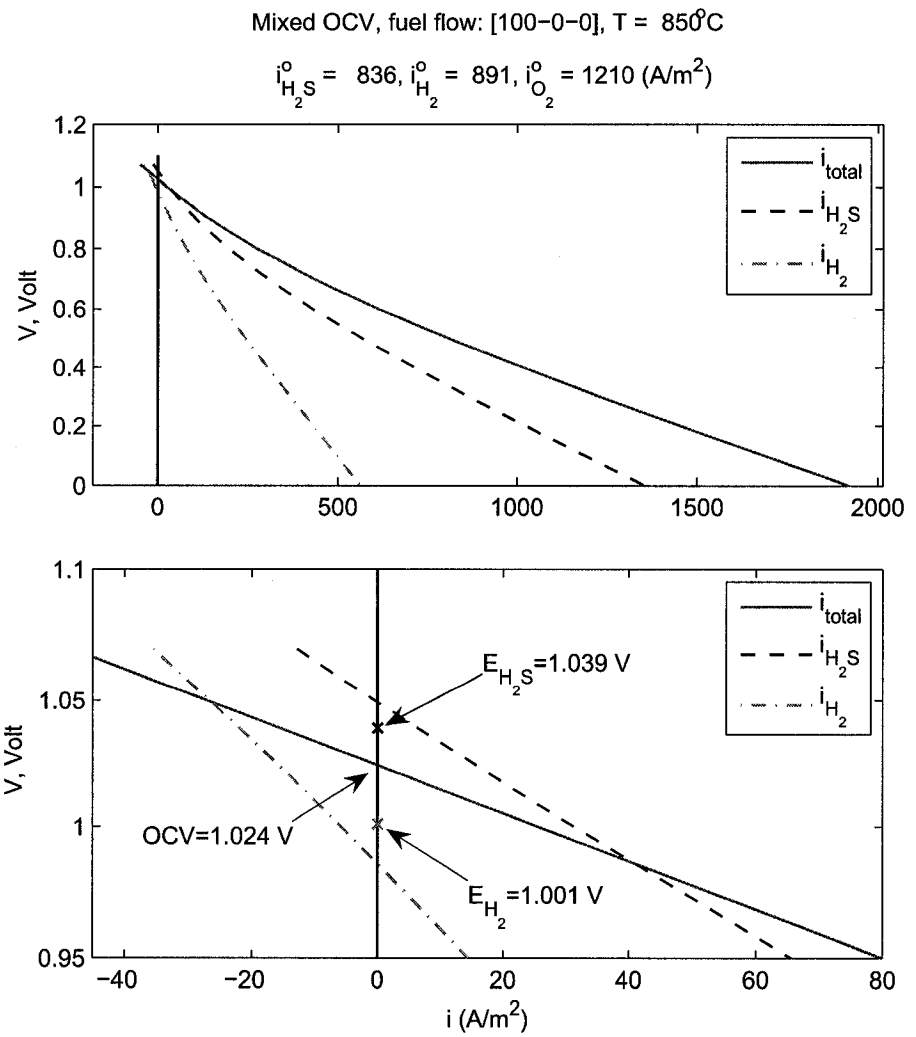

Figure 7.22: Mixed open circuit voltage; both H_2S and H_2 oxidized on the anode

Chapter 8

Some concluding thoughts and recommendations for future work

As outlined in section 1.4, a lot of research is being performed in the area of sulphur tolerant solid oxide fuel cell anodes, and there is a significant amount of research literature on SOFCs utilizing H_2S as fuel. However, there have been very few attempts to approach the above problems from a mathematical modelling perspective. The only modelling work on H_2S fuel cells (other than our work [93, 94]) has been at the atomic level using computational chemistry to predict the likely heterogenous chemistry of hydrogen sulphide poisoning [47], and the solid phases on the anode in the presence of H_2S and their stability [136, 27, 28, 137]. These models describe the chemical interaction of H_2S with the anode material at the smallest scales possible and cannot be used to predict fuel cell performance metrics such as polarization curves.

In spite of two decades of research into H_2S SOFCs, some basic questions about them remain unanswered. These include:

- Which of the chemical species present in the fuel are electro-oxidized on the anode, H_2S, H_2 or S_2? How does fuel composition affect fuel cell performance?
- What is the reaction mechanism for the electrochemistry on the anode? What are the values of the kinetic constants?
- Why does the flow-rate of the fuel affect the open circuit potential for the fuel cell?

I believe that the above questions can only be answered correctly by using a combination of carefully designed (and executed) experiments and first principles modelling of the various transport phenomena, the homogeneous and heterogeneous fuel chemistry, and the electrochemistry in a fuel cell, along with all the couplings between these processes. This dissertation tackles the above task by building a range of first principles based models that describe the transport and reaction processes for a H_2S solid oxide fuel cell. I propose answers to some of the questions above using these first principles models. To my knowledge, this work is the only one thus far to propose such models for a H_2S fuel cell.

8.1 Summary and key contributions

Transport processes in fuel cells include fluid flow, mass transfer, heat transfer, and charge transport. The modelling of these processes is fairly well understood and I outline the equations, boundary conditions and parameters for the transport models in Chapter 2.

The need to include electrochemistry is what distinguishes fuel cell models from chemical reactor models. I introduce the fundamental electrochemistry required to understand the kinetics of the anode and cathode half reactions in Chapter 3. I derive the fundamental electrochemical rate equation for a single electron transfer reaction: the Butler-Volmer equation and show how it can be written in three different equivalent forms. Although all electrochemistry textbooks derive this equation, they present only one (at most two) form(s) of the three forms used in the research literature. I then present the simplest thermodynamically consistent rate equations that can be written for the anode and cathode reactions in a H_2S SOFC. These are the equations I later use in the complete fuel cell models of Chapters 4 and 7.

I also formulate a detailed model for the electrochemical oxidation of H_2S. This model starts by proposing a mechanism with a sequence of elementary reactions in the vicinity of the three phase boundary region in the anode. I present the resulting system of elementary rate equations and outline the coupling with the equations for transport phenomena in a working fuel cell. I also present the overall reaction rate equations obtained when a rate determining step can be assumed from the above mechanism. Again, to the best of my knowledge, this is the first reaction mechanism proposed for H_2S electro-oxidation.

I build a hierarchy of H_2S SOFC models in Chapter 4 to simulate a set of fuel cell data given in Liu et al., 2003 [84]. These four models range from an explicit 1-D model given by a single non-linear equation, to a 2-D axi-symmetric finite element model that takes gas flow, mass transfer, charge transport, and the electrochemical kinetics into account, and requires the simultaneous solution of $\sim 30,000$ equations in as many unknowns. Since electrochemical kinetic parameters are not available for the fuel cell used by Liu et al., I estimate these parameters using non-linear least squares for all the models developed, including the distributed 1-D and 2-D models. The results of this parameter estimation demonstrate the importance of modelling the coupling between the flow, the mass transfer, and the kinetics. To correctly assign the electrochemical resistance, the mass transfer needs to be modelled correctly, which in turn entails correctly coupling it with the flow equations. As flow cannot be modelled correctly using a 1-D model for the geometry used, a 2-D model is indispensable to examine fuel cell performance for the given geometry and operating conditions.

I and a colleague ran experiments to examine the effects of fuel and oxidant composition as well flow-rate on H_2S SOFC performance. These experiments which consisted of measuring the electrochemical impedance spectra at open circuit, and the $i - V$ curves, for different operating conditions. One of the problems with the experimental fuel cell data available in the research literature is that theoretical open circuit values cannot be defined for any of the data sets. To calculate the open circuit value for any of the possible overall reactions in a fuel cell, the Nernst equation requires well defined values for the composition of the reactants as well as the products of the overall reaction. For instance, if one considers the direct oxidation of H_2S to H_2O and S_2, one needs the local concentrations of H_2O and S_2 to solve for the Nernst potential or OCV of this reaction. While the S_2 content can be calculated if I model the H_2S dissociation reaction (as done in Chapters 6 and 7), the water vapour content can be only be fixed by humidifying the fuel. To the best of my knowledge, the experiments I report in Chapter 5 are the first cell performance experiments where the fuel mixture is humidified before being introduced into the fuel cell assembly. One of the motivations behind these experiments was to use humidified fuel so that the concentration of at least one of the anode side products is well defined at open circuit. Primarily, I wanted to systematically examine fuel composition and flow-rate effects in a H_2S SOFC to see if I could answer some of the questions posed at the beginning of this

Chapter. I report the time, composition, and flow-rate dependencies observed in our experimental results in Chapter 5.

As mentioned above, to calculate the S_2 content of the fuel at the anode, one needs to model the H_2S dissociation reaction in the fuel inlet. In Chapter 6 I develop chemical thermodynamics models for $H_2S/H_2/H_2O/N_2$ mixtures and use them to predict equilibrated fuel composition as well as the equilibrium cell voltage. I demonstrate how the Nernst potentials for all the possible anode side electrochemical reactions are identical when the fuel is at chemical equilibrium. In appendix B, I present the proof for the above statement. The equilibrium models are then combined with basic ideas from chemical reaction engineering to predict how the Nernst potentials for the different anode electrochemical reactions change if the fuel is not yet at chemical equilibrium. However, to predict if the fuel is at equilibrium or not, I need to model the kinetics. In the final section of Chapter 6, I review some kinetic models for the H_2S dissociation reaction.

In Chapter 7, I extend the models from Chapter 4 to include the kinetics of H_2S dissociation as well as heat transfer. I have to model the heat transfer in the entire fuel cell assembly, along with all the other transport phenomena, because the fuel side chemistry is temperature dependent. Therefore, to calculate the local composition of the fuel at the anode, the model needs the temperature profile of the fuel stream before it reaches the anode.

I then use these comprehensive models to predict the Nernst voltages for the H_2S and H_2 electro-oxidation reactions, and compare the model output against the experimental data from Chapter 5. Both the composition and flow-rate dependence of the model output suggest that H_2S electro-oxidation is the primary anode reaction for the anode we used in our experiments.

To model $i-V$ performance curves, I need electrochemical kinetic parameters, which I estimate using a similar parameter estimation scheme to the one used in Chapter 4 on combined 1-D/2-D models. In these combined models, I calculate the local fuel composition at the anode and fuel channel interface using the comprehensive 2-D model outlined earlier, and use this composition as boundary conditions for a simpler isothermal 1-D model which solves only the mass transfer and charge transport equations in the fuel cell electrodes and electrolyte. This hybrid model allows us reduce the computational demands of the parameter estimation dramatically. On examining the parameter estimates for the $i-V$ curves, I found that the estimates change with changing fuel composition. I describe the

trends in the above estimates. While the temporal changes in cell performance can be seen clearly in the estimates, the composition dependency of the estimates for both the anode and cathode side kinetic parameters suggests that the electrochemistry models I use do not have the correct functional form. I think that better models are required to correctly describe the electrochemistry at both electrodes.

In spite of the shortcomings in the electrochemical models, the estimated parameters allow us to complete the model definition and thus simulate cell performance curves. I perform several case studies where I compare the model simulations against experimental data to look at composition and flow-rate effects. I use model simulations to assess the importance of including radiation heat exchange between internal surfaces for the button cell geometry. I then examine model simulations to explain and compare the various heat sources/sinks and voltage losses in a working fuel cell. I also demonstrate the ability of my models to calculate mixed fuel performance curves. Although several researchers [26, 76, 81, 146] have developed and used mixed potential models for direct methanol fuel cells (DMFC), to the best of my knowledge, this work is the first reported use of thermodynamically consistent multiphysics models to calculate the mixed OCV and mixed potential $i - V$ curves for a SOFC.

8.2 Directions for future research

Devices that can turn a highly toxic pollutant into useful energy and benign products sound too good to be true. SOFCS running on H_2S produced on-site at petroleum refineries, gas processing plants, coal gasification plants, etc. promise to accomplish the above impressive feat. However, there are a number of problems that need to be addressed through aggressive research before H_2S SOFCs become a reality. In my view, the most important requirement is an anode catalyst that is completely stable in a H_2S environment and has a high activity for electrochemical oxidation of H_2S. Once a candidate material is available, well designed models coupled with carefully planned experiments can speed up the development process for industrial scale H_2S SOFCs.

In my view, half cell experiments that probe the anode polarization behaviour over a whole range of fuel compositions are essential for further progress in understanding H_2S SOFCs. The biggest shortcoming of the models presented in this work is that the electrochemical rate expressions used are too simplistic. While I

propose more complex reaction models that include multiple elementary reaction steps at each electrode as well as competitive adsorption and desorption of reaction species, these models in turn contain a number of parameters that need to be determined before they can be used in simulations. To get reliable estimates for these kinetic parameters and to validate any proposed reaction mechanisms, very careful experimental characterization of the electrodes using half cell experiments [37, 30] is required.

Another possible approach to get at electrode reaction mechanisms, rate equations, and their parameters is through quantum chemistry models. Methods from theoretical chemistry such as Density Functional Theory, which are based on a quantum mechanical description of the bonds between atoms, can be used to find feasible electrode reaction mechanisms [97, 154]. These methods can also give estimates for the kinetic parameters for the elementary reactions in a given reaction mechanism [133, 45]. Sun et al. 2005 [125] have used the above approach to investigate the hydrodesulphurization (HDS) reaction on MoS_2, NiMoS, and CoMoS. In the HDS reaction, H_2 is used to remove S from the sulphided surface, while in a H_2S SOFC anode, H_2S adsorbs and dissociates on the surface. The H atoms near the anode-electrolyte interface then presumably react with oxide ions in the electrolyte to give reaction products. The mechanism proposed in section 3.2.1 uses such an approach. In future work, we propose to use results from the computational chemistry investigations to build better models for anode electrochemistry in SOFCs running on complex fuels.

Once more faithful models of H_2S electrochemistry are available for an appropriate anode catalyst, multiphysics models like the ones developed in this work can be used to design cells and stacks for H_2S SOFCs. Such models would have to be extended to three dimensions to correctly capture the spatial variations of the flow, concentration, and temperature fields in industrial scale fuel cell stacks.

Bibliography

[1] Ali Abbaspour, K. Nandakumar, Jingli Luo, and Karl T. Chuang. A novel approach to study the structure versus performance relationship of SOFC electrodes. *Journal of Power Sources*, 161(2):965 – 970, 2006.

[2] A.A. Adesina, V. Meeyoo, and G. Foulds. Thermolysis of hydrogen sulphide in an open tubular reactor. *International Journal of Hydrogen Energy*, 20 (10):777 – 783, 1995.

[3] Stuart B. Adler. Factors governing oxygen reduction in solid oxide fuel cell cathodes. *Chemical Reviews*, pages 4791–4843, 2004.

[4] Luis Aguilar, Shaowu Zha, Zhe Cheng, Jack Winnick, and Meilin Liu. A solid oxide fuel cell operating on hydrogen sulfide and sulfur-containing fuels. *Journal of Power Sources*, 135:17–24, 2004.

[5] Shabbir Ahmed, Charles McPheeters, and Romesh Kumar. Thermal-hydraulic model of a monolithic solid oxide fuel cell. *Journal of the Electrochemical Society*, 138:2712–2718, 1991.

[6] A. S. Arica, S. Srinivasan, and V. Antonucci. DMFCs: From fundamental aspects to technology development. *Fuel Cells*, 1(2):133–161, 2001.

[7] A. Atkinson, S. Barnett, R.J. Gorte, J.T.S. Irvine, A.J. Mcevoy, M. Mogensen, S.C. Singhal, and J. Vohs. Advanced anodes for high-temperature fuel cells. *Nature Materials*, 3(1):17–27, 2004.

[8] P. Attryde, A. Baker, S. Baron, A. Blake, N.P. Brandon, D. Corcoran, D. Cumming, A. Duckett, K. El-Koury, D. Haigh, M. Harrington, C. Kidd, R. Leah, G. Lewis, C. Matthews, N. Maynard, T. McColm, A. Selcuk, M. Schmidt, R. Trezona, and L. Verdugo. Stacks and systems based around

metal supported SOFCs operating at 500-600°C. In *Proceedings of the Electrochemical Society, Ninth International Solid Oxide Fuel Cells Symposium*, volume 2005-07, pages 113–122, Quebec, Canada, 2005.

[9] P. Bance, N.P. Brandon, B. Girvan, P. Holbeche, S. O'Dea, and B.C.H. Steele. Spinning-out a fuel cell company from a uk university - 2 years of progress at ceres power. *Journal of Power Sources*, 131(1-2):86–90, 2004.

[10] Rasmus Barfod, Mogens Mogensen, Trine Klemenso, Anke Hagen, Yi-Lin Liu, and Peter Vang Hendriksen. Detailed characterization of anode-supported SOFCs by impedance spectroscopy. *Journal of the Electrochemical Society*, 154(4):371–378, 2007.

[11] Evgenij Barsoukov and J. Ross Macdonald, editors. *Impedance spectroscopy.* John Wiley & Sons, Hoboken, New Jersey, U.S.A., 2nd edition, 2005.

[12] Wolfgang G. Bessler. A new computational approach for SOFC impedance from detailed electrochemical reaction-diffusion models. *Solid State Ionics*, 176(11-12):997 – 1011, 2005.

[13] Wolfgang G. Bessler, Stefan Gewies, and Marcel Vogler. A new framework for physically based modeling of solid oxide fuel cells. *Electrochimica Acta*, 53(4):1782 – 1800, 2007.

[14] A. Bieberle and L.J. Gauckler. State-space modeling of the anodic SOFC system $Ni, H_2 - H_2O|YSZ$. *Solid State Ionics*, 146(1-2):23 – 41, 2002.

[15] Manuel Binoist, Bernard Labegorre, Franck Monnet, Peter D. Clark, Norman I. Dowling, Damien Archambault, Edouard Plasari, Paul-Marie Marquaire, and M. Huang. Kinetic study of the pyrolysis of H_2S. *Industrial and Engineering Chemistry Research*, 42(17):3943 – 3951, 2003.

[16] R. Byron Bird, Warren E. Stewart, and Edwin N. Lightfoot. *Transport Phenomena.* John Wiley & Sons, New York, U.S.A., 2nd edition, 2002.

[17] Ludger Blum, Wilhelm A. Meulenberg, Heinz Nabielek, and Robert Steinberger-Wilckens. Worldwide SOFC technology overview and benchmark. *International Journal of Applied Ceramic Technology*, 2(6):482–492, 2005. doi: 10.1111/j.1744-7402.2005.02049.x. URL `http://www.blackwell-synergy.com/doi/abs/10.1111/j.1744-7402.2005.02049.x`.

[18] John O'M. Bockris, Amulya K.N. Reddy, and Maria E. Gamboa-Aldeco. Modern Electrochemistry 2A: Fundamentals of Electrodics. Kluwer Academic, New York, 2nd edition, 2001.

[19] Roberto Bove and Stefano Ubertini. Modeling solid oxide fuel cell operation: Approaches, techniques and results. *Journal of Power Sources*, 159(1 SPEC ISS):543 – 559, 2006.

[20] Nigel P. Brandon, S. Skinner, and Brian C.H. Steele. Recent advances in materials for fuel cells. *Annual Review of Materials Research*, 33:183–213, 2003.

[21] N.P. Brandon, D. Corcoran, D. Cummins, A. Duckett, K. El-Khoury, D. Haigh, R. Leah, G. Lewis, N. Maynard, T. McColm, R. Trezona, A. Selcuk, and M. Schmidt. Development of metal supported solid oxide fuel cells for operation at 500-600°C. *Journal of Materials Engineering and Performance*, 13(3):253 – 256, 2004.

[22] Michael Capone. Sulfur removal and recovery. In *Kirk-Othmer Encyclopedia of Chemical Technology Online*. John Wiley and Sons, 4th edition, 2004. URL `http://www.mrw.interscience.wiley.com/kirk/articles/sulfcapo.a01/sect1%_3-fs.html`.

[23] L. Carrette, K. A. Friedrich, and U. Stimming. Fuel cells – fundamentals and applications. *Fuel Cells*, 1:5–39, 2001.

[24] NASA Glenn Research Center. CEA-ThermoBuild: an interactive tool for using the NASA Glenn Thermodynamic Database. URL `http://cea.grc.nasa.gov/index.html`.

[25] S. H. Chan, K. A. Khor, and Z. T. Xia. Complete polarization model of a solid oxide fuel cell and its sensitivity to the change of cell component thickness. *Journal of Power Sources*, pages 130–140, 2001.

[26] Chih-Hao Chen and Tsung-Kuang Yeh. A mathematical model for simulating methanol permeation and the mixed potential effect in a direct methanol fuel cell. *Journal of Power Sources*, 160(2 SPEC ISS):1131 – 1141, 2006.

[27] Hsin-Tsung Chen, YongMan Choi, Meilin Liu, and M. C. Lin. A first-principles analysis for sulfur tolerance of CeO_2 in solid oxide fuel cells.

Journal of Physical Chemistry C, 111(29):11117–11122, July 26 2007. doi: {10.1021/jp0705774}.

[28] Y.M. Choi, Charles Compson, M.C. Lin, and Meilin Liu. Ab initio analysis of sulfur tolerance of Ni, Cu, and Ni-Cu alloys for solid oxide fuel cells. *Journal of Alloys and Compounds*, 427(1-2):25 – 29, 2007.

[29] K. T. Chuang, A. R. Sanger, S. V. Slavov, and J. C. Donini. A proton-conducting solid state $H_2S - O_2$ fuel cell. iii. operation using H_2S-hydrocarbon mixtures as anode feed. *International Journal of Hydrogen Energy*, pages 103–8, 2001.

[30] Anne Chuy Co. *Oxygen Reduction Kinetics and Mechanism in High Temperature Solid Oxide Fuel Cells.* PhD thesis, University of Calgary, Canada, 2005.

[31] COMSOL. COMSOL Multiphysics 3.2 User's Guide. COMSOL AB, Sweden, 2005. URL `http://comsol.com/products/multiphysics/`.

[32] Paola Costamagna and Supramaniam Srinivasan. Quantum jumps in the pemfc science and technology from the 1960s to the year 2000: Part i. fundamental scientific aspects. *Journal of Power Sources*, 102(1-2):242–252, 2001.

[33] Paola Costamagna and Supramaniam Srinivasan. Quantum jumps in the pemfc science and technology from the 1960s to the year 2000: Part ii. engineering, technology development and application aspects. *Journal of Power Sources*, 102(1-2):253–269, 2001.

[34] H. T. Davis, L. R. Valencourt, and C. E. Johnson. Transport processes in composite media. *Journal of the American Ceramic Society*, 58(9-10): 446–452, 1975.

[35] Hans-Heinrich Möbius. History. In S. C. Singhal and K. Kendall, editors, *High Temperature Solid Oxide Fuel Cells: Fundamentals, Design and Applications*, pages 23–51. Elsevier Advanced Technology, Oxford, 2003.

[36] Hans-Heinrich Möbius. On the history of solid electrolyte fuel cells. *Journal of Solid State Electrochemistry*, 1:2–16, 1997.

[37] Baukje de Boer. SOFC Anodes: Hydrogen oxidation at porous nickel and nickel/yttria-stabilised zirconia cermet electrodes. PhD thesis, Universiteit Twente, the Netherlands, 1998.

[38] P. G. Debenedetti and C. G. Vayenas. Steady-state analysis of high temperature fuel cells. *Chemical Engineering Science*, pages 1817–1829, 1983.

[39] Nicholas W. DeLuca and Yossef A. Elabd. Polymer electrolyte membranes for the direct methanol fuel cell: A review. *Journal of Polymer Science Part B: Polymer Physics*, 44(16):2201–2225, 2006.

[40] Anthony G. Dixon and David L. Cresswell. Theoretical prediction of effective heat transfer parameters in packed beds. *AIChE Journal*, 25(4):663 – 676, 1979. ISSN 0001-1541. URL `http://dx.doi.org/10.1002/aic.690250413`.

[41] Norman I. Dowling, James B. Hyne, and Dennis M. Brown. Kinetics of the Reaction between Hydrogen and Sulfur under High-Temperature Claus Furnace Conditions. *Industrial and Engineering Chemistry Research*, 29(12): 2327–2332, 1990.

[42] Energy Efficiency and U.S. Department of Energy Renewable Energy. Types of fuel cells: SOFCs. URL `http://www1.eere.energy.gov/hydrogenandfuelcells/fuelcells/fc_types.html`.

[43] Jurgen Fleig. Solid oxide fuel cell cathodes: Polarization mechanisms and modeling of the electrochemical performance. *Annual Review of Materials Research*, 33:361 – 382, 2003.

[44] H. Scott Fogler. *Elements of Chemical Reaction Engineering.* Prentice Hall, New Jersey, U.S.A., 3rd edition, 1998.

[45] Natasha M. Galea, Eugene S. Kadantsev, and Tom Ziegler. Studying reduction in solid oxide fuel cell activity with density functional theory-effects of hydrogen sulfide adsorption on nickel anode surface. *Journal of Physical Chemistry C*, 111(39):14457 – 14468, 2007.

[46] Natasha M. Galea, Daniel Knapp, and Tom Ziegler. Density functional theory studies of methane dissociation on anode catalysts in solid-oxide fuel cells: Suggestions for coke reduction. *Journal of Catalysis*, 247(1):20 – 33,

2007. ISSN 0021-9517. URL http://dx.doi.org/10.1016/j.jcat.2006.12.021.

[47] Natasha M. Galea, Eugene S. Kadantsev, and Tom Ziegler. Studying reduction in solid oxide fuel cell activity with density functional theory-effects of hydrogen sulfide adsorption on nickel anode surface. *Journal of Physical Chemistry C*, 111(39):14457–14468, October 4 2007. doi: {10.1021/jp072450k}.

[48] P.E. Gill, W. Murray, and M.H. Wright. *Practical Optimization*. Academic Press, 1981.

[49] Mingyang Gong, Xingbo Liu, Jason Trembly, and Christopher Johnson. Sulfur-tolerant anode materials for solid oxide fuel cell application. *Journal of Power Sources*, 168(2):289–298, 2007.

[50] John B. Goodenough. Oxide-ion electrolytes. *Annual Review of Materials Research*, 33:91 – 128, 2003.

[51] Craig Carl Goodson. Simulation of microwave heating of mullite rods. Master's thesis, Virginia Tech, 1997.

[52] David Goodwin. CANTERA Object-Oriented Software for Reacting Flows. URL http://www.cantera.org.

[53] David Goodwin. A pattern anode model with detailed chemistry. *ECS Meeting Abstracts*, 501(30):1253–1253, 2006. URL http://link.aip.org/link/?ECA/501/1253/1.

[54] R.J. Gorte, J.M. Vohs, and S. McIntosh. Recent developments on anodes for direct fuel utilization in SOFC. *Solid State Ionics*, 175(1-4):1 – 6, 2004.

[55] Gaurav K. Gupta, Jonathan R. Marda, Anthony M. Dean, Andrew M. Colclasure, Huayang Zhu, and Robert J. Kee. Performance predictions of a tubular SOFC operating on a partially reformed JP-8 surrogate. *Journal of Power Sources*, 162(1):553 – 562, 2006.

[56] B.A. Haberman and J.B. Young. A detailed three-dimensional simulation of an IP-SOFC stack. *Journal of Fuel Cell Science and Technology*, 5(1): 011006–1 – 12, 2008.

[57] Sossina M. Haile. Fuel cell materials and components. *Acta Materialia*, 51: 5981–6000, 2003.

[58] William S. Harvey, Jane H. Davidson, and Edward A. Fletcher. Thermolysis of hydrogen sulfide in the temperature range 1350-1600 K. *Industrial and Engineering Chemistry Research*, 37(6):2323 – 2332, 1998.

[59] K.A. Hawboldt, W.D. Monnery, and W.Y. Svrcek. New experimental data and kinetic rate expression for H_2S pyrolysis and re-association. *Chemical Engineering Science*, 55(5):957 – 966, 2000.

[60] Hongpeng He, Raymond J. Gorte, and John M. Vohs. Highly sulfur tolerant Cu-ceria anodes for SOFCs. *Electrochemical and Solid-State Letters*, 8(6): 279–280, 2005.

[61] Ethan S. Hecht, Gaurav K. Gupta, Huayang Zhu, Anthony M. Dean, Robert J. Kee, Luba Maier, and Olaf Deutschmann. Methane reforming kinetics within a Ni-YSZ SOFC anode support. *Applied Catalysis A: General*, 295(1):40–51, 2005.

[62] J.H. Hirschenhofer, D.B. Stauffer, R.R. Engleman, and M.G. Klett. *Fuel Cell Handbook*. U.S. Department of Energy, Morgantown, WV, 7th edition, 2004.

[63] Yun-Hui Huang, Ronald I. Dass, Zheng-Liang Xing, and John B. Goodenough. Double perovskites as anode materials for solid-oxide fuel cells. *Science*, 312(April 14):254–257, 2006.

[64] Shiqiang (Rob) Hui, Dongfang Yang, Zhenwei Wang, Sing Yick, Cyrille Deces-Petit, Wei Qu, Adam Tuck, Radenka Maric, and Dave Ghosh. Metal-supported solid oxide fuel cell operated at 400-600°C. *Journal of Power Sources*, 167(2):336 – 339, 2007.

[65] John H. Lienhard IV and John H. Lienhard V. *A heat transfer textbook*. Phlogiston press, Cambridge, MA, 3rd edition, 2008.

[66] Sadik Kakac, Anchasa Pramuanjaroenkij, and Xiang Yang Zhou. A review of numerical modeling of solid oxide fuel cells. *International Journal of Hydrogen Energy*, 32(7):761 – 786, 2007.

[67] V. Kaloidas and N. Papayannakos. Kinetics of thermal non-catalytic decomposition of hydrogen sulphide. *Chemical Engineering Science*, 44(11):2493 – 2500, 1989.

[68] Kunal Karan, Anil K. Mehrotra, and Leo A. Behie. On reaction kinetics for the thermal decomposition of hydrogen sulfide. *AIChE Journal*, 45(2):383 – 389, 1999.

[69] Robert J. Kee, Michael E. Coltrin, and Peter Galrborg. *Chemically Reacting Flow: Theory and Practice.* John Wiley & Sons, Hoboken, New Jersey, 2003.

[70] Robert J. Kee, Huayang Zhu, and David G. Goodwin. Solid-oxide fuel cells with hydrocarbon fuels. *Proceedings of the Combustion Institute*, 30:2379–2404, 2005.

[71] K. Kendall, C.M. Finnerty, G. Saunders, and J.T. Chung. Effects of dilution on methane entering an SOFC anode. *Journal of Power Sources*, 106(1-2): 323 – 327, 2002.

[72] Kevin Kendall, Nguyen Q. Minh, and Subhash C. Singhal. Cell and stack designs. In S. C. Singhal and K. Kendall, editors, *High Temperature Solid Oxide Fuel Cells: Fundamentals, Design and Applications*, pages 197–228. Elsevier Advanced Technology, Oxford, 2003.

[73] M. A. Khaleel and J. R. Selman. Cell, stack, and system modelling. In S. C. Singhal and K. Kendall, editors, *High Temperature Solid Oxide Fuel Cells: Fundamentals, Design and Applications*, pages 291–331. Elsevier Advanced Technology, Oxford, 2003.

[74] Jai-Woh Kim, Anil V. Virkar, Kuan-Zong Fung, Karun Mehta, and Subhash C. Singhal. Polarization effects in intermediate temperature, anode-supported solid oxide fuel cells. *Journal of The Electrochemical Society*, 146: 69–78, 1999.

[75] T.J. Kirk and J. Winnick. A hydrogen sulfide solid-oxide fuel cell using ceria-based electrolytes. *Journal of the Electrochemical Society*, pages 3494–6, 1993.

[76] A.A. Kulikovsky. On the nature of mixed potential in a DMFC. *Journal of the Electrochemical Society*, 152(6):1121–1127 –, 2005.

[77] Piyush K. Kundu and Ira M. Cohen. *Fluid Mechanics.* Academic Press, San Diego, CA, 2nd edition, 2002.

[78] Hideto Kurokawa, Tal Z. Sholklapper, Craig P. Jacobson, Lutgard C. De Jonghe, and Steven J. Visco. Ceria nanocoating for sulfur tolerant Ni-based anodes of solid oxide fuel cells. *Electrochemical and Solid-State Letters*, 10(9):135 – 138, 2007.

[79] Hideto Kurokawa, Liming Yang, Craig P. Jacobson, Lutgard C. De Jonghe, and Steven J. Visco. Y-doped $SrTiO_3$ based sulfur tolerant anode for solid oxide fuel cells. *Journal of Power Sources*, 164(2):510 – 518, 2007.

[80] Chih-Kuang Lin, Tsung-Ting Chen, Yau-Pin Chyou, and Lieh-Kwang Chiang. Thermal stress analysis of a planar SOFC stack. *Journal of Power Sources*, 164(1):238 – 251, 2007.

[81] Fuqiang Liu and Chao-Yang Wang. Mixed potential in a direct methanol fuel cell. *Journal of the Electrochemical Society*, 154(6):514–522, 2007.

[82] M. Liu, P. He, J. L. Luo, A. R. Sanger, and K. T. Chuang. Performance of a solid oxide fuel cell utilizing hydrogen sulfide as fuel. *Journal of Power Sources*, pages 20–25, 2001.

[83] Man Liu. *Hydrogen sulfide powered solid oxide fuel cells.* PhD thesis, University of Alberta, Edmonton, Canada, 2004.

[84] Man Liu, Guolin Wei, Jingli Luo, Alan R. Sanger, and Karl T. Chuang. Use of metal sulfides as anode catalysts in H_2S-air SOFCs. *Journal of the Electrochemical Society*, pages 1025–1029, 2003.

[85] C. Lu, W.L. Worrell, C. Wang, S. Park, H. Kim, J.M. Vohs, and R.J. Gorte. Development of solid oxide fuel cells for the direct oxidation of hydrocarbon fuels. *Solid State Ionics*, 152-153:393 – 397, 2002.

[86] Yoshio Matsuzaki and Isamu Yasuda. The poisoning effect of sulfur-containing impurity gas on a SOFC anode: Part i. dependence on temperature, time, and impurity concentration. *Solid State Ionics*, 132:261–269, 2000.

[87] Bonnie J. McBride, Sanford Gordon, and Martin A. Reno. Coefficients for calculating thermodynamic and transport properties of individual species (NASA TM-4513), October 1993.

[88] Bonnie J. McBride, Michael J. Zehe, and Sanford Gordon. Nasa glenn coefficients for calculating thermodynamic properties of individual species (NASA report TP-2002-211556), September 2002.

[89] Steven McIntosh and Raymond J. Gorte. Direct hydrocarbon solid oxide fuel cells. *Chemical Reviews*, 104(10):4845 – 4865, 2004.

[90] Remy Mevrel, Jean-Claude Laizet, Alban Azzopardi, Berange're Leclercq, Martine Poulain, Odile Lavigne, and Didier Demange. Thermal diffusivity and conductivity of $Zr_{1-x}Y_xO_{2-x/2}$ (x = 0, 0.084, and 0.179) single crystals. *Journal of the European Ceramic Society*, 24:3081–3089, 2004.

[91] Nguyen Q. Minh. Ceramic fuel cells. *Journal of the American Ceramic Society*, 76(3):563–588, 1993.

[92] Mogens Mogensen and Peter Vang Hendriksen. Testing of electrodes, cells and short stacks. In S. C. Singhal and K. Kendall, editors, *High Temperature Solid Oxide Fuel Cells: Fundamentals, Design and Applications*, pages 261–289. Elsevier Advanced Technology, Oxford, 2003.

[93] Dayadeep Monder, K. Nandakumar, and K.T. Chuang. Modeling an H_2S fed SOFC. volume P 2005-07, pages 837 – 844, Quebec, Canada, 2005.

[94] Dayadeep S. Monder, K. Nandakumar, and Karl T. Chuang. Model development for a SOFC button cell using H_2S as fuel. *Journal of Power Sources*, 162(1):400 – 414, 2006.

[95] Ronald G. Munro. Evaluated material properties for a sintered α-alumina. *Journal of of the American Ceramic Society*, 80(8):1919–1928, 1997.

[96] E. Perry Murray, T. Tsai, and S.A. Barnett. A direct-methane fuel cell with a ceria-based anode. *Nature*, 400(6745):649 – 651, 1999.

[97] Matthew Neurock. Applications: Catalysis. In *WTEC Panel on Applications of Molecular and Materials Modeling: International Technology Research Institute*, pages 77–106. Kluwer Academic, Baltimore, Maryland, 2002.

[98] John Newman and Karen E. Thomas-Alyea. *Electrochemical Systems.* John Wiley & Sons, Inc., Hoboken, N.J., 2004.

[99] Eranda Nikolla, Johannes Schwank, and Suljo Linic. Promotion of the long-term stability of reforming Ni catalysts by surface alloying. *Journal of Catalysis*, 250(1):85 – 93, 2007. ISSN 0021-9517. URL `http://dx.doi.org/10.1016/j.jcat.2007.04.020`.

[100] Michael Nolan, Joanne E. Fearon, and Graeme W. Watson. Oxygen vacancy formation and migration in ceria. *Solid State Ionics*, 177(35-36):3069 – 3074, 2006. ISSN 0167-2738. URL `http://dx.doi.org/10.1016/j.ssi.2006.07.045`.

[101] Ryan P. O'Hayre, Suk-Won Cha, Whitney Colella, and Fritz B. Prinz. *Fuel Cell Fundamentals.* John Wiley & Sons, New York, 2006.

[102] Keith B. Oldham and Jan C. Myland. *Fundamentals of Electrochemical Science.* Academic Press, San Diego, 1994.

[103] H. A. Olschewski, J. Troe, and H. Gg. Wagner. Kinetics of the high-temperature h_2s decomposition. *Journal of Physical Chemistry*, 98(49): 12964–12967, 1994.

[104] R. Mark Ormerod. Solid oxide fuel cells. *Chemical Society Reviews*, 32: 17–28, 2003.

[105] Seungdoo Park, J.M. Vohs, and R.J. Gorte. Direct oxidation of hydrocarbons in a solid-oxide fuel cell. *Nature*, 404(6775):265 – 7, 2000/03/16.

[106] D. Peterson and J. Winnick. A hydrogen sulfide fuel cell using a proton-conducting solid electrolyte. *Journal of the Electrochemical Society*, pages 55–6, 1996.

[107] Rojana Pornprasertsuk, Panchapakesan Ramanarayanan, Charles B. Musgrave, and Fritz B. Prinz. Predicting ionic conductivity of solid oxide fuel cell electrolyte from first principles. *Journal of Applied Physics*, 98(10):103513 –, 2005.

[108] Rojana Pornprasertsuk, Jeremy Cheng, Hong Huang, and Fritz B. Prinz. Electrochemical impedance analysis of solid oxide fuel cell electrolyte using

kinetic Monte Carlo technique. *Solid State Ionics*, 178(3-4):195 – 205, 2007. ISSN 0167-2738. URL `http://dx.doi.org/10.1016/j.ssi.2006.12.016`.

[109] N. U. Pujare, K. W. Semkow, and A. F. Sammells. A direct H_2S/air solid oxide fuel cell. *Journal of the Electrochemical Society*, pages 2639–40, 1987.

[110] Nirupama U. Pujare, Kan J. Tsai, and Anthony F. Sammells. Electrochemical claus process for sulfur recovery. *Journal of the Electrochemical Society*, pages 3662–3678, 1989.

[111] J. M. Ralph, A. C. Schoeler, and M. Krumpelt. Materials for lower temperature solid oxide fuel cells. *Journal of Materials Science*, 36:1161–1172, 2001.

[112] K.P. Recknagle, R.E. Williford, L.A. Chick, D.R. Rector, and M.A. Khaleel. Three-dimensional thermo-fluid electrochemical modeling of planar SOFC stacks. *Journal of Power Sources*, 113(1):109 – 114, 2003.

[113] R. C. Reid, J. M. Prausnitz, and B. E. Poling. *The Properties of Gases and Liquids*. McGraw-Hill, New York, 4 edition, 1987.

[114] R.B. Saeger, L.E. Scriven, and H.T. Davis. Transport processes in periodic porous media. *Journal of Fluid Mechanics*, 299:1–15, 1995.

[115] N.M. Sammes, Y. Du, and R. Bove. Design and fabrication of a 100 W anode supported micro-tubular SOFC stack. *Journal of Power Sources*, 145(2):428 – 434, 2005.

[116] Partho Sarkar, Luis Yamarte, Hongsang Rho, and Lorne Johanson. Anode-supported tubular micro-solid oxide fuel cell. *International Journal of Applied Ceramic Technology*, 4(2):103–S108, 2007.

[117] Wolfgang Schmickler. *Interfacial Electrochemistry*. Oxford University Press, New York, 1996.

[118] J. Robert Selman. Molten-salt fuel cells-technical and economic challenges. *Journal of Power Sources*, 160(2 SPEC ISS):852–857, 2006.

[119] K. Sendt, M. Jazbec, and B. S. Haynes. Chemical kinetic modeling of the H/S system: H_2S thermolysis and H_2 sulfidation. *Proceedings of the Combustion Institute*, 29:2439–2446, 2002.

[120] Robert F. Service. Shrinking fuel cells promise power in your pocket. *Science*, 296(5571):1222–1224, 2002.

[121] Takanobu Shimada, Tohru Kato, and Yohei Tanaka. Numerical analysis of thermal behavior of small solid oxide fuel cell systems. *Journal of Fuel Cell Science and Technology*, 4(3):299 – 307, 2007.

[122] Subhash C. Singhal and Kevin Kendall, editors. *High Temperature Solid Oxide Fuel Cells: Fundamentals, Design and Applications.* Elsevier Advanced Technology, Oxford, 2003.

[123] S. V. Slavov, K. T. Chuang, A. R. Sanger, J. C. Donini, J. Kot, and S. Petrovic. Proton-conducting solid state $H_2S - O_2$ fuel cell. i. anode catalysts, and operation at atmospheric pressure and 20-90°C. *International Journal of Hydrogen Energy*, pages 1203–1212, 1998.

[124] Joseph M. Smith, Hendrick C. Van Ness, and Michael M. Abbott, editors. *Introduction to chemical engineering thermodynamics.* McGraw-Hill, Boston, 7th edition, 2005.

[125] Mingyong Sun, Alan E. Nelson, and John Adjaye. Ab initio DFT study of hydrogen dissociation on MoS_2, NiMoS, and CoMoS: Mechanism, kinetics, and vibrational frequencies. *Journal of Catalysis*, pages 411–421, 2005.

[126] Svein Sunde. Simulations of composite electrodes in fuel cells. *Journal of Electroceramics*, 5(2):153 – 182, 2000.

[127] Toshio Suzuki, Toshiaki Yamaguchi, Yoshinobu Fujishiro, and Masanobu Awano. Fabrication and characterization of micro tubular SOFCs for operation in the intermediate temperature. *Journal of Power Sources*, 160(1):73 – 77, 2006.

[128] Ross Taylor and R. Krishna. *Multicomponent Mass Transfer.* John Wiley & Sons, New York, U.S.A., 1993.

[129] The Mathworks. *Getting Started with MATLAB: Version 7.* The Mathworks Inc., Natick, MA, 2005. URL `http://www.mathworks.com/products/matlab/`.

[130] The Mathworks. *Curve Fitting Toolbox User's Guide: Version 1.* The Mathworks Inc., Natick, MA, 2004.

[131] The Mathworks. *Optimization Toolbox User's Guide: Version 3.* The Mathworks Inc., Natick, MA, 2004.

[132] Piotr Tomczyk. MCFC versus other fuel cells-Characteristics, technologies and prospects. *Journal of Power Sources*, 160(2 SPEC ISS):858–862, 2006.

[133] D. G. Truhlar and K. Morokuma, editors. *Transition State Modeling for Catalysis.* ACS Symposium Series 721. American Chemical Society, Washington D.C., 1999.

[134] Costas G. Vayenas, Pablo G. Debenedetti, Iannis Yentekakis, and L. Louis Hegedus. Cross-flow, solid-state electrochemical reactors: A steady-state analysis. *Industrial & Engineering Chemistry, Fundamentals*, pages 316–324, 1985.

[135] V. Vorontsov, J.L. Luo, A.R. Sanger, and K.T. Chuang. Synthesis and characterization of new ternary transition metal sulfide anodes for H_2S-powered SOFC. *Journal of Power Sources*, in press, 2008. URL `http://www.sciencedirect.com/science/article/B6TH1-4SDPX77-2/1/c8b4d0c50f02a3df6b4db444e16ff225`.

[136] Jeng-Han Wang and Meilin Liu. Computational study of sulfur-nickel interactions: A new S-Ni phase diagram. *Electrochemistry Communications*, 9 (9):2212–2217, September 2007. doi: {10.1016/j.elecom.2007.06.022}.

[137] Jeng-Han Wang and MeiLin Liu. Surface regeneration of sulfur-poisoned Ni surfaces under SOFC operation conditions predicted by first-principles-based thermodynamic calculations. *Journal of Power Sources*, 176(1):23–30, January 21 2008. doi: {10.1016/j.jpowsour.2007.10.025}.

[138] J. Warnatz, U. Maas, and R.W. Dibble. *Combustion: Physical and Chemical Fundamentals, Modeling and Simulation, Experiments, Pollutant Formation.* Springer-Verlag, Berlin, 3rd edition, 2001.

[139] S. Wasmus and A. Küver. Methanol oxidation and direct methanol fuel cells: a selective review. *Journal of Electroanalytical Chemistry*, 461:14–31, 1999.

[140] G. L. Wei, M. Liu, J. L. Luo, A. R. Sanger, and K. T. Chuang. Influence of gas flow rate on performance of H_2S-air solid oxide fuel cells with MoS_2 – NiS – Ag anode. *Journal of the Electrochemical Society*, pages 463–469, 2003.

[141] Guo-Lin Wei, Jing-Li Luo, Alan R. Sanger, and Karl T. Chuang. High-performance anode for H_2S-air SOFCs. *Journal of the Electrochemical Society*, pages 232–237, 2004.

[142] Guo-Lin Wei, Jing-Li Luo, Alan R. Sanger, Karl T. Chuang, and Li Zhong. Li_2SO_4-based proton-conducting membrane for H_2S-air fuel cell. *Journal of Power Sources*, pages 1–9, 2005.

[143] J.R. Wilson, D.T. Schwartz, and S.B. Adler. Nonlinear electrochemical impedance spectroscopy for solid oxide fuel cell cathode materials. *Electrochimica Acta*, 51(8-9):1389 – 1402, 2006.

[144] D. Woiki and P. Roth. Kinetics of the High-Temperature H_2S Decomposition. *Journal of Physical Chemistry*, 98(49):12958–12963, 1994.

[145] Chris Yates and Jack Winnick. Anode materials for a hydrogen sulfide solid oxide fuel cell. *Journal of the Electrochemical Society*, pages 2841–2844, 1999.

[146] Ken-Ming Yin. A theoretical model of the membrane electrode assembly of liquid feed direct methanol fuel cell with consideration of water and methanol crossover. *Journal of Power Sources*, 179(2):700 – 710, 2008.

[147] Harumi Yokokawa and Teruhisa Horita. Cathodes. In S. C. Singhal and K. Kendall, editors, *High Temperature Solid Oxide Fuel Cells: Fundamentals, Design and Applications*, pages 119–147. Elsevier Advanced Technology, Oxford, 2003.

[148] John B. Young. Thermofluid modeling of fuel cells. *Annual Review of Fluid Mechanics*, 39:193 – 215, 2007.

[149] J. Zaman and A. Chakma. Production of hydrogen and sulfur from hydrogen sulfide. *Fuel Processing Technology*, 41:159–198, 1995.

[150] Shaowu Zha, Zhe Cheng, and Meilin Liu. A sulfur-tolerant anode material for SOFCs: $Gd_2Ti_{0.4}Mo_{0.6}O_7$. *Electrochemical and Solid-State Letters*, 8(8): 406–408, 2005.

[151] Zhongliang Zhan and Scott A. Barnett. An octane-fueled solid oxide fuel cell. *Science*, 308(5723):844 – 7, 2005.

[152] Huayang Zhu and Robert J. Kee. Modeling electrochemical impedance spectra in SOFC button cells with internal methane reforming. *Journal of the Electrochemical Society*, 153(9):1765–1772 –, 2006.

[153] Huayang Zhu, Robert J. Kee, Vinod M. Janardhanan, Olaf Deutschmann, and David G. Goodwin. Modeling elementary heterogeneous chemistry and electrochemistry in solid-oxide fuel cells. *Journal of the Electrochemical Society*, 152(12):2427–2440, 2005.

[154] Tom Ziegler and Jochen Autschbach. Theoretical methods of potential use for studies of inorganic reaction mechanisms. *Chemical Reviews*, 105:2695–2722, 2005.

Appendix A

Overall rate equations for a H_2S electro-oxidation mechanism

We give derivations for the overall rate equations (3.67) and (3.69) in chapter 3. The analysis given here assumes that the reaction is at steady state and that one of the elementary reactions is much slower than than the rest. The complete mechanism proposed in chapter 3 is reproduced here for easier reference.

$$H_2S + V_a \rightleftarrows H_2S.V_a \tag{A.1}$$

$$H_2S.V_a + V_a \rightleftarrows SH.V_a + H.V_a \tag{A.2}$$

$$SH.V_a + V_a \rightleftarrows S.V_a + H.V_a \tag{A.3}$$

$$O_O^x + V_e \rightleftarrows O^{2-}.V_e + V_O^{\cdot\cdot} \tag{A.4}$$

$$H.V_a + O^{2-}.V_e \rightleftarrows OH^-.V_e + V_a + e^- \tag{A.5}$$

$$OH^-.V_e + H.V_a \rightleftarrows H_2O.V_e + V_a + e^- \tag{A.6}$$

$$H_2O.V_e \rightleftarrows H_2O + V_e \tag{A.7}$$

$$2S.V_a \rightleftarrows S_2 + 2V_a \tag{A.8}$$

V_e is a surface site on the electrolyte, V_a is a surface site on the anode, O_O^x is an O in the electrolyte bulk, and $V_O^{\cdot\cdot}$ is an oxygen vacancy in the electrolyte bulk.

The net rates of reaction for each of the steps above are given by mass action kinetics (A.9)...(A.16).

$$r_1 = k_1 P_{H_2S}\theta_a - k_{-1}\theta_{H_2S} \tag{A.9}$$

$$r_2 = k_2\theta_{H_2S}\theta_a - k_{-2}\theta_{SH}\theta_H \tag{A.10}$$

$$r_3 = k_3\theta_{SH}\theta_a - k_{-3}\theta_S\theta_H \tag{A.11}$$

$$r_4 = k_4\hat{\theta}_e - k_{-4}\hat{\theta}_O \tag{A.12}$$

$$r_5 = k_5\theta_H\hat{\theta}_O e^{(1-\beta_5)fE_a} - k_{-5}\hat{\theta}_{OH}\theta_a e^{-\beta_5 fE_a} \tag{A.13}$$

$$r_6 = k_6\hat{\theta}_{OH}\theta_H e^{(1-\beta_6)fE_a} - k_{-6}\hat{\theta}_{H_2O}\theta_a e^{-\beta_6 fE_a} \tag{A.14}$$

$$r_7 = k_7\hat{\theta}_{H_2O} - k_{-7}P_{H_2O}\hat{\theta}_e \tag{A.15}$$

$$r_8 = k_8\theta_S^2 - k_{-8}P_{S_2}\theta_a^2 \tag{A.16}$$

P_k is the partial pressure of gas species k, θ_m is the surface coverage of species m on the anode, E_a is the anode electrical potential, $\hat{\theta}_n$ is the surface coverage of species m on the electrolyte, and k_i, k_{-i} are the temperature dependent forward and backward rate constants for reaction i in the list (A.1)...(A.8). The units for the reaction rates r_i are mole/(m_{tpb}.s) where m_{tpb} is the length of the active triple phase boundary (tpb) in the anode in metres. Reactions 5 and 6 will generally have different charge transfer coefficients β_i.

The surface coverage θ_m is defined as the ratio of the number of sites occupied by species m to the total number of sites available on the anode surface. $\hat{\theta}_n$ is defined similarly for the electrolyte surface.

A.1 RDS → Step 2, dissociation of H_2S

If we assume the H_2S dissociation reaction is rate controlling, steps 1, 3, 4, 5, 6, 7, 8 in the above mechanism (A.1, A.3 - A.8) are in quasi-equilibrium as a result of having much higher reaction rates than step 2 (A.2), then the following equations give the various surface coverages.

$$k_1 P_{H_2S}\theta_a = k_{-1}\theta_{H_2S}$$

$$\theta_{H_2S} = K_1 P_{H_2S}\theta_a \tag{A.17}$$

$K_i = k_i/k_{-i}$ is the equilibrium constant for the i^{th} reaction.

$$k_3\theta_{\mathrm{SH}}\theta_a = k_{-3}\theta_{\mathrm{S}}\theta_{\mathrm{H}}$$
$$\theta_{\mathrm{SH}} = K_3^{-1}\theta_{\mathrm{S}}\theta_{\mathrm{H}}\theta_a^{-1} \tag{A.18}$$

$$k_4\hat{\theta}_e = k_{-4}\hat{\theta}_{\mathrm{O}}$$
$$\hat{\theta}_{\mathrm{O}} = K_4\hat{\theta}_e \tag{A.19}$$

$$k_5\hat{\theta}_{\mathrm{O}}\theta_{\mathrm{H}}e^{(1-\beta_5)f\Delta\phi} = k_{-5}\hat{\theta}_{\mathrm{OH}}\theta_a e^{-\beta_5 f\Delta\phi}$$
$$\theta_{\mathrm{H}} = K_5^{-1}\hat{\theta}_{\mathrm{O}}^{-1}\hat{\theta}_{\mathrm{OH}}\theta_a e^{-f\Delta\phi} \tag{A.20}$$

$$k_6\hat{\theta}_{\mathrm{OH}}\theta_{\mathrm{H}}e^{(1-\beta_6)fE_a} = k_{-6}\hat{\theta}_{\mathrm{H_2O}}\theta_a e^{-\beta_6 fE_a}$$
$$\hat{\theta}_{\mathrm{OH}} = K_6^{-1}\theta_{\mathrm{H}}^{-1}\hat{\theta}_{\mathrm{H_2O}}\theta_a e^{-f\Delta\phi} \tag{A.21}$$

$$k_7\hat{\theta}_{\mathrm{H_2O}} = k_{-7}P_{\mathrm{H_2O}}\hat{\theta}_e$$
$$\hat{\theta}_{\mathrm{H_2O}} = K_7^{-1}P_{\mathrm{H_2O}}\theta_e \tag{A.22}$$

$$k_8\theta_{\mathrm{S}}^2 = k_{-8}P_{\mathrm{S_2}}\theta_a^2$$
$$\theta_{\mathrm{S}} = \sqrt{K_8^{-1}P_{\mathrm{S_2}}}\theta_a \tag{A.23}$$

Doing the site balance for the surface coverage:

$$\theta_a + \theta_{\mathrm{S}} + \theta_{\mathrm{H}} + \theta_{\mathrm{SH}} + \theta_{\mathrm{H_2S}} = 1 \tag{A.24}$$

$$\left[1+\sqrt{\frac{P_{S_2}}{K_8}}+K_1P_{H_2S}+\frac{\sqrt{P_{H_2O}}}{K_4K_5K_6K_7}e^{-f\Delta\phi}+\right.$$
$$\left.\frac{\sqrt{P_{H_2O}P_{S_2}}}{K_3\sqrt{K_4K_5K_6K_7K_8}}e^{-f\Delta\phi}\right]\theta_a=1 \tag{A.25}$$

Substituting the expressions for θ_i into A.9 we get:

$$r_2=k_2K_1P_{H_2S}\theta_a^2-k_{-2}\frac{\sqrt{P_{S_2}}P_{H_2O}}{K_3K_4K_5K_6K_7\sqrt{K_8}}e^{-2f\Delta\phi}\theta_a^2 \tag{A.26}$$

$$r_2=k_2K_1\left(P_{H_2S}-\frac{\sqrt{P_{S_2}}P_{H_2O}}{K_{eq}}e^{-2f\Delta\phi}\right)\theta_a^2 \tag{A.27}$$

θ_a, and K_{eq} in (A.27) are given by (A.28) and (A.29) below.

$$\theta_a=\left[1+\sqrt{\frac{P_{S_2}}{K_8}}+K_1P_{H_2S}+\frac{\sqrt{P_{H_2O}}}{K_4K_5K_6K_7}e^{-f\Delta\phi}+\right.$$
$$\left.\frac{\sqrt{P_{H_2O}P_{S_2}}}{K_3\sqrt{K_4K_5K_6K_7K_8}}e^{-f\Delta\phi}\right]^{-1} \tag{A.28}$$

$$K_{eq}=K_1K_2K_3K_4K_5K_6K_7\sqrt{K_8} \tag{A.29}$$

If we substitute the expressions for K_i obtained by setting $r_i=0$ in (A.9 ... A.16) into (A.29), we get (A.30).

$$K_{eq}=\frac{P_{H_2O,in}\sqrt{P_{S_2,in}}}{P_{H_2S,in}}e^{-2f\Delta\phi_{eq}}=\frac{P_{H_2O,in}\sqrt{P_{S_2,in}}}{P_{H_2S,in}}e^{-2fE_{a,eq}} \tag{A.30}$$

$\Delta\phi_{eq}=E_{a,eq}$ is the Nernst potential for the overall H_2S electrochemical oxidation reaction on the anode, and $P_{k,in}$ are the inlet/reference partial pressures of the gas phase species.

If we use $P_{k,in} = 1$, (A.30) can be written as (A.31).

$$K_{eq} = e^{-2fE_a^\circ} \tag{A.31}$$

E° is the unit activity Nernst potential for the overall anode H_2S oxidation reaction.

Writing the rate equation (A.27) in terms of current density and substituting (A.31), we get (A.32) below.

$$i_{a,2} = i_{a,2}^\circ \left(P_{H_2S} - P_{H_2O}\sqrt{P_{S_2}} e^{-2f\eta_a} \right) \tag{A.32}$$

$i_{a,2}^\circ$ and η_a are given by the expressions below.

$$\eta_a = \Delta\phi - \Delta\phi^\circ = E_a - E_a^\circ \tag{A.33}$$

$$i_{a,2}^\circ = \frac{2FK_1'}{\left(1 + K_2'\sqrt{P_{S_2}} + K_3'\sqrt{P_{H_2O}}e^{-f\eta_a} + K_4'\sqrt{P_{H_2O}P_{S_2}}e^{-f\eta_a} + K_5'P_{H_2S}\right)^2} \tag{A.34}$$

$$K_1' = k_2 K_1 \tag{A.35}$$

$$K_2' = \sqrt{\frac{1}{K_8}} \tag{A.36}$$

$$K_3' = \frac{1}{K_4 K_5 K_6 K_7} \tag{A.37}$$

$$K_4' = \frac{1}{K_3\sqrt{K_4 K_5 K_6 K_7 K_8}} \tag{A.38}$$

$$K_5' = K_1 \tag{A.39}$$

A.2 RDS → Step 6, second proton transfer

Here we assume the second proton tranfer reaction (A.6) is rate controlling and steps 1, 2, 3, 4, 5, 7, 8 in the above mechanism (A.1 – A.5, A.7, A.8) are in quasi-equilibrium as a result of having much higher reaction rates than step 6. Equations (A.9 – A.13, A.15, A.16) can be rearranged to get expressions for all the various surface coverages in terms of the gas phase partial pressures, θ_a and $\hat{\theta}_e$.

Plugging these into (A.14), we get equation (A.43) below.

$$r_6 = k_6 \left(K_1 K_2 K_3 K_4 K_5\right)^2 K_6 K_7 K_8 \frac{P_{H_2S}^2}{P_{H_2O} P_{S_2}} e^{(4-\beta_6) f E_a} \theta_a \hat{\theta}_e - \frac{k_{-6}}{K_7} P_{H_2O} e^{-\beta_6 f E_a} \theta_a \hat{\theta}_e \quad \text{(A.40)}$$

$$r_6 = k_6 \left(K_1 K_2 K_3 K_4 K_5\right)^2 K_6 K_7 K_8 \left(\frac{P_{H_2S}^2}{P_{H_2O} P_{S_2}} e^{(4-\beta_6) f E_a} \theta_a \hat{\theta}_e - \frac{1}{K_{eq}^2} P_{H_2O} e^{-\beta_6 f E_a} \right) \theta_a \hat{\theta}_e \quad \text{(A.41)}$$

$$r_6 = k_6 \left(K_1 K_2 K_3 K_4 K_5\right)^2 K_6 K_7 K_8 \frac{P_{H_2S}^2}{P_{H_2O} P_{S_2}} e^{(4-\beta_6) f E_a} \theta_a \hat{\theta}_e - \frac{k_{-6}}{K_7} P_{H_2O} e^{-\beta_6 f E_a} \theta_a \hat{\theta}_e \quad \text{(A.42)}$$

which can be rewritten as:

$$r_6 = k_6 \left(K_1 K_2 K_3 K_4 K_5\right)^2 K_6 K_7 K_8 \left(\frac{P_{H_2S}^2}{P_{H_2O} P_{S_2}} e^{(4-\beta_6) f E_a} - \frac{1}{K_{eq}^2} P_{H_2O} e^{-\beta_6 f E_a} \right) \theta_a \hat{\theta}_e \quad \text{(A.43)}$$

θ_a and $\hat{\theta}_e$ are evaluated using the site balance equations (A.44 and A.45) and lead to equations (A.46 and A.47).

$$\theta_a + \theta_S + \theta_H + \theta_{SH} + \theta_{H_2S} = 1 \quad \text{(A.44)}$$

$$\hat{\theta}_e + \hat{\theta}_O + \hat{\theta}_{OH} + \hat{\theta}_{H_2O} = 1 \quad \text{(A.45)}$$

$$\theta_a = \left[1 + K_2'' \sqrt{P_{S_2}} + K_3'' \frac{P_{H_2S}}{\sqrt{P_{H_2O} P_{S_2}}} e^{fE_a} + K_4'' \frac{P_{H_2S}}{\sqrt{P_{H_2O}}} e^{fE_a} + K_5'' P_{H_2S}\right]^{-1} \tag{A.46}$$

$$\hat{\theta}_e = \left[1 + K_6'' + K_7'' \frac{P_{H_2S}}{\sqrt{P_{H_2O} P_{S_2}}} e^{2fE_a} + K_8'' P_{H_2O}\right]^{-1} \tag{A.47}$$

As in the previous section, we can write the rate equation (A.43) in terms of current density and substitute the expression for K_{eq} in (A.31) to get (A.48) below. The potential dependent terms in equation (A.48) are all in terms of the activation overpotential: $\eta_a = E_a - E_a^o$.

$$i_{a,6} = i_{a,6}^o \left(\frac{P_{H_2S}^2}{P_{H_2O} P_{S_2}} e^{(4-\beta_6) f\eta_a} - P_{H_2O} e^{-\beta_6 f\eta_a} \right) \tag{A.48}$$

$i_{a,6}^o$ is given by equation (A.49) below.

$$i_{a,6}^o = \frac{2FK_1'''}{\left(1 + K_2''' \sqrt{P_{S_2}} + K_3''' P_{H_2S} + K_4''' \frac{P_{H_2S}}{\sqrt{P_{H_2O}}} e^{f\eta_a} + K_5''' \frac{P_{H_2S}}{\sqrt{P_{H_2O} P_{S_2}}} e^{f\eta_a}\right)} \times \frac{1}{\left(1 + K_6''' + K_7''' P_{H_2O} + K_8''' \frac{P_{H_2S}}{\sqrt{P_{H_2O} P_{S_2}}} e^{2f\eta_a}\right)} \tag{A.49}$$

K_i'' and K_i''' are different combinations of the kinetic rate constants k_i, k_{-i}.

Appendix B

Nernst potential for a fuel at chemical equilibrium

If a fuel containing H_2S is brought to chemical equilibrium at high temperature, the H_2S will dissociate to give H_2 and gaseous sulfur at shown in (B.1). At the temperatures of interest to this study, the predominant form of sulfur is diatomic sulfur.

$$H_2S \Leftrightarrow H_2 + \frac{1}{2}S_2 \tag{B.1}$$

This H_2 and S_2 can now be electrochemically oxidized instead of (or along with) the H_2S. The overall oxidation reactions (B.2) - (B.4) and the Nernst potentials (B.5) - (B.7) for some of these possible electrochemical oxidation reactions are given below.

$$H_2S + \frac{1}{2}O_2 \Leftrightarrow H_2O + \frac{1}{2}S_2 \tag{B.2}$$

$$H_2 + \frac{1}{2}O_2 \Leftrightarrow H_2O \tag{B.3}$$

$$S_2 + 2\,O_2 \Leftrightarrow 2\,SO_2 \tag{B.4}$$

$$E_{H_2S\rightarrow S_2} = E^{\circ}_{H_2S} + \frac{RT}{2F}\ln\left\{\frac{P_{H_2S}\sqrt{P_{O_2}}}{P_{H_2O}\sqrt{P_{S_2}}}\right\} \tag{B.5}$$

$$E_{H_2} = E^{\circ}_{H_2} + \frac{RT}{2F}\ln\left\{\frac{P_{H_2}\sqrt{P_{O_2}}}{P_{H_2O}}\right\} \tag{B.6}$$

$$E_{S_2} = E^{\circ}_{S_2} + \frac{RT}{8F}\ln\left\{\frac{P_{S_2}P^2_{O_2}}{P^2_{H_2O}}\right\} \tag{B.7}$$

If the fuel is at chemical equilibrium, reaction (B.1) is at equilibrium, and the chemical potential change for the reaction is zero:

$$\mu_{H_2} + \frac{1}{2}\mu_{S_2} - \mu_{H_2S} = 0 \tag{B.8}$$

We know that $\mu_i = \mu^{\circ}_i + RT\ln a_i$, where μ°_i is the chemical potential at standard pressure, a_i is the activity of component i, and the other symbols have their usual meaning [124]. Note that μ°_i is a function of T. For an ideal gas, $a_i = P_i/P^{\circ}$, where P_i is the partial pressure of i, and P° is the reference pressure. If we stick to normal conventions and write P_i in bar while using $P^{\circ} = 1\text{bar}$, we can replace a_i by P_i. Thus, we can rewrite (B.8) as:

$$\mu^{\circ}_{H_2} + \frac{1}{2}\mu^{\circ}_{S_2} - \mu^{\circ}_{H_2S} = RT\ln\frac{P_{H_2S}}{P_{H_2}\sqrt{P_{S_2}}} \tag{B.9}$$

$$\mu^{\circ}_{H_2} + \frac{1}{2}\mu^{\circ}_{S_2} + RT\ln P_{H_2}\sqrt{P_{S_2}} = \mu^{\circ}_{H_2S} + \ln P_{H_2S} \tag{B.10}$$

$$\left\{\mu^{\circ}_{H_2S} - \frac{1}{2}\mu^{\circ}_{S_2}\right\} + RT\ln\frac{P_{H_2S}}{\sqrt{P_{S_2}}} = \mu^{\circ}_{H_2} + RT\ln P_{H_2} \tag{B.11}$$

Now, let us take the standard state equilibrium voltage in the Nernst equation for H_2S oxidation, $E^{\circ}_{H_2S}$ in (B.5), and rewrite it in terms of the standard chemical potentials.

$$E_{H_2S\rightarrow S_2} = \frac{-\Delta\mu^{\circ}_{H_2S\rightarrow S_2}}{2F} + \frac{RT}{2F}\ln\left\{\frac{P_{H_2S}\sqrt{P_{O_2}}}{P_{H_2O}\sqrt{P_{S_2}}}\right\} \tag{B.12}$$

$$E_{H_2S\rightarrow S_2} = \frac{1}{2F}\left[\mu^{\circ}_{H_2S} + \frac{1}{2}\mu^{\circ}_{O_2} - \frac{1}{2}\mu^{\circ}_{S_2} - \mu^{\circ}_{H_2O} + RT\ln\left\{\frac{P_{H_2S}\sqrt{P_{O_2}}}{P_{H_2O}\sqrt{P_{S_2}}}\right\}\right] \tag{B.13}$$

Substituting (B.11) into (B.13), we get:

$$E_{H_2S\rightarrow S_2} = \frac{1}{2F}\left[\mu^{\circ}_{H_2} + \frac{1}{2}\mu^{\circ}_{O_2} - \mu^{\circ}_{H_2O} + RT\ln P_{H_2} + RT\ln\left\{\frac{\sqrt{P_{O_2}}}{P_{H_2O}}\right\}\right] \tag{B.14}$$

This can be written as:

$$E_{H_2S\rightarrow S_2} = \frac{1}{2F}\left[-\Delta\mu^{\circ}_{H_2\rightarrow H_2O} + RT\ln\left\{\frac{P_{H_2}\sqrt{P_{O_2}}}{P_{H_2O}}\right\}\right] \tag{B.15}$$

$$E_{H_2S\rightarrow S_2} = E^{\circ}_{H_2} + \frac{RT}{2F}\ln\left\{\frac{P_{H_2}\sqrt{P_{O_2}}}{P_{H_2O}}\right\} \tag{B.16}$$

$$E_{H_2S\rightarrow S_2} = E_{H_2} \tag{B.17}$$

Thus, if a fuel mixture containing H_2S is brought to chemical equilibrium, the Nernst potential for the H_2S oxidation reaction is equal to the Nernst potential for the H_2 oxidation reaction. To arrive at the above equality (B.17), we considered the H_2S dissociation reaction to be at equilibrium (B.1). For a mixture at chemical equilibrium all possible reactions between the constituents of the mixture are at equilibrium [124]. If we consider the reaction of S_2 and H_2O to give SO_2 and H_2 (B.18), a similar analysis as the one above gives $E_{H_2} = E_{S_2}$.

$$H_2O + \frac{1}{2}S_2 \Leftrightarrow SO_2 + 2\,H_2 \tag{B.18}$$

In fact, the Nernst potentials for all the possible oxidation reactions are identical in a fuel mixture at chemical equilibrium. In other words, it is not possible to distinguish between the open circuit voltage for different possible fuels in a mixture

if the fuel mixture is at chemical equilibrium.

Appendix C

Parameter estimation: i^{O} estimates for cases 2 and 3

We ran the parameter estimation described in chapter 7 for three different parameter combinations:

1. $i^{\circ}_{H_2S}$ and $i^{\circ}_{O_2}$ i.e., only H_2S is oxidized on the anode.
2. $i^{\circ}_{H_2}$ and $i^{\circ}_{O_2}$ i.e., only H_2 is oxidized on the anode.
3. $i^{\circ}_{H_2S}$, $i^{\circ}_{H_2}$, and $i^{\circ}_{O_2}$ i.e., both H_2S and H_2 are oxidized on the anode.

The case 1 results are presented in section 7.7.1. The i° estimates for cases 2 and 3 are given in tables C.1...C.4.

Table C.1: Estimated $i^{\circ}_{H_2}$ and $i^{\circ}_{O_2}$ (case 2) as functions of y_{H_2S}

$[H_2S - N_2 - H_2]$ (ml/min)	Time (hh:mm)	T (°C)	IV (#)	$i^{\circ}_{H_2}$ (A/m^2)	$i^{\circ}_{O_2}$ (A/m^2)	Scaled fit –
$[100 - 0 - 0]$	1:38		6	4.17×10^3	6.70×10^1	3.67×10^{-2}
$[80 - 20 - 0]$	2:12	750	7	5.11×10^3	7.51×10^1	3.18×10^{-2}
$[40 - 60 - 0]$	3:52		10	9.76×10^3	9.90×10^1	2.33×10^{-2}
$[100 - 0 - 0]$	4:33		11	5.35×10^3	8.78×10^1	2.66×10^{-2}
$[100 - 0 - 0]$	7:24		1	3.28×10^3	3.47×10^2	6.29×10^{-3}
$[80 - 20 - 0]$	8:12	800	2	2.75×10^3	3.95×10^2	5.57×10^{-3}
$[40 - 60 - 0]$	8:49		3	4.60×10^3	6.05×10^2	8.10×10^{-3}
$[100 - 0 - 0]$	10:10		7	3.02×10^3	6.96×10^2	7.10×10^{-3}
$[100 - 0 - 0]$	24:24		11	3.43×10^3	6.56×10^2	7.17×10^{-3}
$[10 - 90 - 0]$	24:47		12	2.94×10^4	2.54×10^2	2.98×10^{-2}
$[20 - 80 - 0]$	25:46		13	2.35×10^4	2.82×10^2	2.02×10^{-2}
$[100 - 0 - 0]$	30:38	850	6	2.34×10^3	1.24×10^3	6.78×10^{-3}
$[40 - 60 - 0]$	31:08		7	2.96×10^3	1.48×10^4	3.91×10^{-3}
$[10 - 90 - 0]$	32:41		10	1.83×10^4	2.57×10^2	2.12×10^{-2}
$[100 - 0 - 0]$	33:33		12	2.19×10^3	1.08×10^3	7.94×10^{-3}

Table C.2: Estimated $i^{\circ}_{H_2}$ and $i^{\circ}_{O_2}$ (case 2) as functions of y_{H_2}

$[H_2S - N_2 - H_2]$ (ml/min)	Time (hh:mm)	T (°C)	IV (#)	$i^{\circ}_{H_2}$ (A/m^2)	$i^{\circ}_{O_2}$ (A/m^2)	Scaled fit –
$[40 - 60 - 0]$	3:52		10	9.76×10^3	9.90×10^1	2.33×10^{-2}
$[40 - 50 - 10]$	5:05	750	12	1.17×10^3	6.02×10^1	1.79×10^{-2}
$[40 - 40 - 20]$	5:25		13	7.75×10^2	5.59×10^1	2.02×10^{-2}
$[40 - 20 - 40]$	6:02		14	4.99×10^2	5.07×10^1	2.21×10^{-2}
$[100 - 0 - 0]$	6:25		15	6.03×10^3	9.89×10^1	2.31×10^{-2}
$[40 - 60 - 0]$	8:49		3	4.60×10^3	6.05×10^2	8.10×10^{-3}
$[40 - 50 - 10]$	9:31	800	5	1.11×10^3	5.18×10^2	3.04×10^{-3}
$[40 - 20 - 40]$	9:52		6	6.59×10^2	2.54×10^2	1.38×10^{-3}
$[100 - 0 - 0]$	10:10		7	3.02×10^3	6.96×10^2	7.10×10^{-3}
$[20 - 80 - 0]$	25:46		13	2.35×10^4	2.82×10^2	2.02×10^{-2}
$[20 - 60 - 20]$	26:14		14	1.06×10^3	4.49×10^2	6.68×10^{-3}
$[40 - 60 - 0]$	31:08		7	2.96×10^3	1.48×10^4	3.91×10^{-3}
$[40 - 50 - 10]$	31:40	850	8	1.20×10^3	1.81×10^3	6.06×10^{-3}
$[40 - 20 - 40]$	32:03		9	8.51×10^2	3.62×10^2	3.12×10^{-3}
$[10 - 90 - 0]$	32:41		10	1.83×10^4	2.57×10^2	2.12×10^{-2}
$[10 - 80 - 10]$	33:05		11	1.35×10^3	7.47×10^2	2.23×10^{-3}
$[100 - 0 - 0]$	33:33		12	2.19×10^3	1.08×10^3	7.94×10^{-3}

Table C.3: Estimated $i^{\circ}_{H_2S}$, $i^{\circ}_{H_2}$, and $i^{\circ}_{O_2}$ (case 3) as functions of y_{H_2S}

$[H_2S - N_2 - H_2]$ (ml/min)	Time (hh:mm)	T (°C)	IV (#)	$i^{\circ}_{H_2S}$ (A/m^2)	$i^{\circ}_{H_2}$ (A/m^2)	$i^{\circ}_{O_2}$ (A/m^2)	Scaled fit –
$[100 - 0 - 0]$	1:38		6	4.71×10^2	1.32×10^3	4.75×10^1	3.45×10^{-2}
$[80 - 20 - 0]$	2:12	750	7	6.10×10^2	1.60×10^3	5.10×10^1	2.92×10^{-2}
$[40 - 60 - 0]$	3:52		10	1.24×10^2	2.69×10^3	6.19×10^1	1.76×10^{-2}
$[100 - 0 - 0]$	4:33		11	6.25×10^2	1.72×10^3	6.00×10^1	2.31×10^{-2}
$[100 - 0 - 0]$	7:24		1	8.20×10^2	8.16×10^2	3.38×10^2	2.66×10^{-3}
$[80 - 20 - 0]$	8:12	800	2	7.79×10^2	5.90×10^2	3.79×10^2	2.17×10^{-3}
$[40 - 60 - 0]$	8:49		3	1.20×10^3	1.22×10^3	5.46×10^2	1.65×10^{-3}
$[100 - 0 - 0]$	10:10		7	7.90×10^2	6.98×10^2	6.68×10^2	4.29×10^{-3}
$[100 - 0 - 0]$	24:24		11	8.80×10^2	7.20×10^2	6.33×10^2	2.91×10^{-3}
$[10 - 90 - 0]$	24:47		12	6.46×10^3	9.01×10^3	1.73×10^2	2.55×10^{-2}
$[20 - 80 - 0]$	25:46		13	2.94×10^3	7.07×10^3	3.19×10^2	1.53×10^{-2}
$[100 - 0 - 0]$	30:38	850	6	8.36×10^2	8.91×10^2	1.21×10^3	6.66×10^{-3}
$[40 - 60 - 0]$	31:08		7	4.17×10^2	2.10×10^3	1.25×10^4	3.11×10^{-3}
$[10 - 90 - 0]$	32:41		10	3.21×10^3	1.23×10^4	2.45×10^2	2.07×10^{-2}
$[100 - 0 - 0]$	33:33		12	7.98×10^2	8.05×10^2	1.06×10^3	7.79×10^{-3}

Table C.4: Estimated $i^{\circ}_{H_2S}$, $i^{\circ}_{H_2}$, and $i^{\circ}_{O_2}$ (case 3) as functions of y_{H_2}

$[H_2S - N_2 - H_2]$ (ml/min)	Time (hh:mm)	T (°C)	IV (#)	$i^{\circ}_{H_2S}$ (A/m^2)	$i^{\circ}_{H_2}$ (A/m^2)	$i^{\circ}_{O_2}$ (A/m^2)	Scaled fit –
[40 – 60 – 0]	3:52		10	1.24×10^2	2.69×10^3	6.19×10^1	1.76×10^{-2}
[40 – 50 – 10]	5:05	750	12	0	1.17×10^3	6.02×10^1	1.79×10^{-2}
[40 – 40 – 20]	5:25		13	0	7.75×10^2	5.59×10^1	2.02×10^{-2}
[40 – 20 – 40]	6:02		14	0	4.99×10^2	5.07×10^1	2.21×10^{-2}
[100 – 0 – 0]	6:25		15	6.96×10^2	1.89×10^3	6.82×10^1	1.81×10^{-2}
[40 – 60 – 0]	8:49		3	1.20×10^3	1.22×10^3	5.46×10^2	1.65×10^{-3}
[40 – 50 – 10]	9:31	800	5	6.55×10^3	8.42×10^2	5.15×10^2	3.02×10^{-3}
[40 – 20 – 40]	9:52		6	1.21×10^3	5.16×10^2	2.53×10^2	1.37×10^{-3}
[100 – 0 – 0]	10:10		7	7.90×10^2	6.98×10^2	6.68×10^2	4.29×10^{-3}
[20 – 80 – 0]	25:46		13	2.94×10^3	7.07×10^3	3.19×10^2	1.53×10^{-2}
[20 – 60 – 20]	26:14		14	9.60×10^3	0	4.19×10^2	6.08×10^{-3}
[40 – 60 – 0]	31:08		7	4.17×10^2	2.10×10^3	1.25×10^4	3.11×10^{-3}
[40 – 50 – 10]	31:40	850	8	1.08×10^3	6.56×10^2	1.79×10^3	6.06×10^{-3}
[40 – 20 – 40]	32:03		9	3.89×10^3	2.85×10^2	3.55×10^2	3.11×10^{-3}
[10 – 90 – 0]	32:41		10	3.21×10^3	1.23×10^4	2.45×10^2	2.07×10^{-2}
[10 – 80 – 10]	33:05		11	9.74×10^2	1.21×10^3	7.45×10^2	2.23×10^{-3}
[100 – 0 – 0]	33:33		12	7.98×10^2	8.05×10^2	1.06×10^3	7.79×10^{-3}